Determining the Neutrino Mass Hierarchy with KM3NeT/ORCA

Liam Quinn, La Détermination de La Hiérarchie, Justin Evans, Jason Koskinen, Cristinel Diaconu, Paschal Coyle

To cite this version:

Liam Quinn, La Détermination de La Hiérarchie, Justin Evans, Jason Koskinen, Cristinel Diaconu, et al.. Determining the Neutrino Mass Hierarchy with KM3NeT/ORCA. High Energy Physics - Experiment [hep-ex]. Aix Marseille Universitè, 2018. English. NNT : . tel-02265297

HAL Id: tel-02265297
https://hal.in2p3.fr/tel-02265297

Aix-Marseille Université

Physique et Sciences de la Matière

KM3NeT

Centre de Physique des Particules de Marseille

Thèse présentée pour obtenir le grade universitaire de docteur
en physique des particules et astroparticules

Liam Quinn

Determining the Neutrino Mass Hierarchy with KM3NeT/ORCA

La Détermination de la Hiérarchie de Masse des Neutrinos avec KM3NeT/ORCA

Soutenue le 09/11/2018 devant le jury composé de:

Jennifer Thomas	University College de Londres	Rapporteur
Juan Zúñiga Román	Université de Valence	Rapporteur
Justin Evans	Université de Manchester	Examinateur
Jason Koskinen	Université de Copenhague	Examinateur
Anne Stutz	Université Grenoble Alpes	Examinateur
Cristinel Diaconu	Aix-Marseille Université, CPPM	Directeur du CPPM
Paschal Coyle	Aix-Marseille Université, CPPM	Directeur de thèse

To Sophie, for being so patient the last three years.

Résumé

ORCA (Recherche d'Oscillations avec les Rayons Cosmiques dans l'Abysse) est un detecteur Tcherenkov de neutrinos à l'échelle des megatonnes, actuellement en construction par la collaboration KM3NeT, à 2450m de profondeur dans la mer méditerranée. Les neutrinos atmosphériques traversent la Terre le long d'un large éventail de lignes des bases, en subissant l'éffet de matière qui augmentent les oscillations des neutrinos avec énergies à l'ordre de peu GeV, qui dependent de la hiérarchie de masse des neutrinos (NMH). La conception d'ORCA comprise une dense configuration de modules optiques, qui contiennent 31 photomultiplicateurs (PMTs) de 72 mm, qui exploitent les excellentes propriétés de l'eau de la mer pour reconstruire à la fois les cascades (principalement ν_e) et les traces (principalement ν_μ) jusqu'à quelques GeV. Il est prévu que ORCA mesurera la NMH avec une significance statistique plus grand que 3σ après quelques années d'operation continue. Ce travail s'axe sur la reconstruction d'évenements ainsi que les méthodes et resultats des études de sensibilité à la hiérarchie de masse et aux paramètres d'oscillation θ_{23} et Δm^2_{32}.

Abstract

ORCA (Oscillation Research with Cosmics in the Abyss) is a megaton-scale Cherenkov neutrino detector currently under construction by the KM3NeT collaboration, at a depth of 2450m in the Mediterranean Sea. Atmospheric neutrinos cross the Earth along a wide range of baselines, undergoing matter effects which enhance neutrino oscillations in the few GeV energy range with a dependence on the neutrino mass hierarchy (NMH). The ORCA design consists of a dense configuration of optical modules, containing 31 3” photomultiplier tubes (PMTs), exploiting the excellent optical properties of deep seawater to reconstruct both cascade events (mostly ν_e) and track events (mostly ν_μ) down to a few GeV. ORCA is expected to measure the NMH with a median significance greater than 3σ after a few years of operation. This work focuses on event reconstruction, as well as the methods and results of the sensitivity studies for the measurement of the mass hierarchy and the oscillation parameters θ_{23} and Δm^2_{32}.

> "Qu'a vist Paris e noun Cassis a ren vist."
>
> Frédéric Mistral

Résumé en Français

Le Détecteur KM3NeT/ORCA

KM3NeT est une expérience sous marine de neutrino faisant partie de la prochaine generation de capteurs de neutrinos. Elle exploite le rayonnement Tcherenkov émis par les interactions des neutrinos dans l'eau pour le detecteur. KM3NeT est actuellement en construction au fond de la mer méditerranée, sur deux sites. Le réseau haute énergie, appelé ARCA (Recherche d'Astroparticules avec les Rayons Cosmiques dans l'Abysse), est situé à $36° \ 16'$ N $16° \ 06'$ E, approximativement 100 km de Portopalo di Capo Passero en Sicile. Le réseau basse énergie, appelé ORCA (Recherche d'Oscillations avec les Rayons Cosmiques dans l'Abysse), est situé à $42° \ 48'$ N $06° \ 02'$ E, à 2450 m de profondeur, au large de Toulon en France. ARCA a été dessiné pour capter les neutrinos cosmiques avec des énergies plus grandes que 1 TeV. ORCA a été dédié pour l'étude d'oscillations des neutrinos entre 1 et 100 GeV, et pour l'astronomie des neutrinos en dessous de 1 TeV.

Les conceptions d'ARCA et ORCA sont similaires; les différences principales sont leurs tailles et leurs densités. Pour cette raison, ce résumé ne décrira que celle d'ORCA (la conception d'ARCA et disponible dans Réf. [1]). ORCA se composera de 115 Unités de Détection (DUs), deployées avec une distance moyenne horizontale de 23 m. Chaque DU comprendra 18 Modules Optiques Digitaux (DOMs), separés de 9 m, le long d'une corde verticale, solidement fixée avec une ancre au fond et une bouée en haut. Un DOM est une sphère en verre transparent avec un diamètre de 17", laquelle contient 31 photomultiplicateurs (PMTs) de 3", optimisés pour capter la radiation Tcherenkov emise par les interactions de neutrinos dans l'eau de la mer.

Le dessin de DOM KM3NeT représente un changement par rapport à ceux des autres détecteurs Tcherenkov des neutrinos, tels qu'ANTARES [2] et IceCube [3]. Les avantages d'une conception multi-PMT (voir Fig. 1) incluent:

- Une couverture prèsque uniforme

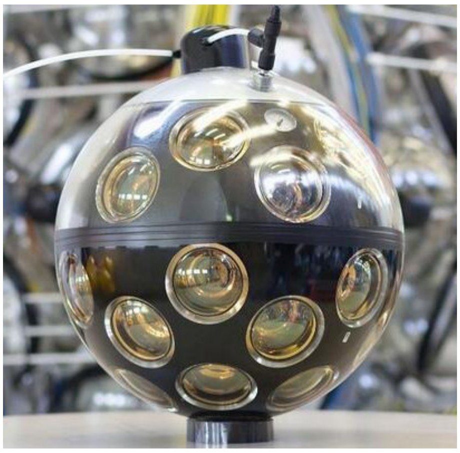

Figure 1: Une photographie d'un DOM complet, dans la galerie d'assemblage du CPPM (extrait de Réf [1]).

- Une superficie des photo-cathodes prèsque quatre fois superieure que les dessins traditionnels
- Il est possible de résoudre des photons coincidents séparément s'ils arrivents dans des PMTs adjacents
- Il y a une meilleure résistance aux pannes de PMTs; la perte d'un PMT n'entraînera qu'une perte de 3% d'efficacité

Les Oscillations des Neutrinos

Les neutrinos peuvent osciller entre leurs 3 saveurs car leurs états propres de masse sont distincts de leurs états propres de saveur. Les états propres de saveur ($|\nu_{e,\mu,\tau}\rangle$) et les états propres de masse ($|\nu_{1,2,3}\rangle$) sont reliés par une matrice de rotation 3 × 3,

$$\begin{pmatrix}\nu_e\\ \nu_\mu\\ \nu_\tau\end{pmatrix} = \begin{pmatrix}U_{e1} & U_{e2} & U_{e3}\\ U_{\mu1} & U_{\mu2} & U_{\mu3}\\ U_{\tau1} & U_{\tau2} & U_{\tau3}\end{pmatrix}\begin{pmatrix}\nu_1\\ \nu_2\\ \nu_3\end{pmatrix}. \tag{1}$$

Cette matrice, appelée la matrice PMNS en l'honneur de Bruno Pontecorvo, Ziro Maki, Masami Nakagawa, et Shoichi Sakata, est souvent parameterisée par trois angles de mélange ($\theta_{12}, \theta_{13}, \theta_{23}$) et une phase complèxe (δ):

$$\mathbf{U} = \begin{pmatrix}1 & 0 & 0\\ 0 & \cos\theta_{23} & \sin\theta_{23}\\ 0 & -\sin\theta_{23} & \cos\theta_{23}\end{pmatrix}\begin{pmatrix}\cos\theta_{13} & 0 & e^{-i\delta}\sin\theta_{13}\\ 0 & 1 & 0\\ -e^{i\delta}\sin\theta_{13} & 0 & \cos\theta_{13}\end{pmatrix}\begin{pmatrix}\cos\theta_{12} & \sin\theta_{12} & 0\\ -\sin\theta_{12} & \cos\theta_{12} & 0\\ 0 & 0 & 1\end{pmatrix}. \tag{2}$$

Le états propres de masse se propagent comme une onde plane et, par conséquent, la probabilité de transition entre des états propres de saveur (α, β) peut être décrite en termes de la différence des masses carrées ($\Delta m^2_{jk} = m^2_j - m^2_k$). Dans la

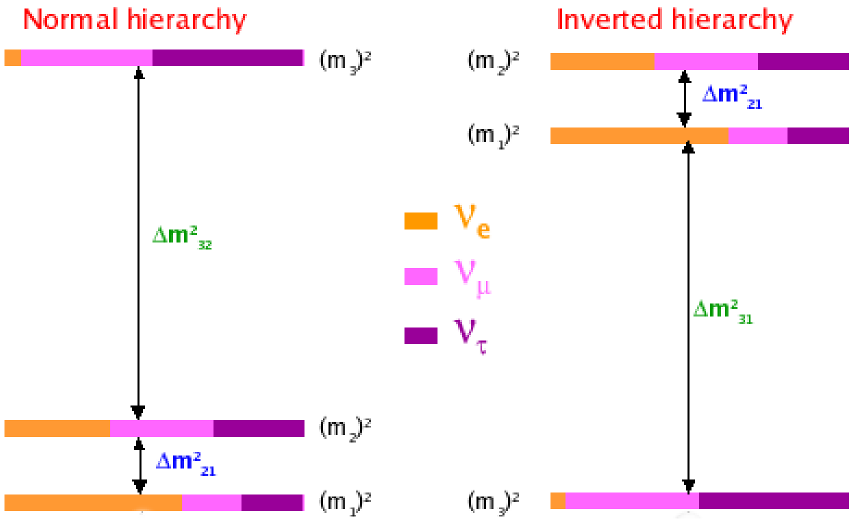

Figure 2: Les deux hiérachies de masse possibles. Ici les couleurs représentent la contribution relative de chaque composante de saveur dans chaque état propre de masse (extrait de Réf. [1]).

vide, cela est donnée par

$$|\langle \nu_\alpha | \nu_\beta(t) \rangle|^2 = \sum_{j=1}^{3} \sum_{k=1}^{3} U_{\alpha j} U^*_{\beta j} U^*_{\alpha k} U_{\beta k} e^{\frac{-i\Delta m^2_{jk} L}{2E_\nu}}, \tag{3}$$

où E_ν est l'energie du neutrino, L est la distance qu'il a voyagé. Il est évident qu'aucune mesure des oscillations dans la vide ne sera sensible ni aux valeurs absolus des masses ni aux signes des differences des masses carrées. Après avoir défini que $m_2 > m_1$, il reste deux possibles hiérarchies de masse des neutrinos. Elles sont la hiérarchie normale (NH), où $m_3 > m_2$, et l'hierarchie inversée (IH), où $m_3 < m_1$ (voir Fig. 2).

Le signe de Δm^2_{32} peut être déterminé grâce à l'éffet de la matière quand un neutrino traverse la Terre. La composante ν_e du flux de neutrinos atmosphériques subit une diffusion élastique à courant chargé avec les électrons dans la matière. Cela introduit un potentiel effectif (V_c), donné par

$$V_c = \pm G_F N_e \sqrt{2}, \tag{4}$$

où N_e est la densité d'electrons dans la matière et G_F est la constante de couplage de Fermi. Elle est positive pour les neutrinos et negative pour les antineutrinos. Après avoir pris en compte la perturbation donnée par ce potentiel effectif, les probabilités de transition deviennent sensibles à la'hiérarchie de masse (voir Fig. 3).

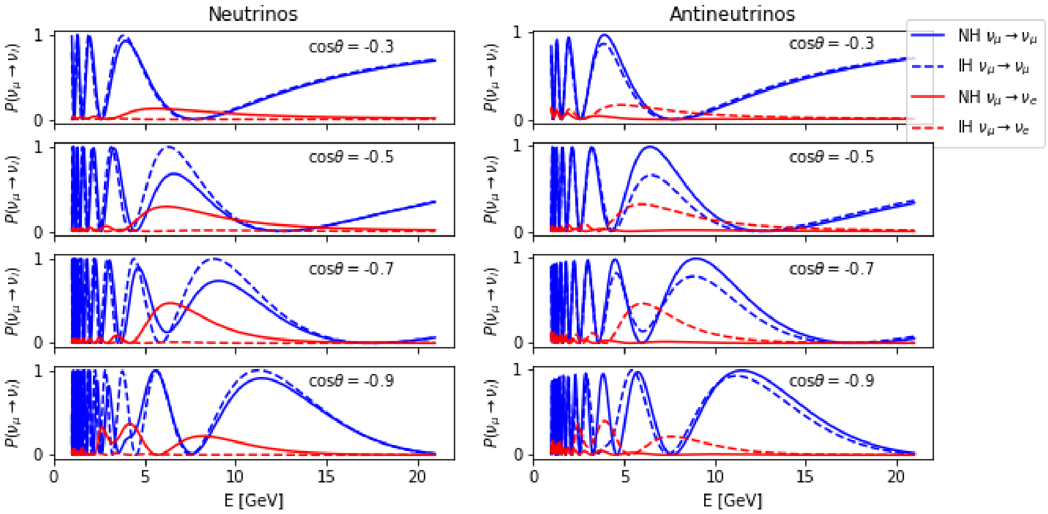

Figure 3: Les probabilités de transition $\mathcal{P}(\nu_\mu \to \nu_e)$ et $\mathcal{P}(\nu_\mu \to \nu_\mu)$ en fonction de l'énergie, pour différents angles de zénith et pour les deux hiércharchies de masse.

La Sensibilité à la Hiérarchie de Masse

Le nombre de neutrinos d'une saveur et une chiralité indiquées par i, qui interagissent avec l'eau de la mer, par unité de volume, est donné par

$$N_i^{\text{int}}(\theta_\nu, E_\nu) = \frac{\sigma_i(E_\nu)\Delta t}{m_{\text{nucleon}}} \sum_j \Phi_j(\theta_\nu, E_\nu)\mathcal{P}_{ji}^{\text{osc}}(\theta_\nu, E_\nu), \tag{5}$$

où σ est la section efficace, Δt est la durée de l'expérience, m_{nucleon} est la masse des nucleons dans l'eau, Φ_j est le flux de neutrinos atmosphériques avant oscillation (pour chaque saveur j), et $\mathcal{P}_{ij}^{\text{osc}}$ sont les probabilités de transition.

La matrix de réponse du detecteur $\mathbf{\Omega}$ et definie pour relier les propriétés des neutrinos incidents: leurs directions, énergies, saveurs et chiralités, aux informations mesurées par le detecteur: la direction reconstruite, l'énergie reconstruite et deux catégories selon la topologie d'événement. En général, les événements $\nu_\mu/\bar{\nu}_\mu$-CC sont classifiés comme *traces*, grâce à la longue portée des muons dans l'eau. Tous les autres interactions sont definies comme *cascades*. Ainsi, la matrix de réponse est la probabilité qu'un neutrino avec une saveur, une chiralité, un zénith et une énergie donnés soit reconstruit avec une énergie E_ν^{rec} et un zénith et θ_ν^{rec}, et assigné la catégorie α, multipliée avec le volume effectif du detecteur. Par conséquent, la distribution d'événements prévue en fonction d'énergie et de zénith reconstruits est la suivante:

$$N_\alpha(\theta_\nu^{\text{rec}}, E_\nu^{\text{rec}}) = 2\pi \int d\cos\theta_\nu dE_\nu \sum_i \Omega_{i\alpha}(\theta_\nu^{\text{rec}}, E_\nu^{\text{rec}}; \theta_\nu, E_\nu) N^{\text{int}}(\theta_\nu, E_\nu). \tag{6}$$

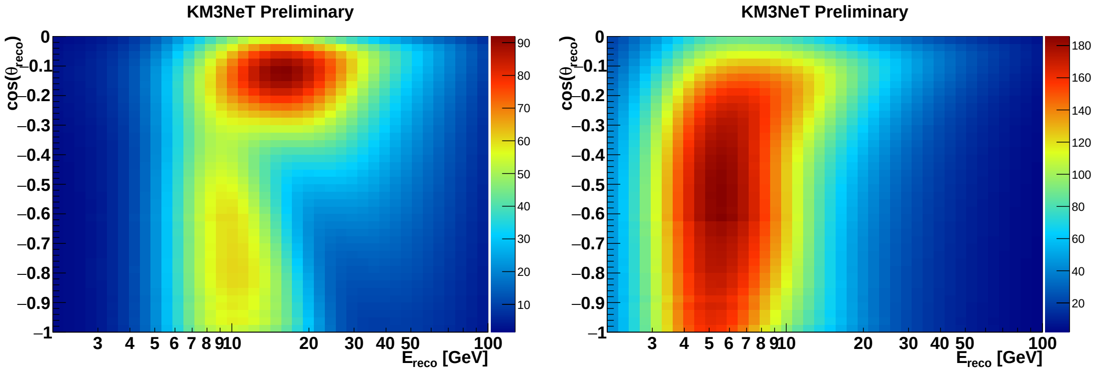

(a) Traces

(b) Cascades

Figure 4: La distribution des événements en fonction d'énergie et de zénith reconstruits pour chaque catégorie, en supposant que la hiérarchie de masse est normale, $\theta_{23} = 45°$ et $\delta^{CP} = 0°$

.

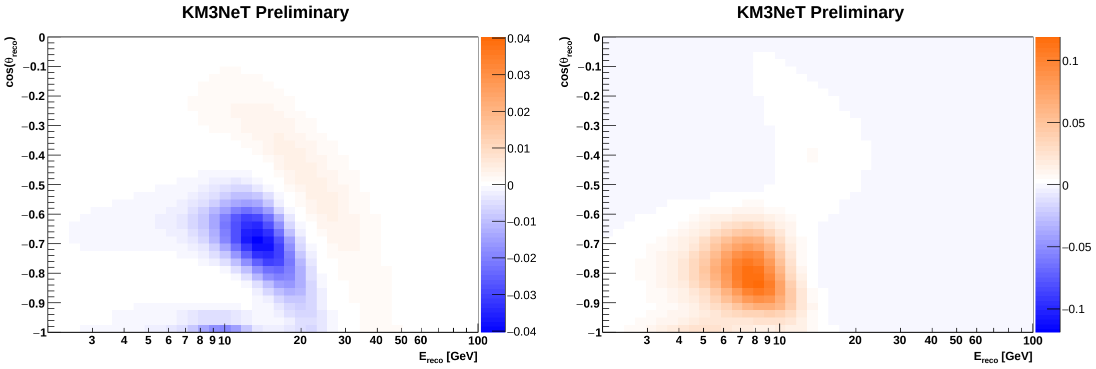

(a) Traces

(b) Cascades

Figure 5: Le chi carré signé pour chaque catégorie, en supposant que $\theta_{23} = 45°$ et $\delta^{CP} = 0°$.

Paramètre	Traitement	Valeur Vrai	Contrainte
$\Delta m^2_{12}[\mathrm{eV}^2]$	Fixé	7.40×10^{-5}	N/A
$\Delta m^2_{23}[\mathrm{eV}^2]$	Libre	2.420×10^{-3}	N/A
$\theta_{12}[°]$	Fixé	33.4	N/A
$\theta_{13}[°]$	Contraint	8.62	0.15°
$\theta_{23}[°]$	Libre	$40 - 50$	N/A
$\delta^{CP}[°]$	Libre	0 or 180	N/A
Normalisation des traces	Libre	1	N/A
Normalisation des cascades	Libre	1	N/A
Normalisation des événements NC	Contraint	1	10%
Inclinsaison du spectre	Libre	0	N/A
Asymmétrie $\nu/\bar{\nu}$	Contraint	0	3%
Asymmétrie $\nu_e/\bar{\nu}_e$	Contraint	0	10%
Asymmétrie $\nu_\mu/\bar{\nu}_\mu$	Contraint	0	10%
Asymmétrie ν_e/ν_μ	Contraint	0	5%
Déplacement d'énergie	Contraint	0	10%

Table 1: La liste complète de paramètres d'oscillation et nuisances inclus dans cette étude, avec leur traitements statistiques et leurs contraintes, il y a lieu.

Cette distribution est représentée la Fig. 4.

La significance moyenne avec laquelle la hiérarchie inversée sera rejetée, dans le cas où la hiérarchie est normale, est donnée par la racine carrée du chi carré.

$$\Delta\chi^2 = \sum_i^N \frac{(\mu_i^{NH} - \mu_i^{IH})^2}{\mu_i^{IH}}, \tag{7}$$

où μ est le nombre d'événements prévu dans chaque catégorie d'énergie et zénith selon chaque hypothèse NH/IH. Pour rejeter la hiérarchie normale, il suffit d'échanger les exposants. La Fig. 5 montre l'asymmetrie resultant entre l'NH et l'IH après avoir pris en compte la réponse du detecteur.

Cependant, l'expression dans Eq. 7 présume que les paramètres d'oscillation sont déjà connus avec une précision parfaite. En réalité, il faut prendre en compte les incertitudes associés avec paramètres d'oscillation et les paramètres de nuisance, ainsi nommés parce qu'ils dégradent la sensibilité du detecteur. On choisit l'ensemble de valeurs $\boldsymbol{\eta}$ qui minimise la significance moyenne. Eq. 7 devient

$$\Delta\chi^2(\boldsymbol{\eta}) = \sum_i^N \frac{(\mu_i^{NH}(\boldsymbol{\eta}^{\mathrm{vrai}}) - \mu_i^{IH}(\boldsymbol{\eta}))^2}{\mu_i^{IH}(\boldsymbol{\eta})} + \sum_i^M \left(\frac{\eta_i - \eta_i^{\mathrm{vrai}}}{\sigma_i^{\eta}}\right)^2, \tag{8}$$

où la deuxième terme reflète les contraintes externes imposées sur les paramètres de nuisance (la liste complète est montré dans la Table 1).

Dans la Fig. 6, la significance moyenne avec laquelle la mauvaise hiérarchie de masse sera rejetée est montrée, pour toutes les valeurs favorisées de θ_{23}, pour la valeur la plus optimiste et la valeur la plus pessimiste de δ^{CP}. Une significance près de 3σ est prévue après trois ans d'opération continue.

Outre la sensibilité à la hiérarchie de masse, le contour 90% C.L. en θ_{23} et Δm_{32}^2 a été calculé, en supposant que la hiérarchie de masse est normale. La même approche a été employée, en suivant Eq. 8,

$$\Delta\chi^2(\boldsymbol{\eta}|\theta_{23}, \Delta m_{32}^2 \in \boldsymbol{\eta}) = \sum_i^N \frac{(\mu_i^{NH}(\boldsymbol{\eta}^{\mathrm{vrai}}) - \mu_i^{NH}(\boldsymbol{\eta}))^2}{\mu_i^{NH}(\boldsymbol{\eta})} + \sum_i^M \left(\frac{\eta_i - \eta_i^{\mathrm{vrai}}}{\sigma_i^{\eta}}\right)^2. \tag{9}$$

La Fig. 7 montre le contour resultant, surimposé sur les limites actuelles obtenues par NOvA [4], Minos [5], IceCube [6], Super Kamiokande [7], T2K [8].

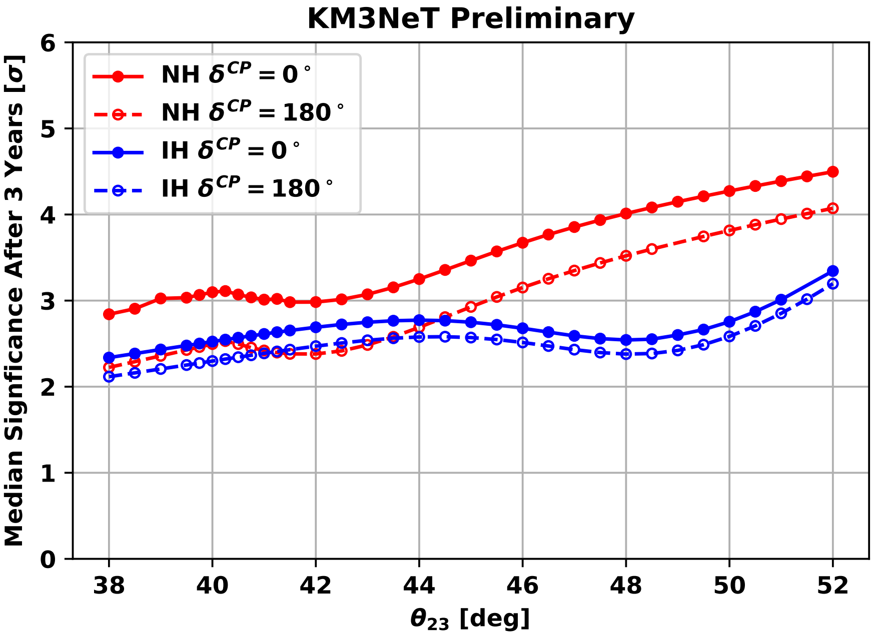

Figure 6: La significance moyenne après 3 ans, en fonction de θ_{23} avec la traitement d'erreurs systematiques descrits dans Table 1, pour les valeurs la plus optimiste et la plus pessimiste de δ^{CP}.

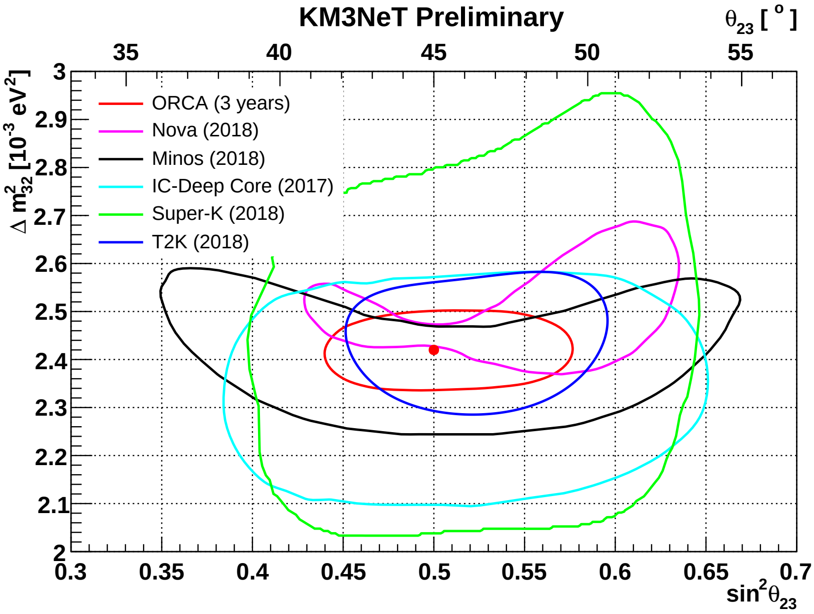

Figure 7: Le contour à 90% CL, montré parmi les resultats actuels de NOvA [4], Minos [5], IceCube [6], Super Kamiokande [7], T2K [8]. Il était supposé que $\theta_{23} = 45°$, $\delta^{CP} = 0°$.

Conclusion

Les oscillations des neutrinos sont la première indication de physique nouvelle, hors le modèle standard. Jusqu'ici, la hiérarchie de masses de neutrinos est inconnue. ORCA pourra la déterminer après trois ans d'opération continue, ainsi que fournir des contraintes sur θ_{23} et Δm^2_{32} competitives avec les meilleures limites au monde.

Acknowledgements

I would like to express my gratitude to Paschal, my supervisor, for his help and support over the last three years. Throughout this PhD, I have been able to count on the knowledge and expertise of my colleagues at CPPM: Jürgen Brunner, Vincent Bertin, Damien Dornic, Matthieu Perrin-Terrin, Alexander Enzenhöfer, Vladimir Kulikovsky, Dmitry Zaborov, Giuliano Maggi, Ilenia Salvadori, Alba Domi, and Massilimiliano Lincetto. For that I am truly grateful.

The entire KM3NeT and ANTARES collaborations are deserving of thanks. Ours is a relatively small physics experiment, where everyone knows each other by first name and everybody is approachable. I couldn't have been happier with the atmosphere and environment we worked in. Special thanks to Maarten de Jong, João Coelho and everyone else whose software development laid the groundwork for this thesis. Of course, none of this would have happened were it not for the IFIC Group who took me in and treated me as one of their own during my Master's project in Valencia. Sabéis quienes sois. Gracias a cada uno de vosotros.

I would also like to give a special mention to those students who went through their PhDs at the same time as me, with whom I was able to swap war stories and commiserate over software bugs. Venugopal Ellajosyula, Joan Arnau Romeu, Robert Wolff, Martijn Jongen, Karel Melis, Robert Bormuth, Marta Colomer, Jannik Hofestädt, Steffen Hallman, and Simon Bourret, thank you all.

To my friends and family in Linslade and Leighton Buzzard, thank you for being so supportive and welcoming on my far too infrequent visits back. Thank you to my long-suffering language teachers at Cedars Upper School. I couldn't have guessed quite how crucial those French and Spanish A-Levels turned out to be.

Finally, I would like to thank Sophie, who has tolerated my running off to Southern Europe, not once, but twice. Let's try to live in the same country from now on.

Declaration

This thesis was funded through the ASERICS project, as part of the European Commission's Horizon 2020 Programme. Software developed during the course of this thesis shall be released publicly as part of the OBELICS D-ANA repository, to be completed in April 2019.

Contents

Chapter 1

Theory and Background

This work concerns neutrinos, fundamental particles of neutral charge, and very little mass, which only rarely interact with matter, via the weak force. The primary focus of this thesis shall be on neutrino mass, for whose discovery Takaaki Kajita and Arthur B. McDonald were jointly awarded the 2015 Nobel Prize in Physics. The discovery of neutrino mass opens up an exciting new chapter in the history of particle physics, representing Nature's first known detour from the Standard Model (SM).

There remain many unanswered questions regarding neutrino mass, which will be discussed in more detail in Section 1.5. This work will discuss the prospect of measuring the neutrino mass hierarchy (NMH), the order of the neutrino masses, by deploying a detector on the Mediterranean seafloor, at a depth of 2450 m, in order to detect the Cherenkov signatures of atmospheric neutrinos that have passed through the Earth. See Chapter 2 for an overview of the KM3NeT design and infrastructure.

This introductory chapter will start with a brief discussion of the Standard Model in Section 1.1, followed by a historical overview of neutrino physics in Section 1.3. Neutrino mass will be discussed in general terms in Section 1.5, including the theoretical motivation for measuring the NMH.

1.1 The Standard Model

The 17 known fundamental particles of the standard model (Table 1.1) comprise 12 fermions, with spin $\frac{1}{2}$, and 5 bosons, with integer spin. They are the 4 force-carrying vector bosons, the gluon, the photon, and the W and Z bosons; the

	Fermions			Vector Bosons	Scalar Bosons
Quarks	u d	c s	t b	g	H
Leptons	e ν_e	μ ν_μ	τ ν_τ	γ $Z^0/W^\pm$	

Table 1.1: An overview of all the fundamental particles in the Standard Model. The fermions can only interact through the exchange of a vector boson on their own row or lower.

6 quarks, which interact with all four fundamental forces and whose bound states include protons and neutrons; the 6 leptons, which are not subject to the strong interaction; and the recently discovered Higg's Boson, an excitation in the Higgs field, through which SM particles get their mass.

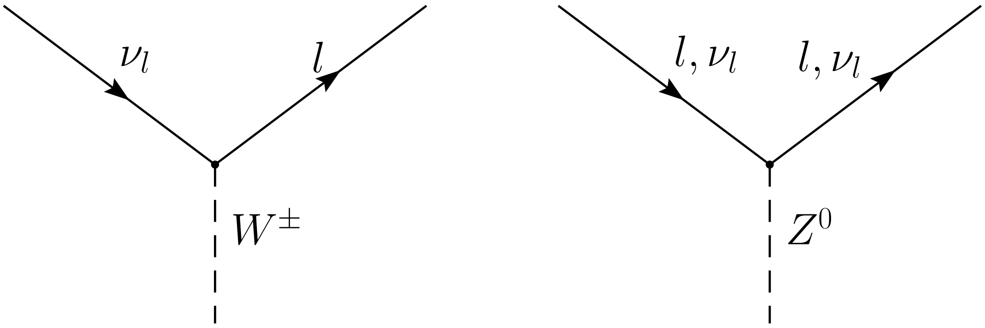

(a) Charged current

(b) Neutral current

Figure 1.1: Two neutrino interaction weak interaction vertices, where l denotes any of the three charged leptons.

In brief, the four fundamental forces are as follows.

The Strong Force is mediated by the gluon, and holds together bound states of quarks, such as atomic nuclei.

The Electromagnetic Force is mediated by the photon and is responsible for electric fields, magnetic fields and light.

The Weak Force is mediated by the W and Z bosons and is the only interaction which changes the flavour of quarks and violates the P and CP symmetries.

Gravity is by far the weakest fundamental force and is not included in the SM. It is described by general relativity.

Each of the 3 flavours of charged lepton (e, μ, τ) has an associated neutrino $(\nu_e, \nu_\mu, \nu_\tau)$. Weak interactions involving neutrinos preserve the total number of leptons of each flavour. For example, the decay $\mu^- \to e^- + \bar{\nu}_e + \nu_\mu$ has been observed, but $\mu^- \to e^- + \gamma$ has not.

Another interesting property of the weak force is its dependence on chirality, also called handedness. In the high energy limit, this is equivalent to the helicity:

$$h = \frac{\boldsymbol{p}}{|\boldsymbol{p}|} \cdot \boldsymbol{s}, \tag{1.1}$$

where $\boldsymbol{p}$ and $\boldsymbol{s}$ are the particle's momentum and spin respectively. If its momentum and spin are parallel, a particle is said to be right handed. If they are antiparallel, it is said to be left handed. The weak interaction only involves left handed particles and right handed antiparticles.

1.2 Neutrino Interaction Cross Sections

As shown in Fig. 1.2, there are three processes that dominate neutrino interactions in the energy region of interest for ORCA. They are (quasi-)elastic scattering, resonance production and deep inelastic scattering. Elastic scattering refers to a neutral current interaction, mediated by a Z^0 boson. On the other hand, charged-current interactions, mediated by a $W^\pm$ and resulting in the creation of a charged lepton, are referred to as quasi elastic. Resonance production refers to processes where the target nucleon is excited to a resonant state, (Δ, N) [9], which subsequently emits pions on its decay. In the case of deep inelastic scattering, the neutrino can probe the consituent quarks within the nucleon, resulting it breaking up and expelling a shower of hadrons.

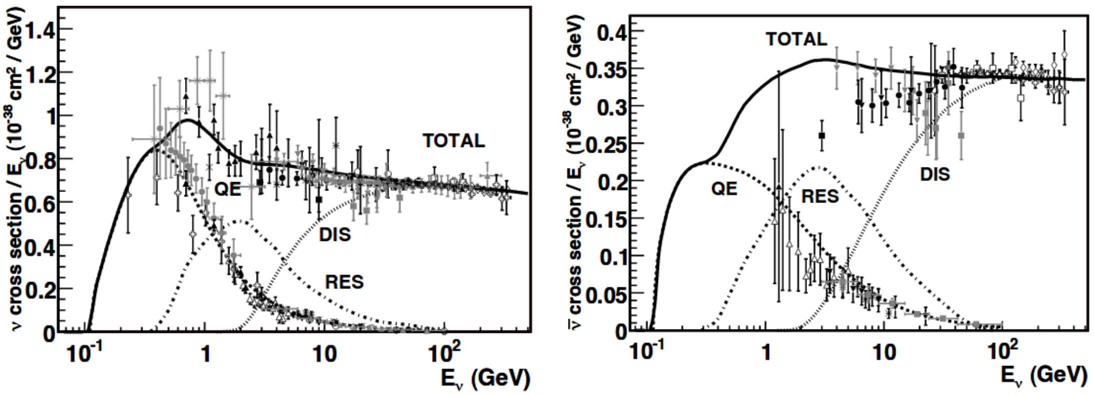

(a) Neutrinos (b) Antineutrinos

Figure 1.2: The total neutrino charged-current cross sections as a function energy, for an isoscalar target. Taken from Ref. [9].

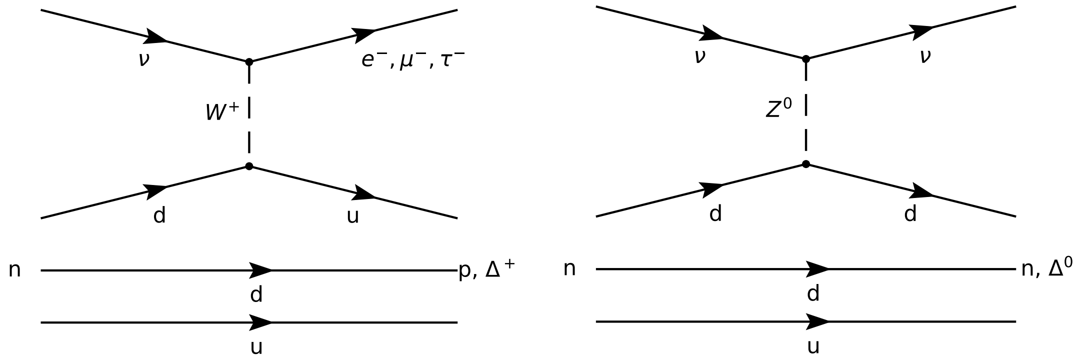

(a) Charged current (b) Neutral current

Figure 1.3: A schematic overview of (quasi-)elastic scattering and resonance production between a neutrino and a neutron.

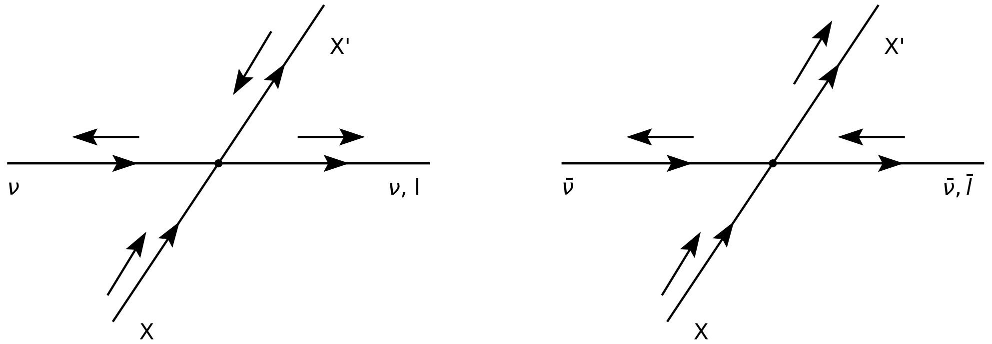

(a) $J_z = 0$ (b) $J_z = 1$

Figure 1.4: A neutrino or antineutrino scattering off a target (X), showing the helicity of each particle in the interaction, based on arguments in Ref. [10].

Weak interactions are only observed between left-handed particles (and right-handed antiparticles). In the limit $|\mathbf{p}| \gg m$, chirality is equivalent to helicity, the projection of a particle's spin vector in the direction of its momentum. Left and right handed leptons have helicity $-\frac{1}{2}$ and $\frac{1}{2}$ respectively. For antineutrinos, this results in a net angular momentum along the axis of the interaction, whose conservation introduces a preference for forward scattering (see Fig. 1.4). This can be described as follows,

$$\frac{d\sigma_{J_z=0}}{d\theta} \propto \text{const}, \tag{1.2}$$

$$\frac{d\sigma_{J_z=1}}{d\theta} \propto \left(\frac{1-cos\theta}{2}\right)^2, \tag{1.3}$$

where θ is the centre of mass scattering angle. Integrating Equations 1.2 and 1.3 over the scattering angle yields the ratio

$$\frac{\sigma_{J_z=0}}{\sigma_{J_z=1}} = 3, \tag{1.4}$$

which approximately explains the difference between the neutrino and antineutrino cross sections shown in Fig. 1.2. This can also be related to the inelasticity, defined in terms of the neutrino and lepton energy (E_ν and E_l),

$$y = \frac{E_\nu - E_l}{E_\nu}, \tag{1.5}$$

$$= \frac{1-cos\theta}{2}. \tag{1.6}$$

By comparing equations 1.3 and 1.6, it can be seen that antineutrino interactions generally have a smaller scattering angle and transfer more energy into the outgoing lepton.

1.3 Historical Background

The existence of a hitherto undetected neutrally charged particle was proposed in 1930 by Wolfgang Pauli in order to explain the apparent non-conservation of energy in beta decay. Pauli named his hypothesised particle the neutron, two years before the discovery of what is now called the neutron. The word "neutrino" is attributed to Enrico Fermi.

The first neutrino detection would not be until the late 1950s, by the Cowan-Reines experiment [11][12]. The detection mechanism was as follows

$$\bar{\nu}_e + p \rightarrow n + e^+, \tag{1.7}$$

in tanks of water and Cadmium Chloride, placed between two scintillation detectors, next to a nuclear fission reactor. An incoming antineutrino would then be identified by two pulses in a short time window, one from the positron annihilation and the second from neutron capture. For this discovery, Frederick Reines was awarded half a share in the 1995 Nobel Prize for Physics.

In the 1970s, the Homestake Experiment [13] would be the first to detect solar neutrinos. The mechanism was inverse beta decay using tanks of perchloroethylene as the target volume

$$\nu_e +^{37}\mathrm{Cl} \rightarrow^{37}\mathrm{Ar} + e^-. \tag{1.8}$$

The neutrino flux could then be determined by measuring the amount of ^{37}Ar produced. A deficit was measured with respect to the expected solar ν_e flux, which was known as the Solar Neutrino Problem. Note that fusion processes in the Sun only produce ν_es. By this time, a mechanism had already been proposed by Bruno Pontecorvo in which, if neutrinos were massive, they could transition between flavours [14]. As the Homestake experiment was not sensitive to ν_μs or ν_τs, this could explain the observed deficit.

The first evidence of atmospheric neutrino oscillations came from the Super-Kamiokande experiment in 1998 [15]. Super-Kamiokande is composed of a 22.5 kton tank of purified water, surrounded by 11,146 photomultiplier tubes, which detect the Cherenkov radiation emitted by neutrino interactions in the water (see Chapters 2 and 3 for a more detailed discussion of Cherenkov radiation in water). In Fig. 1.5 a clear deficit of ν_μ events can be seen compared to the expectation without neutrino oscillations, by which the expected event rate in the presence of $\nu_\mu \rightarrow \nu_\tau$ oscillations is well described. Note that the high mass of the τ imposes a higher energy threshold on ν_τ-CC interactions, which suppresses their appearance in the energy range measured by Super-Kamiokande in Ref. [15], so ν_τ appearance was not observed (see Refs. [16, 17] for subsequent ν_τ observations with an upgraded Super-Kamiokande detector).

The Sudbury Neutrino Observatory (SNO) [18] is another water Cherenkov Neutrino detector, located within the Creighton Mine near Sudbury, Canada. Using heavy water as its target, SNO is sensitive to solar neutrinos via three mechanisms:

$$\nu_e + d \rightarrow p + p + e^- \qquad \text{(charged current)}, \tag{1.9}$$

$$\nu_l + d \rightarrow p + n + \nu_l \qquad \text{(neutral current)}, \tag{1.10}$$

$$\nu_l + e^- \rightarrow \nu_l + e^- \qquad \text{(elastic scattering)}, \tag{1.11}$$

where the index l simply refers to any lepton flavour. In SNO, charged current reactions are only sensitive to ν_es, neutral current reactions are equally sensitive to all flavours, and elastic scattering is sensitive to all flavours, but this sensitivity is

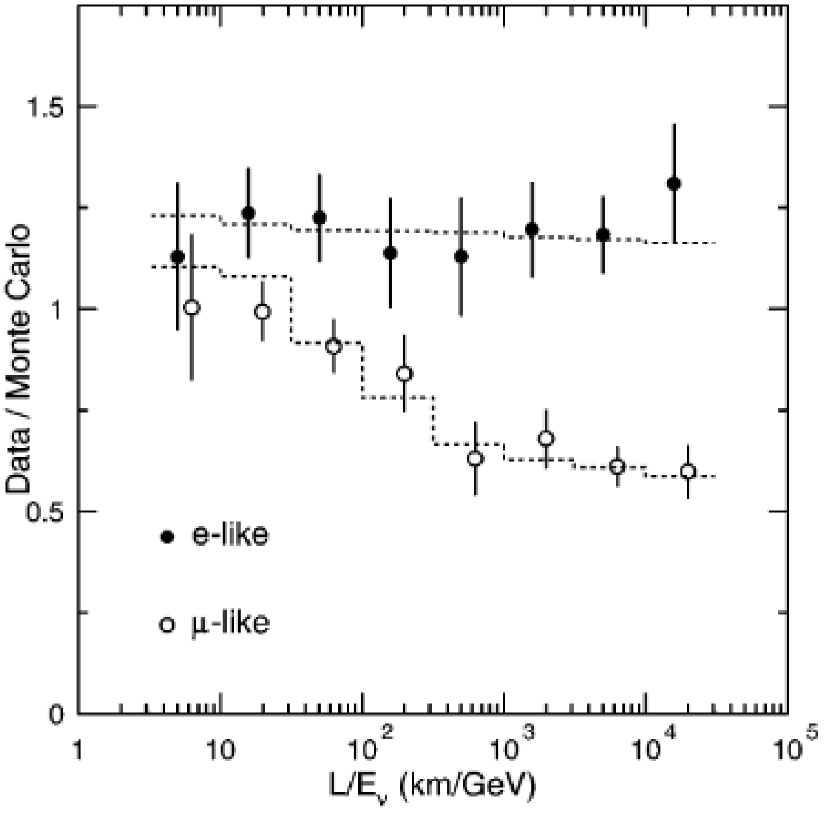

Figure 1.5: The ratio of fully-contained event rates with respect to the expectation without oscillations. The dashed line shows the expected shape for $\nu_\mu \rightarrow \nu_\tau$ transitions. Taken from Ref. [15].

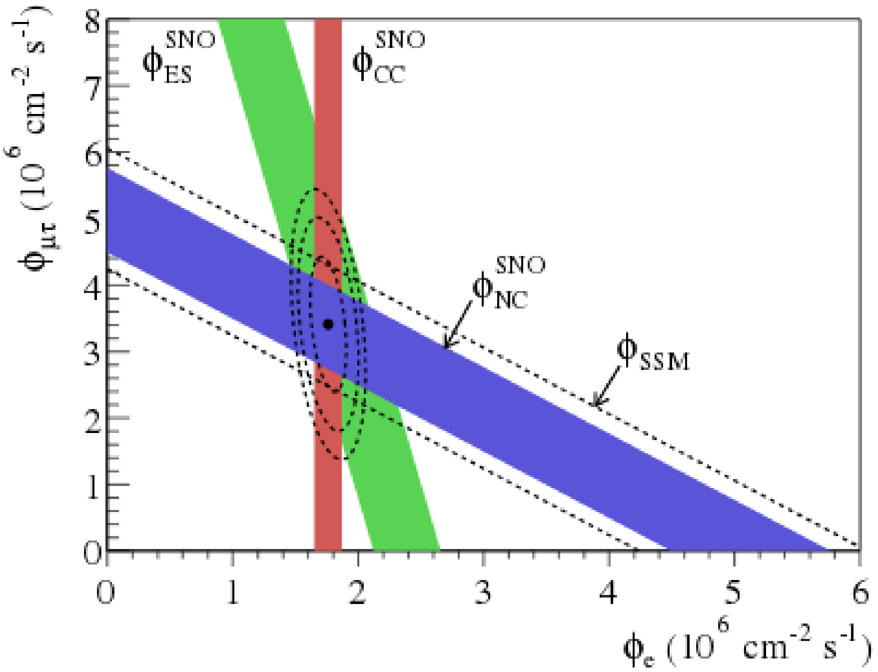

Figure 1.6: The solar neutrino flux corresponding to each interaction channel in SNO, compared against the standard solar model. The width of each band against the axes represents the ±1σ error. Taken from Ref. [19].

enhanced for ν_es. It was therefore possible to determine not only the ν_e contribution of the solar neutrino flux, but also the sum contributions of all flavours and to determine whether solar neutrinos were changing flavour. In 2002, SNO published their analysis combining all three channels [19]. It was shown that the solar neutrino flux did contain a ν_μ/ν_τ component and that the sum of all three flavour contributions was consistent with the Standard Solar Model expectation (Fig. 1.6). The KamLAND Collaboration would go on to confirm the existence of neutrino oscillations, by measuring $\bar{\nu}_e$ disappearance from reactor neutrinos emitted 180 km away [20]. This was at the Kamiokande site, Super-Kamiokande's predecessor, using inverse beta decay and liquid scintillation as its detection mechanism. This would represent the beginning of precision measurements in the neutrino sector. Takaaki Kajita and Arthur B. McDonald from Super-Kamiokande and SNO would go on to be awarded the Nobel Prize in 2015 for the discovery of neutrino oscillations.

1.4 Atmospheric Neutrinos

As the main focus on this work will be studies of atmospheric neutrinos, this section is dedicated to their production mechanism and flux. Atmospheric neutrinos are produced when high-energy cosmic rays interact with the Earth's atmosphere. These interactions create a cascade of particles, among which are

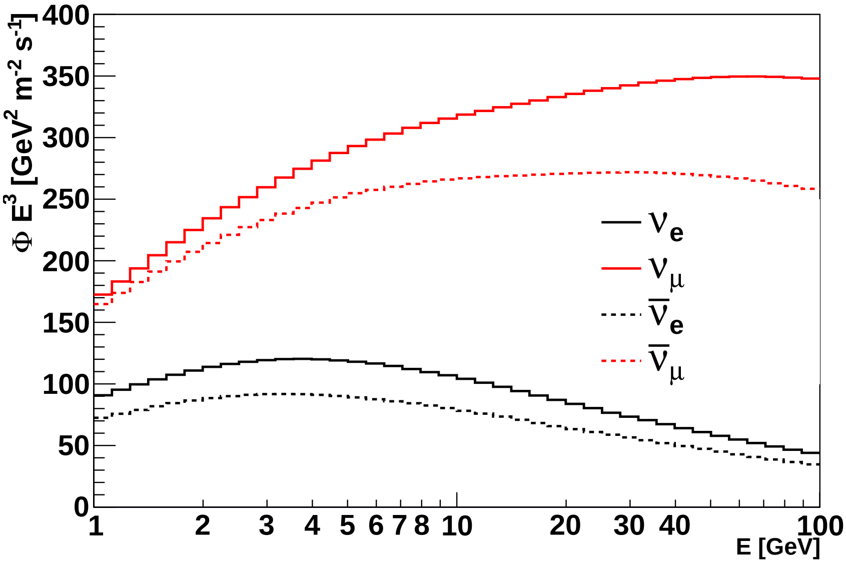

Figure 1.7: The Honda atmospheric neutrino flux [22].

kaons and charged pions, which decay to leptons and neutrinos. The most common decay modes and their branching ratios (rounded to the nearest percent) are shown below,

$$\begin{array}{lr} \pi^+ \to \mu^+\nu_\mu & (99\%) \\ K^+ \to \mu^+\nu_\mu & (64\%) \\ K^+ \to \pi^+\pi^0 & (21\%) \\ K^+ \to \pi^+\pi^+\pi^- & (6\%) \\ K^+ \to \pi^0 e^+\nu_e & (5\%) \\ K^+ \to \pi^+\pi^-\mu^+\nu_\mu & (4\%) \\ K^+ \to \pi^0\mu^+\nu_\mu & (3\%) \\ K^+ \to \pi^+\pi^0\pi^0 & (2\%) \\ \mu^+ \to \bar{\nu_\mu}\nu_e e^+ & (\approx 100\%) \end{array}$$

where the decays of negatively-charged particles are just the charge conjugate [21]. The unoscillated atmospheric neutrino flux is dominated by muon neutrinos, with most of the ν_e component coming from muon decays.

In Figs. 1.7 and 1.8, the atmospheric neutrino flux predicted in Ref. [22], is plotted for each flavour and chirality, and indeed the ratio $\frac{\nu_\mu+\bar{\nu}_\mu}{\nu_e+\bar{\nu}_e}$ is close to 2, as would be roughly expected purely from charged pion decays. In Fig. 1.9, the energy and zenith dependence of this ratio is plotted. It can be seen that this rule of thumb regarding the ν_μ/ν_e ratio starts to break down when considering either vertical or high energy neutrinos. This is because horizontal atmospheric muons have a longer path length in which to decay before reaching the ground and more energetic

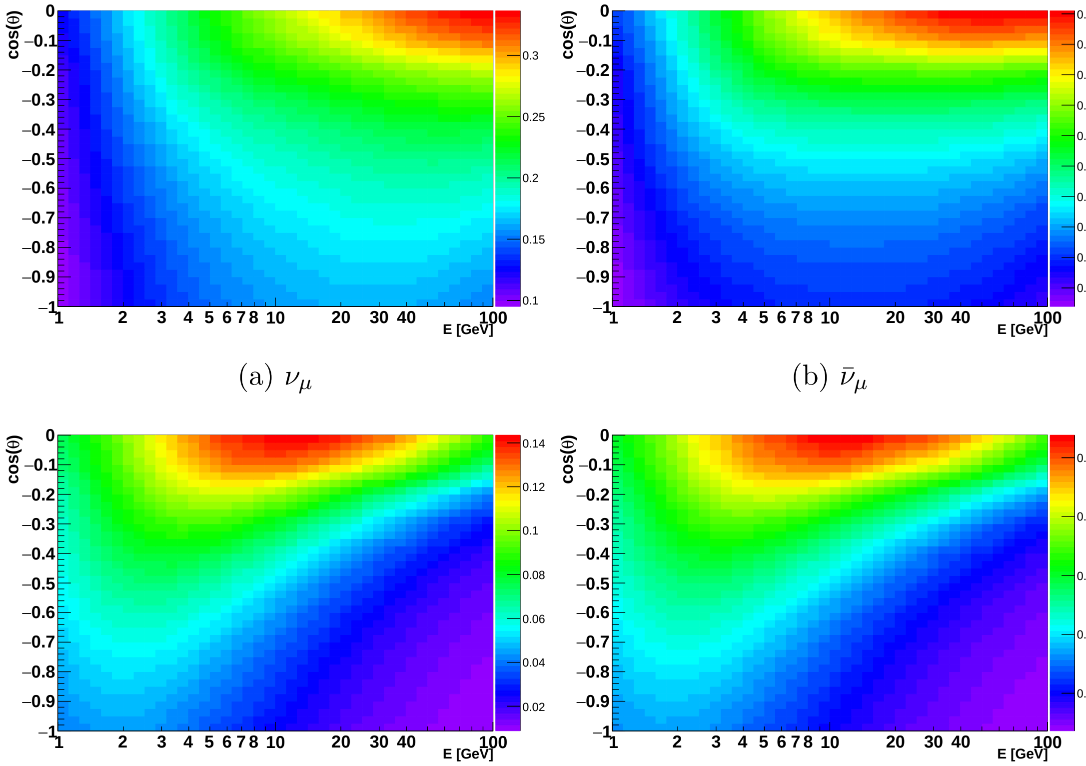

(a) ν_μ (b) $\bar{\nu}_\mu$

(c) ν_e (d) $\bar{\nu}_e$

Figure 1.8: The Honda atmospheric neutrino flux [22]. The z axis corresponds to $\Phi_\nu E^3$ in $\mathrm{GeV}^2\mathrm{m}^{-2}\mathrm{s}^{-1}$.

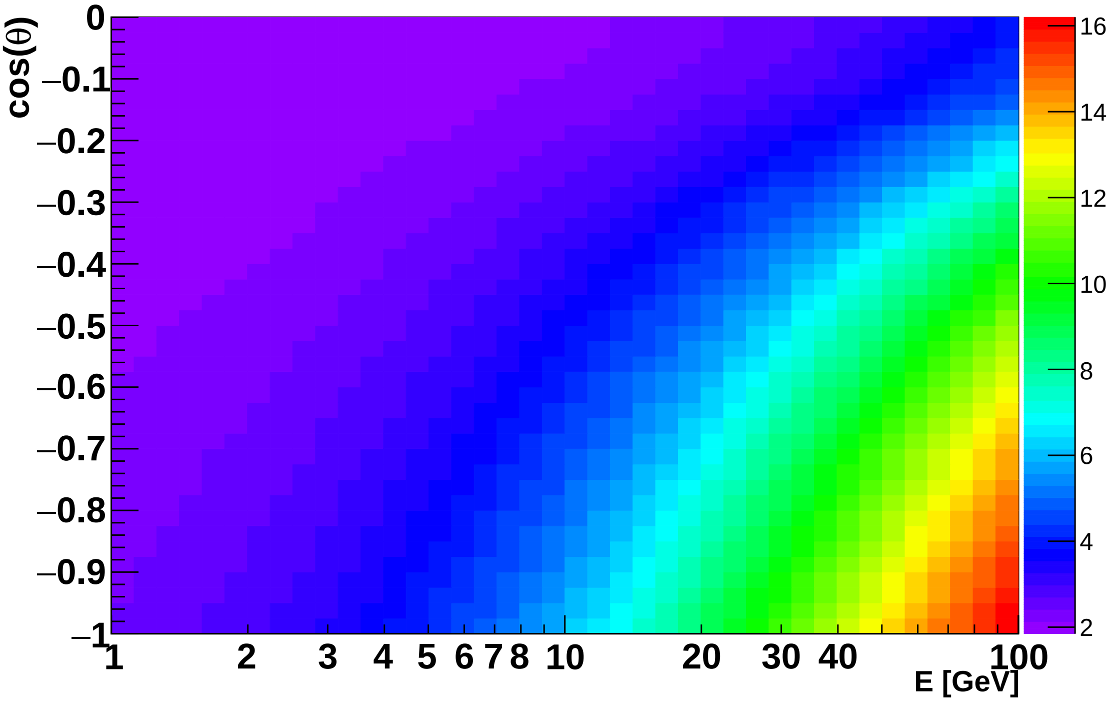

Figure 1.9: The ratio $\frac{\nu_\mu+\bar{\nu}_\mu}{\nu_e+\bar{\nu}_e}$ present in the Honda atmospheric neutrino flux [22], as a function of zenith angle and energy.

muons have a longer lifetime in the Earth's reference frame, due to time dilation.

This atmospheric neutrino flux prediction was calibrated against measurements taken at Gran Sasso, Sudbury, Kamioka, INO, Soudan and the Fréjus Road Tunnel, the latter of which is only ~ 265 km from the KM3NeT/ORCA site. In this work, the Fréjus flux tables are used.

1.5 Neutrino Masses and Vacuum Oscillations

In this section, the mechanism behind neutrino oscillations in vacuum is explained, as well as its implications for neutrino mass. Neutrinos are able to oscillate between flavours because their flavour eigenstates are different from their mass eigenstates. Neutrino mass eigenstates ($|\nu_{1,2,3}\rangle$) and flavour eigenstates ($|\nu_{e,\mu,\tau}\rangle$) form two complete eigenbases, which can by related by a 3×3 rotation matrix,

$$\begin{pmatrix} \nu_e \\ \nu_\mu \\ \nu_\tau \end{pmatrix} = \begin{pmatrix} U_{e1} & U_{e2} & U_{e3} \\ U_{\mu 1} & U_{\mu 2} & U_{\mu 3} \\ U_{\tau 1} & U_{\tau 2} & U_{\tau 3} \end{pmatrix} \begin{pmatrix} \nu_1 \\ \nu_2 \\ \nu_3 \end{pmatrix} . \tag{1.12}$$

This matrix, named the PMNS matrix after Bruno Pontecorvo, Ziro Maki, Masami Nakagawa and Shoichi Sakata, is usually parametrised according to three mixing angles ($\theta_{12}, \theta_{13}, \theta_{23}$) and one complex phase (δ^{CP}):

$$\mathbf{U} = \begin{pmatrix} 1 & 0 & 0 \\ 0 & \cos\theta_{23} & \sin\theta_{23} \\ 0 & -\sin\theta_{23} & \cos\theta_{23} \end{pmatrix} \begin{pmatrix} \cos\theta_{13} & 0 & e^{-i\delta^{CP}}\sin\theta_{13} \\ 0 & 1 & 0 \\ -e^{i\delta^{CP}}\sin\theta_{13} & 0 & \cos\theta_{13} \end{pmatrix} \begin{pmatrix} \cos\theta_{12} & \sin\theta_{12} & 0 \\ -\sin\theta_{12} & \cos\theta_{12} & 0 \\ 0 & 0 & 1 \end{pmatrix} . \tag{1.13}$$

In analogy with the Cabbibo-Koyabashi-Maskawa (CKM) matrix, which relates the eigenstates of quarks undergoing weak interactions with their mass eigenstates, the introduction of δ^{CP} allows for charge-parity (CP) symmetry violation in the neutrino sector. Note that the CKM matrix is close to a diagonal matrix, unlike the PMNS matrix [23]. CP violation was thought to be a fundamental symmetry of nature, before its discovery in neutral kaons [24, 25]. See Section 1.7.5, for the current experimental status of CP violation in the neutrino sector.

Assuming that the mass eigenstates $|\nu_k\rangle$ propagate as plane waves.

$$|\nu_k(t)\rangle = e^{-i(E_k t - \mathbf{p}_k \cdot \mathbf{r})} |\nu_k(t=0)\rangle \tag{1.14}$$

where $\mathbf{p}_k, E_k$ are the momentum and energy of the mass eigenstate, m_k is its eigenvalue and $\mathbf{r}$ is its position. In the relativistic limit, this can be approximated as

$$|\nu_k(t)\rangle = e^{\frac{-i m_k^2 L}{2E_\nu}} |\nu_k(t=0)\rangle , \tag{1.15}$$

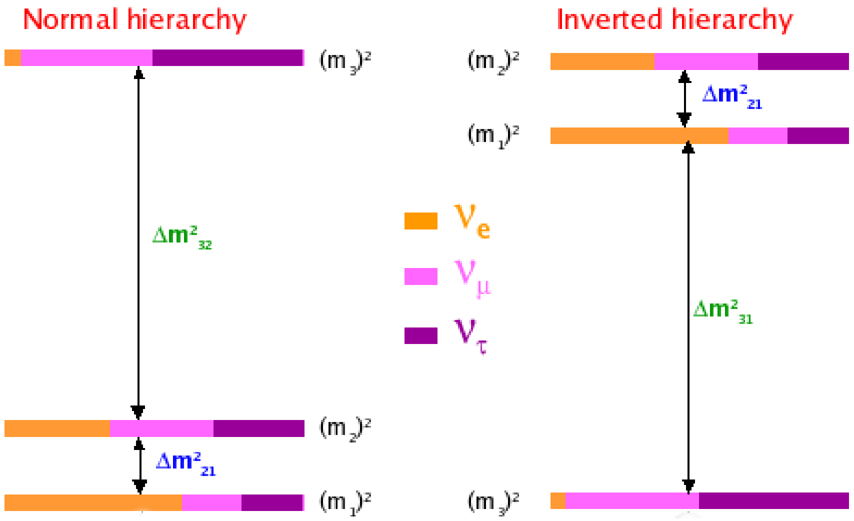

Figure 1.10: The two possible neutrino mass hierarchies. Here the colours represent the relative contribution of each flavour component in each mass eigenstate.

where E_ν is the neutrino energy and L is the distance travelled. Consequently, the transition probability between two flavours states (α, β) can be described in terms of the squared mass difference $(\Delta m^2_{jk} = m^2_j - m^2_k)$;

$$|\langle\nu_\alpha|\nu_\beta(t)\rangle|^2 = \sum_{j=1}^{3}\sum_{k=1}^{3} U_{\alpha j}U^*_{\beta j}U^*_{\alpha k}U_{\beta k}e^{\frac{-i\Delta m^2_{jk}L}{2E_\nu}}. \tag{1.16}$$

It is often decomposed into its real and imaginary components

$$\begin{aligned}|\langle\nu_\alpha|\nu_\beta(t)\rangle|^2 = \delta_{\alpha\beta} - 4\sum_{j>k}\Re(U_{\alpha j}U^*_{\beta j}U^*_{\alpha k}U_{\beta k})\sin^2\left(\frac{\Delta m^2_{jk}L}{4E_\nu}\right) \\ \pm 2\sum_{j>k}\Im(U_{\alpha j}U^*_{\beta j}U^*_{\alpha k}U_{\beta k})\sin^2\left(\frac{\Delta m^2_{jk}L}{2E_\nu}\right),\end{aligned} \tag{1.17}$$

the latter of which is only non-zero in the case of CP violation. It can be seen in Eqs. 1.16 and 1.17 that vacuum oscillation measurements are not sensitive to the absolute value of the mass or even the sign of the squared mass differences. Therefore, after fixing $m_2 > m_1$, two neutrino mass hierarchies[1] (NMHs) are possible (Fig. 1.10). They are the normal hierarchy (NH), in which m_3 is the greatest neutrino mass, and the inverted hierarchy (IH), in which it is the lowest.

A common approximation, particularly in early solar and accelerator experiments, is to assume a 2×2 neutrino scheme, with a single mixing angle θ and squared

---

[1] In some publications, the term "neutrino mass ordering" is preferred and hierarchy refers instead to the absolute mass scale.

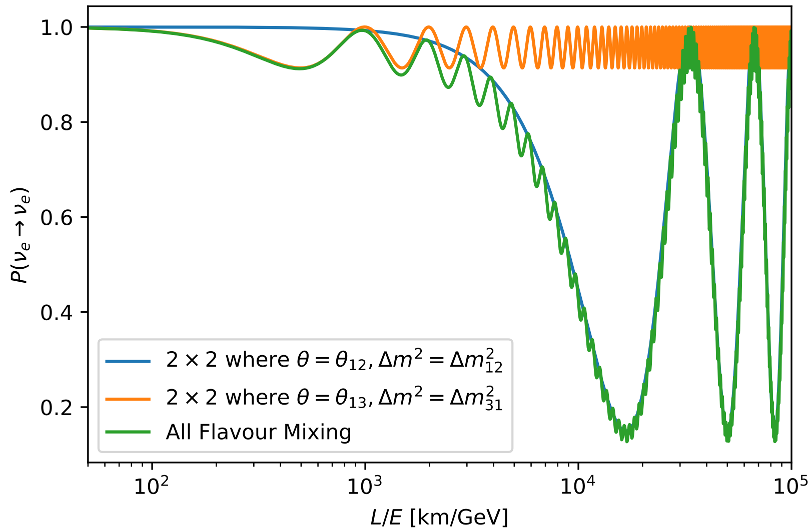

Figure 1.11: A comparison of the ν_e survival probability as a function of L/E for 3×3 neutrino mixing and two different 2×2 neutrino assumptions. It can be seen that, to first order, oscillations from θ_{13} and Δm^2_{31} dominate at short baselines, whereas θ_{12} and Δm^2_{12} are more important over long baselines.

mass difference Δm^2. Under this condition, Eq. 1.16 simplifies to

$$| \langle \nu_\alpha | \nu_\beta(t) \rangle |^2 = \sin^2(2\theta) \sin^2 \left(\frac{\Delta m^2 L}{4E_\nu} \right), \tag{1.18}$$

where $\alpha \neq \beta$, using natural units. Alternatively, where the energy is in GeV and the distance in kilometres, the factor $\frac{1}{4}$ is replaced with 1.27. See Fig. 1.11 for an overview of the L/E regions where this approximation is applicable. Higher order approximations are discussed in Ref. [26], exploiting $\Delta m^2_{12} \ll \Delta m^2_{31}$.

1.6 Matter Effects

Whilst vacuum oscillation measurements are not sensitive to the sign of Δm^2_{31}, it can be measured by exploiting matter effects. The ν_e component of the atmospheric neutrino flux can undergo charged-current elastic scattering with the electrons in matter (see Fig. 1.12). This introduces an effective potential V_c, given by

$$V_c = \pm G_F N_e \sqrt{2}, \tag{1.19}$$

where N_e is the electron density in matter and G_F is the Fermi coupling constant [27]. The effective potential is positive for neutrinos and negative for antineutrinos. This perturbation to the vacuum oscillation probabilities and its enhancing effect on neutrino oscillations is called the MSW effect, named after physicists Stanislav

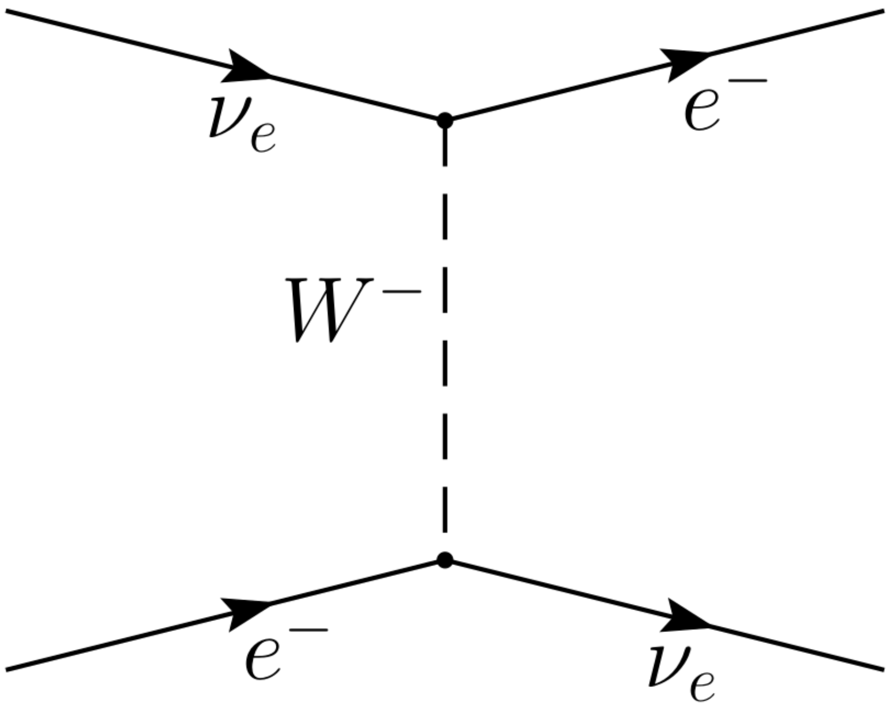

Figure 1.12: An illustration of charged-current elastic scattering between ν_es and electrons in matter.

Mikheyev, Alexei Yu. Smirnov, and Lincoln Wolfenstein [28, 29].

In order to discuss its effect on the time evolution of a neutrino flavour eigenstate, it is useful to adopt a more formal approach than in Section 1.5. The time evolution of quantum mechanical states is described in terms of the time evolution operator $\hat{U}$, such that

$$\begin{aligned} |\nu_k(t)\rangle &= \hat{U}(t)\,|\nu_k(t=0)\rangle \\ &= e^{-i\hat{H}t}\,|\nu_k(t=0)\rangle\,, \end{aligned} \tag{1.20}$$

where $\hat{H}$ is the Hamiltonian operator [30]. By inspection of Eq. 1.15, it is clear that the Hamiltonian describing neutrinos propagating as plane waves in a vacuum is expressed by the following matrix:

$$\boldsymbol{H}_0 = \frac{1}{2E_\nu}\boldsymbol{U}\begin{pmatrix} m_1^2 & 0 & 0 \\ 0 & m_2^2 & 0 \\ 0 & 0 & m_3^2 \end{pmatrix}\boldsymbol{U}^\dagger \tag{1.21}$$

in the flavour basis. The addition of the effective potential yields the following Hamiltonian in matter:

$$\boldsymbol{H}_m = \frac{1}{2E_\nu}\boldsymbol{U}\begin{pmatrix} m_1^2 & 0 & 0 \\ 0 & m_2^2 & 0 \\ 0 & 0 & m_3^2 \end{pmatrix}\boldsymbol{U}^\dagger + \begin{pmatrix} V_c & 0 & 0 \\ 0 & 0 & 0 \\ 0 & 0 & 0 \end{pmatrix}, \tag{1.22}$$

which can then be solved to derive the neutrino oscillation probabilities in matter.

Approxmimate expressions for ν_μ oscillations are expressed below [31, 32]:

$$\mathcal{P}(\nu_\mu \to \nu_e) \approx \sin^2\theta_{23}\sin^2(2\theta_{13}^M)\sin^2\left(\Delta^M\frac{L}{4E_\nu}\right), \tag{1.23}$$

$$\begin{aligned}\mathcal{P}(\nu_\mu \to \nu_\mu) \approx 1 &- \sin^2\theta_{23}^M\sin^2(2\theta_{23})\sin^2\left[(\Delta m_{23}^2 - \Delta^M + 2V_cE_\nu)\frac{L}{8E_\nu}\right] \\ &- \cos^2\theta_{23}^M\sin^2(2\theta_{23})\sin^2\left[(\Delta m_{23}^2 - \Delta^M + 2V_cE_\nu)\frac{L}{8E_\nu}\right] \\ &- \sin^4\theta_{23}\sin^2(2\theta_{13}^M)\sin^2\left[\Delta^M\frac{L}{4E_\nu}\right],\end{aligned} \tag{1.24}$$

in terms of the effective mixing parameters

$$\sin\theta_{13}^M = \frac{\Delta m_{31}^2\sin(2\theta_{13})}{\Delta^M}, \tag{1.25}$$

$$\Delta^M = \sqrt{(\Delta m_{31}^2\cos(2\theta_{13}) - 2V_cE_\nu)^2 + (\Delta m_{31}^2\sin(2\theta_{13}))^2}. \tag{1.26}$$

It can be clearly seen in Eqs. 1.23 and 1.24 that the introduction of V_c also introduces a dependence on the sign of Δm_{23}^2. From Eq. 1.26, it is simple to find the resonant energy, where $\theta_{13}^M = 90°$ and oscillations are maximised, at

$$E_\nu^{\mathrm{res}} = \frac{\Delta m_{31}^2\cos(2\theta_{13})}{2\sqrt{2}G_FN_e}, \tag{1.27}$$

as long as Δm_{31}^2 and V_c have the same sign. Consequently, detecting this resonance allows the measurement of the NMH. On the other hand, if
$E_\nu \gg \Delta m_{31}^2\cos(2\theta_{13})/2V_c$, then the dependence on the NMH is suppressed.

ORCA will detect atmospheric neutrinos over a wide range of baselines. Consequently, particular care needs to be paid to the density profile and chemical composition of the Earth, as the electron density is not constant. V_c therefore evolves as the neutrinos propagate and the Hamiltonian needs to be recalculated as a function of the neutrino's path length. This work assumes the Preliminary Earth Reference Model [33], which is shown in Fig. 1.13 (see Table A.1 in the appendix for the exact numbers used).

The matter-dependent 3 × 3 oscillation probabilities for ν_μs are shown in Fig. 1.14 for various zenith angles (and hence baselines). It can be seen that this resonant energy, where ν_e appearance is maximal, is between 3 and 7 GeV. As predicted by Eq. 1.27, ν_e appearance is enhanced for the normal hierarchy, as opposed to $\bar{\nu}_e$ appearance for the inverted hierarchy. To first order, the matter effects are reversed for neutrinos and antineutrinos. The saturation regime, where the NMH dependence is suppressed, can also be clearly seen above 15 GeV.

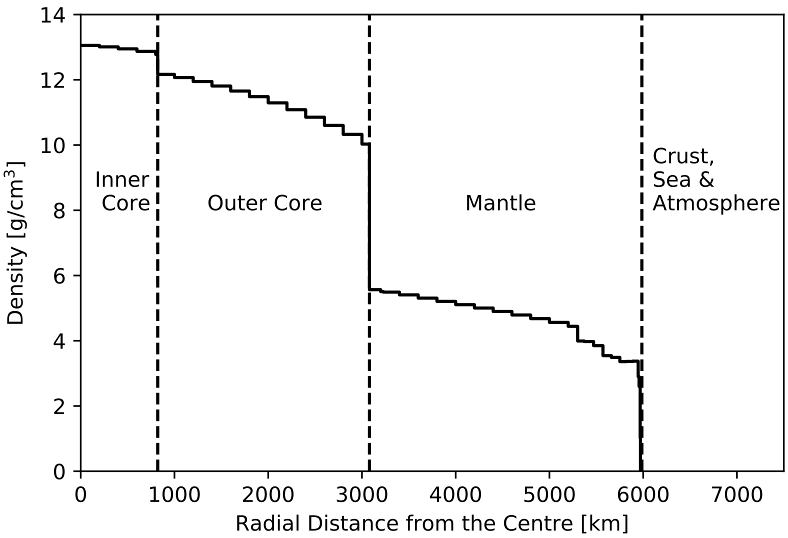

Figure 1.13: The density profile of the PREM Model [33], data taken from [34].

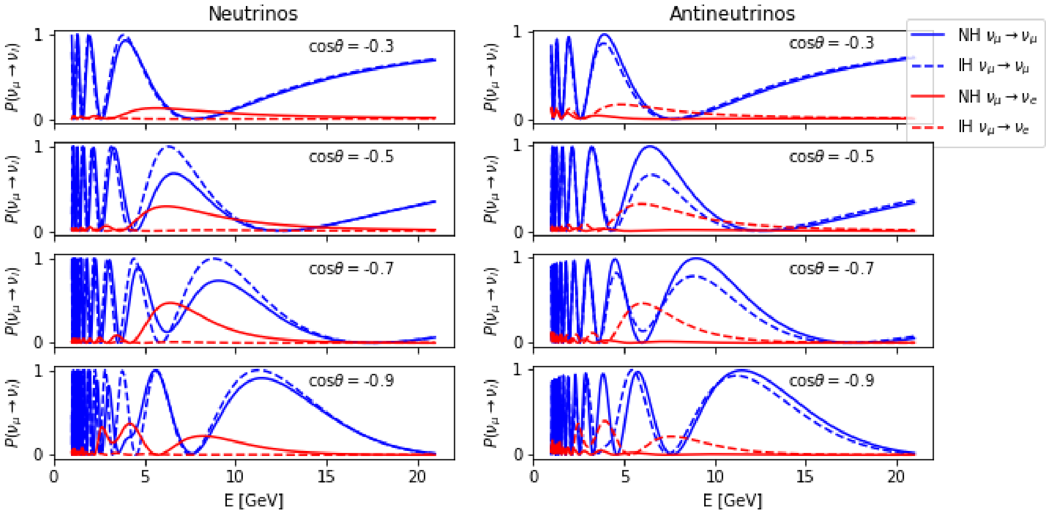

Figure 1.14: The oscillation probabilities $\mathcal{P}(\nu_\mu \to \nu_e)$ and $\mathcal{P}(\nu_\mu \to \nu_\mu)$ for neutrinos passing through the Earth, as a function of energy, shown for different zenith angles and mass hierarchies.

1.7 Current Experimental Constraints

Parameter	Best Fit Value	3σ range
$\theta_{12}[^\circ]$	33.62	$31.42 - 36.05$
$\theta_{13}[^\circ]$	8.54	$8.09 - 8.98$
$\theta_{23}[^\circ]$	47.2	$40.3 - 51.5$
$\Delta m^2_{21}[10^{-5}\text{eV}]$	7.40	$6.80 - 8.02$
$\Delta m^2_{31}[10^{-3}\text{eV}]$	2.494	$2.399 - 2.593$
$\delta^{CP}[^\circ]$	234	$144 - 374$

Table 1.2: The NUFIT 3.2 best fit oscillation parameters with their 3σ uncertainties, assuming a normal hierarchy. Note that $\delta^{CP} = 360^\circ$ is equivalent to $\delta^{CP} = 0^\circ$. Taken from Ref. [35].

In this work, the NUFIT 3.2 best fit values from January 2018 are used, unless stated otherwise [35]. They are reproduced here in Table 1.2. Throughout the rest of this section, the experimental evidence for these constraints is discussed.

1.7.1 Absolute Mass Scale

The absolute mass scale of electron neutrinos can be constrained by measuring the end point of beta decay. The Troitsk and Mainz experiments have placed 95% C.L. upper limits on the effective ν_e mass of 2.05 and 2.3 eV respectively, by measuring the spectrum of decaying tritium [36, 37].

1.7.2 θ_{12} and Δm^2_{12}

The constraints on θ_{12} and Δm^2_{12} are dominated by solar neutrino measurements and KamLAND. In addition to the Homestake, Super-Kamiokande and SNO experiments, important contributors to the global solar data include the Borexino liquid scintillation experiment [38] and the GALLEX experiment [39], which measured ^{71}Ge created by inverse beta decay of ^{71}Ga. At the reactor energy scale and KamLAND's baseline, the contributions of θ_{23}, and Δm^2_{32} can be neglected. In this regime, Eq. 1.16 can then be simplified to yield an antineutrino survival probability of

$$\mathcal{P}_{\bar{\nu}_e\bar{\nu}_e} \approx \cos^4\theta_{13}\left(1 - \sin^2\theta_{12}\sin^2\frac{\Delta m^2_{12}L}{4E_\nu}\right), \tag{1.28}$$

and hence θ_{12} and Δm^2_{12} can be obtained from the measured oscillation pattern. Solar neutrinos, on the other hand, change flavour while traversing a medium of slow changing density. See Refs. [40, 29, 41] for a detailed discussion. The electron

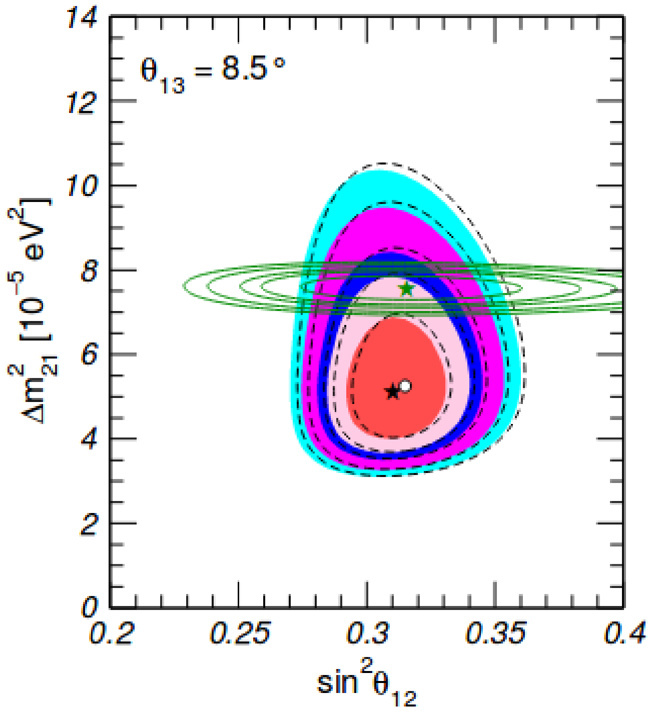

Figure 1.15: The allowed regions ($1\sigma, 90\%, 2\sigma, 99\%, 3\sigma$) for global solar data (filled) and KamLAND (green). Taken from Ref. [35].

neutrino survival probability in the Sun is of the form

$$\mathcal{P}_{\nu_e\nu_e} \propto \cos 2\theta_{12}^M \cos 2\theta_{12} + \text{const}, \tag{1.29}$$

where θ_{12}^M, is the mixing angle in matter, in analogy with Eq. 1.25. As with reactor neutrino oscillations, solar experiments are not sensitive to θ_{23} or Δm^2_{32}.

At present, there exists a 2σ tension between the global solar and KamLAND best fit values of Δm^2_{12}.

1.7.3 θ_{23} and Δm^2_{32}

Whereas solar neutrino measurements are sensitive to θ_{12} and Δm^2_{12}, atmospheric neutrino experiments are sensitive to θ_{23} and Δm^2_{32}. In Fig. 1.16 the current allowed region is shown (90% C.L) for two atmospheric neutrino measurements: IceCube [6], and Super-Kamiokande [7], and three long baseline accelerator experiments: NOvA [4], Minos [5], and T2K [8].

Neutrino beams are generated by focusing a proton beam on to a target, producing mesons whose decay products include neutrinos, through a similar set of decay modes to the ones shown in Section 1.4 (see Ref. [42] for an in depth review).

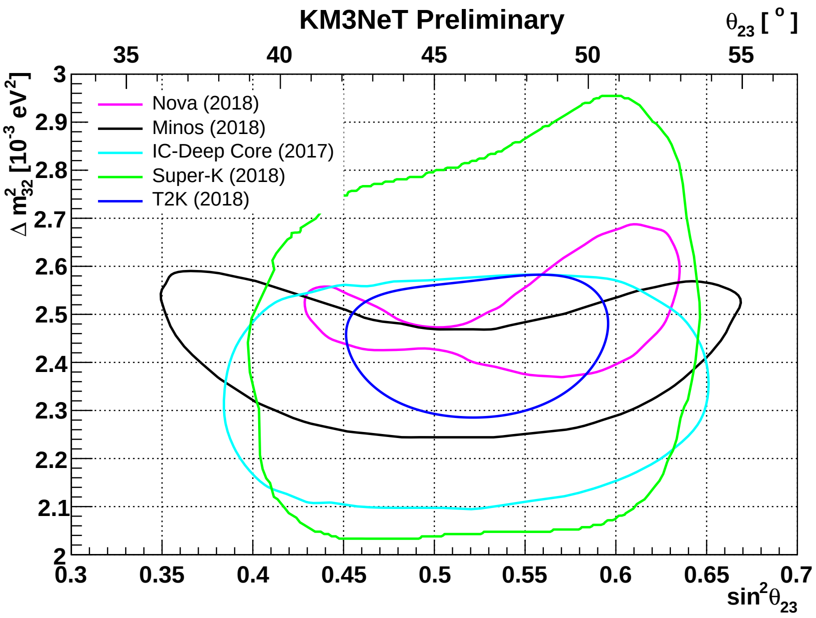

Figure 1.16: The 90% CL allowed region for θ_{23} and Δm^2_{32} according to latest results from NOvA [4], Minos [5], IceCube [6], Super-Kamiokande [7], and T2K [8]. A normal NMH has been assumed.

Shielding is employed to remove all particles except for neutrinos, which will mostly be ν_μs, with some contamination from ν_es produced by muon decay. The unoscillated neutrino beam composition is then typically measured with a near detector and far detector, for precision measurements of ν_μ disappearance in the beam.

In Eq. 1.24, it can be seen that the ν_μ survival probability depends on $\sin^2 2\theta_{23}$ and is symmetrical around $\theta_{23} = 45°$. Therefore, to first order, ν_μ disappearance on its own is insufficient to measure the octant of θ_{23}. Where ν_e appearance data is also included, there remains a degeneracy between the two octants, with mirrored best fit solutions of θ_{23} appearing in each.

1.7.4 θ_{13}

After having discussed solar, atmospheric, and accelerator experiments, the final mixing angle is primarily measured by reactor experiments, namely Double Chooz [43], Daya Bay [44] and RENO [45]. These experiments use commercial nuclear power stations as their sources, measuring $\bar{\nu}_e$s emitted by beta decay of fission products, over baselines of the order of 1 km. The full antineutrino survival probability, assuming negligible matter effects, is

$$\mathcal{P}_{\bar{\nu}_e\bar{\nu}_e} = 1 - \cos^4\theta_{13}\sin^2\theta_{12}\sin^2\left(\frac{\Delta m^2_{21}L}{4E_\nu}\right) \\ - \sin^2 2\theta_{13}\left[\cos^2\theta_{12}\sin^2\left(\frac{\Delta m^2_{31}L}{4E_\nu}\right)\sin^2\theta_{12}\sin^2\left(\frac{\Delta m^2_{32}L}{4E_\nu}\right)\right]. \tag{1.30}$$

As the baseline is short and $\Delta m^2_{21} \ll \Delta m^2_{32}$ and $\Delta m^2_{32} \approx \Delta m^2_{31}$, this can clearly be simplified to a 2 neutrino scheme, where $\Delta m^2 \approx \Delta m^2_{32}$ and $\theta \approx \theta_{13}$; i.e.

$$\mathcal{P}_{\bar{\nu}_e\bar{\nu}_e} \approx 1 - \sin^2 2\theta_{13}\sin^2\left(\frac{\Delta m^2_{32}L}{4E_\nu}\right). \tag{1.31}$$

It is clear that antineutrino disappearance measurements over short baselines are sensitive to θ_{13}, as also shown in Fig. 1.11. The oscillated antineutrino rate can then be measured by exploiting inverse beta decay and liquid scintillators. All three experiments also make use of a near detector, closer to the reactor, in order to measure the unoscillated neutrino flux and better control their systematics.

1.7.5 δ^{CP}

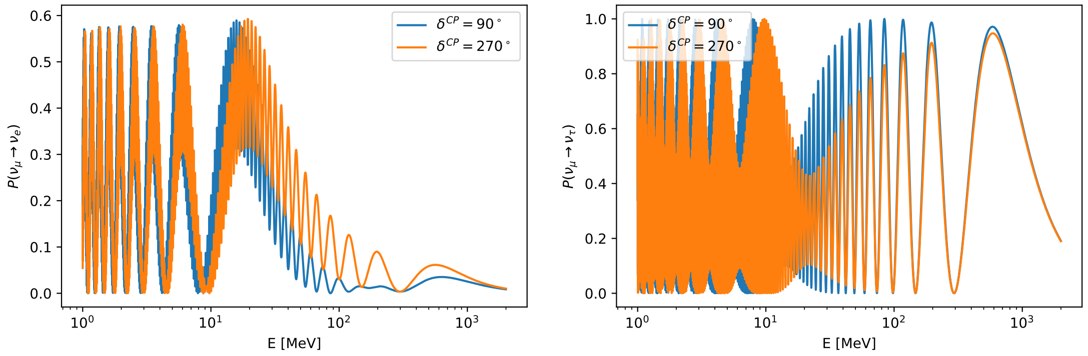

(a) $\nu_\mu \to \nu_e$

(b) $\nu_\mu \to \nu_\mu$

Figure 1.17: The $\nu_\mu \to \nu_e/\nu_\tau$ appearance probabilities, as a function of energy, over a baseline of 295 km, equivalent to T2K.

From Eq. 1.17, the inclusion of CP phase in the flavour transition probability introduces an extra term, given by

$$\Delta\mathcal{P}_{\alpha\beta} = \pm 2\sum_{j>k}\Im(U_{\alpha j}U^*_{\beta j}U^*_{\alpha k}U_{\beta k})\sin^2\left(\frac{\Delta m^2_{jk}L}{2E_\nu}\right). \tag{1.32}$$

It is clear from inspection that a survival probability, $\mathcal{P}_{\nu_\mu\nu_\mu}$ for example, is unaffected by the CP phase as

$$\Im(U_{\mu j}U^*_{\mu j}U^*_{\mu k}U_{\mu k}) = 0 \quad \forall \quad j,k. \tag{1.33}$$

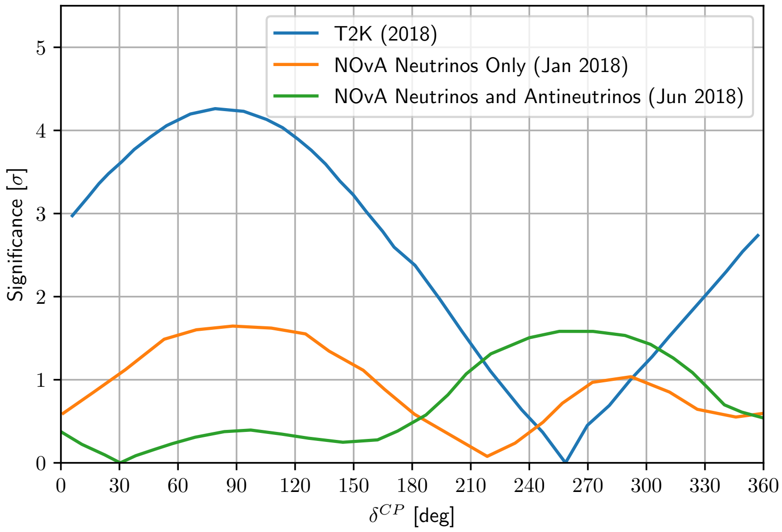

Figure 1.18: The significance to reject different values of δ^{CP} according to latest results from NOvA [4, 46] and T2K [8]. A normal NMH has been assumed.

As with the octant of θ_{23}, in order to measure δ^{CP} with a beam, it is necessary to measure ν_e appearance. ν_τ apperance is not practical in the region of interest (see Fig. 1.17), as the neutrinos have insufficient energy to create a τ. ν_e appearance has been measured by MINOS [47], T2K [48], and later by NOvA [49]. The latest results [4, 8, 46] from NOvA and T2K is shown in Fig. 1.18. There exists a tension between the NOvA neutrino and antineutrino data which, when combined with the neutrino data, causes the preferred value of δ^{CP} to flip from $\sim 220°$ to $\sim 30°$, in contradiction with the latest T2K result. For the purposes of this study, it will be assumed that all possible values of δ^{CP} are permitted.

1.7.6 Measuring the Neutrino Mass Hierarchy

As discussed in Section 1.6, neutrino oscillations in matter are sensitive to the sign of Δm^2_{23} and thus to the neutrino mass hierarchy, but these matter effects are reversed for neutrino and antineutrinos. Water Cherenkov detectors, such as ORCA, are not sensitive to the chirality of the incoming neutrinos. However, as neutrinos and antineutrinos have different cross sections and there are significantly more neutrinos than antineutrinos in the initial, unoscillated atmospheric neutrino flux, there remains a measurable asymmetry between the NH and IH hypotheses (see Fig. 1.19). See Chapter 5 for discussion on the sensitivity calculation carried out in this work.

In addition to ORCA, the planned Precision IceCube Next Generation Upgrade (PINGU) will be sensitive to the NMH [50]. For PINGU, the detection principles,

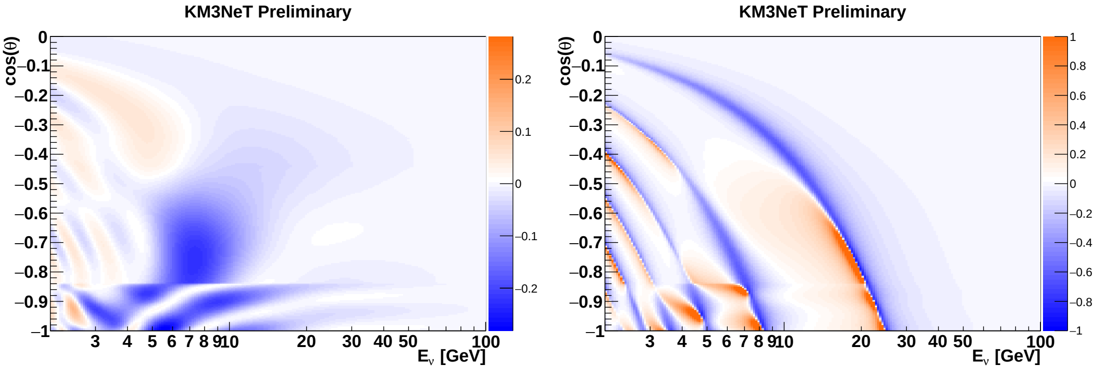

(a) ν_e-CC + $\bar{\nu}_e$-CC (b) ν_μ-CC + $\bar{\nu}_e$-CC

Figure 1.19: The measurable asymmetry $(N_{IH} - N_{NH})/N_{NH}$ for electron and muon neutrino charged-current events in ORCA.

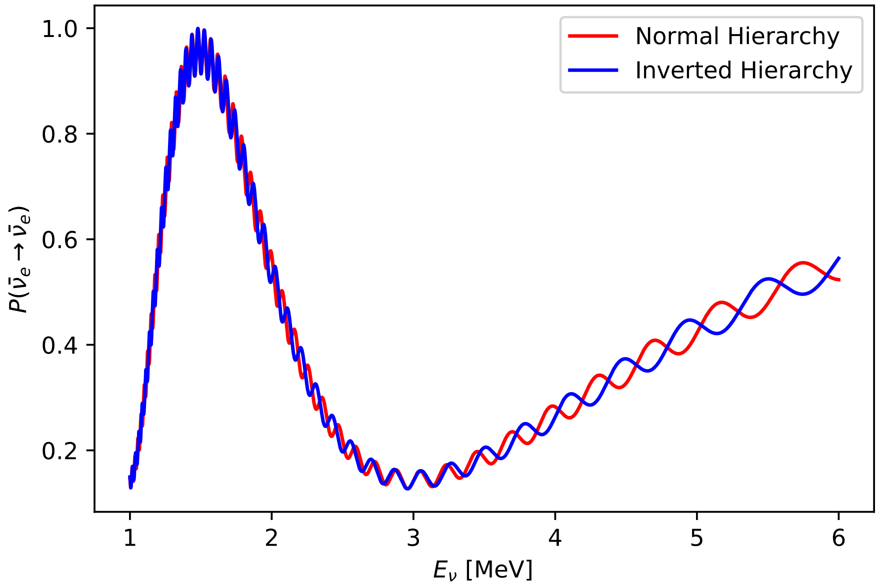

Figure 1.20: $\bar{\nu}_e \rightarrow \bar{\nu}_e$ survival probabilities in vacuum over a baseline of 50km, for both the normal and inverted NMHs.

methods and approaches are similar to those used in this work, except that Antartic ice is used as a detection medium instead of seawater. PINGU is expected to reject the wrong NMH with 3σ significance after four years of operation.

Construction of another atmospheric neutrino experiment, the India-Based Neutrino Observatory (INO) is planned in Bodi West Hills, Tamil Nadu, India [51, 52]. INO will consist of an iron calorimeter, tracking muons emitted by ν_μ-CC interactions. It will measure the same muon and antimuon appearance and disappearance as ORCA and PINGU. However, as it will be magnetised, INO will be able to separate neutrinos from antineutrinos, and expects to be able to measure the NMH with a sensitivity of 3σ in ten years.

The upcoming Jiangmen Neutrino Observatory (JUNO) is [53] is a 20kton underground liquid scintillator, located 215km from the Daya Bay nuclear power station and $\sim$ 50 km from the Yiangjiang and Taishan nuclear power stations [53]. As well as measuring the solar oscillation parameters with improved precision, it will be sensitive to the NMH through a different mechanism to atmospheric neutrino experiments, which does not require matter effects. The $\bar{\nu}_e \to \bar{\nu}_e$ survival probability in the reactor neutrino range is shown in Fig. 1.20, where a beat frequency is visible between the two possible NMH hypotheses. In order to measure this beat frequency, it is absolutely crucial that JUNO should achieve an energy uncertainty no greater than 3% and energy scale uncertainty no greater than 1% [54].

The matter effects measured by atmospheric neutrino experiments, such as ORCA and PINGU, will also be exploitable by sending a neutrino beam through the Earth's crust. Consequently, NOvA [4] and T2K [8] have recently presented results favouring the normal hierarchy, with significance $\sim 2\sigma$. The planned Deep Underground Neutrino Experiment (DUNE) will measure matter effects from a neutrino beam sent from FermiLab over a baseline of 1300 km [55] and anticipates a significance of at least 5σ after 7 years.

1.8 Consequences of Measuring the Neutrino Mass Hierarchy

This section touches on the nature of neutrino mass and the consequences of a NMH measurement. If the NMH is normal, then the lightest charged lepton flavour is also mostly present in the lightest mass state, in a way that's qualitively similar to the quark sector, as is common in Grand Unified Theories, whereas an IH allows for interesting breaks from that scheme, such as a one where two states form a degenerate pair and the lightest is massless [56]. While the existence of neutrino mass has been confirmed, the nature of that mass has not. It is possible that neutrinos have Dirac mass, in which case neutrinos and antineutrinos are distinct particles, or Majorana mass in which case a neutrino is its own antiparticle, distinguished only by its chirality [57]. It may be possible to determine the nature of neutrino mass by searching for neutrinoless double beta decay, as described in section 1.8.1. Determining the NMH also has consequences for neutrino astrophysics, particularly in the light curves of supernovae (see Section 1.8.2) and for measurements of CP violation (Section 1.8.3), which is necessary for leptogenesis [58], a possible explanation for the matter-antimatter symmetry in the universe.

1.8.1 Neutrinoless Double Beta Decay

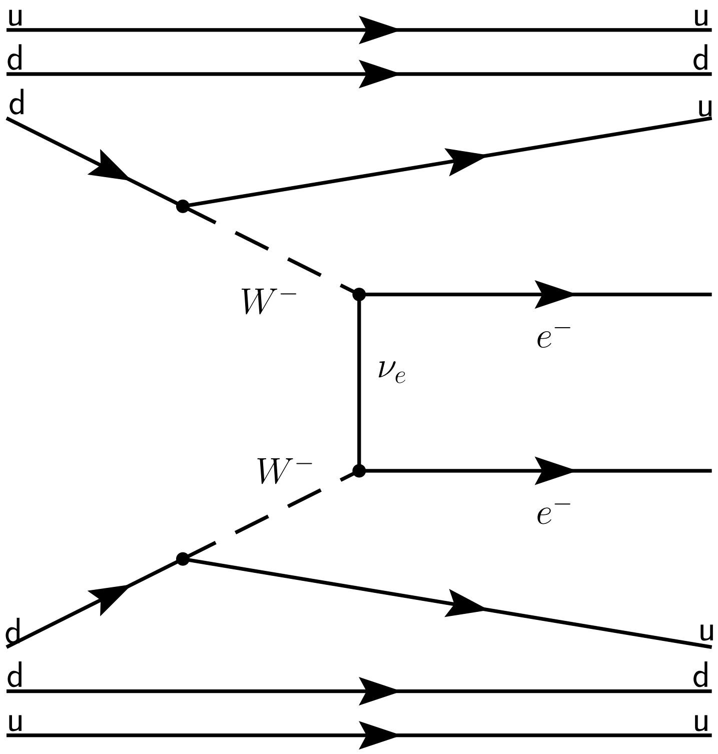

Figure 1.21: The mechanism through which neutrinoless double beta decay is permitted, if a neutrino has Majorana mass.

If neutrinos are indeed Majorana particles, then it should be possible to observe neutrinoless double beta decay, according to the mechanism shown in Fig. 1.21. This can be distinguished from normal double beta decay by measuring the energy of the emitted electrons. In the absence of neutrinos, the usual energy spectrum is replaced by a sharp peak at the decay energy. See Refs. [59, 60] for a detailed

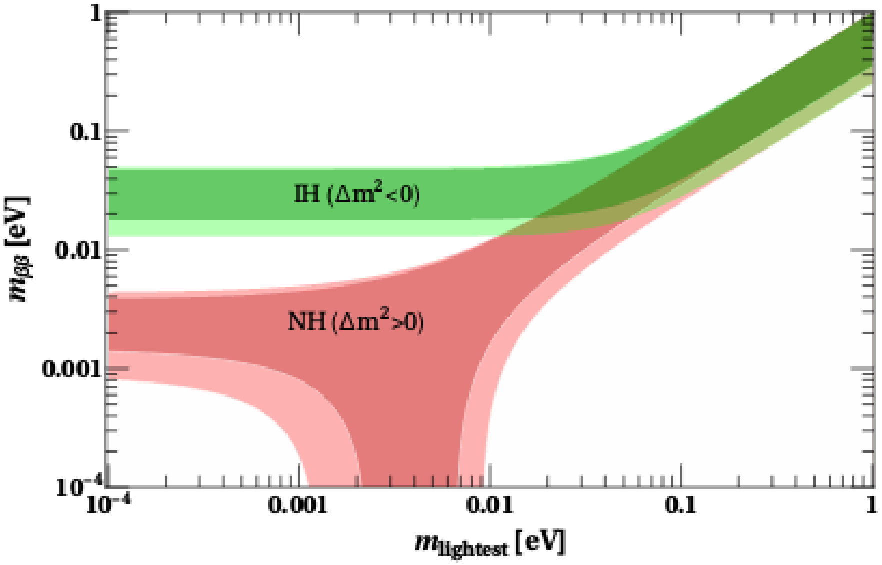

Figure 1.22: The predicted regions of $m_{\beta\beta}$ as a function of the lightest neutrino mass. Taken from Ref. [61].

review of the neutrinoless double beta decay searches so far.

Constraints on the neutrinoless double beta lifetime can be converted into limits on the effective Majorana mass, defined in terms of the PMNS matrix

$$m_{\beta\beta} = \left| \sum_{i=1}^{3} e^{i\xi_i} |U_{ei}^2| m_i \right| , \tag{1.34}$$

in which three new complex "Majorana phases" have been introduced [60]. The predicted values of $m_{\beta\beta}$ as a function of the lightest neutrino mass are shown in Fig. 1.22 for both the NH and IH. It is apparent that an independent measurement of the NMH is useful in this field. If the NMH is inverted and $m_{\beta\beta}$ is excluded down to ~ 0.01 eV, then neutrinoless beta decay can be ruled out, whereas a Majorana neutrino mass may never be fully excluded in the NH case.

1.8.2 Supernova Neutrinos

The NMH also has consequences for the flavour composition of neutrinos produced by nuclear processes in supernovae. Supernova neutrinos undergo the MSW effect with ordinary matter within the star itself, as well as interactions with other neutrinos. See Ref. [62] for a review of neutrino oscillations in the presence of self coupling, such as in a core collapse supernova. In numerical simulations, the most dramatic consequence of changing the NMH is a flip in the expected energy spectrum between ν_es and ν_μs [63]. The consequence of this for a terrestrial neutrino detector, sensitive to supernova $\bar{\nu}_e$s via inverse beta decay, is a change in the shape of the supernova light curve over time [64, 65]. This has been proposed as a method of measuring the NMH (as in Ref. [64]) in the past but, given the rarity of galactic supernovae, such a measurement would likely come after the NMH has been determined by other means and be very model dependent. Instead an independent measurement of the NMH will allow for tighter constraints of supernova neutrino emission models, having removed one source of uncertainty.

1.8.3 CP Phase Measurements

In Fig. 1.23, the most recent constraints on δ^{CP} from NOvA [4], T2K [8] and Minos [66] are shown. It can be seen that changing the fitted NMH hypothesis introduces a degeneracy in δ^{CP}, where its best fit value assuming NH is not equal to its best fit value assuming IH. Whilst these experiments do have some sensitivity to the NMH on their own, an independent rejection of one NMH hypothesis over the other would reduce the uncertainty on δ^{CP}. It would also reduce the risk of a situation where a long baseline experiment finds the wrong NMH and consequently also finds a wrong value of δ^{CP}.

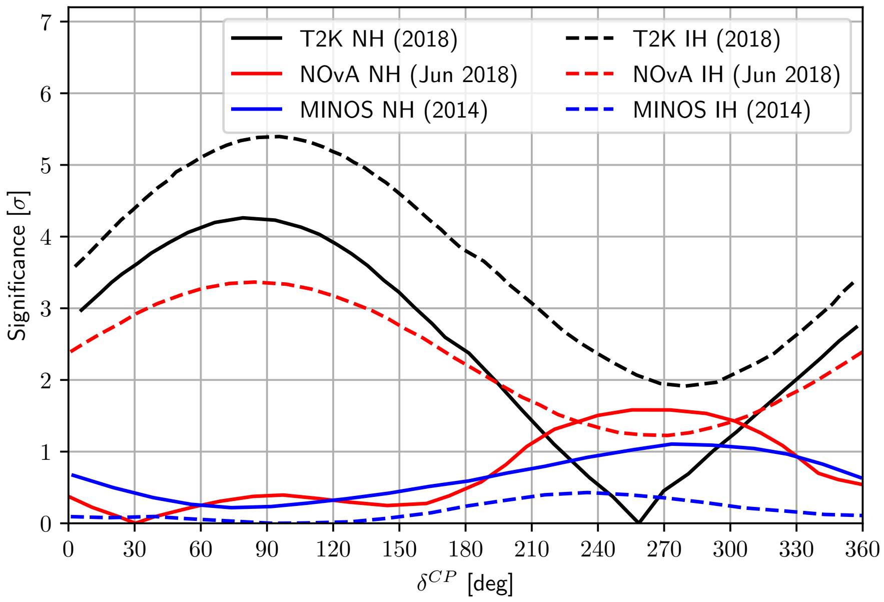

Figure 1.23: The significance to reject different values of δ^{CP}, from NOvA [4], T2K [8] and Minos [66]. The best fit to the data is shown assuming both NH and IH.

Chapter 2

The KM3NeT/ORCA Detector

2.1 KM3NeT Introduction

KM3NeT is a next-generation undersea neutrino experiment, under construction in the Mediterranean Sea. The experiment is split between two sites, both of which detect the Cherenkov signatures of charged particles, emitted by neutrino interactions in the seawater. The high-energy array, named ARCA (Astroparticle Research with Cosmics in the Abyss), is located at 36° $16'$ N 16° $06'$ E, approximately 100 km from Portopalo di Capo Passero in Sicily. The low-energy arrray, named ORCA (Oscillation Research with Cosmics in the Abyss), is located at $42^\circ\ 48'\ N\ 06^\circ\ 02'\ E$, at a depth 2450 m, 40 km from Toulon in France. ARCA is primarily designed to detect TeV-range cosmic neutrinos, ORCA has an energy range of $1 - 100$ GeV and is dedicated to oscillation research, using atmospheric neutrinos and low-energy astrophysics.

The ORCA and ARCA designs are very similar, the most prominent difference being their sizes and densities. For that reason, this thesis will describe ORCA only. For details of the ARCA design, see Ref. [1]. ORCA will consist of an array of 115 vertical detection units, deployed with an average horizontal separation of 23 m, forming a cylinder on the seafloor. Each line consists of 18 Digital Optical Modules (DOMs) spaced 9 m apart, starting 28 m from the seafloor. A DOM is a transparent glass sphere, 17" in diameter, housing 31 3" photomultiplier tubes (PMTs), optimise to detect Cherenkov radiation emitted by neutrino interactions in the seawater.

2.2 Neutrino Interactions in Seawater

Although neutrinos are only weakly interacting and thus cannot be detected directly, they can exchange a $W^{\pm}$ or Z^0 with nucleons in the seawater, creating charged particles which are detectable. Charged-current interactions produce a hadronic cascade and a lepton which, due to flavour conservation, will have a flavour matching that of the parent neutrino. In the neutral current case, only a hadronic cascade will be produced, therefore all three flavours will have the same topology. These four distinct interaction channels are shown in Fig. 2.1. The characteristic signatures of electrons and muons passing through the water are discussed in Sections 2.4 and 2.5 respectively.

However, it should be noted that for ν_τ charged-current interactions the energy range of interest to ORCA ($1 - 100$ GeV), the distance between the τ creation and decay vertices is of the order 1 cm. Consequently, the two vertices cannot be resolved separately and ν_τ-CC events will appear to be a single cascade, whose composition will depend on the τ decay mode. The main τ decays and their branching ratios are as follows:

$$\begin{aligned}
&\tau^- \rightarrow \pi^-\pi^0\nu_\tau && (25.5\%)\\
&\tau^- \rightarrow e^-\bar{\nu}_e\nu_\tau && (17.8\%)\\
&\tau^- \rightarrow \mu^-\bar{\nu}_\mu\nu_\tau && (17.4\%)\\
&\tau^- \rightarrow \pi^-\nu_\tau, && (10.8\%)\\
&\tau^- \rightarrow \pi^0\pi^0\pi^+\nu_\tau && (9.3\%)\\
&\tau^- \rightarrow \pi^-\pi^-\pi^+\nu_\tau && (9.0\%)
\end{aligned}$$

where the corresponding τ^+ decays simply take the charge conjugate [23]. Any neutral hadrons created at the initial interaction vertex or by τ decay do not emit Cherenkov radiation, and then can consequently only be detected via decays to charged particles or photons, such as the neutral pion decay $\pi^0 \rightarrow 2\gamma$.

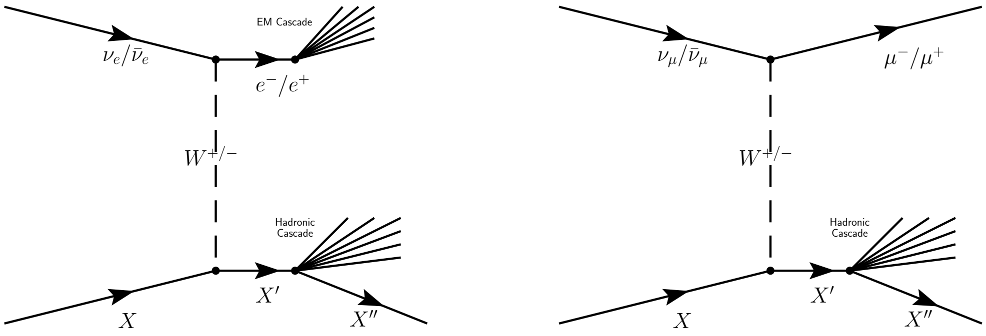

(a) ν_e charged current (b) ν_μ charged current

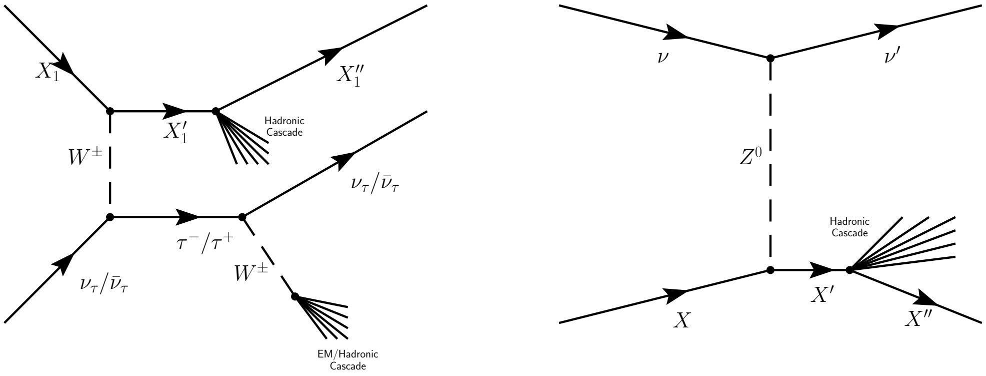

(c) ν_τ charged current (d) Neutral current

Figure 2.1: An illustration of the types of neutrino interaction detectable in the KM3NeT detector. The event topologies shown are an EM cascade overlaying a hadronic cascade (a), a muon with a hadronic cascade near the interaction vertex (b), a hadronic cascade at the tau creation vertex and either an EM or hadronic cascade at the decay vertex (c) , and a single hadronic cascade (d). Note that τs can decay both hadronically and leptonically. If a muon is created in its decay, then the resulting topology will not be a cascade (see Section 2.4). The X particle represents any nucleon in the seawater.

2.3 Cherenkov Radiation

Cherenkov radiation is emitted when a charged particle passes through a dielectric medium at a speed greater than the phase velocity of light in that medium. As it travels, it creates small disruptions in the local electromagnetic field, causing it to emit visible light according to the characteristic formula below [68].

$$\cos\theta_c = \frac{1}{\beta\eta}, \tag{2.1}$$

where θ is the angle of emission with respect to the path of the particle, β is the particle's speed as a fraction of the speed of light, α is the fine structure constant, and η is the refractive index of the medium. In seawater, where $\eta \sim 1.33$, the Cherenkov angle is close to 41° and the light is emitted according to the following spectrum:

$$\frac{d^2N}{d\lambda dz} = \frac{2\pi\alpha}{\lambda^2}\left(1 - \frac{1}{\beta^2\eta^2(\lambda)}\right) \tag{2.2}$$

where λ is the wavelength of the emitted light and z is the distance travelled by the particle [23]. However, light absorption in water is minimum close to 450 nm [69][67], so in practice most of the detected light is in the visible blue part of the spectrum (see Fig. 2.2).

Both the light absorption and scattering probabilities take the form of an exponential decay, expressed in terms of scattering length (λ_s) and absorption length (λ_{abs}). In each case, this length is defined as the distance at which the proportion of unabsorbed (or unscattered) photons falls to $\frac{1}{e}$.

Light scattering in seawater can be modelled as a mixture of Rayleigh scattering off the water molecules and geometric scattering off larger particles:

$$\frac{d\mathcal{P}_s}{d\Omega_s} = p\frac{d\mathcal{P}_{\text{Rayleigh}}}{d\Omega_s} + (1-p)\frac{d\mathcal{P}_{\text{Geo}}}{d\Omega_s}, \tag{2.3}$$

where Ω_s is the solid scattering angle, $\mathcal{P}_s$ is the total scattering probability, and the relative contributions of each are fixed by the parameter p, such that $0 < p < 1$. Both of these models are rotationally symmetric around the photon direction. The Rayleigh scattering probability ($\mathcal{P}_{\text{Rayleigh}}$) can be parameterised in terms of the scattering angle (θ_s) according to

$$\frac{d\mathcal{P}_{\text{Rayleigh}}}{d\Omega_s}(\theta_s) = \alpha(1 + \beta\cos^2\theta_s). \tag{2.4}$$

The geometric scattering probability ($\mathcal{P}_{\text{Geo}}$) is described using a Henley-Greenstein function

$$\frac{d\mathcal{P}_{\text{Geo}}}{d\Omega_s}(\theta_s) = \frac{1}{4\pi}\frac{1-a^2}{(1+a^2-2a\cos\theta_s)^{\frac{3}{2}}}, \tag{2.5}$$

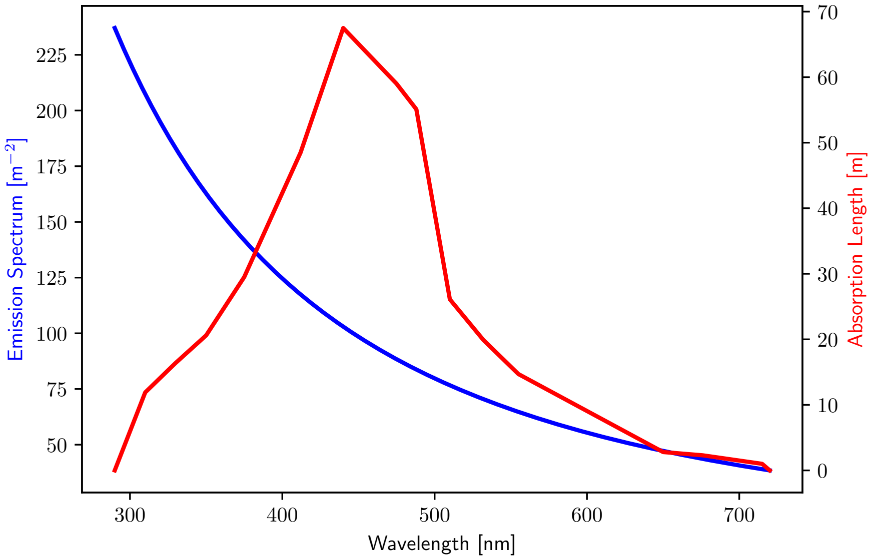

Figure 2.2: The emission spectrum and absorption length of Cherenkov light in water, as a function of wavelength, taken from Ref. [67].

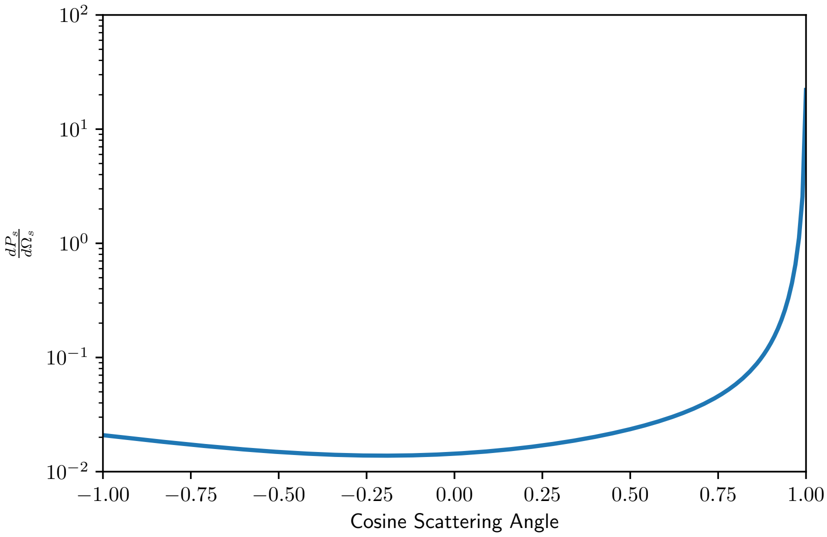

Figure 2.3: The normalised scattering probability per solid angle, as a function of the cosine scattering angle.

where the parameters p, α, β, a are set according to in situ measurements [67][70] (see Fig 2.3).

2.4 Muon Propagation

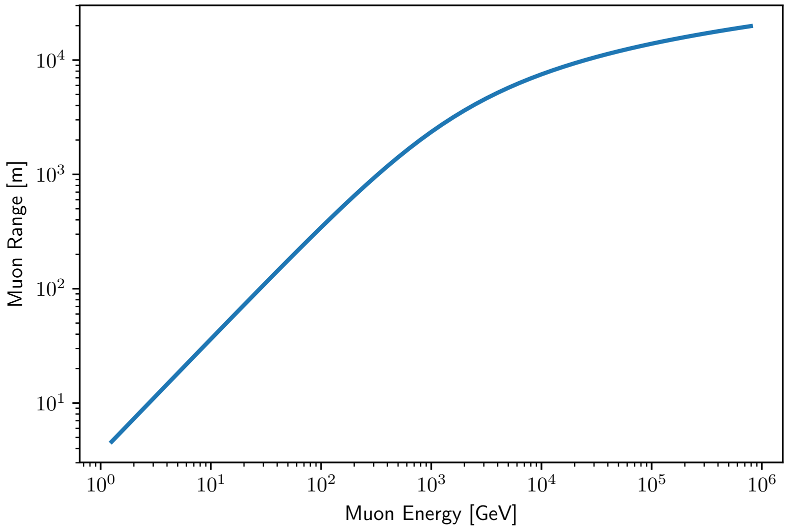

Figure 2.4: The muon range as a function of energy. Under 100 GeV, the energy loss is almost constant (dominated by ionisation).

The rate of energy loss for a muon in water can be approximated by

$$\frac{dE_\mu}{dz} = a + bE_\mu, \tag{2.6}$$

where E_μ is the muon energy and z is the distance travelled by the muon [71]. The parameters $a = 0.274$ GeV m^{-1} and $b = 3.492 \times 10^{-4}$ m^{-1} are due to ionisation and the combined effects of pair production, brehmsstrahlung and photonuclear interactions respectively. Below $\sim$ 100 GeV, as seen in Fig. 2.4, the muon energy loss is almost constant and dominated by ionisation. Consequently, the characteristic topology of a muon event is of a long track of uniform luminescence.

2.5 Cascades

Electrons, unlike muons, have a short mean free path in matter and will produce high-energy photons via brehmsstrahlung, which will produce electron-positron pairs in turn. The emission profile of this cascade will still peak at the same Cherenkov angle as the muon tracks, but will be more dispersed, due to the

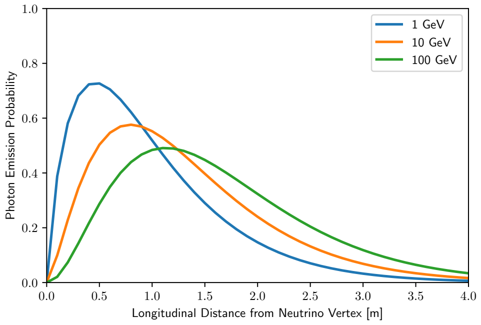

Figure 2.5: The parameterised longitudinal photon emission profiles of EM cascades in water for various energies.

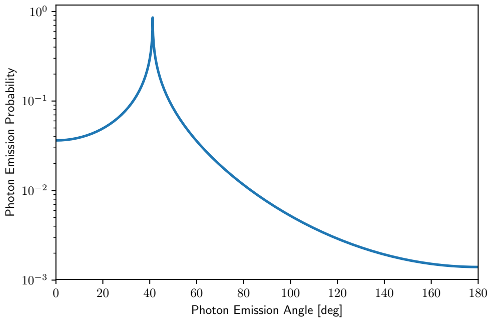

Figure 2.6: The parameterised angular photon emission profile of EM cascades in water.

contributions of all secondary electrons with energies above the Cherenkov threshold (see Fig. 2.6). In water, the longitudinal profile of EM cascades can be parameterised according to

$$\frac{dN}{dz} \propto z^{a-1}\frac{e^{\frac{-z}{b}}}{b^a\Gamma(a)}; \tag{2.7}$$

$$a = a_0 + a_1 \log(E), \tag{2.8}$$

where a_0, a_1 and b are approximately constant and E is the cascade energy [72], as shown in Fig. 2.5. The general form of the angular emission profile is given by

$$\frac{dN}{d\theta} \propto e^{\beta|\cos(\theta)-\frac{1}{\eta}|^{\alpha}}, \tag{2.9}$$

where α and β are constants and θ is the angle of emission with respect to the cascade direction [73].

2.6 The Digital Optical Module

The approach taken in designing the KM3NeT Digital Optical Module (DOM), represents a shift away from other Cherenkov neutrino detectors, such as ANTARES [2] and IceCube [3]. The advantages of the spherical, multi-PMT design include (see Figs. 2.7 and 2.8):

- Almost uniform angular coverage
- Increased photocathode area, almost a factor 4 greater than in traditional designs
- The possibility of separately resolving individual photons which arrive on

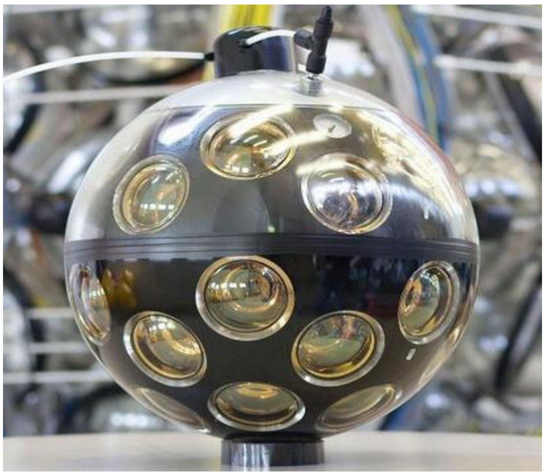

Figure 2.7: A photograph of a completed DOM.

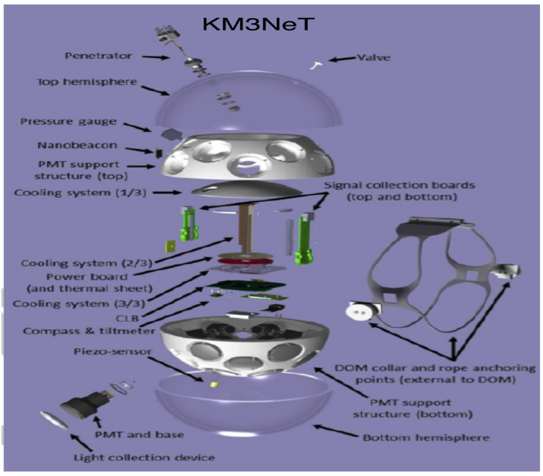

Figure 2.8: A schematic showing the internal components of a DOM.

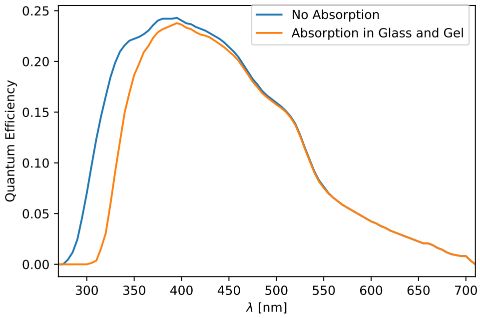

Figure 2.9: A parameterisation of the KM3NeT 3” PMT quantum efficiency, data taken from Ref. [74].

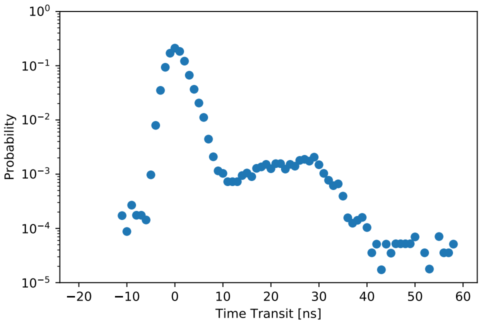

Figure 2.10: The measured time transit spread of the KM3NeT 3” PMTs, data taken from Ref. [74].

adjacent PMTs

- Resistance to failure, loss of a single PMT results in an average efficiency decrease of just 3%

PMTs (Fig. 2.13) were selected for a good quantum efficiency for wavelengths characteristic of Cherenkov radiation (see Figs. 2.2 and 2.9). A time resolution of the order of ~ 1 ns is also desirable for event reconstruction and so measurements have been performed of the photoelectron transit time. In Fig. 2.10, the transit time distribution is shown for a single photoelectron pulse, shifted such that the peak of the distribution appears at zero. The gaussian width of the main peak is close to 2 ns. Prepulses and afterpulses, defined as those appearing 6 ns before or 10 ns after the main peak, make up only 0.1% and 3.5% of the distribution respectively [74]. To prevent unwanted reflections, the empty space between the PMT support and the glass is filled with optical gel. The collection efficiency of the PMTs is improved further by the placement of a reflector ring around the edge, effectively increasing the diameter by another 13 mm [1]. For each pulse exceeding

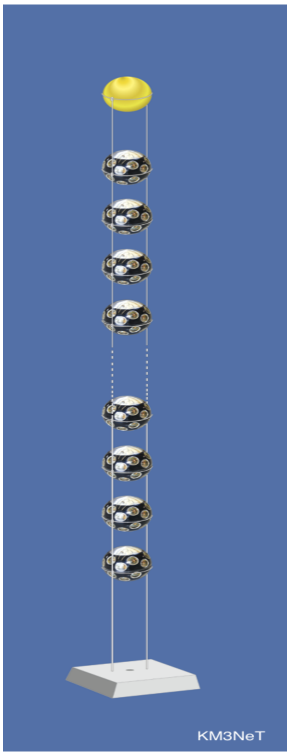

Figure 2.11: A KM3NeT Detection Unit.

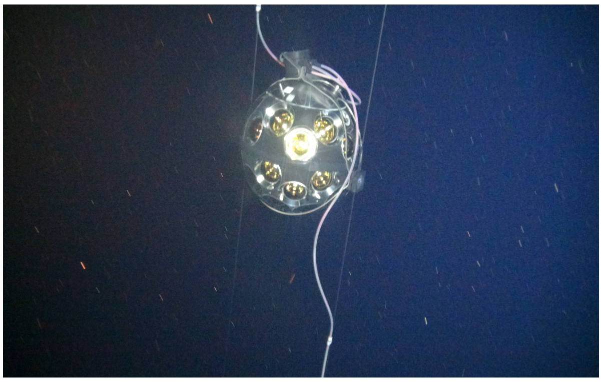

Figure 2.12: A photograph of a digital optical module, deployed at the ORCA site.

Figure 2.13: A photograph of a photomultiplier tube.

the threshold on a single PMT, the time of the leading edge and the time over threshold (ToT) are digitised and all the data is sent back to shore via an optical fibre. The threshold is typically equivalent to 30% of a single photoelectron pulse height, although it can be retuned in situ, and time synchronisation between the detector and shore is ensured using a modified white rabbit protocol.

The PMTs are housed in a 3D printed support frame, with PMTs placed facing outwards in rings of five, as well as a single downward-facing PMT at the bottom. Together with the glass sphere, this is enough to withstand the hydrostatic pressure of the deep sea environment. 18 DOMs constitute a Detection Unit (DU), vertically separated by 9m, secured to two thin ropes by a titanium collar (see Fig 2.11 and 2.12). The base of the DU is anchored to the sea floor and the ropes held taut by a buoy at the top of the line.

In order to perform in situ detector calibrations, each DOM also contains an LED nanobeacon, an internal compass and tiltmeter, and an acoustic piezoelectric sensor. The nanobeacon is orientated facing upwards, in order to illuminate the DOM directly above it on the DU and thus perform inter-DOM time calibrations. The acoustic sensor is used for acoustic measurements of the DU position on the seabed and the internal compasses and tiltmeters record real time DOM orientation information, which is transmitted back to shore.

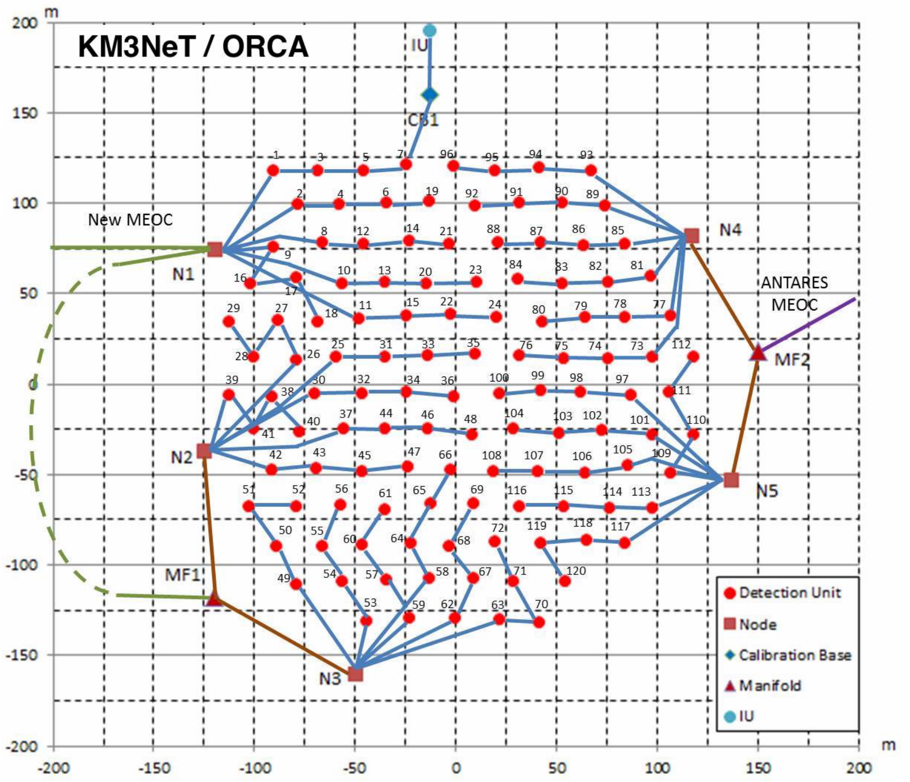

Figure 2.14: The planned KM3NeT/ORCA detector footprint, taken from Ref. [1]. Note that junction boxes are here referred to as "nodes."

2.7 Seafloor Infrastructure

The planned detector infrastructure is shown in Fig. 2.14. Two main electro-optical cables (MEOCs) carry the power from the shore to the DUs, via five junction boxes (see Figs. 2.15 and 2.16), as well as returning all the data to the shore. Each junction box connects to five "daisy chains" of four DUs, connected in series. In addition to the DUs, some daisy chains incorporate Calibration Units, housing laser beacons for inter-DU calibrations [75], and hydrophone emitters for acoustic positioning. The first cable was deployed in late 2014. After the decommissioning of ANTARES, its main cable will then be reused to power the second half of the detector.

Figure 2.15: The first KM3NeT/ORCA junction box, photographed at CPPM before deployment.

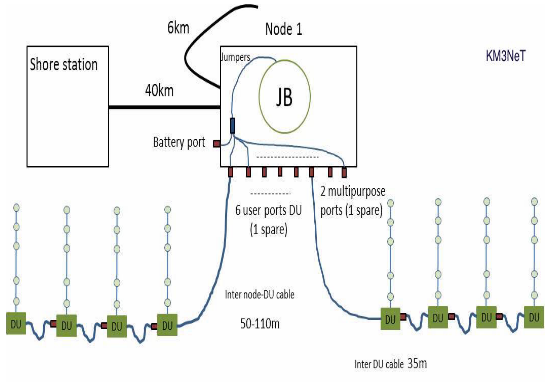

Figure 2.16: A schematic overview of the KM3NeT/ORCA junction box, showing its connection to the DUs.

2.8 Deployment

To date, the milestones in terms of ORCA's deployment have been as follows:

Apr 2013 A prototype KM3NeT DOM is deployed on an ANTARES instrumentation line [76].

May 2014 A prototype DU, consisting of three DOMs, is deployed at the ARCA site.

Dec 2014 The ORCA MEOC is connected.

Apr 2015 The first ORCA junction box is deployed.

Oct 2016 The junction box is redeployed after a fault in the MEOC.

Sep 2017 The first ORCA DU is deployed and begins taking data.

A sea operation is planned for late 2018, in which several DUs will be deployed. As the ORCA (and indeed ARCA) detector design requires faster deployment of DUs than in ANTARES, a novel method of deployment has been developed.

The DU is wrapped around a spherical metal frame, called a launch vehicle, which is affixed to the anchor. The launch vehicle is then lowered on to the sea bed, as shown in Figs. 2.17 and 2.17. Once the DU is securely anchored, the launch vehicle begins to unroll, releasing DOMs one at a time, before eventually surfacing, where it can be recovered and reused.

Figure 2.17: The DOM launch vehicle during deployment (photograph taken by CNRS images).

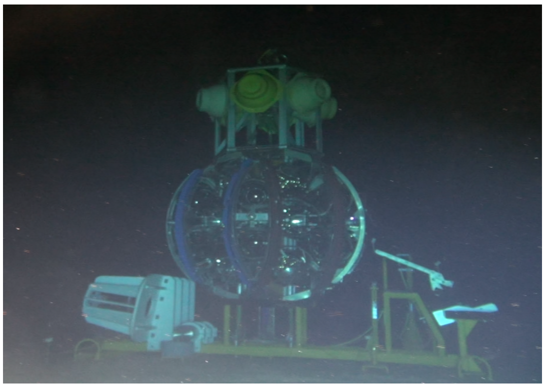

Figure 2.18: The DOM launch vehicle anchored to the seafloor (photograph taken by COMEX).

2.9 Triggering

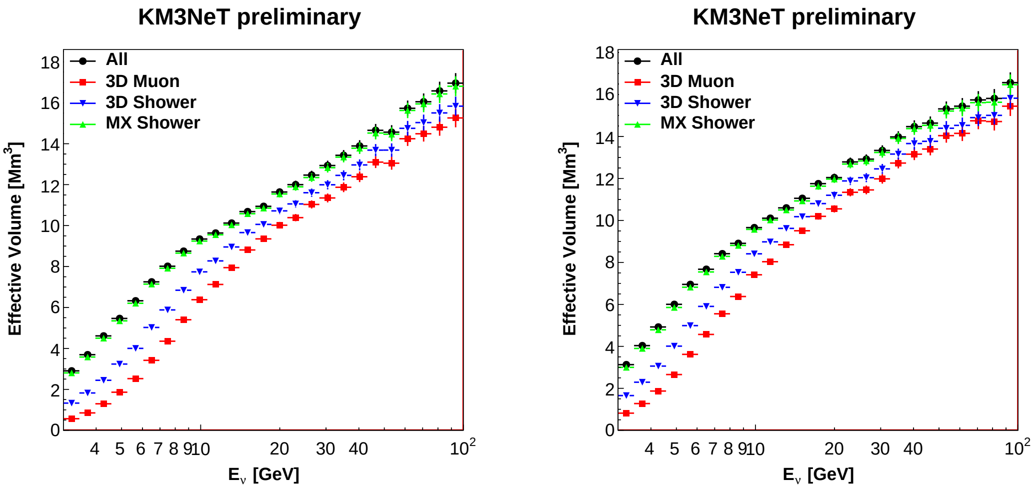

(a) $\nu_e - \mathrm{CC}$

(b) $\nu_\mu - \mathrm{CC}$

Figure 2.19: The effective volume at the trigger level for each of the trigger algorithms and their sums.

As it would be impractical to store every photoelectron registered by the detector, a series of triggering and filter algorithms are applied to the data offshore. In KM3NeT, there are three sets of criteria used to define a hit: level 0 (L0), an anologue pulse which exceeds the PMT threshold; level 1 (L1), two or more coincident L0s within a predefined time window; level 2 (L2), an L1 where the constituent L0s are separated by a predefined minimum space angle on the DOM.

In ORCA, 3 trigger algorithms are used, whose contributions to the detector effective volume are shown in Fig. 2.19. The 3D cascade trigger assumes that light is emitted isotropically from the neutrino interaction vertex and looks for 3 causally connected L1s on DOMs separated by the maximum distance D_{max}. Here, two hits are said to be causally connected if they meet the following criterion:

$$c|t_i - t_j| < \eta|\mathbf{r}_i - \mathbf{r}_j| + ct_{\text{extra}}, \tag{2.10}$$

where η is the refractive index of seawater $\mathbf{r}$ and t represent the hit position and time respectively and t_{extra} can be tuned to yield the desired signal to noise ratio. The 3D muon trigger is designed to look for the track-like topology described in Section 2.2. It looks for at least 4 causally connected hits L1s within a cylinder of width R_{max}. Here causal connection is defined by

$$c|t_i - t_j| < (z_i - z_j) + \eta \sin\theta_c \sqrt{(x_i^2 - x_j^2) + (y_i^2 - y_j^2)} + ct_{\text{extra}}, \tag{2.11}$$

with the coordinate system defined such that the z is along the cylinder axis. This search is carried out in 200 equidistant directions across the whole sky. Finally, the mixed (MX) trigger uses a mixture of L0s and L1s, in order to lower the trigger threshold and include fainter, low-energy events which do not emit the minimum of 3 causally connected L1s required by the 3D cascade trigger. During periods of high bioluminescence, the parameters $D_{\text{max}}, t_{\text{extra}}$, and R_{max} used in the muon trigger can be retuned and lower-threshold triggers even switched off in order to minimise contamination from pure noise events.

2.10 Background

2.10.1 Optical Background

The two main optical backgrounds affecting KM3NeT are bioluminescence and naturally occuring radioactivity in the seawater. The main radioactive isotope in seawater is ^{40}K, which decays according to the following two modes:

$$^{40}K \rightarrow^{40} Ca + e^- + \bar{\nu}_e \qquad (89.3\%)$$
$$^{40}K + e^- \rightarrow^{40} Ar + \bar{\nu}_e + \gamma \qquad (10.7\%)$$

The electrons emit Cherenkov radiation, whilst also undergoing Rutherford scattering, resulting in an isotropic source of ~ 100 detectable photons. In the case of electron capture, Cherenkov radiation is emitted by electrons Compton scattered by the emitted photon [76, 77]. The baseline count rate per PMT due to ^{40}K has been measured in the region 6-8 kHz (see Fig. 2.20).

Bioluminescence is light emitted by living organisms in and around the detector. In both KM3NeT and its predecessor, ANTARES [78], this typically manifests itself as an elevated count rate on a single PMT or a localised cluster of PMTs. An

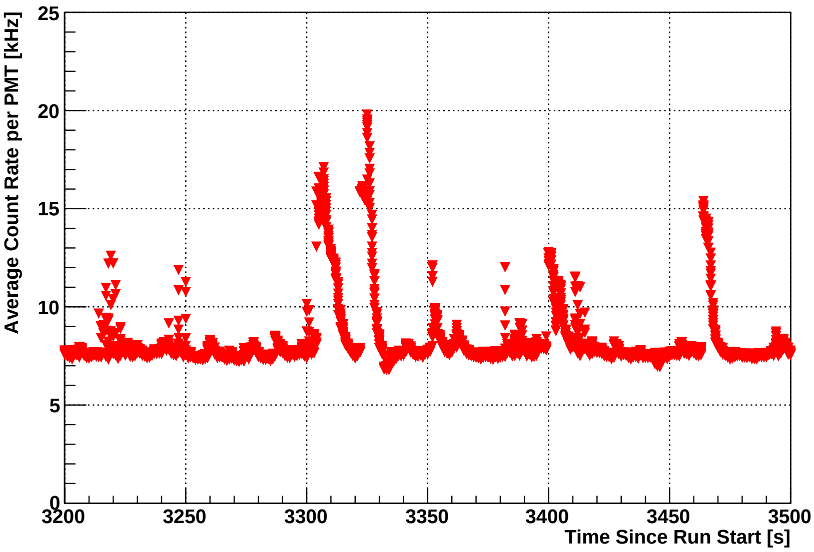

Figure 2.20: The count rate as a function of time, averaged over all the PMTs in a single DOM, for five minutes of ORCA data taken in December 2017. The 8 kHz floor is caused by ^{40}K, whereas the peaks are caused by bursts of bioluminescence.

example of bioluminescence bursts found in the ORCA data is shown in Fig. 2.20. In order to reduce this impact of bioluminescence, PMTs with high counting rates (typically defined as > 19 kHz), are filtered from the data. In periods of especially high activity, the trigger algorithms can be retuned or even turned off, in order to improve the data quality.

2.10.2 Atmospheric Muons

Atmospheric muons are produced by the same atmospheric cosmic ray interactions as atmospheric neutrinos, typically coming from the decays of charged pions. If their energy exceeds ~ 1 TeV, then they can propagate all the way to the detector, despite the 2.5 km of seawater shielding it. Typically, neutrinos are distinguished from atmospheric muons by their direction, as only neutrinos can pass through the Earth. However, an upwards travelling Cherenkov front can mimic the signature of an upgoing neutrino, especially on the outer edges of the detector. This issue is discussed further in Chapters 3 and 4, as the measurable atmospheric muon rate is ~ 4 orders of magnitude greater than that of atmospheric neutrinos. Even the small proportion of atmospheric muons mistakenly reconstructed pointing upwards can be a significant source of background.

2.11 Software and Simulations

In brief, these are the software and simulation packages used in this work. A schematic overview of the entire Monte Carlo simulation chain is shown in Fig. 2.21.

gSeaGen is a neutrino generator based on GENIE [79], implemented specifically for neutrino telescopes [80].

MUPAGE is an atmospheric muon generator [81], based on parametric formulae obtained from a full MC simulation using the HEMAS code [82]. It is in good agreement with atmospheric muon flux measurements by ANTARES [83].

KM3Sim is a package based on GEANT4, which generates Cherenkov light emitted by primary and secondary particles produced by the neutrino interaction and propagates it to the PMTs [84].

KM3 also generates Cherenkov light from muons or EM cascades, but uses lookup tables rather than a full simulation [85].

JTE simulates the PMT electronics, adds the ^{40}K background and then applies the trigger algorithms described in Section 2.9.

JGandalf is the muon track reconstruction algorithm described in Chapter 3.

orcaDusj is the standard KM3NeT cascade reconstruction algorithm, explained in detail in Ref. [86].

ECAP PID is the Particle Identification (PID) algorithm, developed at the Erlangen Centre for Astroparticle Physics. It is used to separate neutrinos from atmospheric muons and track-like events from cascade-like events. Its performance is discussed in Section 3.7.2.

OscProb is the package used for all 3×3 neutrino mixing calculations throughout this work [34]. It contains an internal Earth model [33] calculating all matter effects, with particular care shown to the chemical composition of the Earth. The exact Earth model used in this work can be found in the Appendix (Table A.1).

paramNMH is the software package developed to simulate the detector response and calculate the sensitivity to the NMH and the oscillation parameters θ_{23} and Δm^2_{32}. It is described in detail in Chapter 5.

A full overview of common tools, such as GENIE, will not be provided here. However, the following sections will describe the assumptions and approximations made in calculating the neutrino oscillation probabilities and simulating the detector response.

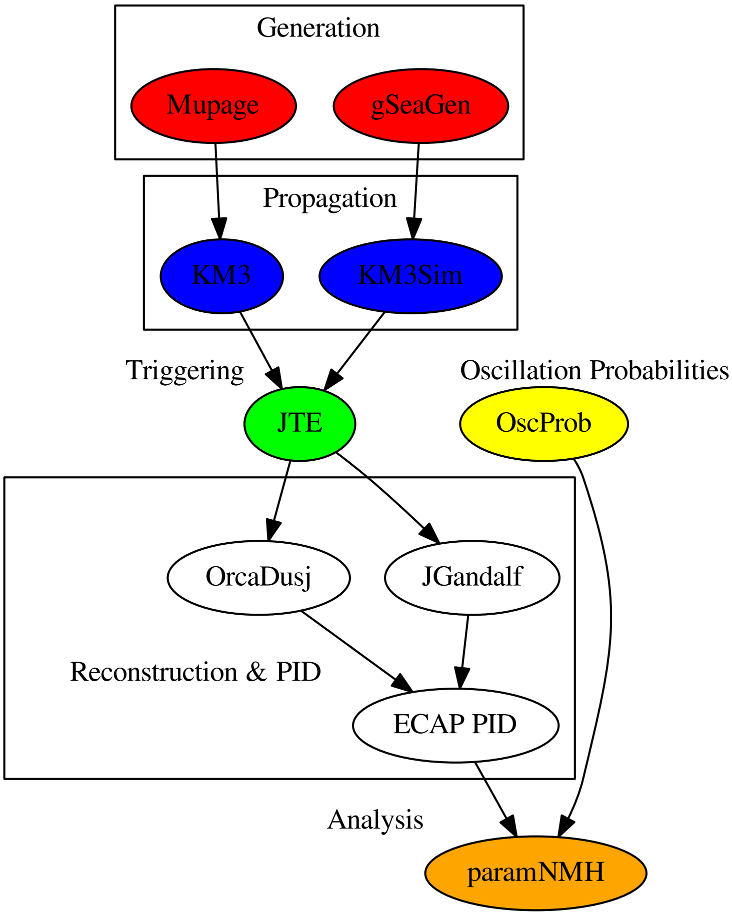

Figure 2.21: A schematic overview of all the software used in this analysis, starting from event generation and finishing with the final sensitivity calculation.

2.11.1 JTE and the Benchmark Detector

The previous sensitivity study in Refs. [1, 87] assumed an idealised detector footprint, with all DUs spaced exactly 20 m apart. This time, care has been taken to reproduce the seafloor infrastructure plan shown in Fig. 2.14. A before and after comparison is shown in Fig. 2.22. After the light propagation has been simulated, gaussian smearing is applied to the hit arrival times to simulate the time transit spread of the PMTs. Coincident hits on the same PMT are also merged into a single pulse with an increased ToT.

Environmental background is modelled as a uniformly distributed series of ^{40}K events. Each ^{40}K decay can illuminate multiple PMTs on the same DOM. A set of N hits, detected within a 20 ns time window is known as an Nth level coincidence. Each coincidence level is simulated at a different rate, based on in situ

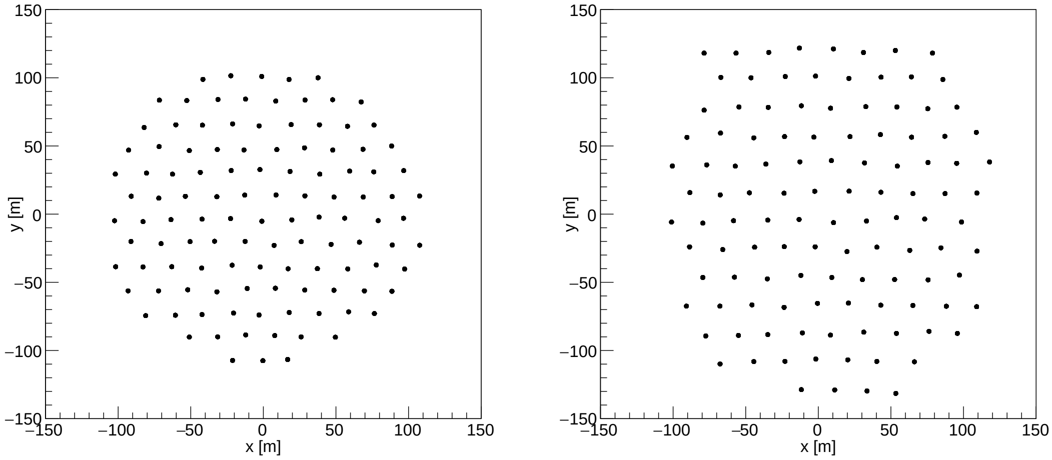

(a) KM3NeT Letter of Intent [1]

(b) New detector

Figure 2.22: The detector footprints assumed in the KM3NeT Letter of Intent sensitivity study [1] and the one used in this work. The new detector footprint matches the planned seafloor infrastructure presented in Fig. 2.14 and is more sparsely spaced. The average horizontal spacing between DUs has increased from 20 m to 23 m.

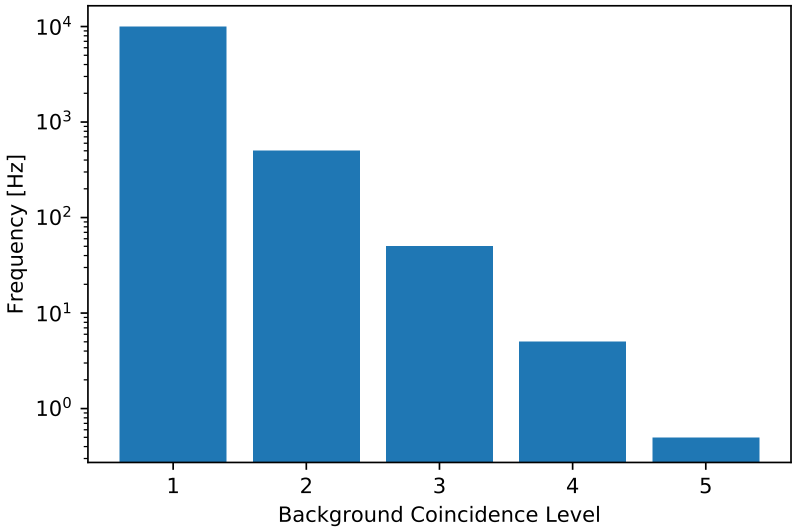

Figure 2.23: The assumed background coincidence rate, defining an Nth level coincidence as N hits on different PMTs within a 20 ns time window.

measurements [76], as shown on Fig. 2.23. Particularly conservative values were chosen for 1st and 2nd level coincidences (10 kHz and 500 Hz respectively), in order to allow for a higher than expected contribution from bioluminescence.

2.12 Other Physics Studies

The focus of this thesis is on determining the NMH and atmospheric oscillation parameters. However, the physics programme of ORCA will be considerably broader, and so this section is dedicated to briefly summarising other applications of the detector, which might otherwise go overlooked.

Cherenkov neutrino telescopes have already been used to carry out indirect dark matter (DM) searches. An overview of the requirements for a DM candidate is available in Ref. [88], but for the purposes of this section, it is sufficient to say that it should be stable, massive, and neutral and is often assumed to be weakly interacting. While popular DM candidates, such as the neutralino, are forbidden from decaying to SM particles, due to a symmetry of nature, such as the R-parity, DM co-annihilation to SM particles is often permitted. The subsequent decay of those SM particles, through channels such as $\chi\chi \rightarrow \tau\bar{\tau}$ for example, would result in a detectable neutrino flux from massive objects where DM is known to accumulate. Both ANTARES and IceCube have used this technique to publish constraints on the cross sections of DM present in the Sun [89, 90], Earth [91, 92, 93], Galactic Centre [94, 95] and Galaxy Clusters [96]. ORCA will continue to perform DM searches in the same vein, but ORCA's lowered energy threshold would allow for more stringent cross section constraints at lower masses.

As mentioned in Section 1.8.2, neutrinos are emitted by supernovae, to which both KM3NeT sites will be sensitive. Supernova neutrinos are too low energy (∼MeV) to be resolved independently in ARCA and ORCA. Instead, the rate of L1 hits with high numbers of PMTs hit is monitored [97]. A high rate could correspond to Cherenkov radiation from positrons created by inverse beta decay with supernova neutrinos.

ORCA will also function as a neutrino telescope, much like ANTARES and will be sensitive to GeV energy emissions from sources such as colliding wind binaries [98] and gamma ray bursts [99]. Finally, it will also be possible to measure the chemical composition of the Earth, by measuring the size of matter enhancements to the oscillation probability as a function of zenith angle [100].

Chapter 3

Reconstruction

3.1 Fit Procedure

In order to reconstruct tracks, a likelihood-based method is applied, combining the spatial and time distribution of Cherenkov photons, as well as the PMT response. Function minimisation algorithms generally employed in such an approach typically find only local minima. It is therefore important to employ multiple possible starting points, so that the global minimum is found and to allow for multiple compatible solutions. In order to achieve this, two reconstruction chains have been designed (see Fig. 3.1). They were optimised separately for both the full 115-line ORCA detector and for the single line deployed in 2017. At every stage of the chain, multiple reconstructed track hypotheses are fitted, ranked and then a subset of the best tracks is passed to the next stage. The number of tracks in this subset has been chosen for the fastest possible computing time, without sacrificing angular resolution. See Table 3.1 for the number of hypotheses used at each stage of the chain.

Reconstruction Stage	N. of Tracks (Single Line)	N. of Tracks (Full Detector)
Prefit	844	844
χ^2 Fit	288	N/A
Full PDF Fit	50	96
Length Calculation	50	96

Table 3.1: The number of track hypotheses used at each stage of the reconstruction chain for both the full 115-line ORCA configuration and the single line case.

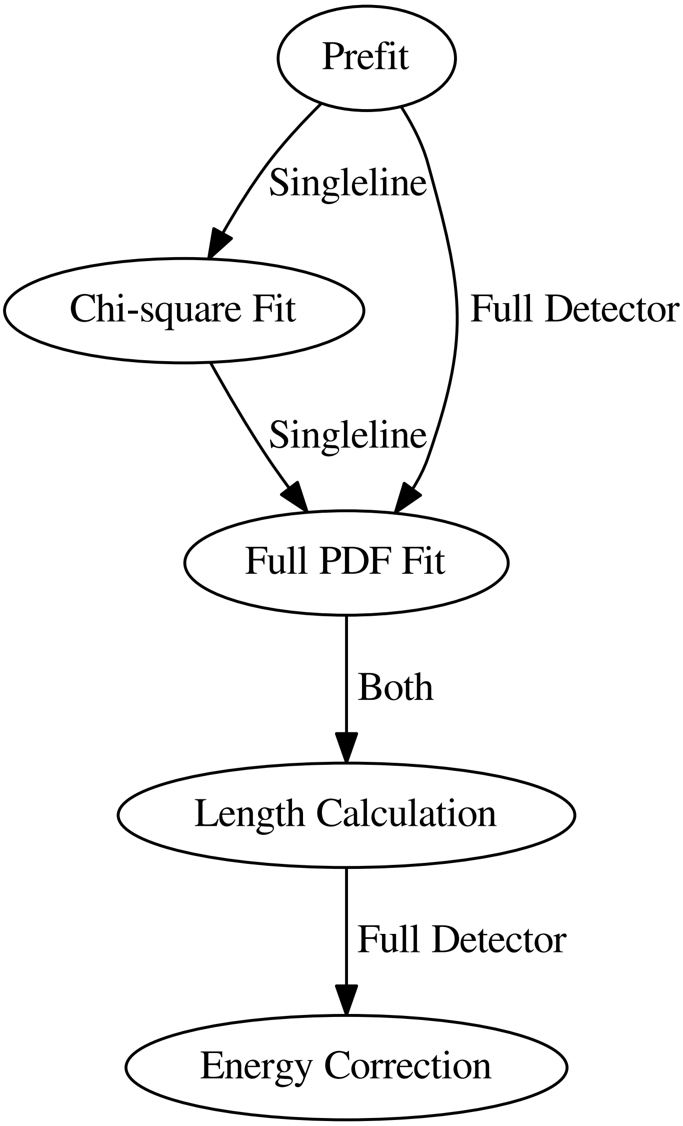

Figure 3.1: A step by step overview of the muon track fitting procedure, showing the two different approaches used for the full ORCA detector and for the single line deployed in 2017.

3.2 Muon Prefit

3.2.1 Linearising the Track Position Fit

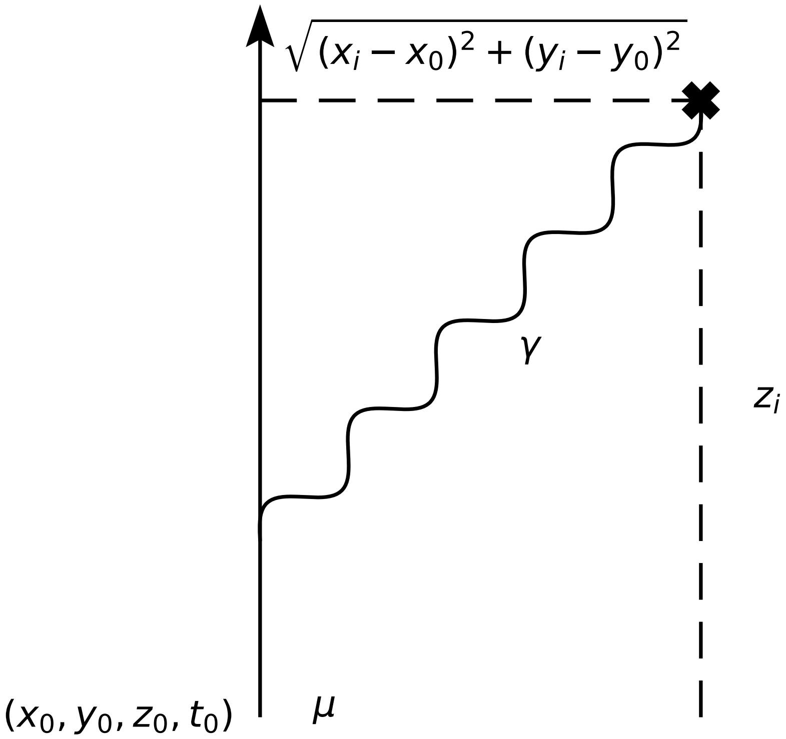

Figure 3.2: The coordinate system used to describe the muon prefit. Note that the coordinates (x_0, y_0, z_0, t_0) simply describe a position and time along the muon path and not the interaction vertex.

The derivation in this subsection is based on Ref. [101], with subsequent subsections going on to describe the prefit in more detail. The key principle behind the prefit is that, if the direction of the muon is assumed, then a system of linear equations can be constructed whose solution will be the position of the track. Hypothesising that the photon is emitted at the Cherenkov angle, according to the convention shown in Fig. 3.2, its expected hit time is given by

$$c(t_i - t_0) = z_i - z_0 - \frac{\sqrt{(x_i - x_0)^2 + (y_i - y_0)^2}}{\tan\theta_c} + \eta_g \frac{\sqrt{(x_i - x_0)^2 + (y_i - y_0)^2}}{\sin\theta_c}, \quad (3.1)$$

where η_g is the group refractive index in seawater. Taking the approximation $\eta_g = \frac{1}{\cos\theta_c}$, this can be simplied to

$$c(t_i - t_0) = z_i - z_0 + \tan\theta_c \sqrt{(x_i - x_0)^2 + (y_i - y_0)^2}. \quad (3.2)$$

Finally, defining two new variables

$$t'_0 = \frac{t_0}{\tan\theta_c}, \tag{3.3}$$

$$t'_j = \frac{t_j - (z_i - z_0)}{c\tan\theta_c}, \tag{3.4}$$

it simplifies even further to

$$(ct'_i - ct'_0)^2 = (x_i - x_0)^2 + (y_i - y_0)^2. \tag{3.5}$$

For a system of N hits, this can be expressed in terms of a $3 \times N$ matrix

$$\begin{pmatrix} 2(x_2 - x_1) & 2(y_2 - y_1) & -2(t'_2 - t'_1) \\ 2(x_3 - x_2) & 2(y_3 - y_2) & -2(t'_3 - t'_2) \\ \vdots & \vdots & \vdots \\ 2(x_1 - x_n) & 2(y_1 - y_n) & -2(t'_1 - t'_n) \end{pmatrix} \begin{pmatrix} x_0 \\ y_0 \\ {t'}_0 \end{pmatrix} = \begin{pmatrix} x_2^2 - x_1^2 + y_2^2 - y_1^2 - {t'}_2^2 + {t'}_1^2 \\ x_3^2 - x_2^2 + y_3^2 - y_2^2 - {t'}_3^2 + {t'}_2^2 \\ \vdots \\ x_1^2 - x_n^2 + y_1^2 - y_n^2 - {t'}_1^2 + {t'}_n^2 \end{pmatrix}, \tag{3.6}$$

which can be solved for x_0, y_0 and t'_0.

3.2.2 Fit Procedure

In order to apply the method described in Section 3.2.1, it is necessary to have a pure sample of hits. Firstly, a cluster of DOMs is selected, each of which has at least one hit compatible with the assumed muon direction, as described in Section 2.9. At least one DOM in the selected cluster must have two hits within a time window of 18 ns and have contributed to the trigger. This requirement makes the clustering algorithm less sensitive to noise. The chi square associated with the track is then calculated from the covariance matrix with respect to the assumed track direction

$$\chi^2 = \boldsymbol{\Delta}^T \boldsymbol{V}^{-1} \boldsymbol{\Delta}, \tag{3.7}$$

where $\boldsymbol{\Delta}$ is a vector containing all the time residuals $(\delta t_1, \delta t_2, ..., \delta t_N)$. If there are 8 DOMs or fewer in the selected cluster, the chi square is calculated for every permutation of 5 to 8 DOMs, and the subset with lowest chi square per degree of freedom is finally selected. Otherwise, up to 3 DOMs are removed from the cluster in order to improve the chi square further. The DOM with the greatest contribution to the total chi square is removed first, unless its contribution is within 3 standard deviations of the expected mean.

This is done for 844 directions covering the entire sky, separated by a grid angle of 5°. The fitted tracks associated with each direction are then ranked, according to the discriminator Q, given by

$$Q = N_{\text{DOMs}} - \frac{\chi^2}{4N_{\text{DOMs}}}. \tag{3.8}$$

It was chosen to favour prefitted tracks with a higher number of compatible DOMs. In Fig. 3.3, it can be seen that Q is higher closer to the true neutrino direction.

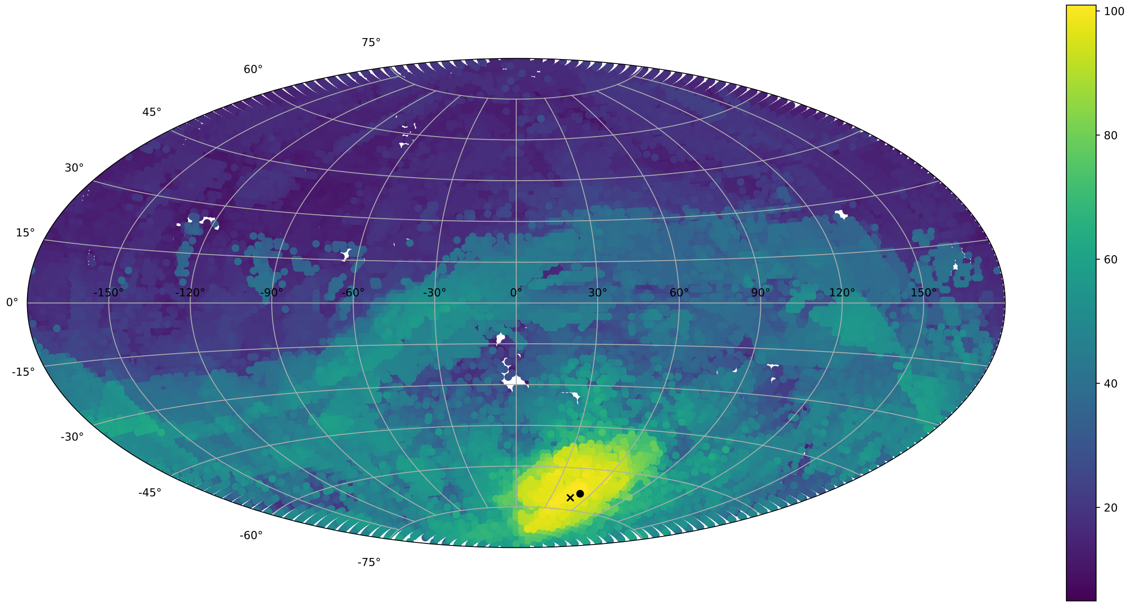

Figure 3.3: A map of Q for each scanned direction for a 60 GeV ν_μ-CC event, 23 GeV of which has gone into the muon. It can be seen that the Q is highest near to the true neutrino and muon directions, indicated by a dot and cross respectively.

3.3 χ^2 Fit

This is the most straightforward step in the reconstruction chain. A time residual (δt) is defined as the difference between the true and expected arrival time of a photon, assuming it was emitted at the Cherenkov angle with respect to the track (see Fig. 3.2). A set of DOMs is selected within a radial distance of less than 50 m from the prefitted track and with at least one hit fulfilling $|\delta t| < 15$ ns. A chi square is defined as

$$\chi^2 = \sum_{i \in \text{DOMs}} w_i \frac{\delta t_i^2}{\sigma}, \tag{3.9}$$

where, on each DOM, δt_i is the time residual of the first selected hit, w_i is the number of selected hits and σ is assumed width of the distribution, set to 3 ns. The position and direction with the minimum chi square is found using the Nelder-Mead [102] method for each prefitted track hypothesis. The Q discriminator defined in Eq. 3.8 is used to rank the tracks as before.

3.4 Full PDF Fit

3.4.1 Light Emission Model

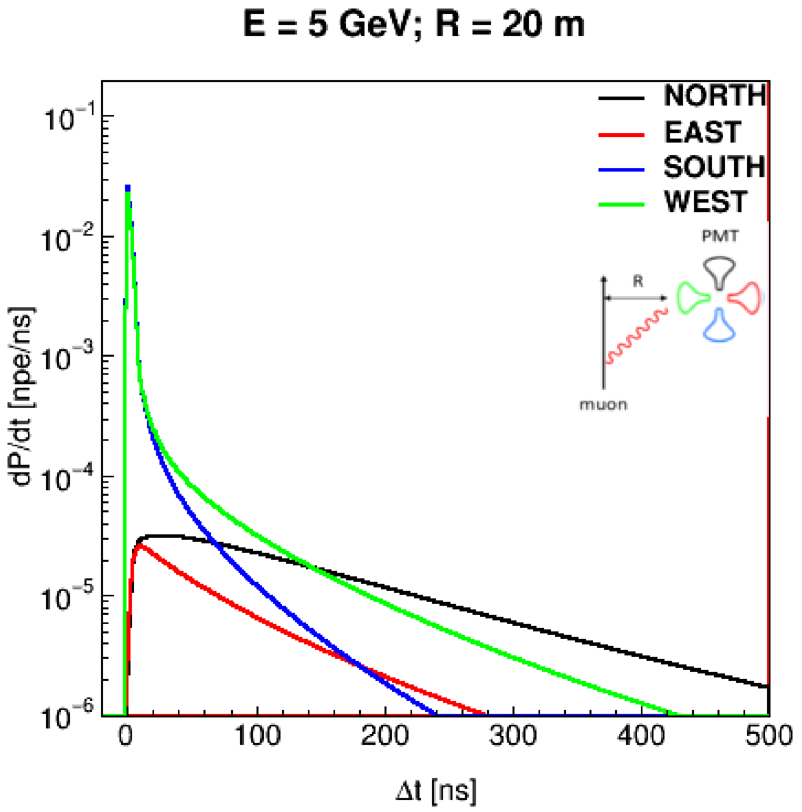

Figure 3.4: The expected time residual distribution for a 5 GeV muon on a PMT 20 m away. The distribution is shown for four PMT orientations: North, parallel to the track; South, antiparallel with the track; East, facing away from the track; and West, perpendicular facing the track. The South and West facing PMTs see mostly direct light, while the North and East facing PMTs see mostly scattered light.

The light emission profile of muons in seawater is well understood, with parametrisations inherited from ANTARES [103]. With the new multi-PMT DOM design, a new set of lookup tables has been created, taking into account both the position and orientation of the PMT relative to the track (see Fig. 3.4). The probability density function (PDF) of unscattered light from a muon is given by

$$\left.\frac{d\mathcal{P}}{dt}\right|_{\text{Direct}} = \Phi_0(R,\lambda)A\left(\frac{\partial t}{\partial\lambda}\right)^{-1}\epsilon(\theta_{\text{impact}})QE(\lambda)e^{\frac{-d}{\lambda_{\text{abs}}}}e^{\frac{-d}{\lambda_s}}, \tag{3.10}$$

where A is the photocathode area, QE is the PMT quantum efficiency, and ϵ is the its angular acceptance as a function of impact angle, taken from Ref. [70]. Here, Φ_0 is the number of detectable photons as a function of distance (R) and wavelength (λ), related to the Cherenkov spectrum given in Eq. 2.2:

$$\Phi_0(R,\lambda) = \frac{1}{2\pi R \sin\theta_c}\frac{d^2N}{d\lambda dz}. \tag{3.11}$$

The chromatic dispersion is given in terms of the group and phase indices of refraction (η_g, η), which depend on wavelength:

$$\frac{\partial t}{\partial \lambda} = \frac{R}{c}\left(\frac{1}{\sin\theta_{\mathrm{emit}}}\frac{d\eta_g}{d\lambda} + \frac{\eta-\eta_g}{\tan^3\theta_{\mathrm{emit}}}\frac{d\eta}{d\lambda}\right), \tag{3.12}$$

where θ_{emit} is the emission angle of the photon with respect to the muon direction. The equivalent expression for scattered light is derived by assuming only single scattering and integrating over all possible photon paths. The resulting PDF is shown in Fig. 3.4, with PMTs facing the track seeing mostly unscattered light and PMTs facing away from the track seeing mostly unscattered light.

3.4.2 Fit Procedure

For a set of hits, distributed according to the PDF $\mathcal{P}(t)$, the continuous Poisson probability of detecting a hit at a given time t is given by

$$\mathcal{P}_{\mathrm{Poisson}}(t) = \frac{\mathcal{P}(t)e^{-\int_{t_{\mathrm{min}}}^{t}\mathcal{P}dt}}{1-e^{-\int_{t_{\mathrm{min}}}^{t\mathrm{max}}\mathcal{P}dt}}. \tag{3.13}$$

The reconstructed track, described by two position coordinates (x, y), a time (t), and two direction cosines $(\delta x, \delta y)$, is the one which maximises the likelihood function shown below:

$$\mathcal{L}(x,y,t,\delta x,\delta y|\mathrm{hits}) = \prod_{i\in\mathrm{hits}} \frac{\mathcal{P}_{\mathrm{Poisson}}(\mathrm{Signal} +^{40} K|t_i,x_i,y_i,z_i,\theta_i,\phi_i)}{\mathcal{P}_{\mathrm{Poisson}}(^{40}K|t_i)}, \tag{3.14}$$

where two angles have been introduced (θ_i, ϕ_i), describing the PMT orientation with respect to the track. The denominator, equal to the probability of seeing a hit from random noise, is calculated using a constant, flat PDF. The numerator is calculated using the sum of the PDF described in Subsection 3.4.1 with the random noise PDF.

For each reconstructed track passed to this stage of the chain, hits are selected in a cylinder of radius 50 m around the track and with time residual satisfying $-50\mathrm{ns} < \delta t < 450$ ns. The negative log likelihood function is minimised using the Levenberg-Marquardt algorithm [104].

3.5 Track Length and Energy Calculation

For a given PMT, an expected number of hits N^{sig} can be defined by integrating a PDF over a time window Δt. The correspond number of hits from random background N^{bkg} is simply the product of the background rate with the duration of Δt. Using the poisson probability of no hits on a single PMT, a probability ratio given by

$$\frac{\mathcal{P}^{\text{sig}}_{\text{PMT}}}{\mathcal{P}^{\text{bkg}}_{\text{PMT}}} = \begin{cases} \frac{1-e^{-(N^{\text{sig}}-N^{\text{bkg}})}}{1-e^{-N^{\text{bkg}}}} & \text{if the PMT was hit,} \\ e^{-(N^{\text{sig}}-N^{\text{bkg}})} & \text{otherwise.} \end{cases} \tag{3.15}$$

can be used to assess the compatibility of a track hypothesis with the data. Assuming that photons are emitted at the Cherenkov angle, every PMT has an associated emission point (see Fig. 3.5). The length is therefore just the distance between the first and last DOM along the track where the likelihood, given by

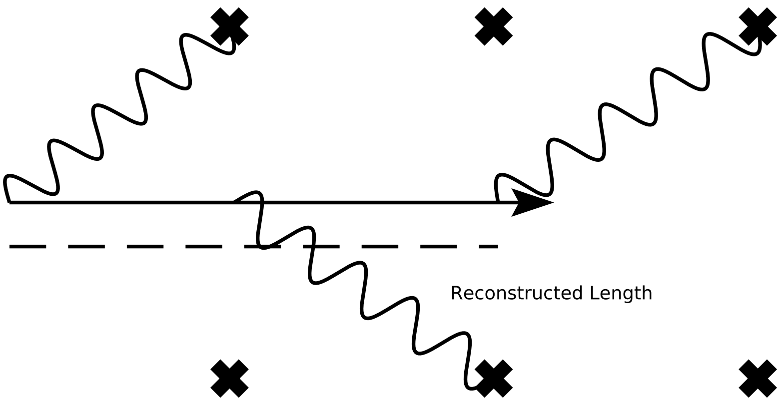

Figure 3.5: The geometry of the track length calculation.

$$\mathcal{L}^{\text{sig}}_{\text{DOM}} = \prod_{\text{DOM}} \frac{\mathcal{P}^{\text{sig}}_{\text{PMT}}}{\mathcal{P}^{\text{bkg}}_{\text{PMT}}}, \tag{3.16}$$

exceeds a predefined threshold. In this work, the time window had a duration of 20 ns and only DOMs within 50 metres of the track were selected. As shown in Fig. 2.4, muon energy scales linearly with track length below 100 GeV. To obtain the muon energy, the length is simply multiplied by a constant.

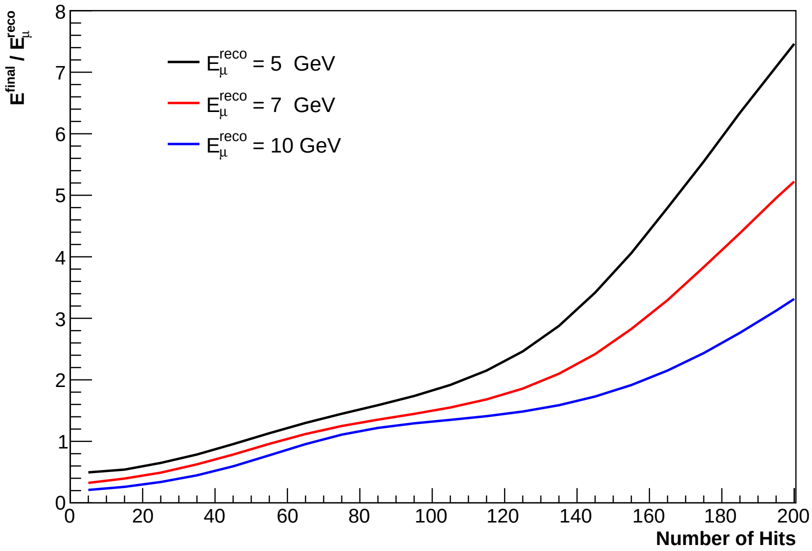

Figure 3.6: The energy correction applied to the reconstruction muon energy as a function of the number of hits, shown here for reconstructed muon energies of 5, 7 and 10 GeV.

To go from a muon energy to a neutrino energy, a correction is applied based on the number of selected hits around the track (see Fig. 3.6). A short track with a high number of hits, for example, is indicative of a more energetic hadronic shower and the neutrino energy is scaled up accordingly. Long tracks with low numbers of hits, on the other hand, are evidence of an over estimated muon energy and so the final energy estimate can also be scaled downwards.

3.6 Performance

3.6.1 Direction Fit

As the azimuth measurement is unimportant for NMH determination, plots in this section will show the zenith zenith instead. In the single line case, the distribution of this uncertainty is shown in Fig. 3.7, with the median error as a function of energy shown in Fig. 3.8. For the full detector resolution, see Figs. 3.9 and 3.10. Here, only a very loose event pre-selection has been applied in order not to show a biased view of the reconstruction performance. In the full detector case, only events whose reconstructed vertices are inside the detector volume are selected.

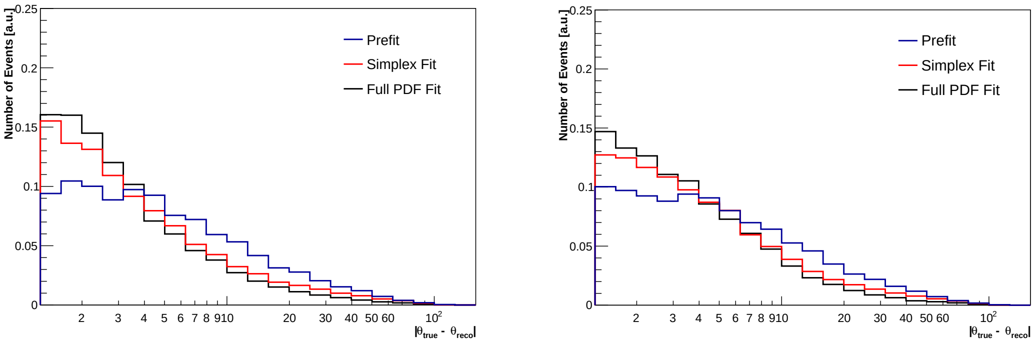

(a) μ direction (b) ν_μ direction

Figure 3.7: The zenith uncertainty in degrees for ν_μ-CC interactions, weighted with the unoscillated Honda flux, reconstructed with a single ORCA line. It is shown with respect to both the neutrino direction and the outgoing muon direction for the first three stages of the reconstruction chain.

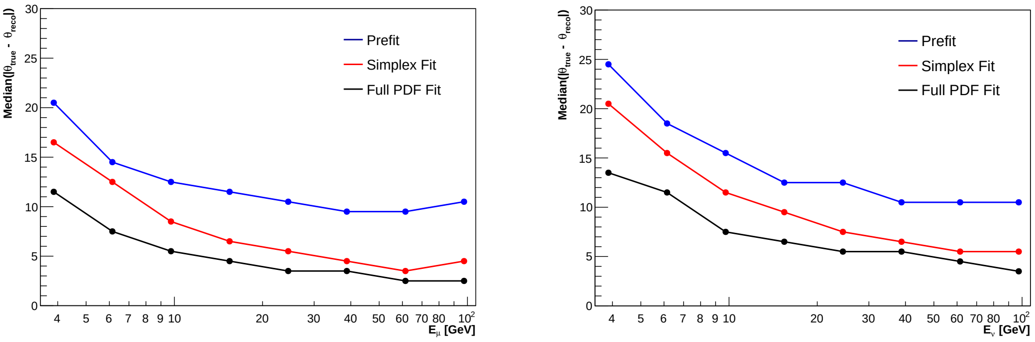

(a) μ direction versus energy (b) ν_μ direction versus energy

Figure 3.8: The median zenith uncertainty in degrees for ν_μ-CC interactions, weighted with the unoscillated Honda Flux, reconstructed using a single ORCA line. It is shown with respect to both the neutrino direction and the outgoing muon direction for the first three stages of the reconstruction chain.

The zenith angle of a muon propagating through the full ORCA detector can be reconstructed with a high level of accuracy. This is particularly striking above 10 GeV, where the error is less than 1° on average. However, the reconstruction performance is intrinsically limited by the opening angle between the muon and the neutrino (see Fig. 3.10). Another limiting factor is the contribution from the hadronic shower. In Fig. 3.11, it can be clearly seen that the resolution degrades as the hadronic contribution to the event increases. This is because hadronic showers are not necessarily colinear with the muon and also exhibit large fluctuations compared to muon tracks or even EM showers [105]. Nevertheless, this reconstruction algorithm is still able to resolve the direction of a hadronic shower, as can be seen when $y > 0.75$ and the reconstructed zenith is closer to the neutrino zenith than the muon zenith.

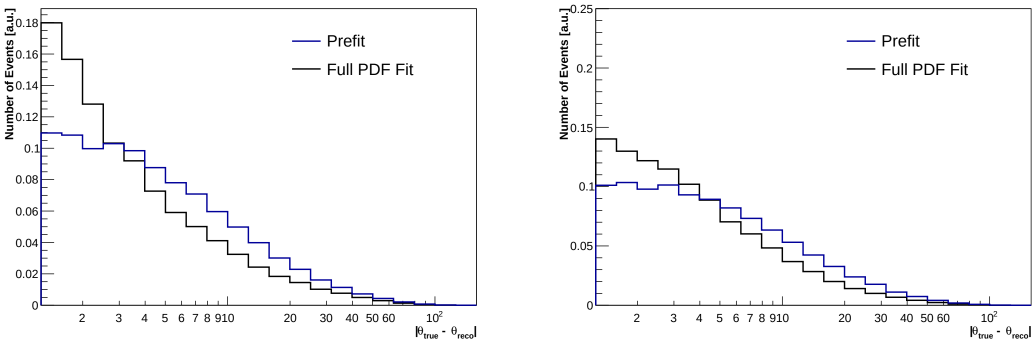

(a) μ direction (b) ν_μ direction

Figure 3.9: The zenith uncertainty in degrees for ν_μ-CC interactions, weighted with the unoscillated Honda flux, reconstructed with the full ORCA detector, where the reconstructed track begins inside the detector volume. It is shown with respect to both the neutrino direction and outgoing muon direction for the prefit and full PDF fit stages of the reconstruction chain.

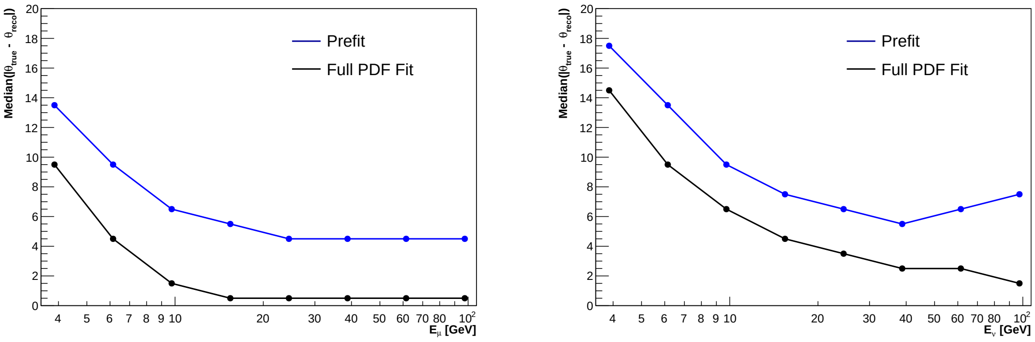

(a) μ direction versus energy (b) ν_μ direction versus energy

Figure 3.10: The median zenith uncertainty in degrees for ν_μ-CC interactions, weighted with the unoscillated Honda Flux, reconstructed with the full ORCA detector, where the reconstructed track begins inside the detector volume. It is shown with respect to the both the neutrino direction and outgoing muon for direction for the prefit and full PDF fit stages of the reconstruction chain. Above muon energies of 10 GeV, ν_μ direction uncertainty is dominated by the kinematic angle between the muon and the neutrino.

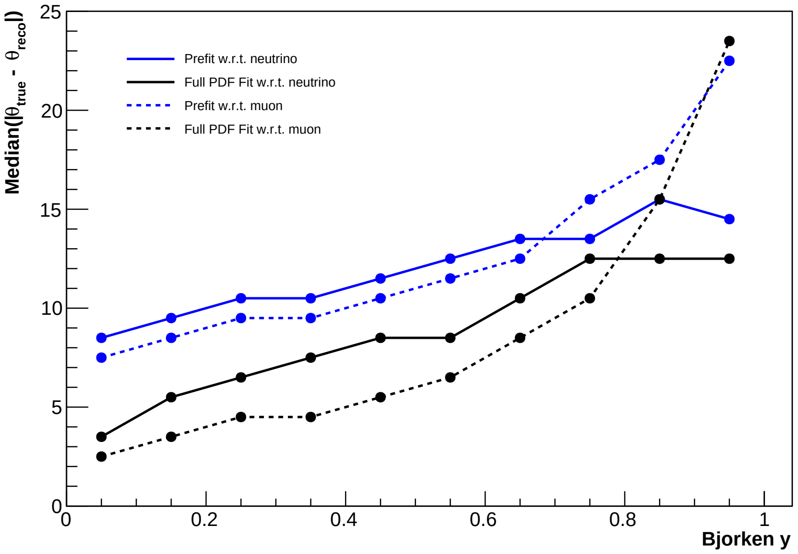

Figure 3.11: The median zenith uncertainty in degrees for ν_μ-CC interactions as a function of inelasticity, weighted with the unoscillated Honda Flux, reconstructed with the full ORCA detector, where the reconstructed track begins inside the detector volume. When $y > 0.75$, the fitted direction starts to be dominated by the hadronic shower direction, instead of the muon. The reconstruction performs best for events where most of the neutrino energy is deposited into the muon.

3.6.2 Energy Calculation

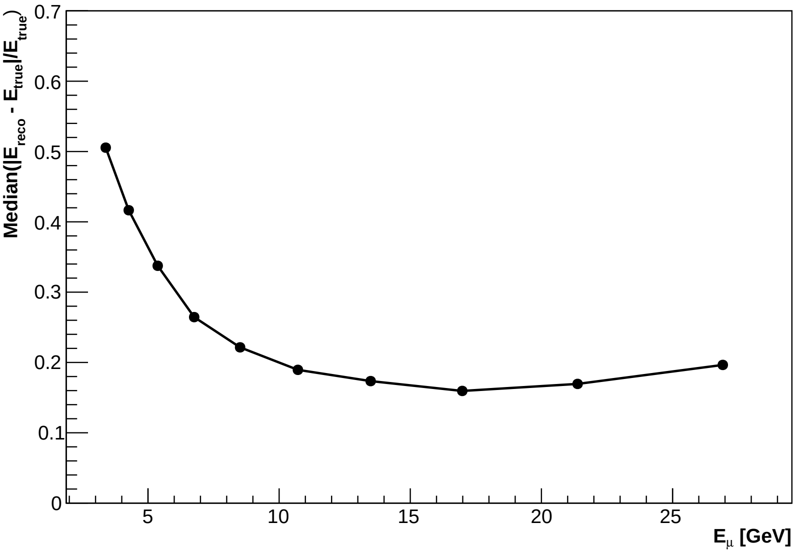

Figure 3.12: The median relative error on the muon energy for ν_μ-CC events reconstructed with the full detector, as a function of true muon energy. Events were selected whose reconstructed vertex is inside the detector volume.

The median muon and neutrino energy resolutions are better than 30% above 5 GeV (see Figs 3.12 and 3.13). The muon energy resolution is intrinsically limited by two factors. Firstly, if a muon exits the detector, its length will be underestimated as that information is lost. Secondly, it is limited by the density of DOMs along the track. The start and end points are only registered on the nearest DOM. The former is more important at high energies and the latter at low energies, as can be seen on Fig. 3.12. The corrected neutrino energy is subsequently limited by fluctuations in the light yield (see Ref. [105]) for a full discussion.

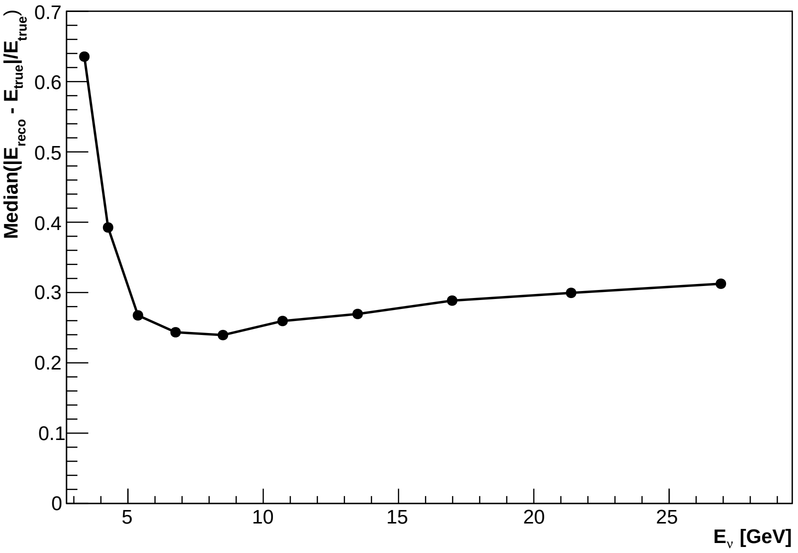

Figure 3.13: The median relative error on the neutrino energy for ν_μ-CC events reconstructed with the full detector, as a function of true neutrino energy. Events were selected whose reconstructed vertex is inside the detector volume.

3.7 Particle Identification

Water Cherenkov neutrino detectors such as ORCA can only distinguish different neutrino flavours by examining the event topologies, as described in Section 2.2. It is also important to extract a clean sample of signal from the data, eliminating as many misreconstructed atmospheric muons or triggered ^{40}K events as possible (see Section 2.10 for the causes of this background).

3.7.1 Noise Rejection

The event rate is dominated by atmospheric muons. The vast majority of these can be cut away by only considering events which are reconstructed as pointing upwards. However, this is insufficient on its own to reduce the atmospheric muon background to the percent level required by the oscillation analysis (see Fig. 3.14).

In Figs. 3.15 and 3.16, it can be seen that misreconstructed atmospheric muons are found around the edges of the detector. By taking only events with start points reconstructed inside the instrumented volume, the atmospheric muon contamination can be reduced by a factor 1000 (see Fig. 3.17).

Random noise, on the other hand, is reconstructed with a much weaker preference for position or direction. It is found inside the instrumented volume, due to the

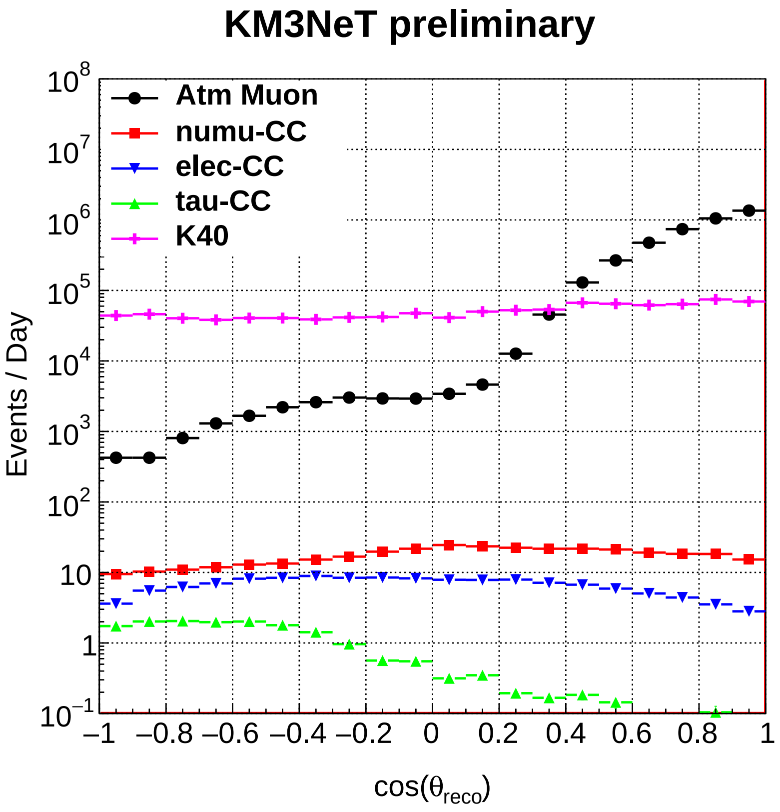

Figure 3.14: The total event rate for signal and background after reconstruction - before any filtering, as a function of the reconstructed zenith angle using the track reconstruction.

higher PMT density, and more often reconstructed as downgoing (see Fig. 3.14). It is, however, reconstructed with a lower likelihood and features lower hit multiplicities than neutrino or atmospheric muon events. It can be separated from the signal by looking at both the likelihood and the difference between the number of PMTs and DOMs hit within the reconstruction time window (see Fig. 3.18).

A preliminary set of cuts was applied to the simulated data before the more sophisticated methodology described in Section 3.7.2 could be applied. The intention here was to simply speed up the processing chain by removing the most obvious atmospheric muon background, reducing it by a factor 1000, without cutting into the signal. Therefore very loose cuts were chosen, with the expectation that they could be tightened up at a later stage of the analysis. Two sets of preliminary cuts were defined, one for track-like events and the other for cascade-like events, using variables from the track and shower reconstructions respectively. See Ref. [86] for more details of the cascade reconstruction. Any events that passed either set were kept.

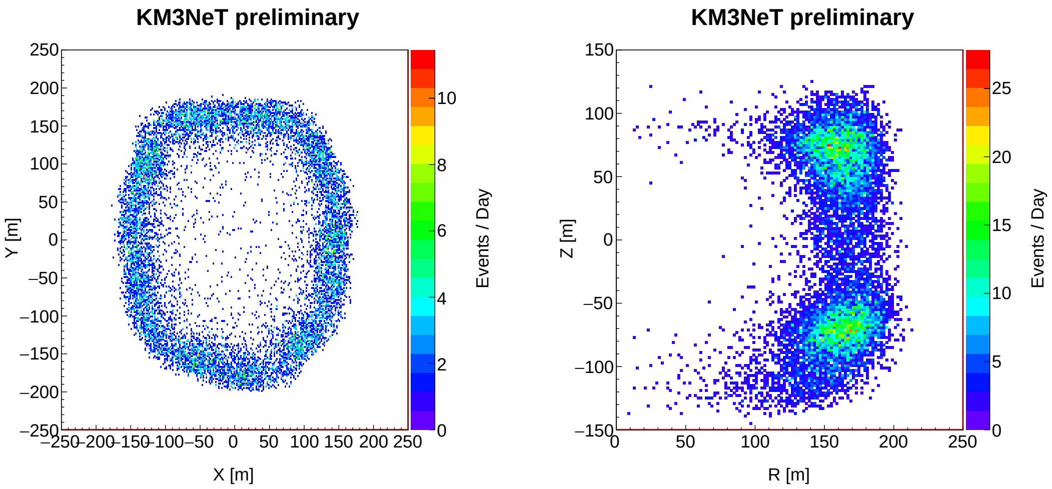

Figure 3.15: The reconstructed track start positions of atmospheric muons misreconstructed as upgoing. They are generally located around the edges of the detector.

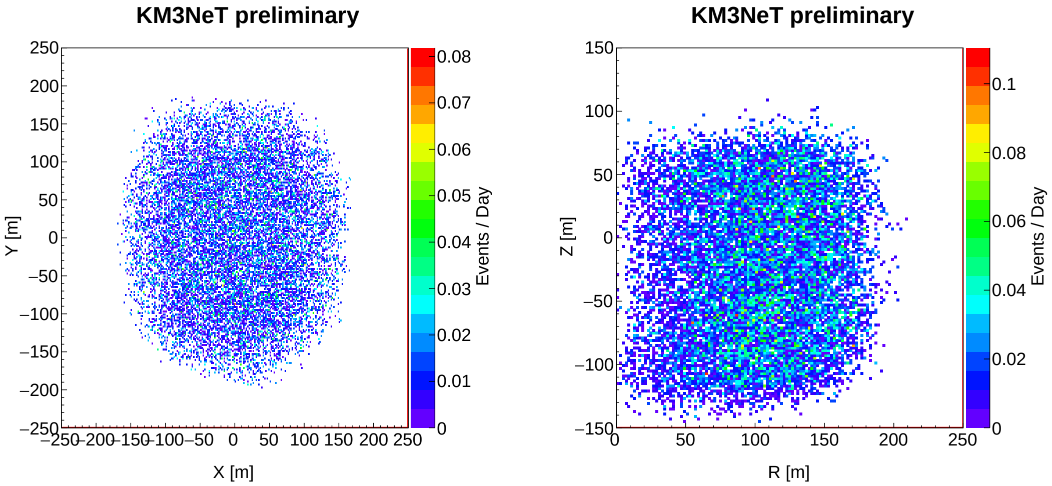

Figure 3.16: The reconstructed track start positions of ν_μ-CC events reconstructed as upgoing.

Preliminary Track Selection Cuts

- The event is reconstructed pointing upwards
- The reconstructed track length is greater than zero
- The log likelihood per degree of freedom is greater than 0.5
- The track start point is inside the instrumented volume

Preliminary Shower Selection Cuts

- The event is reconstructed pointing upwards

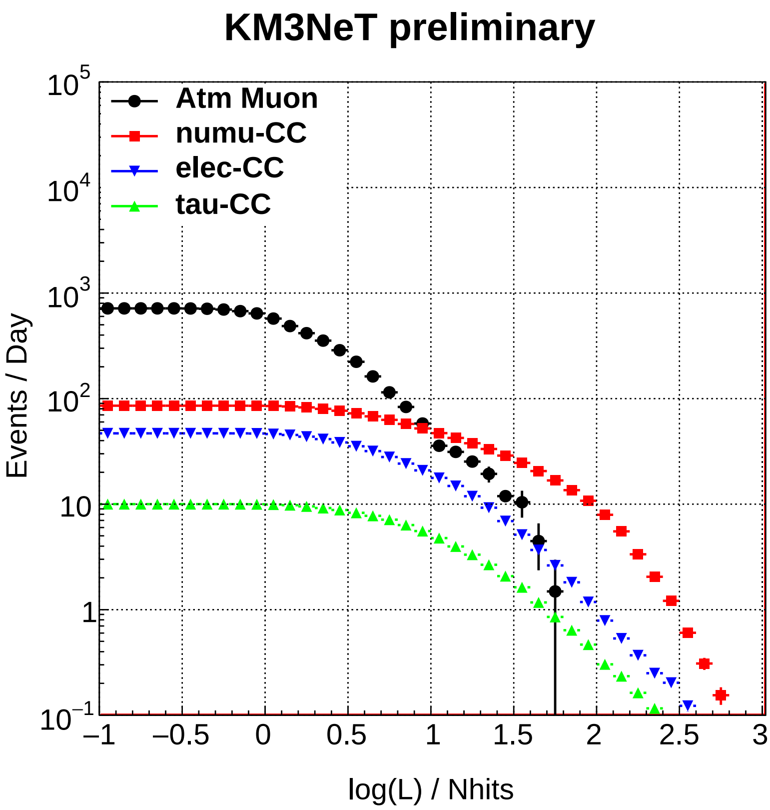

Figure 3.17: The rate of atmospheric muons and (anti)neutrino charged-current events of all flavours with start points reconstructed inside the instrumented volume as a function of a cut on the reconstruction likelihood per hit.

- The reconstructed energy is greater than 1 GeV

- The final fitted vertex position must be within 6 m and 30 ns of the initial fitted vertex position

- Of the 15 initial attempts at fitting the vertex position, at least 5 must be within 2 m and 10 ns of the best fit vertex position

- Of the 10 subsequent attempts at fitting the vertex position, at least 2 must be within 2 m and 10 ns of the best fit vertex position

- For 4 cones of opening angles 20°, 45°, 60° and 75° around the final reconstructed cascade position and direction, assuming an isotropic photon distribution around the shower axis, photons emitted at these angles should have a path length of at least 20 metres inside the instrumented volume at least 40% of the time

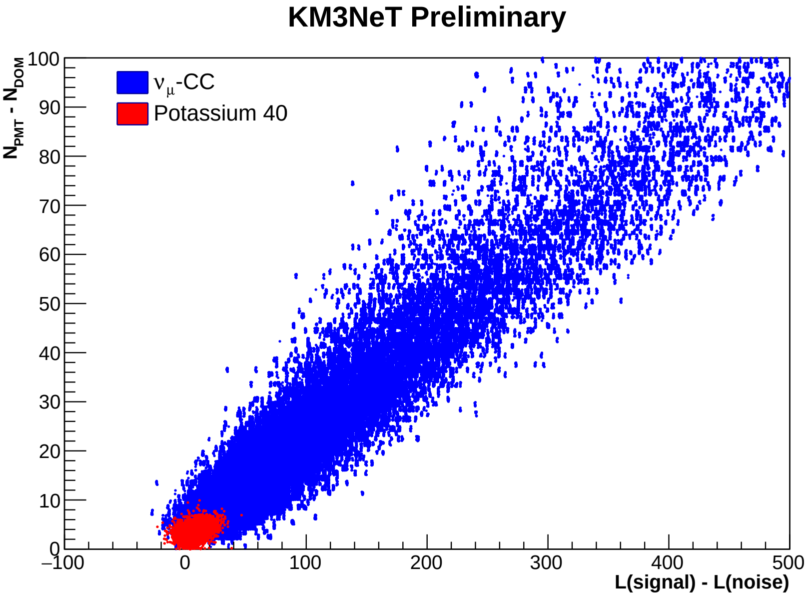

Figure 3.18: The rate of ^{40}K and $\nu_\mu - CC$ events as a function of the track reconstruction likelihood and the difference between the number of PMTs and DOMs with at least one selected hit. See Chapter 3 for more details on the reconstruction.

3.7.2 Random Decision Forest

Three Random Decision Forests (RDFs) are employed to separate signal from noise and to classify the signal according to its topology [106]. Each is composed of 101 decision trees, which are trained to classify the events into one of two categories, based on a random subset of event features. In this context, a feature is any variable derived from the reconstruction. Subsequently, each event can be allocated a score, corresponding to the proportion of trees in the forest that place the event in a given class. For example, if 51 trees classify a given event as an atmospheric muon, this event is said to have a muon score of 0.505. By applying three separate RDFs to the Monte Carlo, three independent score variables are derived, which can then be cut on. From now on, these score variables shall be referred to as the muon score, the noise score and the track score (see Fig. 3.19). As seen in Fig. 3.20 and 3.21, the noise and muon score are extremely effective. A 5% loss in signal is sufficient to reduce the contamination to a few percent.

In the case of discriminating track-like events from cascade-like events, it is not immediately obvious where to cut. It is not necessarily the case that defining every event with track score < 0.5 as a shower and all remaining events as tracks would yield the best possible sensitivity to the NMH. The optimum cutoff value was found by defining $\theta_{23} = 45°$ and $\delta^{CP} = 0°$, varying the track score cut and calculating the $\Delta\chi^2$ for each point, summed over reconstructed energy and zenith

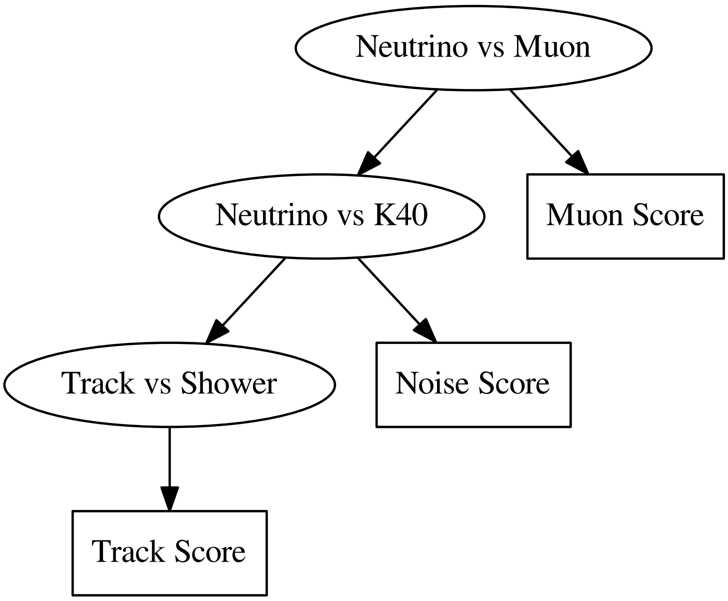

Figure 3.19: A schematic overview of the particle identification process. Each stage returns a value between 0 and 1, indicating the probability of a given event being classifed as an atmospheric muon, a random noise event or a track-like event.

for both PID classes separately [107].

$$\Delta\chi^2 = \frac{(N_{\mathrm{NH}} - N_{\mathrm{IH}})^2}{N_{NH}}, \tag{3.17}$$

where N_{NH} and N_{IH} are the number of events expected for the normal and inverted NMH hypotheses respectively. As shown in Fig. 3.22, the optimum cutoff point is a track score of 0.6. This choice of test statistic is discussed in detail in Section 5.3. For now, it can be thought of simply as a way of quantifying the asymmetry between the two possible NMH hypotheses.

The final probability of a given event being classified as a track or shower is shown in Fig. 3.23. The performance of the RDF is linked to its ability to identify a muon emerging from a hadronic shower. Consequently, the PID performance is better for $\bar{\nu}_\mu$s than ν_μs as their interactions produce more energetic muons on average (see Section 2.2). At present, muons with energy greater than 8 GeV can be identified consistently. Although performance deteriorates as a function of decreasing muon energy, there remains a statistical separation between electron and muon (anti)neutrinos which still makes a strong contribution to the overall NMH sensitivity.

The track and cascade cuts defined in Section 3.7.1 are then reapplied to all events

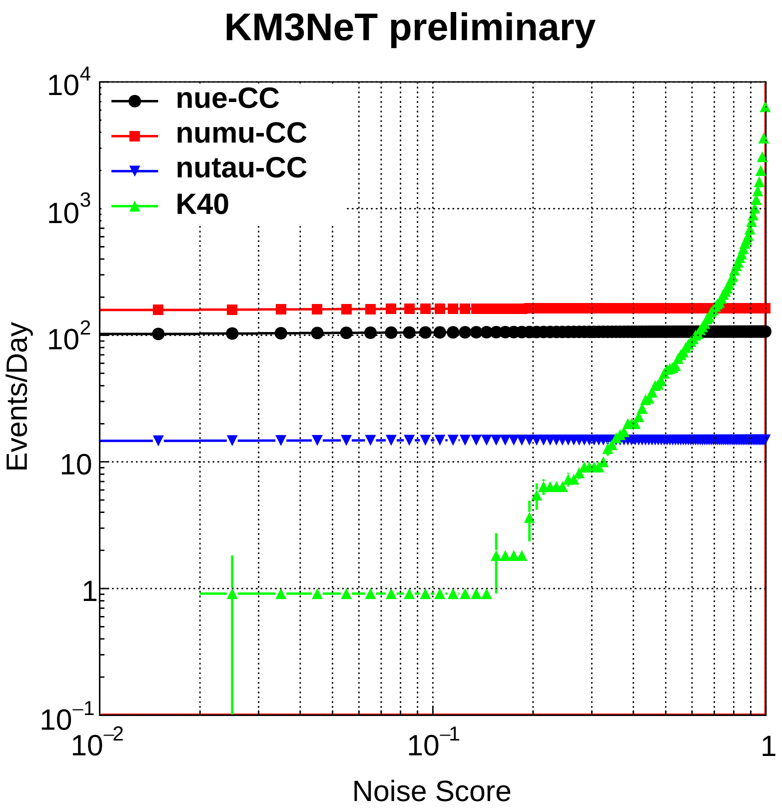

Figure 3.20: The rate of triggered ^{40}K and (anti)neutrino charged-current events of each flavour, as a function of the noise score cutoff. The triggered noise can be eliminated with very little impact on the signal.

according to their PID classification (i.e. only events classified as tracks which pass the track cuts are included in the final sample). In addition the following two cuts are required:

- muon score < 0.05
- noise score < 0.15

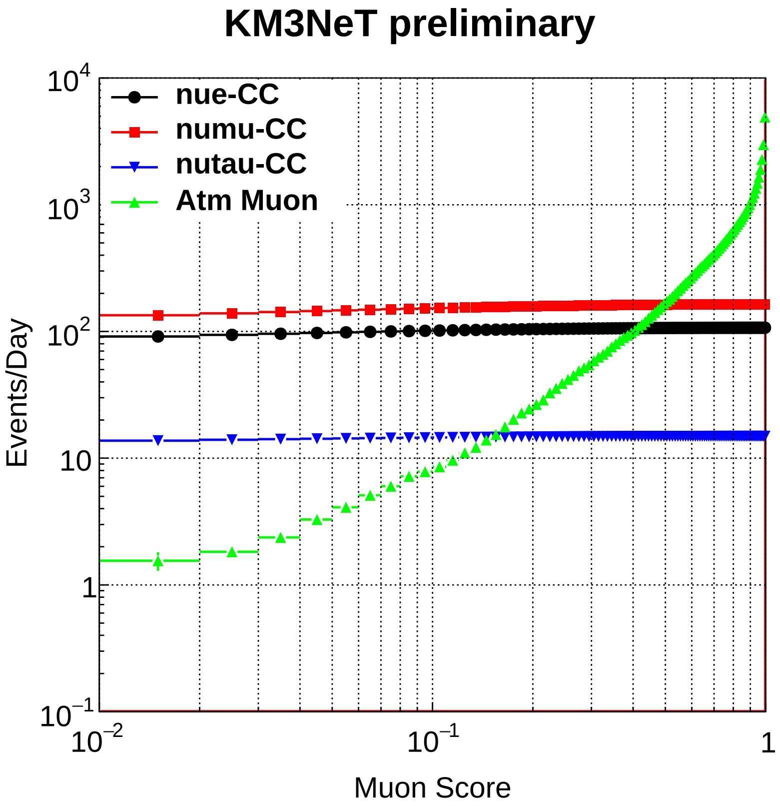

Figure 3.21: The rate of atmospheric muon and (anti)neutrino charged-current events of each flavour, as a function of the muon score cutoff. Atmospheric muon contamination can be reduced to ~ 3% at the cost of just 5% of the signal.

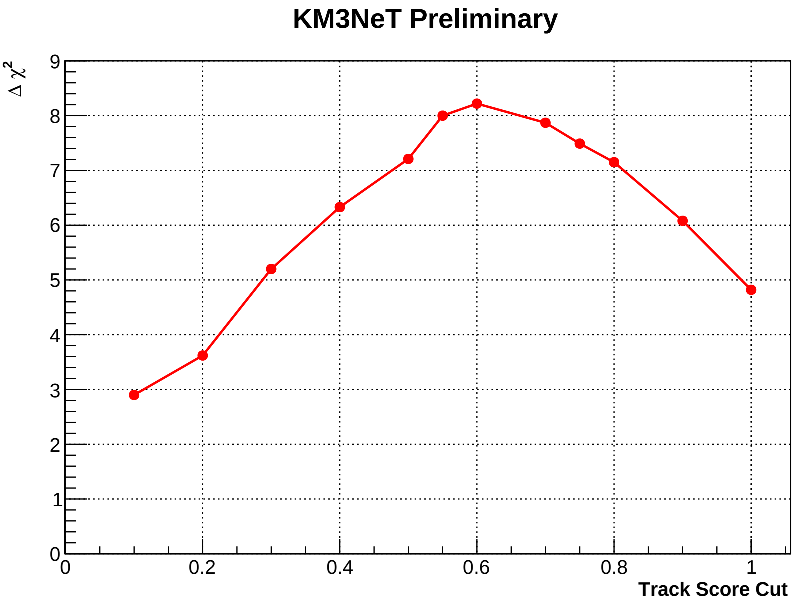

Figure 3.22: The total $\Delta\chi^2$ for a test point of $\theta_{23} = 45°$ and $\delta^{CP} = 0°$, as a function of the track score cut. Taken from Ref. [107].

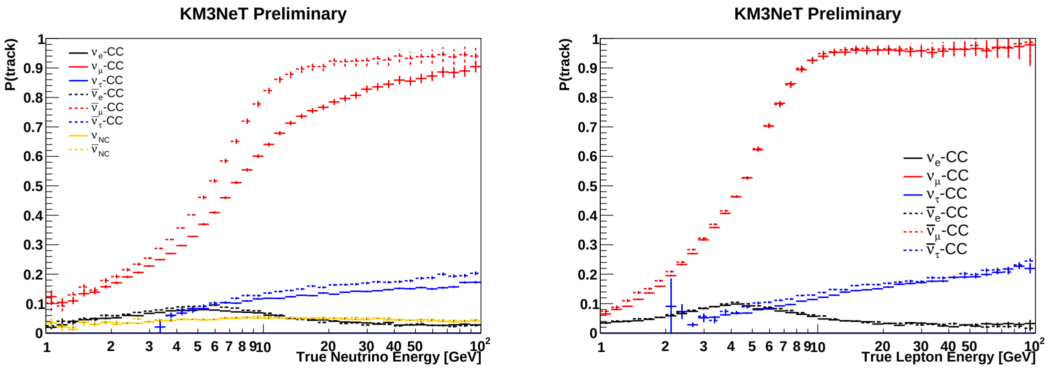

(a) Neutrino energy (b) Lepton energy

Figure 3.23: The probability of given event being classified as a track, for all channels, as a function of neutrino and outgoing lepton energy. The PID performance is closely linked to the energy of the outgoing muon, with close to perfect separation for muon energies above 8 GeV.

Chapter 4

Preliminary Data Analysis

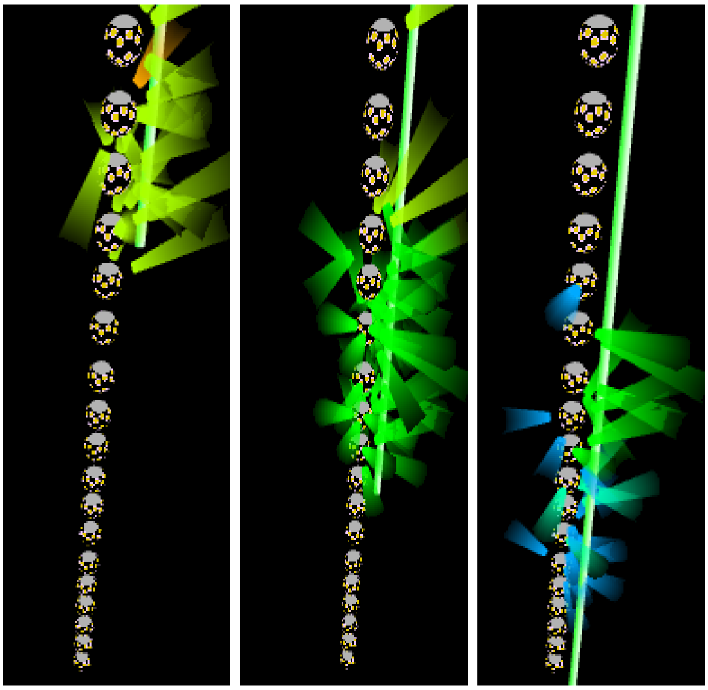

Figure 4.1: An atmospheric muon event, detected early in the morning of the 22nd of September 2017, the day after connection.

Within a day of the connection of the first ORCA DU, described in Chapter 4, physics data was already being taken. In Fig. 4.1, an atmospheric muon event is shown from the morning after deployment. It can be seen that the trigger and reconstruction algorithms were already working successfully within a short time period after the sea operation. For this preliminary analysis, data were selected from physics runs taken between September and December of 2017, whose trigger rate was close to the Monte Carlo expectation from atmospheric muons (see Fig. 4.2), comprising a total livetime of 45 days.

As mentioned in Chapter 2, inter-DOM time calibration is performed in situ by

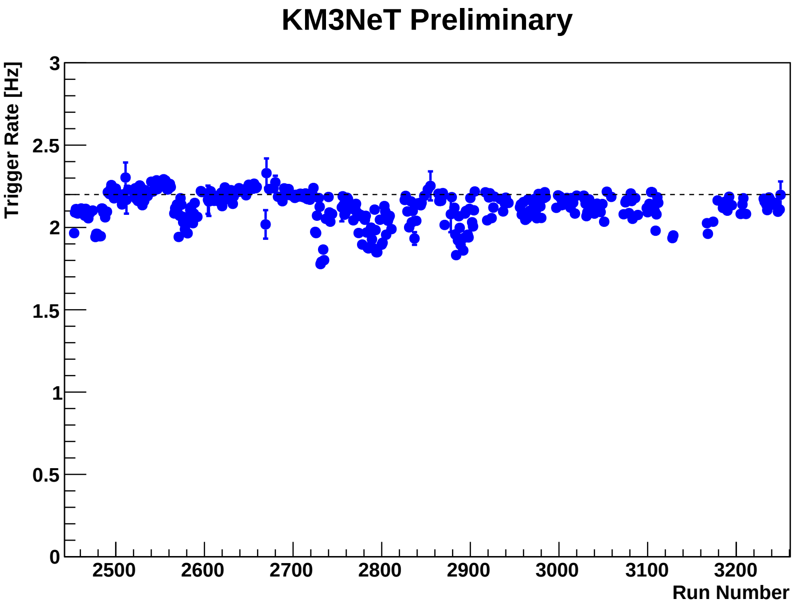

Figure 4.2: The triggered event rate as a function of run number for selected physics runs taken between September and December of 2017. The dotted line shows the expected average rate from atmospheric muons.

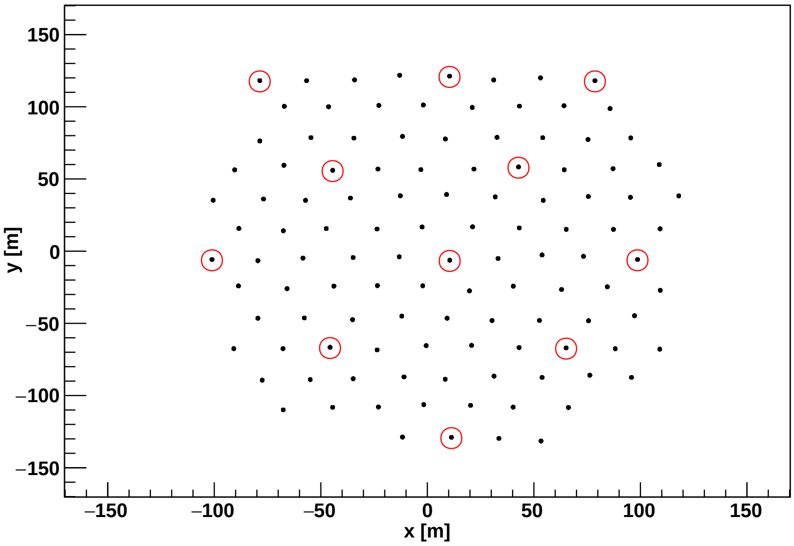

Figure 4.3: The ORCA detector footprint with selected DUs highlighted with a red circle.

flashing the DOM nanobeacons, each of which illuminates the DOM immediately above itself. The time of arrival of the light is then measured on a single reference PMT on each DOM. Inter-PMT calibration is performed exploiting the ^{40}K in the seawater, by searching for coincident hits from the same decay on adjacent PMTs. Both these techniques can also be employed onshore. In this case, the decaying ^{40}K present in the glass is measured instead.

In order to have a Monte Carlo sample to compare to the data quickly, with a long livetime, the neutrino and atmospheric muon generators and light propagation already simulated for the full detector Monte Carlo were reused. The trigger and reconstruction algorithms were rerun, excluding the contributions of all but a single DU. This process was repeated for 12 different DUs, yielding a total Monte Carlo livetime of 24 weeks. DUs were selected with a horizontal spacing approximately equal to one absorption length, in order to minimise any repetition of data (see Fig. 4.3). Work is underway to produce another Monte Carlo, reproducing run by run fluctuations in the optical background, caused by variations in sea conditions. For this first look, sea conditions are assumed to remain constant.

4.1 Comparison with Monte Carlo

In order to confirm the validity of this fast Monte Carlo production and as a crosscheck for the full-detector production, some comparisons with the data are shown. As the data is dominated by atmospheric muons before any cuts are applied, this comparison is made with the atmospheric muon Monte Carlo sample only. Where comparisons refer to “selected hits,” this means hits within 50 m of the reconstructed track and with time residuals in the range -50 ns $< \delta t <$ 50 ns.

The time residual distribution, which is important for accurately assessing the accuracy of the reconstruction, is shown in Fig. 4.4. Here, the form of the distribution is well described, there is a sharp peak close to $\delta t = 0$ ns from unscattered Cherenkov light, then a drop off from scattered light, which arrives later. However, the height of the noise floor differs. This can be seen in the region where the contribution of atmospheric muons is very small, $\delta t < -10$ ns. This difference is simply due to the choice of background rate from ^{40}K and bioluminescence in the Monte Carlo. A baseline rate of 10 kHz was assumed, which is more conservative than the average of 9 kHz measured in the data so far. In Fig. 4.5, it is shown that the reconstructed track length, related to the muon energy, is also well reproduced.

In Figs. 4.6, 4.7, and 4.8, there are visible features in the data not present in the Monte Carlo. In all cases, these discrepancies are under investigation. Firstly, in

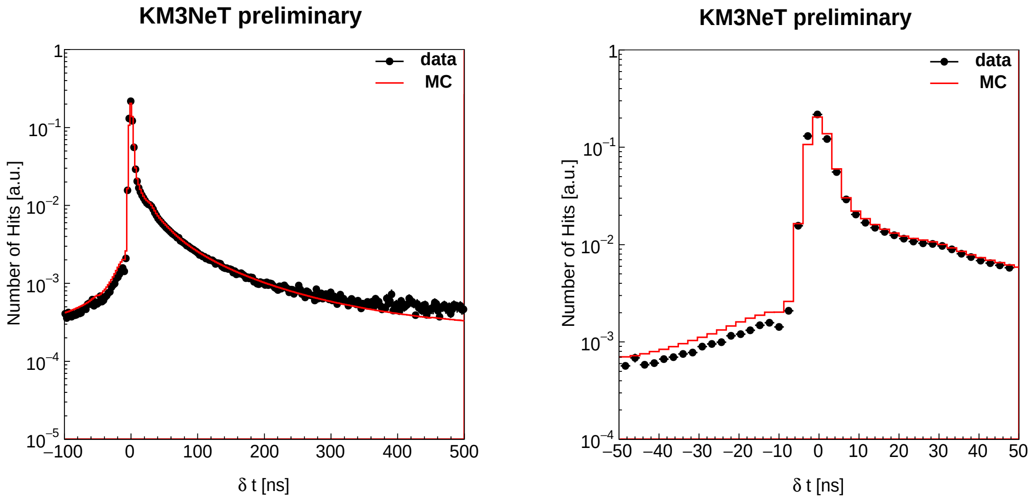

Figure 4.4: The difference between the true and expected time of arrival for hits assuming a muon hypothesis, averaged over all events in the sample, compared against the Monte Carlo expectation for atmospheric muons. The distribution has been normalised so that the sum of each bin over the full range (left) is equal to one.

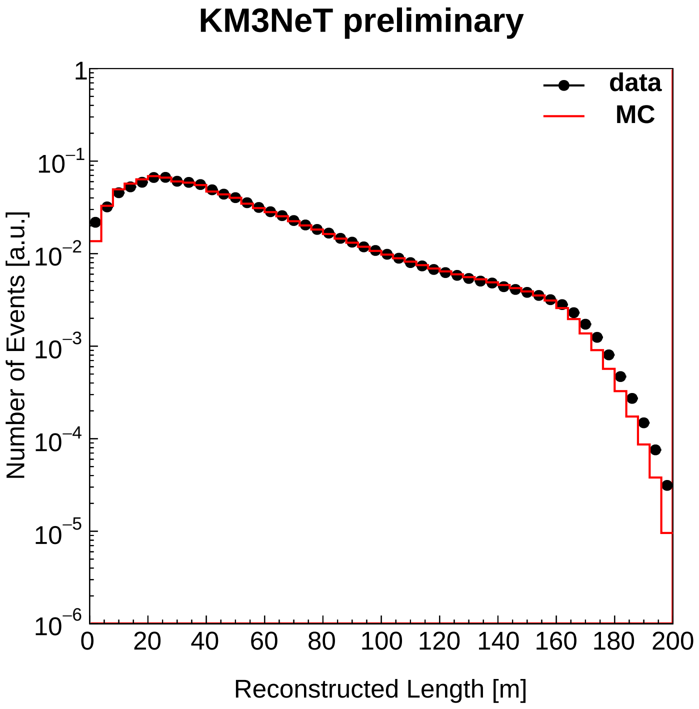

Figure 4.5: The reconstructed track length distributuion for data in selected runs, compared against the Monte Carlo expectation for atmospheric muons.

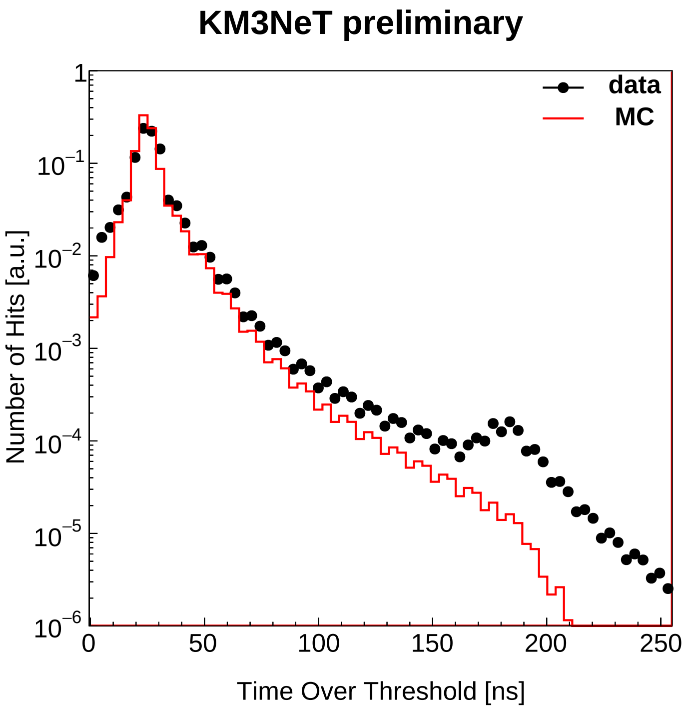

Figure 4.6: The maximum time over threshold distribution, averaged over all events in the sample, compared against the Monte Carlo expectation for atmospheric muons. The bump at 180 ns is hypothesised to be caused by atmospheric muons hitting a DOM directly, which is not currently simulated.

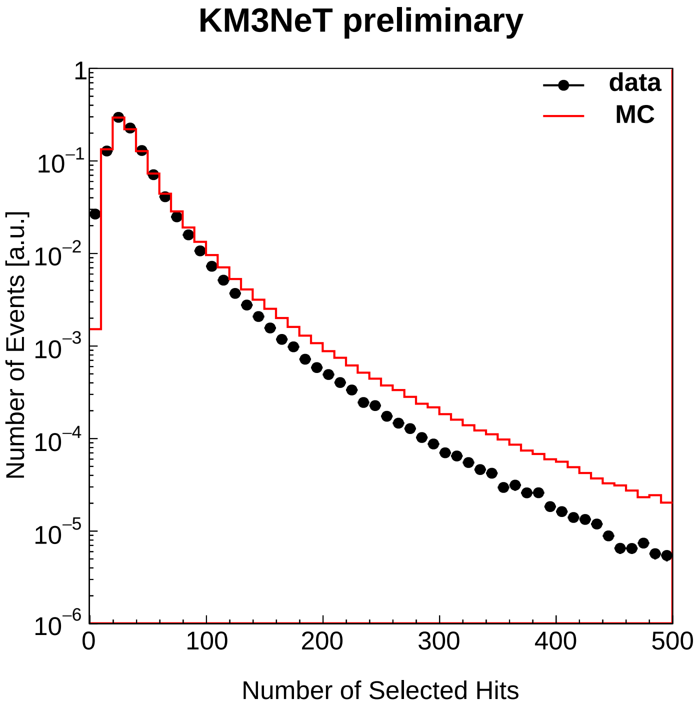

Figure 4.7: The distribution of the number of selected hits per event, compared against the Monte Carlo expectation for atmospheric muons.

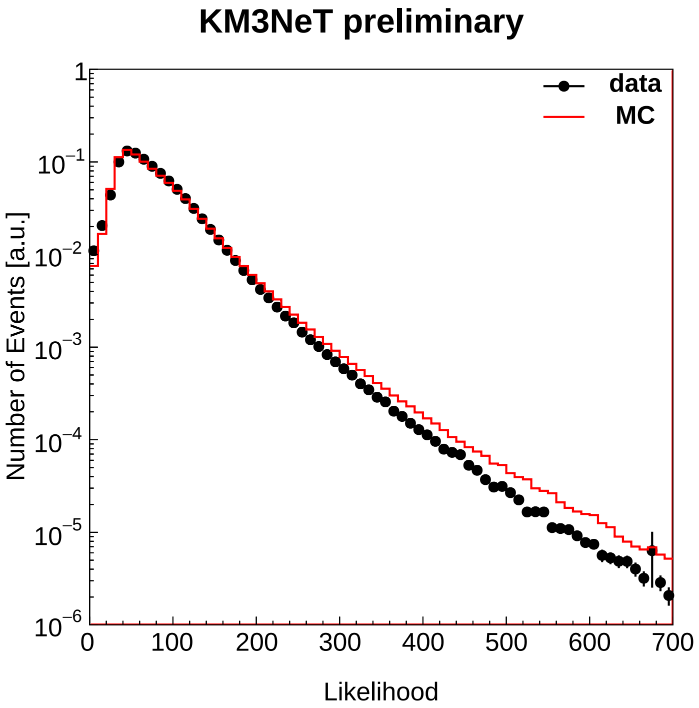

Figure 4.8: The reconstructed event log likelihood for data in selected runs, compared against the Monte Carlo expectation for atmospheric muons. A higher likelihood indicates a better quality reconstruction and typically also correlates with a higher energy.

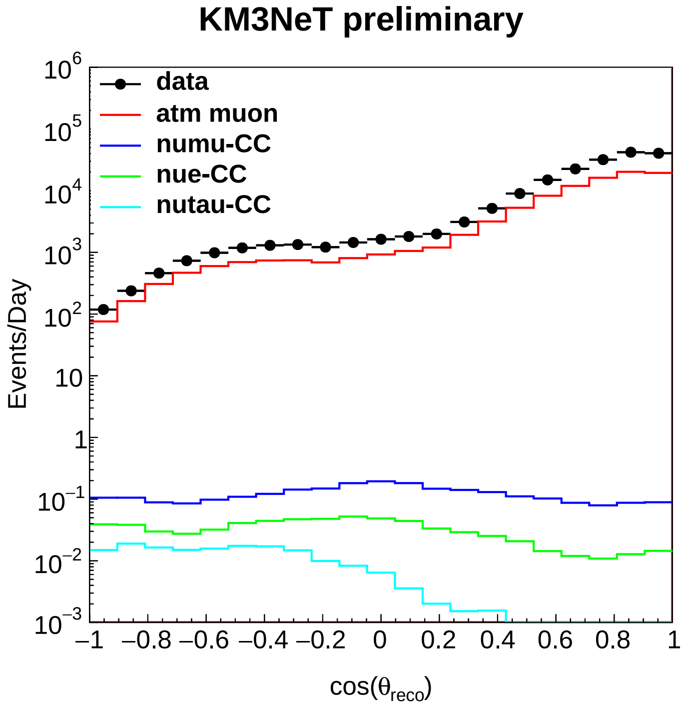

Figure 4.9: The reconstructed zenith distribution of all triggered events in the sample, compared against the Monte Carlo expectation for atmospheric muon and neutrino charged current events (with oscillations).

Fig. 4.6, the maximum time over threshold over all selected hits in each event is shown. A bump in the data is visible at ~ 180 ns. At time of writing, this bump is believed to be caused by atmospheric muons which hit the DOM directly, something not currently taken into account in KM3NeT simulations. In Figs. 4.7 and 4.8, the number of selected hits and the log likelihood distributions per event are shown respectively. Here, it can be observed that a small proportion of events have high numbers of selected hits in the Monte Carlo, compared with the data. One possible explanation for this could be a difference in the absorption length of the seawater. More photons from energetic, but distant, atmospheric muons could be absorbed than expected. Another possiblility is that the atmopheric muon flux assumed in MUPAGE needs to be retuned. Nevertheless, in Fig. 4.9, it can be seen that the overall shape of the reconstructed zenith distribution of atmospheric muons is well described.

4.2 Neutrino Candidates

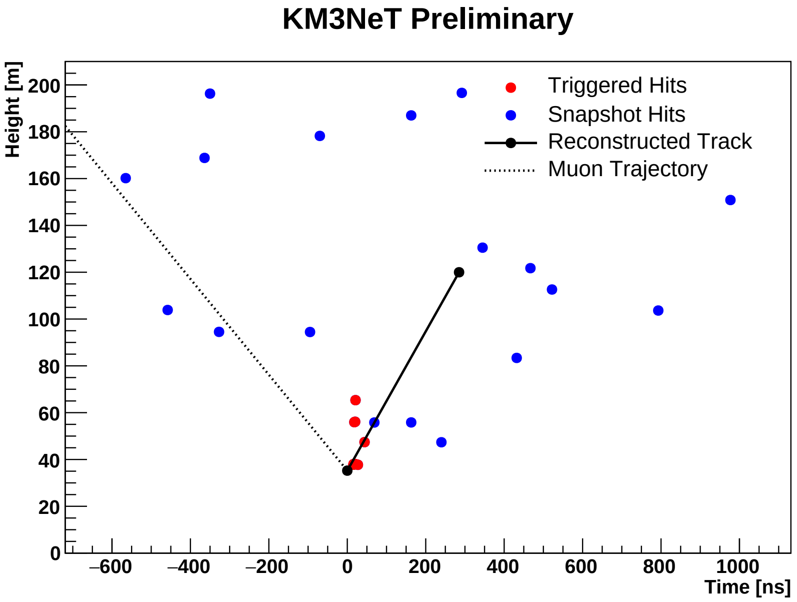

Figure 4.10: A zt diagram of a misreconstructed atmospheric muon event from the Monte Carlo, distinguishing between triggered hits (i.e. hits that have contributed to the trigger) and snapshot hits (all hits in the sample). An atmospheric muon has hit the base of the DU, producing an upwards-going Cherenkov front, which is misconstrued as an upwards-travelling track.

Despite the discrepancies present in this Monte Carlo production, this section will detail a first search for neutrinos in the early ORCA data. The most important background for neutrinos is misreconstructed atmospheric muons. As shown in Fig. 4.9, simply requiring tracks reconstructed pointing upwards is insufficient, reducing the background by only a factor 100. Furthermore, when considering only a single DU, there are geometrical effects which degrade the atmospheric muon

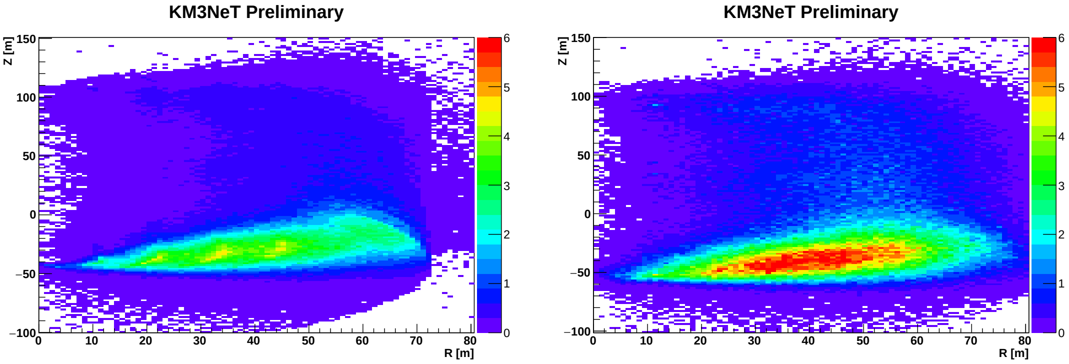

(a) Monte Carlo (atmospheric muons)

(b) Data

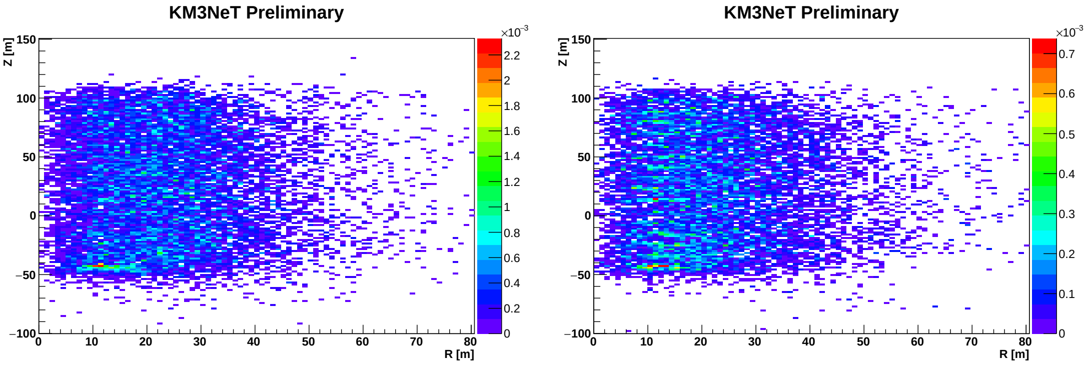

(c) Monte Carlo (ν_μ-CC)

(d) Monte Carlo (ν_e-CC)

Figure 4.11: The daily rate of events reconstructed as upgoing for data and atmospheric muons, as a function of the reconstructed horizontal distance from the line (R) and height with respect to its centre (Z). It can be seen that misreconstructed atmospheric muons typically have track start points close to the base of the line.

rejection. An inclined atmospheric muon that hits the bottom of the DU, can create at upwards-travelling Cherenkov front, which can be misconstrued as an upgoing track by the reconstruction algorithm (see Fig. 4.10). This hypothesis is also supported by the data, where most upgoing tracks begin near the base of the DU (see Fig. 4.11).

In such a situation, there are multiple degenerate solutions, some upgoing and some downgoing. For this analysis, the reconstruction algorithm was slightly modified from the scheme described in Chapter 3. If none of the solutions kept at a given stage in the chain were downgoing, the best downgoing solution would be kept as well, ensuring that the best upgoing and downgoing solutions can always be compared. For this analysis, the atmospheric muon rejection factor (Q_μ) is defined

$$Q_\mu = \log \mathcal{L}_{\text{up}} - \log \mathcal{L}_{\text{down}}, \tag{4.1}$$

such that $\mathcal{L}_{\text{up}}$ and $\mathcal{L}_{\text{down}}$ are the best fit likelihoods of the best upgoing and downgoing reconstructed track, respectively. The data Monte Carlo comparison for this quantity is shown in Fig. 4.12, where the general shape shows some agreement, although the atmospheric muon plateau is higher in the data than in

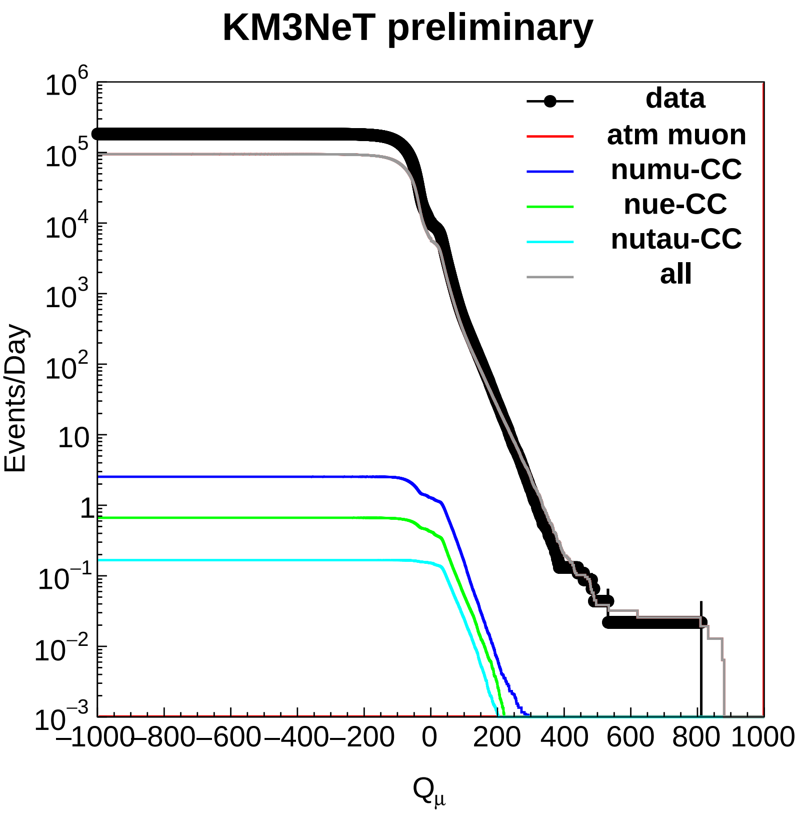

Figure 4.12: A comparison of the daily rate of events as a function of a cutoff in the muon rejection factor, shown for data, atmospheric muons and all flavours of neutrino charged current events.

the Monte Carlo. Cutting on this quantity on its own is also insufficient to remove all of the atmospheric muon background, so the reconstructed spatial distribution of the atmospheric muons needs to be exploited. The following additional cuts are included:

- $R < 10$ m
- -40 m $< Z < 95$ m
- Maximum time over threshold < 100 ns

where R is the distance between the reconstructed track start position and the DU and Z is the vertical distance from the track start position and the DU centre. The cut on the time over threshold is to eliminate any events whose behaviour is not simulated in the Monte Carlo (see Fig. 4.6).

In Fig. 4.13, the distribution of events is shown as a function of Q_μ, from the data and Monte Carlo. At $Q_\mu > 100$, a population of neutrino candidates is visible. Here, the term "candidates" is used because, although neutrinos are expected to

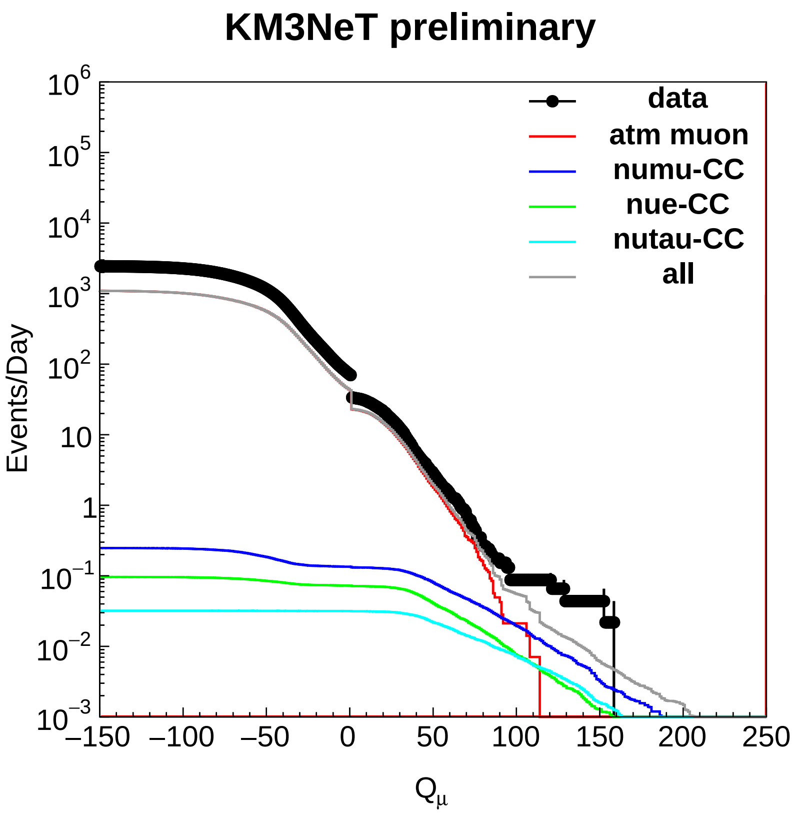

Figure 4.13: A comparison of the data with the Monte Carlo, as a function of Q_μ. A population of neutrino candidates can be seen at $Q_\mu > 100$. A flat scaling factor has been applied to all MC channels to bring the total event rate up to match the measured atmospheric muon flux before any cuts were applied.

contribute more to this region than muons, any given event could still easily be a misreconstructed atmospheric muon. If the discrepancy in normalisation between the data and Monte Carlo is caused by a systematic error in the detector response, such as in the trigger efficiency, then neutrinos and atmospheric muons would be expected to be affected equally and the Monte Carlo curves could all be scaled up to match the data. In this scenario, the sample of candidate events would be mostly made up of neutrinos. This was assumed and a flat scale factor was applied. However, the difference could also be caused by an underestimation of the atmospheric muon flux normalisation. In this scenario, the candidate sample could still be dominated by atmospheric muons. This problem should be resolved after taking more data with more DUs.

As there are only a handful of neutrino candidates, they can be examined by eye. In Fig. 4.14, height-time plots of the four events with the highest value of Q_μ are shown. None of them is a “smoking gun” event; their placement on Fig. 4.13 makes a more persuasive case for their candidacy as neutrinos than their topologies. All four events have some downgoing component below the track start point, which could be a backwards-scattered component of a cascade, which would

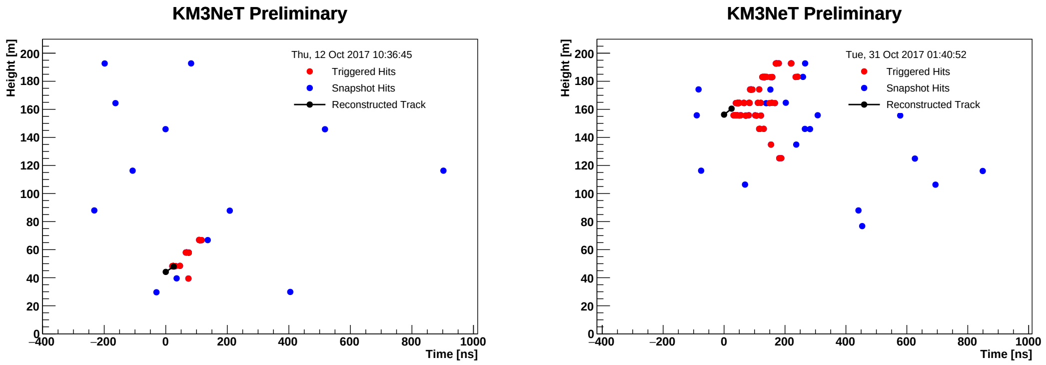

(a) Candidate A (b) Candidate B

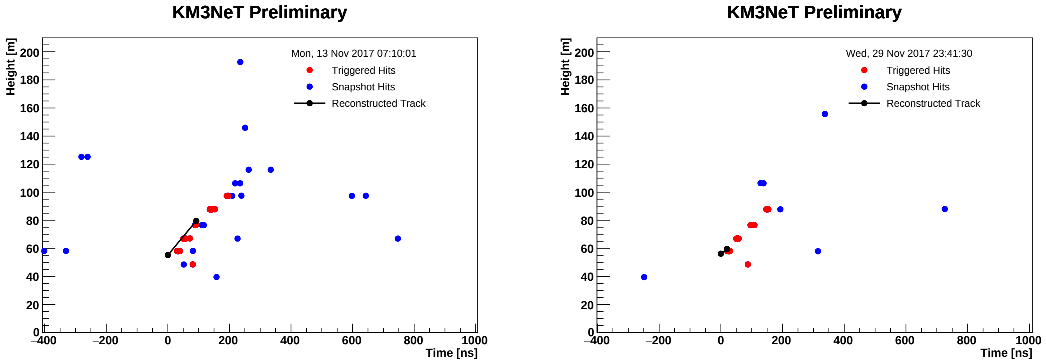

(c) Candidate C (d) Candidate D

Figure 4.14: Height-time plots of the most likely neutrino candidates according to the muon rejection factor. From visual inspection, there are three track-like events and one cascade-like event.

be hadronic in the case of ν_μ-CC events, or it could be the downwards orientated part of the Cherenkov cone from an inclined atmospheric muon. Although no particle identification has been performed at this stage, by examining the reconstructed length of each candidate, candidate C makes a more convincing ν_μ-CC event, where the others may be cascades. Candidate B contains a few features atypical of a physics event. It contains almost 100 ns of triggered hits on a single DOM and an upgoing afterpulse 200 ns after the event start time. Sparking PMTs have been observed in the ANTARES data. However, they are typically associated with expiring PMTs, which does not appear to be the case in ORCA. No PMT was lost after this event. Investigation is ongoing into events of this type.

To conclude, this analysis has found a sample of events consistent with the expectation from atmospheric neutrinos in the first set of ORCA data, but these events could still be qualitively explained as misreconstructed atmospheric muons. This analysis will be renewed in future with more data and a Monte Carlo simulation which better describes its run by run fluctuations.

Chapter 5

Neutrino Mass Hierarchy Sensitivity

5.1 Simulating the Event Distribution

For a given neutrino flavour and chirality, denoted by the index i, the number of interacting events per unit mass of seawater can be expressed as

$$N_i^{\text{int}}(\theta, E) = \frac{\sigma_i(E)\Delta t}{m_{\text{nucleon}}} \sum_j \Phi_j(\theta, E)\mathcal{P}_{ji}^{\text{osc}}(\theta, E), \tag{5.1}$$

where m_{nucleon} is the mass of the nucleons in the water, σ is the cross section, Δt is the live time, Φ is the unoscillated atmospheric neutrino flux, and $\mathcal{P}^{\text{osc}}$ is the oscillation probability described in Chapter 1. Eq. 5.1 is independent of the detector response and can be thought of as the physics contribution to the event count.

In order to link the interacting event distribution to the detector response, it is useful to define the effective mass (M^{eff}). For MC events generated in a volume V_{gen}, it is defined as

$$M_i^{\text{eff}}(\theta, E) = \rho_{\text{water}} V_{\text{gen}} \frac{N_i^{\text{sel}}(\theta, E)}{N_i^{\text{int}}(\theta, E)}, \tag{5.2}$$

where N^{sel} and N^{int} are the number of selected and interacting events respectively and ρ_{water} is the density of seawater. The effective mass is hence the mass of the water contained by a detector with 100% efficiency.

The number of events of a given PID classification α as a function of reconstructed energy and zenith is given by

$$N_\alpha(\theta,^{\rm rec} E^{\rm rec}) = \int dE d\Omega \sum_i \mathcal{P}^{\rm ID}_{i\alpha}(E)\mathcal{P}^{\rm rec}_{i\alpha}(\theta,^{\rm rec} E^{\rm rec}|\theta, E)M^{\rm eff}_i(\theta, E)N^{\rm int}_i(\theta, E), \quad (5.3)$$

where $\mathcal{P}^{\rm ID}$ is the particle ID classification probability and $\mathcal{P}^{\rm rec}$ is the detector response function (i.e. the probability of an event with a given zenith and energy being reconstructed with another zenith and energy).

For convenience, the detector response function is broken down further such that

$$\mathcal{P}^{\rm rec}_{i\alpha}(\theta,^{\rm rec} E^{\rm rec}|\theta, E) = \mathcal{P}^{E}_{i\alpha}(E^{\rm rec}|E) \times \mathcal{P}^{\theta}_{i\alpha}(\theta^{\rm rec}|E, \theta), \quad (5.4)$$

where $\mathcal{P}^{E}_{i\alpha}$ and $\mathcal{P}^{\theta}_{i\alpha}$ are the energy and zenith response functions respectively. The reconstructed energy is assumed to depend only on the true energy, whereas as the reconstructed zenith angle depends on both the true zenith angle and the true energy. Each detector-dependent term on the right hand side of Eq. 5.3 is derived in Section 5.2.

5.2 Parameterising the Detector Response

The method described in this section was developed alongside the approach described in the KM3NeT Letter of Intent [1]. It was designed to be easily shared outside of the KM3NeT Collaboration, for works such as Ref. [108], and to be robust against statistical fluctuations caused by low Monte Carlo statistics. To meet these requirements, the detector response is described by smooth parameterised functions, derived from the full Monte Carlo production. The functional forms of these parameterisations is usually derived from observation, however physical explanations will also be discussed where applicable.

5.2.1 Effective Mass

The effective mass parameterisation is described by a hyperbolic tangent

$$M^{\rm eff}_i(E, \theta_i) = N_i \tanh\left(\frac{E - E^{\rm min}_i}{\sigma^M_i(\theta_i)}\right), \quad (5.5)$$

$$\sigma^M_i(\theta_i) = -q_{i1}\cos(\theta_i)^{q_{i2}}, \quad (5.6)$$

with four free parameters. N_i is the plateau, $E^{\rm min}_i$ is the cutoff below which no events are detected, and the parameters q_{i1} and q_{i2} describe the zenith dependence of the slope. Note that in the case of ν_τ-CC events, the $E^{\rm min}_i$ parameter comes

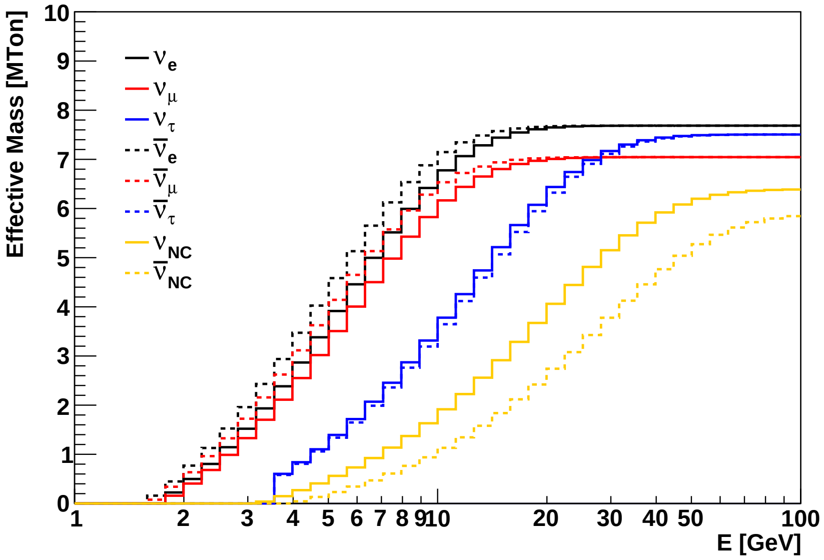

(a) Parameterised

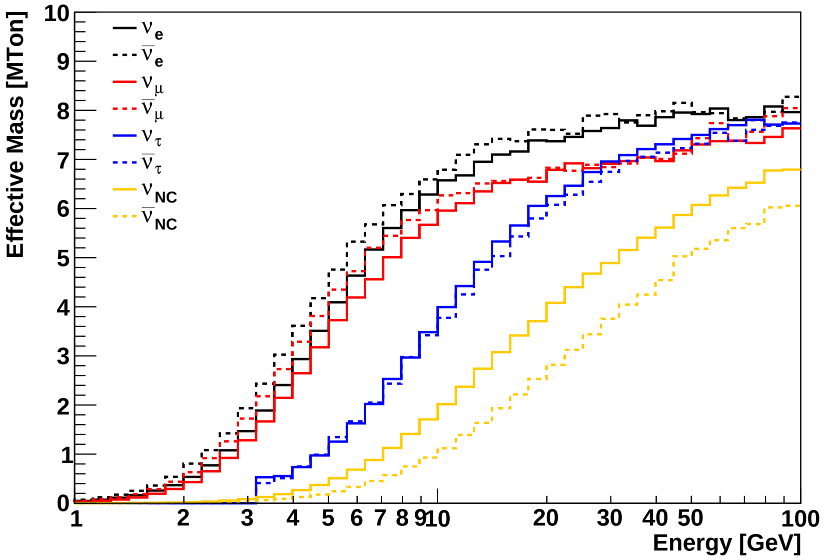

(b) Monte Carlo

Figure 5.1: The effective mass, averaged over zenith angle, shown for charged current events of all flavours and for the sum of all neutral current events.

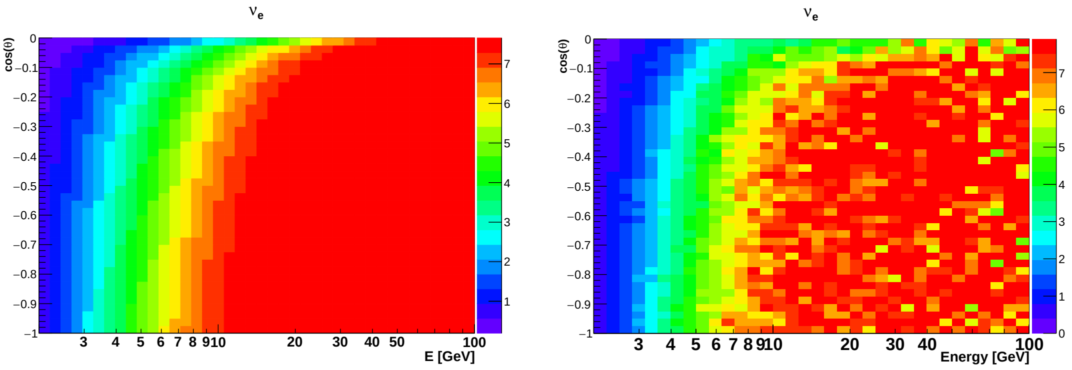

(a) Parameterised (b) Monte Carlo

Figure 5.2: The effective mass in megatons, shown for ν_e-CC events. It can be seen that the parameterisation matches the form of the effective mass quite well, but smooths out all the fluctuations from the Monte Carlo.

directly from the energy required to create a τ above the Cherenkov threshold (~ 3 GeV). Otherwise, it comes from the minimum threshold of the trigger. Neutral-current events, with no visible lepton, are less bright and consequently have a higher threshold.

5.2.2 Energy Resolution

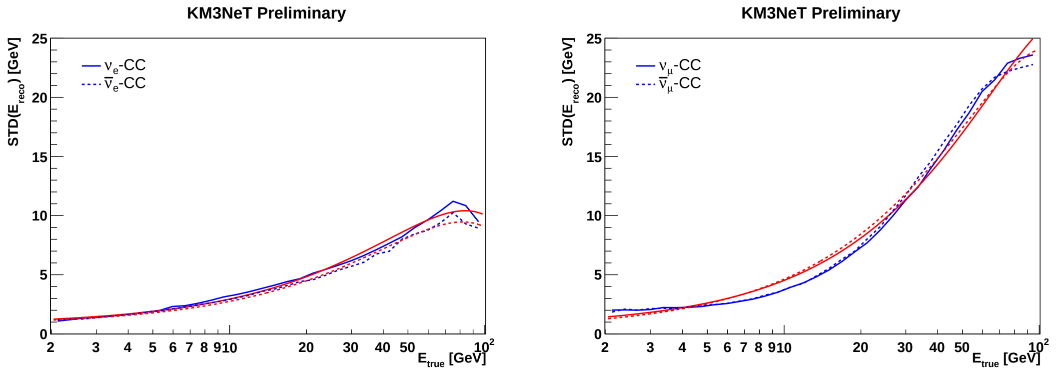

(a) $\bar{\nu}_e/\nu_e$-CC, classified as cascades. (b) $\bar{\nu}_\mu/\nu_\mu$-CC, classified as tracks.

Figure 5.3: The standard deviation of the reconstructed energy as a function of true energy, for correctly-classified muon and electron (anti)neutrino charged-current events. The parameterisation is plotted in red alongside the Monte Carlo values.

The energy response function is parameterised as a Gaussian of integral 1, with expection value ($\langle E^{\text{rec}} \rangle$) and width ($\sigma^E$), described by

$$\langle E_i^{\text{rec}} \rangle = E(m_{i1} + m_{i2}\log_{10}(E) + m_{i3}\log^2_{10}(E)), \tag{5.7}$$

$$\sigma_i^E = s_{i1} + s_{i2}E + s_{i3}E^2, \tag{5.8}$$

where the parameters m_{ik} and s_{ik} are fitted for each interaction channel and PID

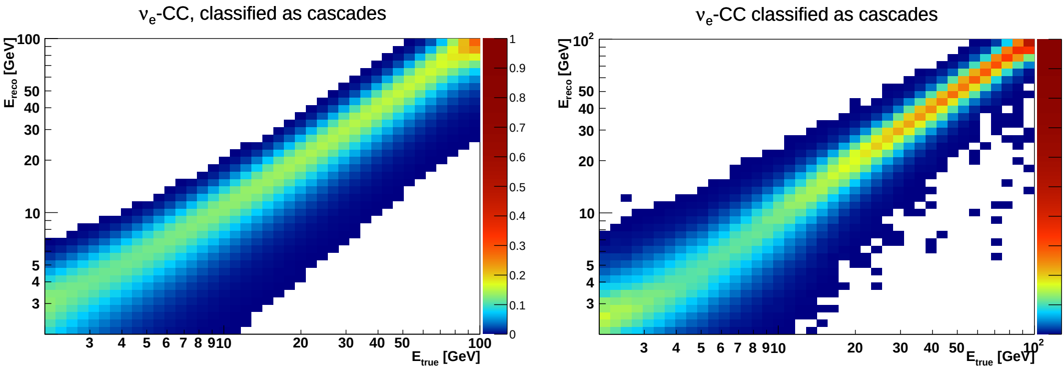
ν_e-CC, classified as cascades

ν_e-CC classified as cascades

(a) Parameterised (b) Monte Carlo

Figure 5.4: The parameterised probability distribution function of reconstructed energy as a function of true energy, shown alongside the equivalent energy distribution from the Monte Carlo, for correctly-classified electron (anti)neutrino charged-current events.

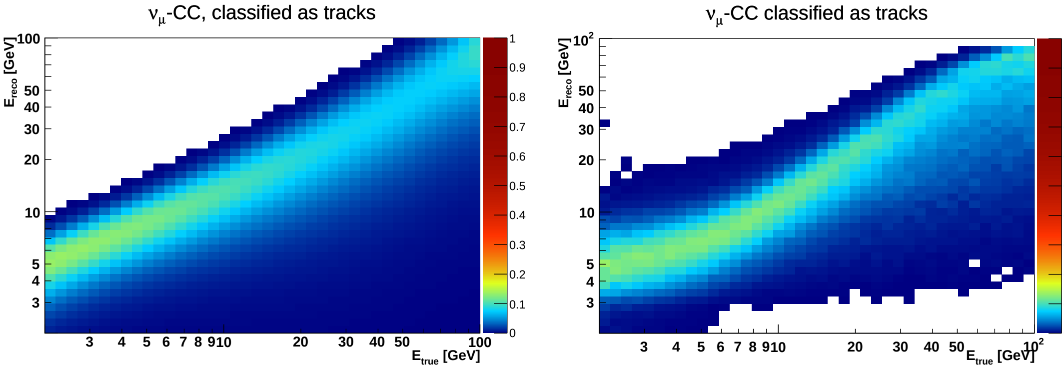
ν_μ-CC, classified as tracks

ν_μ-CC classified as tracks

(a) Parameterised (b) Monte Carlo

Figure 5.5: The parameterised probability distribution function of reconstructed energy as a function of true energy, shown alongside the equivalent energy distribution from the Monte Carlo, for correctly-classified muon (anti)neutrino charged-current events.

class (see Fig. 5.3). The parameterisation can be directly compared to the Monte Carlo energy distribution for correctly-classified ν_e and ν_μ charged-current events in Figs. 5.4 and 5.5, where there is good agreement.

5.2.3 Angular Resolution

When describing the detector angular resolution, it is assumed that there is no directional bias. This is in fact the case, as the detector is close to rotationally symmetric in the x-y plane and PMT coverage on the DOMs is close to uniform in all directions. A Gaussian smearing of width $\sigma^{\theta\phi}$ is applied to the event zenith and azimuth angle together on the surface of a sphere. It evolves as a function of energy according to

$$\sigma_i^{\theta\phi} = s_{i1}E^{-s_{i2}}, \tag{5.9}$$

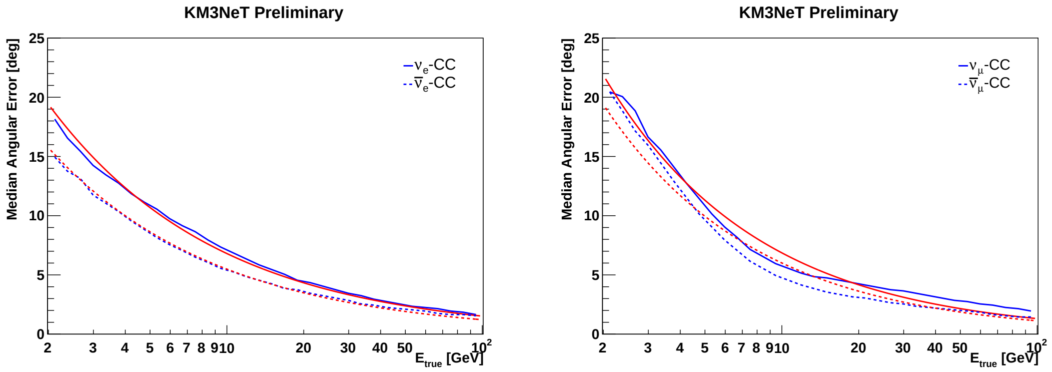

(a) $\bar{\nu}_e/\nu_e$-CC, classified as cascades.

(b) $\bar{\nu}_\mu/\nu_\mu$-CC, classified as tracks.

Figure 5.6: The median angular error as a function of true energy, for correctly-classified muon and electron (anti)neutrino charged-current events. The parameterisation is plotted in red alongside the Monte Carlo values.

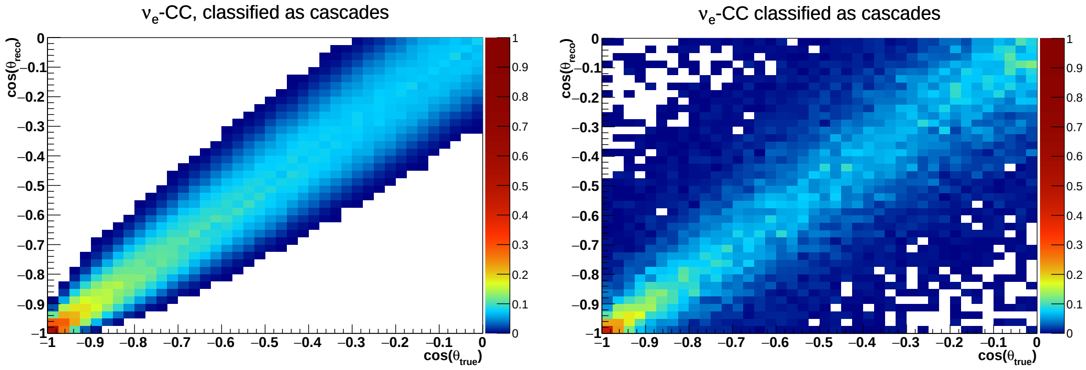

(a) Parameterised

(b) Monte Carlo

Figure 5.7: The parameterised probability distribution function of reconstructed zenith as a function of true zenith angle, for neutrinos in the energy range 6.5 – 7.1 GeV, for correctly-classified electron (anti)neutrino charged-current events. It is shown alongside the equivalent distribution from the Monte Carlo.

where s_{i1} and s_{i2} are fitted for each interaction channel and PID class see Fig. 5.6. The smeared event distribution is then projected back on to the cosine zenith axis to get the final angular response function, as a function of true neutrino energy, true zenith angle and reconstructed zenith angle. A 2D projection of this function for a small energy range is plotted alongside the equivalent distribution from the Monte Carlo in Figs. 5.7 and 5.8 and there is a good agreement.

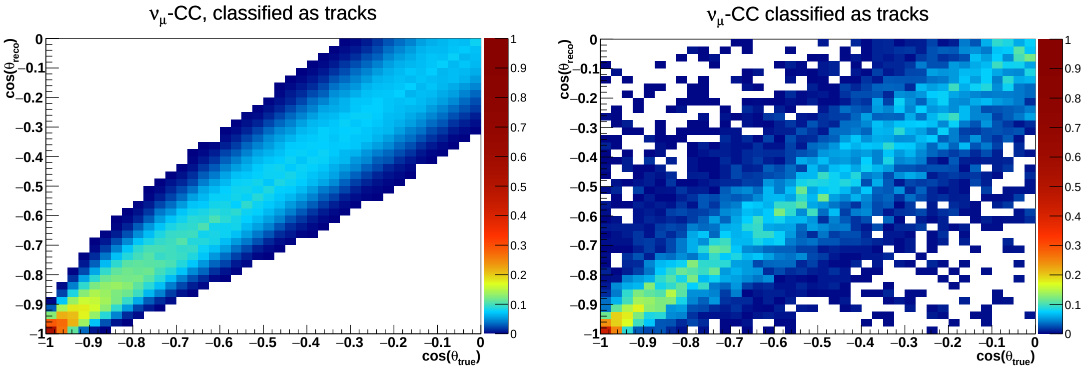

(a) Parameterised

(b) Monte Carlo

Figure 5.8: The parameterised probability distribution function of reconstructed zenith as a function of true zenith angle, for neutrinos in the energy range $6.5 - 7.1$ GeV. It is shown alongside the equivalent distribution from the Monte Carlo, for correctly-classified muon (anti)neutrino charged-current events.

5.2.4 Particle Identification

As discussed in Section 3.7, the performance of the PID mainly depends on the lepton energy, rather than the neutrino energy. Here, this effect is only present as a dependence on the neutrino chirality. However, future fully-correlated Monte Carlo studies could exploit the fact that well-reconstructed events are also more likely to be correctly classified. The functional form of the track classification probability is given by

$$\mathcal{P}_i^{ID}(\text{track}|E) = \begin{cases} p_{i0} + p_{i1}E^{-p_{i2}} & \text{if } E > E_i^{\text{thr}} \\ p_{i3} + p_{i4}E + p_{i5}E^2 + p_{i6}E^3 & \text{otherwise,} \end{cases} \tag{5.10}$$

where the parameters p_{ik} and the threshold energy E^{thr} are fitted to the Monte Carlo.

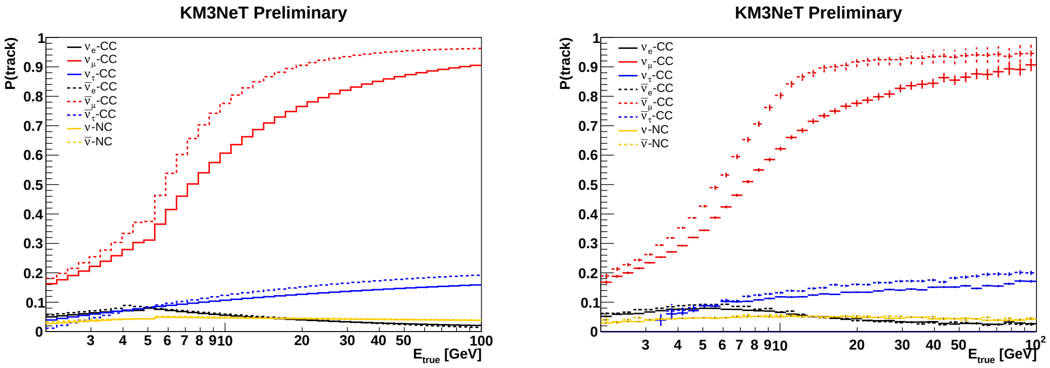

(a) Parameterised

(b) Monte Carlo

Figure 5.9: The probability of an event being classified as a track, as a function of neutrino energy for each interaction channel. The distribution taken from the Monte Carlo and the parameterisations are shown side by side.

5.2.5 Event Rates

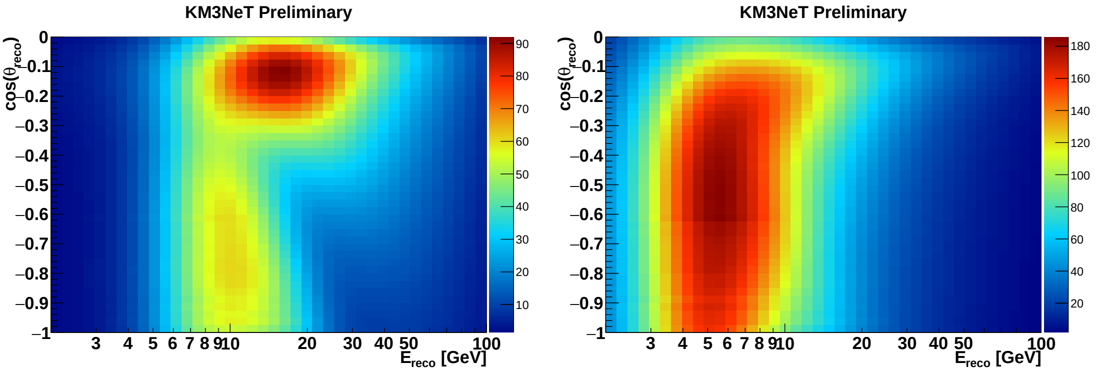

(a) Tracks (b) Cascades

Figure 5.10: The expected event rate per 3 years as a function of reconstructed energy and zenith angle in each channel. A normal hierarchy has been assumed, as well as $\theta_{23} = 45^\circ$ and $\delta^{CP} = 0^\circ$.

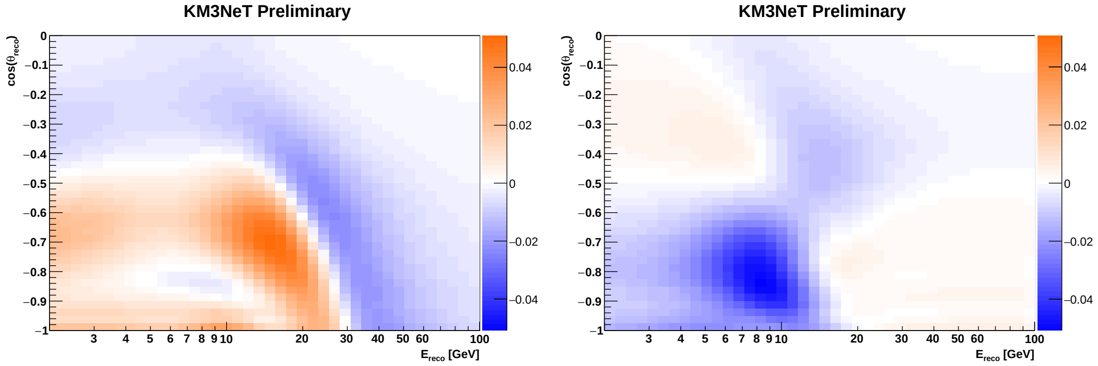

(a) Tracks (b) Cascades

Figure 5.11: The asymmetry $(N_{IH} - N_{NH})/N_{NH}$ per year as a function of reconstructed energy and zenith angle in each channel. A normal hierarchy has been assumed, as well as $\theta_{23} = 45^\circ$ and $\delta^{CP} = 0^\circ$.

The expected event rate (Fig. 5.10) is derived by combining all the parameterisations, as described in Section 5.1. From the event expectation for each NMH hypothesis, it can be seen that ORCA will measure an effect of the order 4% (see Fig. 5.11), with a different pattern for tracks and cascades.

5.3 Determining the Median NMH Sensitivity

At the most fundamental level, this work is an attempt to distinguish between two hypotheses, $\mathcal{H}_1$ and $\mathcal{H}_0$, where $\mathcal{H}_1$ is the hypothesis being tested and $\mathcal{H}_0$ is the alternative hypothesis. After carrying out a measurement on real data, it will be necessary to quantify the degree of confidence with which one hypothesis can be excluded with respect to the other. In this work, the sensitivity in the case of a normal hierarchy (NH) and inverted hierarchy (IH) will be assessed in turn. In Sections 5.3.1 and 5.3.2, $\mathcal{H}_0$ is assumed to be the opposite NMH to $\mathcal{H}_1$, with all other oscillation parameters remaining fixed. A more sophisticated definition of the alternative hypothesis is discussed in Section 5.3.3.

In order to quantify the future performance of the detector in a single number, it is useful to define the median sensitivity. Taking a frequentist view of future measurements, the median sensitivity is defined as the minimum confidence level at which 50% of NMH measurements would exclude $\mathcal{H}_0$ with respect to $\mathcal{H}_1$, if an arbitrarily large number of measurements were performed.

5.3.1 Likelihood Ratio Approach

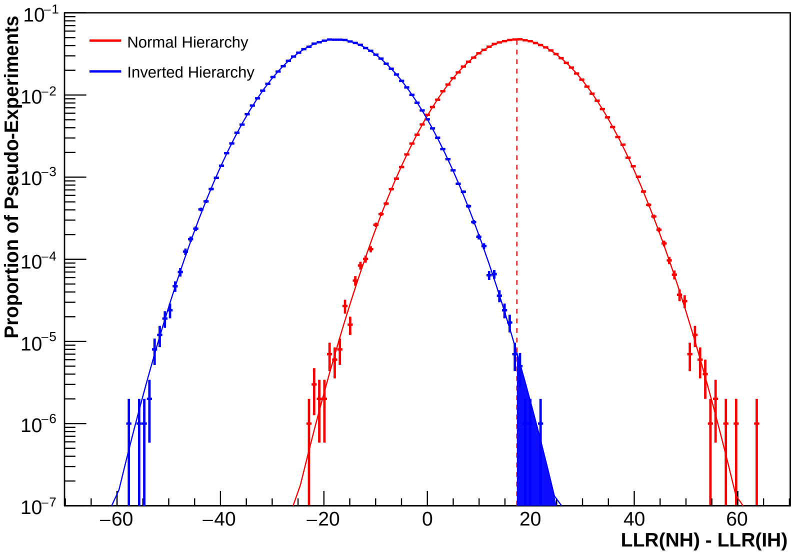

Figure 5.12: The log likelihood ratio distribution for pseudo-experiments generated according to the normal and inverted NMHs, using the $\theta_{23} = 40°$ and $\delta^{CP} = 180°$, fitted with a Gaussian. A livetime of three years was assumed and no systematic errors are included. In each case, the alternative hypothesis is the opposite NMH with the same oscillation parameters. The IH can be rejected with respect to the NH with a p-value greater than or equal to the blue, shaded area 50% of the time.

Of the two ways to calculate the median sensitivity, this is the most accurate but also the most time consuming. It has already been employed in previous ORCA sensitivity studies [1, 87]. For a given NMH hypothesis, the expected number of events in all bins of reconstructed zenith angle, energy and particle ID class ($\boldsymbol{\mu}$) can be derived, using the methodology laid out in Section 5.1. A corresponding set of pseudo data or pseudo-experiment ($\boldsymbol{x}$) can be randomly drawn by fluctuating the expectation value by a Poisson distribution. The likelihood of any set of expectation values, given a pseudo data set distributed in N bins of reconstructed energy, zenith angle, and PID class, is then given by the Poisson probability;

$$\mathcal{L}(\boldsymbol{\mu}|\boldsymbol{x}) = \prod_{i}^{N} \frac{\mu_i^{x_i} e^{-\mu_i}}{x_i!}. \tag{5.11}$$

To compare two alternative hypotheses, with two corresponding event expectations $(\boldsymbol{\mu_1}, \boldsymbol{\mu_0})$, the log likelihood ratio (LLR) is defined:

$$\mathrm{LLR}(\boldsymbol{\mu_1}, \boldsymbol{\mu_0}|\boldsymbol{x}) = \ln\left(\frac{\mathcal{L}(\boldsymbol{\mu_1}|\boldsymbol{x})}{\mathcal{L}(\boldsymbol{\mu_0}|\boldsymbol{x})}\right), \tag{5.12}$$

where the pseudo-experiments can be generated according to either hypothesis.

By examining the LLR distribution of pseudo-experiments generated according to each hypothesis in turn, an associated p-value can be calculated. It is equal to the proportion of pseudo-experiments generated according to $\mathcal{H}_0$ whose LLR exceeds the median LLR of the pseudo-experiments generated according to $\mathcal{H}_1$. This is shown graphically on Fig. 5.12, where it can also be seen that the LLR distribution is Gaussian. Therefore, the median significance (S_{med}) can be simply calculated by fitting the width.

$$S^{\mathcal{H}_1}_{\text{med}} = \frac{|\mu^{\mathcal{H}_1} - \mu^{\mathcal{H}_0}|}{\sigma^{\mathcal{H}_0}}, \tag{5.13}$$

where μ and σ are the mean and standard deviation of the LLR distributions for each hypothesis.

5.3.2 Asimov Approach

In an alternative approach, rather than using the expectation value of the data to generate multiple sets of pseudo data, an Asimov dataset is used. An Asimov dataset[1] is one where every data point, in this case the number of events in each bin, is set to its expectation value. In Ref. [109], a formal mathematical justification is shown for the calculation of the median sensitivity from an Asimov dataset.

$$\begin{aligned} S^{\text{med}} &= \sqrt{-2\ln\frac{\mathcal{L}(\boldsymbol{\mu}_1|\boldsymbol{\mu}_0)}{\mathcal{L}(\boldsymbol{\mu}_0|\boldsymbol{\mu}_0)}} \\ &\approx \sqrt{\Delta\chi^2_A}, \end{aligned} \tag{5.14}$$

---

[1] Named after the 1955 Isaac Asimov short story Franchise, in which a single voter is chosen to represent an entire electorate.

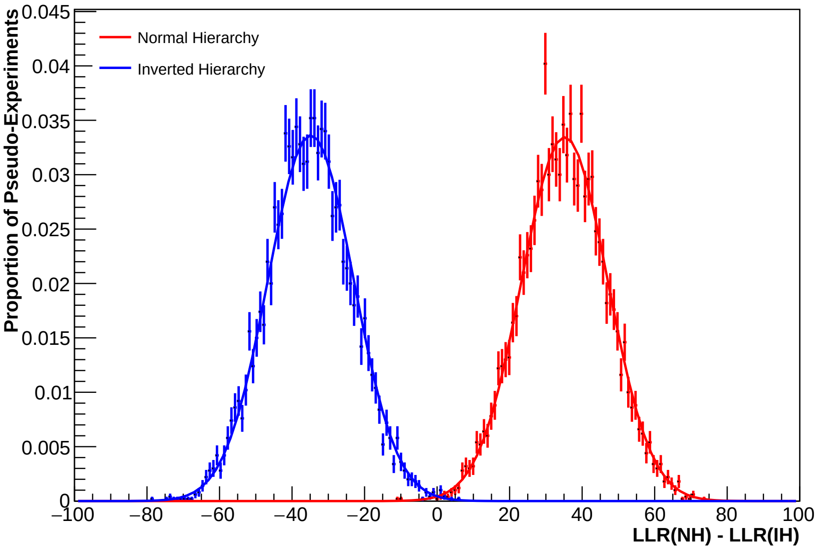

Figure 5.13: The LLR ratio distribution for pseudo-experiments generated according to the normal and inverted NMHs, for $\theta_{23} = 45°$ and $\delta^{CP} = 0°$. Overlaid over the top are Gaussians with means of $\pm\Delta\chi^2_A$ and widths of $2\sqrt{\Delta\chi^2_A}$.

where the delta chi square ($\Delta\chi^2_A$) is given by

$$\Delta\chi^2_A = \sum_i^N \frac{(\mu_i^{\mathcal{H}_1} - \mu_i^{\mathcal{H}_0})^2}{\mu_i^{\mathcal{H}_0}}. \tag{5.15}$$

Notice that the term on the right hand side of Eq. 5.14 is simply the LLR defined in Eq. 5.12, where the pseudo-data has been replaced by its expectation values according to $\mathcal{H}_0$.

However, this proof uses Wilks' and Wald's theorems [110, 111], which show that for large numbers of events, the distribution of the LLR follows a non-central χ^2 distribution. These theorems do, however, assume nested hypotheses, which is not the case for the NMH. Nevertheless, it can be shown empirically that the approximation in 5.14 does indeed hold true (see Fig. 5.13).

Another advantage of this approach is that the θ_ν, E_ν regions which best contribute to the sensitivity can be easily visualised. Choosing $\mathcal{H}_0$ and $\mathcal{H}_1$ to be the NH and IH respectively, a signed variant of $\Delta\chi^2_A$ can be defined as

$$\Delta\chi^2_A = \frac{(\mu^{NH} - \mu^{IH}) \times |\mu^{NH} - \mu^{IH}|}{\mu^{NH}}, \tag{5.16}$$

which is shown in Fig. 5.14. The most important contribution to the NMH sensitivity is cascade (ν_e) appearance in the NH case and disappearance in the IH case.

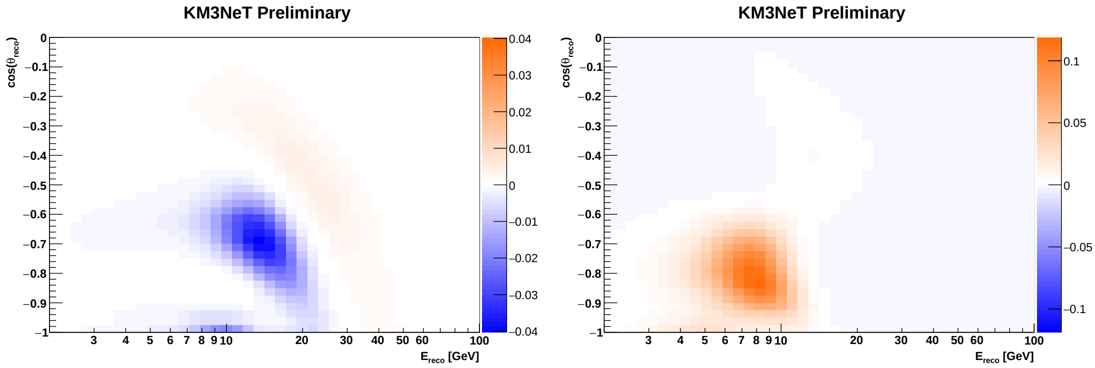

(a) Tracks (b) Cascades

Figure 5.14: The signed $\Delta\chi^2_A$ in each bin of reconstructed energy and zenith angle for events classified as tracks and cascades. The corresponding median significance is the square root of the sum of the absolute values of each bin. In this case, where $\theta_{23} = 45°$ and $\delta^{CP} = 0°$, the significance is 6.06σ.

5.3.3 Choosing the Alternative Hypothesis

Until now, it has been assumed that $\mathcal{H}_0$ is simply $\mathcal{H}_1$ with the NMH reversed. However, it is necessary to allow for the possibility that associating a different set of oscillation parameters with $\mathcal{H}_0$ might better describe the expected signal according to $\mathcal{H}_1$.

For example, in Fig. 5.15, $\mathcal{H}_1$ and $\mathcal{H}_0$ are taken to be the normal and inverted hierarchies respectively. However, rather than simply fixing the value of θ_{23} associated with $\mathcal{H}_0$, it has been allowed to vary. It can be clearly seen that in the case where the NMH is normal and $\theta_{23} = 42°$, for example, the alternative hypothesis that best describes the expected signal is that where $\theta_{23} \approx 49°$.

It is useful to think about this concept in terms of a real physics experiment. Having found that the data is better fitted by the NH than the IH and having measured $\theta_{23} = 42°$ in the NH case, it is more useful to quote the most likely alternative hypothesis can be excluded than to assert that θ_{23} was measured perfectly.

The choice of $\mathcal{H}_0$ for this study is therefore the alternative hypothesis that best fits the expected signal from $\mathcal{H}_1$, as a function of all the oscillation parameters to which ORCA is sensitive, i.e. the set of oscillation parameters which minimise $\Delta\chi^2$. This minimum is found using the Minuit2 package [112], using the migrad minimiser. Like most function minimisers, migrad will not always find the global minimum if multiple local minima exist. Therefore, special care is taken to find the global best fit value of θ_{23}, where there is often one local minimum in each octant, see Fig. 5.15. Each minimisation procedure is performed twice, with a starting point in each octant, and the best of the two final results is selected. It is also

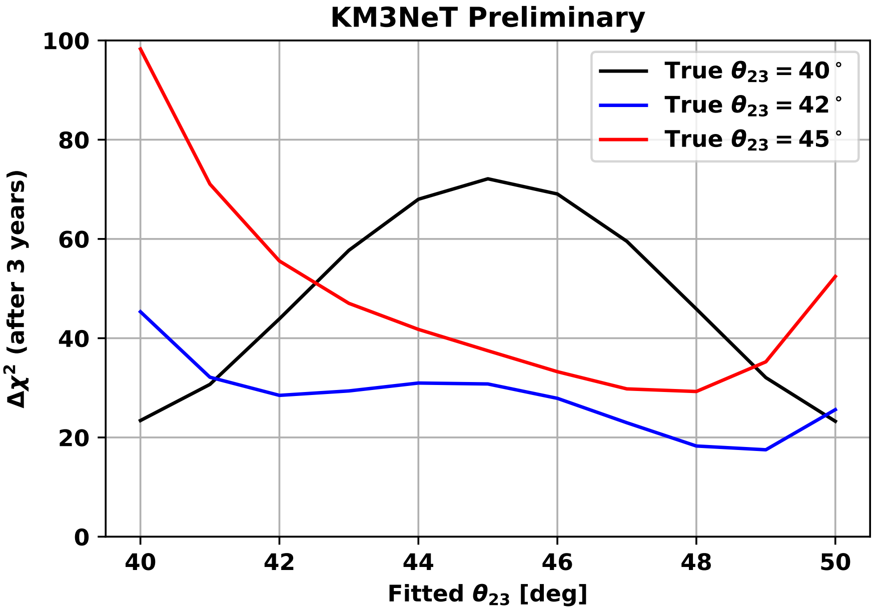

Figure 5.15: The $\Delta\chi^2$ with which the IH can be rejected as a function of the mixing angle θ_{23} corresponding to the IH hypothesis.

necessary to fit other variables which are not interesting from a physical perspective, but whose uncertainties may affect the final sensitivity calculation, called nuisance parameters. See Section 5.4 for a discussion of their treatment.

When using the Asimov approach, it is effectively assumed that all pseudo-experiments would find the same set of best fit values, except for the LLR, which would be distributed according to a Gaussian distribution. Previous NMH sensitivity studies [87] have found that this is usually the case, except for θ_{23}. There are often two possible best fit values of θ_{23} (see Fig. 5.15), one in each octant. Due to statistical fluctuations, pseudo-experiments will sometimes find the more optimistic of the two in terms of sensitivity to the NMH, improving the median sensitivity overall. In this sense, the Asimov approach is more conservative than the LLR method.

5.3.4 External Constraints

For some variables, most notably θ_{13}, pre-existing experimental constraints are much more stringent than ORCA would determine on its own. In order to take this into account, the $\Delta\chi^2$ test statistic can be extended with a series of chi square like terms, known as priors. For an ensemble of variables $\boldsymbol{y}$ of length M, with associated experimental best fit values and uncertainties $\boldsymbol{y}^{\text{true}}$ and $\boldsymbol{\sigma}^{y}$, the new test statistic is given by

$$\Delta\chi^2_A = \sum_i^N \frac{(\mu_i^{\mathcal{H}_1} - \mu_i^{\mathcal{H}_0})^2}{\mu_i^{\mathcal{H}_0}}. + \sum_i^M \left(\frac{y_i - y_i^{\text{true}}}{\sigma_i^y}\right)^2. \tag{5.17}$$

5.4 Systematics and Nuisance Parameters

Parameter	Treatment	True Value	Prior
$\Delta m^2_{12}[\text{eV}^2]$	Fixed	7.40×10^{-5}	N/A
$\Delta m^2_{23}[\text{eV}^2]$	Free	2.420×10^{-3}	N/A
$\theta_{12}[^\circ]$	Fixed	33.4	N/A
$\theta_{13}[^\circ]$	Fitted with prior	8.62	0.15°
$\theta_{23}[^\circ]$	Free	$40 - 50$	N/A
$\delta^{CP}[^\circ]$	Free	0 or 180	N/A
Track Normalisation	Free	1	N/A
Cascade Normalisation	Free	1	N/A
Neutral Current Normalisation	Fitted with prior	1	10%
Spectral Tilt	Free	0	N/A
$\nu/\bar{\nu}$ Skew	Fitted with prior	0	3%
$\nu_e/\bar{\nu}_e$ Skew	Fitted with prior	0	10%
$\nu_\mu/\bar{\nu}_\mu$ Skew	Fitted with prior	0	10%
ν_e/ν_μ Skew	Fitted with prior	0	5%
Energy Scale Shift	Fitted with prior	0	10%

Table 5.1: The full list of oscillation and nuisance parameters used in this study, along with their statistical treatment and prior if applicable.

The full set of oscillation and nuisance parameters considered in this work is shown in Table 5.1. Throughout this section, all plots are generated using the values in the True Value column, unless otherwise specified.

These parameters are broken down into four categories: oscillation parameters and their experimental uncertainties; flux uncertainties derived from current best measurements of the atmospheric neutrino flux, cross section uncertainties and finally detector effects. In order to be as independent of external constraints as possible, only 4 priors are used, which will be justified in subsequent subsections.

5.4.1 Oscillation Parameters

Atmospheric neutrino experiments, such as ORCA, are not sensitive to the so-called solar oscillation parameters: θ_{12} and Δm^2_{12}. However, ORCA is able to measure θ_{23} and Δm^2_{32}, whereas δ^{CP} and θ_{13} take on the role of nuisance parameters. They aren't measured with a high degree of certainty, but impact the measurements of other variables.

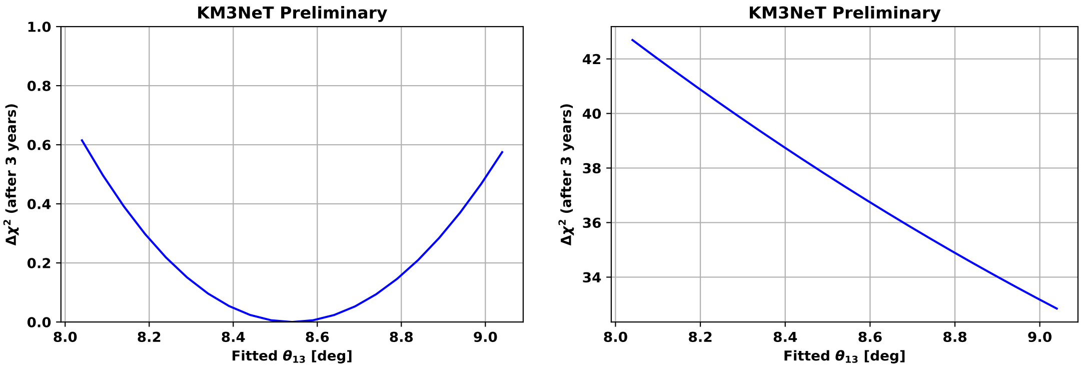

(a) Normal Hierarchy

(b) Inverted Hierarchy

Figure 5.16: The $\Delta\chi^2$ after 3 years as a function of θ_{13}, with all other variables kept fixed, with respect to a true value of $\theta_{23} = 45°$, $\delta^{CP} = 0°$ and a normal hierarchy. It can be seen that while ORCA does not have much discrimination power over θ_{13} when the NMH is known, it must be constrained in order to measure the NMH.

In this section, the impact of each oscillation parameter to which ORCA is sensitive is examined by varying it, whilst fixing all other variables to their nominal true values. The true NMH is assumed to be normal. The $\Delta\chi^2$ is then calculated at each point, with respect to the nominal value, for both the true hierarchy (NH) and the opposite hierarchy (IH). The former indicates how well the given parameter can be measured, whereas the latter describes the effect its experimental uncertainty has on the NMH measurement.

In Fig. 5.16, it can be seen that ORCA is not particularly sensitive to the true value of θ_{13} when the NMH is known. However, leaving θ_{13} unconstrained can degrade the NMH sensitivity. As it is already well constrained experimentally [35], this is reflected by a prior of 0.15°.

As expected, ORCA is sensitive to the atmospheric oscillation parameters, θ_{23} and Δm^2_{32} (see Figs. 5.17 and 5.18). As these are the parameters that ORCA will be measuring, it does not make much sense to impose any external constraints. However, it should be noted that the loss in NMH sensitivity due to the uncertainty on θ_{23} is mostly caused by the uncertainty over the octant of θ_{23}. If the octant is known, then the NMH sensitivity improves.

Finally, in Fig 5.19, it is shown that while the CP phase cannot be measured with a competitive significance using atmospheric neutrinos in ORCA (see Ref. [113] for prospects of measuring δ^{CP} with a neutrino beam). However, assuming the wrong hierarchy causes the best fit value of δ^{CP} to flip by 180°, suggesting that the flipping the CP phase mimics the opposite hierarchy to some extent. As current experimental constraints on the CP phase remain very broad, no constraint is

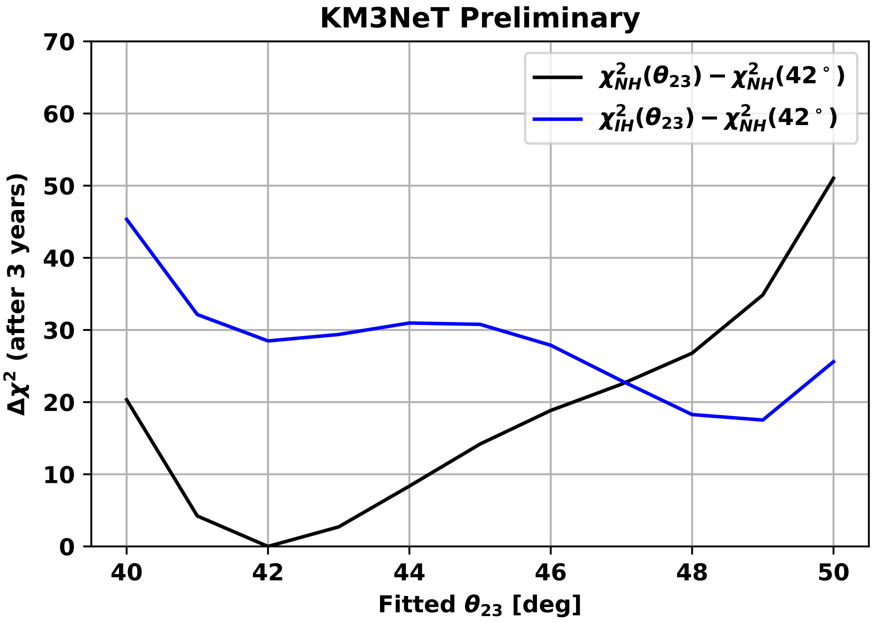

Figure 5.17: The $\Delta\chi^2$ after 3 years as a function of θ_{23}, with all other variables kept fixed, with respect to a true value of $\theta_{23} = 42^\circ$, $\delta^{CP} = 0^\circ$ and a normal hierarchy. Both NMH hypotheses are shown, in order to show the sensitivity to θ_{23}, but the NH is assumed to be true. In this example, the best fit value of θ_{23} for the wrong hierarchy is found in the wrong octant. If the octant were known, the overall sensitivity to the NMH could be improved.

applied.

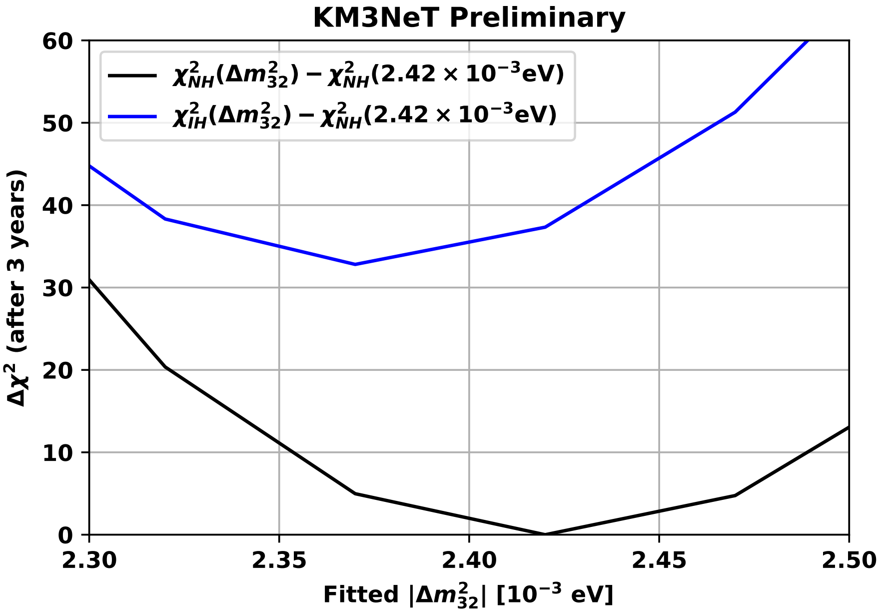

Figure 5.18: The $\Delta\chi^2$ after 3 years as a function of $|\Delta m^2_{32}|$, with all other variables kept fixed, with respect to the assumed true values of $\theta_{23} = 45°$, $\delta^{CP} = 0°$ and a normal hierarchy. Both the correct and opposite NMHs are shown in order to show the sensitivity to the absolute value of Δm^2_{32} and its behaviour when the wrong hierarchy is fitted.

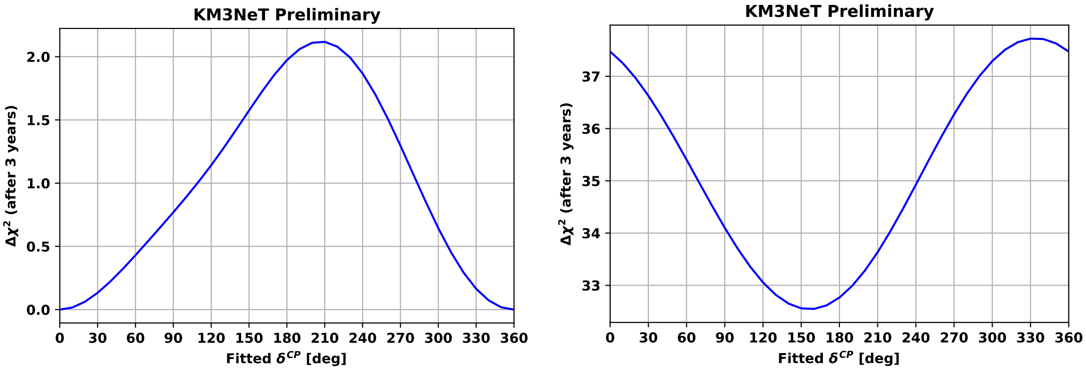

(a) Normal Hierarchy

(b) Inverted Hierarchy

Figure 5.19: The $\Delta\chi^2$ after 3 years as a function of δ^{CP}, with all other variables kept fixed, with respect to the assumed true values of $\theta_{23} = 45°$, $\delta^{CP} = 0°$ and a normal hierarchy. Both the correct and opposite NMHs are shown, in order to show the sensitivity to δ^{CP} when the NMH is correctly identified and its behaviour when the wrong hierarchy is fitted. It can be seen that ORCA is not able to measure the CP phase with a competitive significance, but that the uncertainty on δ^{CP} does reduce the sensitivity to the NMH.

5.4.2 Flux Uncertainties

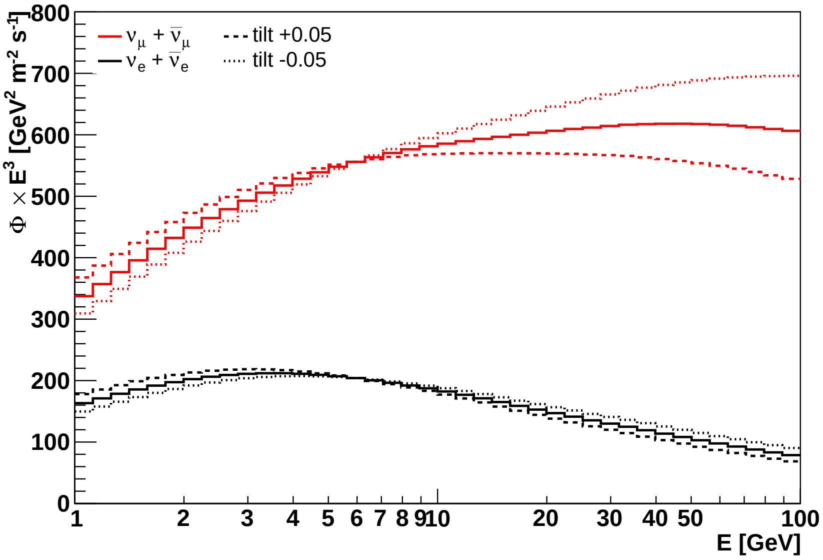

Figure 5.20: The Honda [22] atmospheric neutrino flux, with a spectral tilt of ±0.05 around 6 GeV.

In this section, nuisance parameters relating to the atmospheric neutrino flux uncertainties will be discussed. They are the track and cascade normalisations, the $\nu/\bar{\nu}$ and ν_e/ν_μ skews and the spectral tilt.

The normalisation in each channel can be left free, as it will be constrained by the region where matter effects are suppressed (i.e. $E_\nu \gtrsim 20$ GeV). In any case, any priors on the event rate normalisation would have to incorporate not only the uncertainties on the flux normalisation, but also the effective mass and cross sections.

The spectral tilt, on the other hand, is a perturbation to the shape of the spectrum itself. The following transformation is applied

$$\Phi_\nu(E) \rightarrow \Phi_\nu(E) \times \left(\frac{E}{E_0}\right)^\gamma, \tag{5.18}$$

where γ is the spectral tilt parameter and E_0 is the pivot energy, set to 6 GeV. In Fig. 5.20, the atmospheric neutrino flux is plotted for γ values of -0.05, 0, and +0.05. The pivot energy was chosen to be close to the maximum event rate as a function of energy, in order to decorrelate the spectral tilt from the flux normalisation as much as possible. The spectral tilt was found to have only a small impact on the sensitivity and were therefore left free in the fit.

The impact of the $\nu/\bar{\nu}$ and ν_μ/ν_e skews, on the other hand, was found to be more substantial. The implementation of the skew systematics is as follows. Supposing that the atmospheric neutrino flux can be broken down into two constituent parts Φ_{ν_1} and Φ_{ν_2}, a perturbation can be applied to Φ_{ν_1} as follows:

$$\Phi_{\nu_1} \to \Phi_{\nu_1}(1+\delta). \tag{5.19}$$

In order to preserve the flux normalisation, Φ_{ν_2} must be shifted in the opposite direction;

$$\Phi_{\nu_2} \to \Phi_{\nu_2}(1-\frac{\Phi_{\nu_1}}{\Phi_{\nu_2}}\delta). \tag{5.20}$$

The following set of flux skew parameters are defined:

$\boldsymbol{\epsilon}$ a shift to the ν_e component of the atmospheric neutrino flux, whose ν_μ counterpart is given by $-\frac{\Phi_{\nu_e}}{\Phi_{\nu_\mu}}\epsilon$

$\boldsymbol{\delta_e}$ a shift to the ν_e component of the atmospheric neutrino flux, whose $\bar{\nu}_e$ counterpart is given by $-\frac{\Phi_{\nu_e}}{\Phi_{\bar{\nu}_e}}\delta_{\nu_e}$

$\boldsymbol{\delta_\mu}$ a shift to the ν_μ component of the atmospheric neutrino flux, whose $\bar{\nu}_\mu$ counterpart is given by $-\frac{\Phi_{\nu_\mu}}{\Phi_{\bar{\nu}_\mu}}\delta_{\nu_\mu}$

The oscillated neutrino flux of flavour a given flavour Φ^{osc}_α is then given by

$$\Phi^{\text{osc}}_\alpha = (1+\delta_{\nu_e})(1+\epsilon)\Phi_{\nu_e}\mathcal{P}_{\nu_e\alpha} + (1+\delta_{\nu_\mu})\left(1-\frac{\Phi_{\nu_e}}{\Phi_{\nu_\mu}}\epsilon\right)\Phi_{\nu_\mu}\mathcal{P}_{\nu_\mu\alpha}, \tag{5.21}$$

$$\Phi^{\text{osc}}_{\bar{\alpha}} = (1-\frac{\Phi_{\nu_e}}{\Phi_{\bar{\nu}_e}}\delta_{\nu_e})(1+\epsilon)\Phi_{\bar{\nu}_e}\mathcal{P}_{\bar{\nu}_e\bar{\alpha}} + \left(1-\frac{\Phi_{\nu_\mu}}{\Phi_{\bar{\nu}_\mu}}\delta_{\nu_\mu}\right)\left(1-\frac{\Phi_{\bar{\nu}_e}}{\Phi_{\bar{\nu}_\mu}}\epsilon\right)\Phi_{\bar{\nu}_\mu}\mathcal{P}_{\bar{\nu}_\mu\bar{\alpha}}, \tag{5.22}$$

in terms of the unoscillated neutrino fluxes Φ_{ν_e} and Φ_{ν_μ} and the oscillation probabilities $\mathcal{P}_{\nu_e\alpha}$ and $\mathcal{P}_{\nu_\mu\alpha}$. Priors are added to the test statistic according to:

$$\begin{aligned}\Delta\chi^2_{\text{sys+stat}} = \Delta\chi^2_{\text{stat}} &+ \left(\frac{\Delta(\nu/\bar{\nu})}{\sigma_{\nu/\bar{\nu}}}\right)^2 + \left(\frac{\Delta(\nu_e/\bar{\nu}_e)}{\sigma_{\nu_e/\bar{\nu}_e}}\right)^2 \\ &+ \left(\frac{\Delta(\nu_\mu/\bar{\nu}_\mu)}{\sigma_{\nu_\mu/\bar{\nu}_\mu}}\right)^2 + \left(\frac{\Delta(\nu_\mu/\nu_e)}{\sigma_{\nu_\mu/\nu_e}}\right)^2\end{aligned} \tag{5.23}$$

where Δ denotes a shift to the quantity in brackets and σ is its assumed uncertainty, as was shown in Eq. 5.17. For example,

$$\Delta(\nu_\mu/\nu_e) = \frac{\frac{\Phi'_{\nu_\mu}}{\Phi'_{\nu_e}} - \frac{\Phi_{\nu_\mu}}{\Phi_{\nu_e}}}{\frac{\Phi_{\nu_\mu}}{\Phi_{\nu_e}}} \tag{5.24}$$

where Φ' is the atmospheric flux after the shift has been applied. The exact value of the shift parameters will depend on the neutrino flux as a function of energy

Skew	Average Ratio
ν_μ/ν_e	2.00
$\nu_e/\bar{\nu}_e$	1.11
$\nu_\mu/\bar{\nu}_\mu$	1.30

Table 5.2: The average flux ratios assumed in order to calculate the priors on the flux skew systematics.

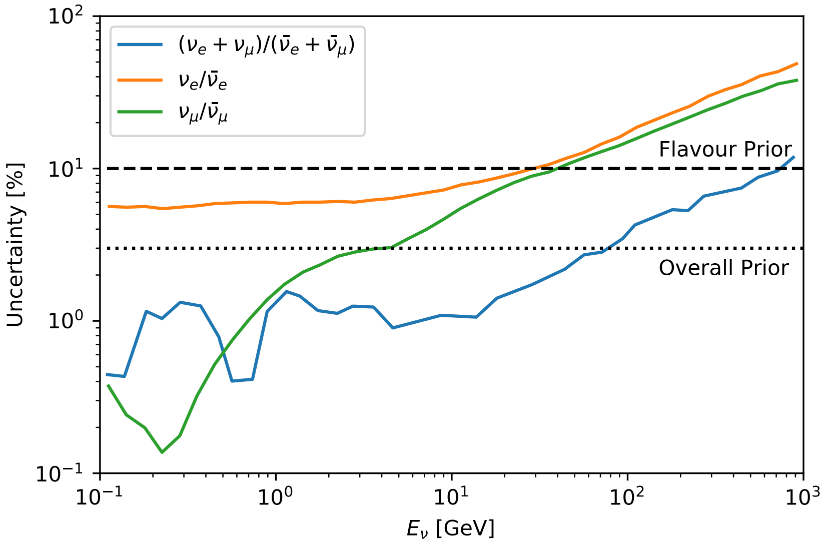

Figure 5.21: The estimated uncertainty in the $\nu/\bar{\nu}$ ratio, both overall and for each flavour component, as a function of energy. The dashed lines at 3% and 10% represent the priors assumed in this thesis (see Table 5.1). Data taken from Ref. [114].

and zenith angle. However, an approximation can be derived by simply assuming an average value of the $\nu/\bar{\nu}$ and ν_e/ν_μ ratios (see Table 5.2).

A detailed study of the dominant sources of uncertainty in the atmospheric neutrino flux, hadron production and primary flux, was carried out in Ref. [114]. The corresponding uncertainties are shown in Figs. 5.21 and 5.22. It can be seen that the priors assumed in this work, which are independent of energy and zenith angle, are in fact more conservative than the current estimated flux uncertainties, roughly corresponding to the uncertainty at $E_\nu = 100$ GeV.

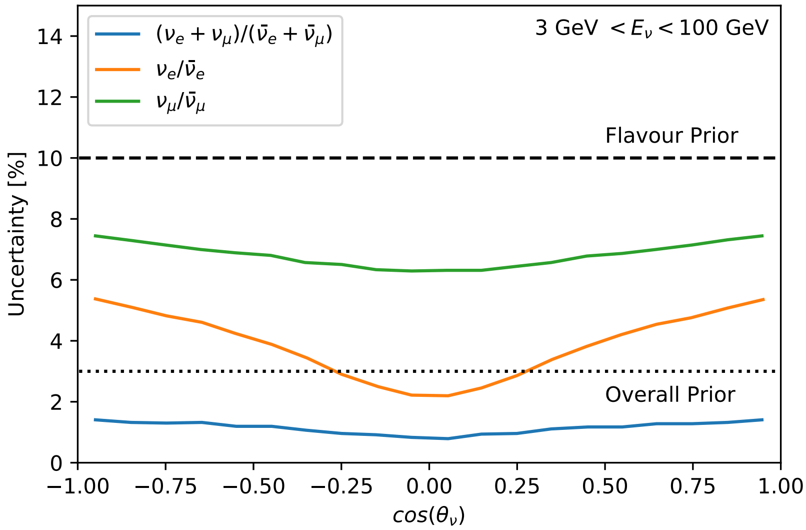

Figure 5.22: The estimated uncertainty in the $\nu/\bar{\nu}$ ratio, both overall and for each flavour component, as a function of zenith angle, for neutrinos in the range $3 - 30$ GeV. The dashed lines at 3% and 10% represent the priors assumed in this thesis (see Table 5.1). Data taken from Ref. [114].

5.4.3 Cross Section Uncertainties

In this section, uncertainties on the absolute value of the CC cross sections are not considered, as these would be degenerate with the event rate normalisations described in Section 5.4.2. However, NC events make up a signficant background, particularly in the cascade channel. While lepton universality means the cross section ratios between flavours are well known, the same is not necessarily the case for the ratio between CC and NC events. Therefore the neutral current event normalisation is also fitted.

5.4.4 Detector Effects

Of the nuisance parameters incorporated into this analysis, the track and cascade normalisations and energy scale shift could be considered detector effects. If there is a miscalibration of the PMTs and physics events are systematically brighter or less bright than expected, this will cause a shift to the normalisation of the effective mass. There will also be a systematic shift to the detector response. This is simulated by adding a shift ΔE to the true energy, when calculating the detector response function, but not the atmospheric neutrino flux or cross sections.

Eq. 5.3 becomes

$$N_\alpha(\theta,^{\text{rec}} E^{\text{rec}}) = \int dE d\Omega \sum_i \mathcal{P}^{\text{ID}}_{i\alpha}(E+\Delta E)\mathcal{P}^{\text{rec}}_{i\alpha}(\theta,^{\text{rec}} E^{\text{rec}}|\theta, E+\Delta E) \\ \times M^{\text{eff}}_i(\theta, E+\Delta E)N^{\text{int}}_i(\theta, E). \tag{5.25}$$

5.5 Results and Discussion

In this section, all of the methods discussed previously in this chapter will be put together. Firstly, in Section 5.5.1 the median sensitivity to reject the wrong NMH is shown, by assuming each NMH hypothesis in turn and then finding the most compatible wrong hierarchy hypothesis in terms of all the oscillation and nuisance parameters shown in Table 5.1. The special case where the θ_{23} octant is already known will be examined. Secondly, in Section 5.5.2, the sensitivity of a future ORCA measurement of θ_{23} and Δm^2_{32} is shown in comparison with the current world's best limits. An assessment of the power of ORCA to reject the wrong θ_{23} octant has also been performed.

5.5.1 NMH Sensitivity

The median sensitivity to the NMH after three years is shown without fitting any additional parameters in Figs. 5.23 and 5.24. The final sensitivity after three years, including all fitted parameters, is shown as a function of θ_{23} in Fig. 5.25. For the maximal mixing case, it is shown as a function of time in Fig. 5.26. It can be seen that ORCA can be expected to reach 3 sigma faster if the NMH is normal than if it is inverted. If the current global best fits are to be believed, then ORCA will confirm a NH result with 3σ significance in less than three years and reach 5σ within a decade. However, if the NMH is in fact inverted, then it may take up to five years just to reach 3σ.

The oscillatory shape in the final sensitivity is caused by the octant of θ_{23}. Recall from Fig. 5.17 that the best fit value of θ_{23} can be found in the wrong octant, if the wrong NMH is also assumed, as is done when determining the sensitivity. Of course, when using an Asimov approach, i.e. in the absence of any statistical fluctuations from the expectation, the best fit value of θ_{23} will be the same value used to generate the Asimov dataset. The best fit values of θ_{23} and δ^{CP} are shown in Figs. 5.29 and 5.30, where it can be seen that the best fit value of θ_{23} is indeed found in the wrong octant when its true value is in the range $40-45°$ for a normal hierarchy and $> 45°$ for an inverted hierarchy.

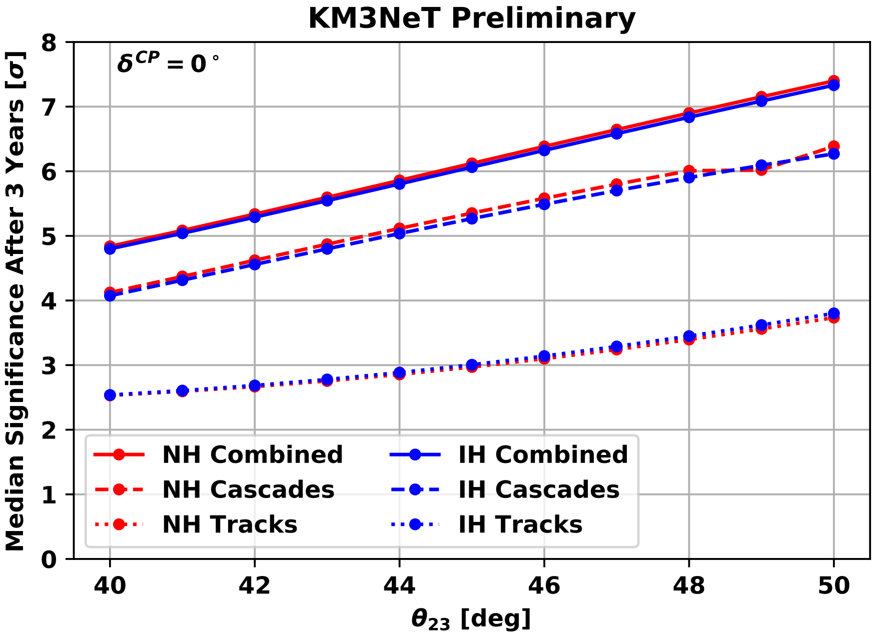

Figure 5.23: The median significance to reject the wrong NMH hypothesis after 3 years, without including any systematic errors, as a function of θ_{23}. The contribution from each channel is shown separately, as well as the combined significance, to which the cascade channel makes the greatest contribution.

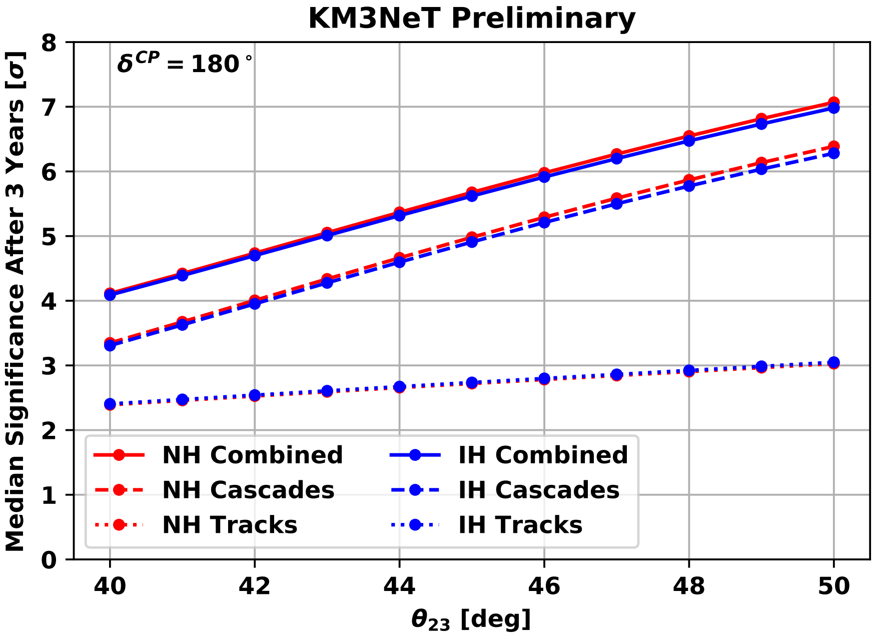

Figure 5.24: The median significance to reject the wrong NMH hypothesis after 3 years, without including any systematic errors, as a function of θ_{23}. The contribution from each channel is shown separately, as well as the combined significance, to which the cascade channel makes the greatest contribution.

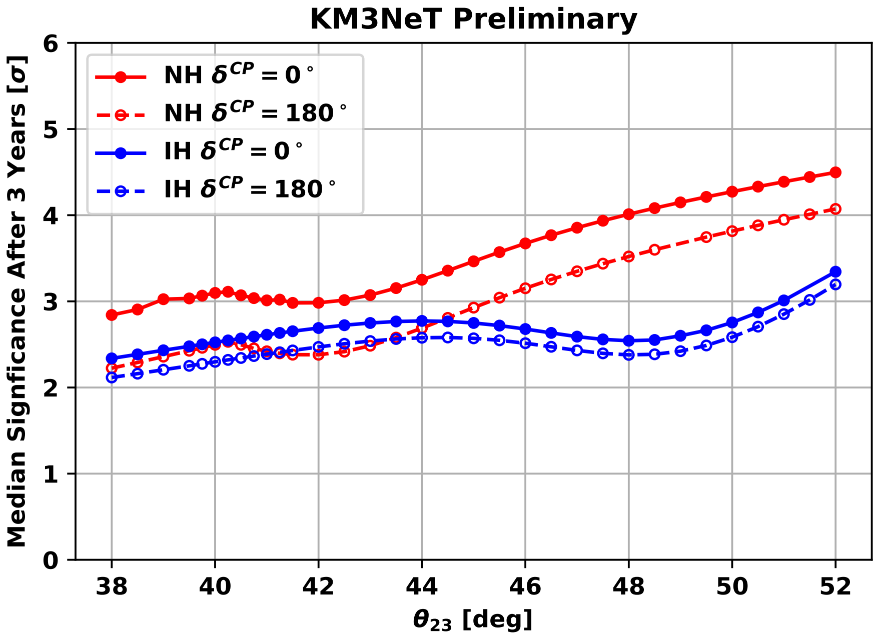

Figure 5.25: The median significance to reject the wrong NMH hypothesis after 3 years, as a function of θ_{23}, using the full systematics treatment described in Table 5.1, for two test values of δ^{CP}.

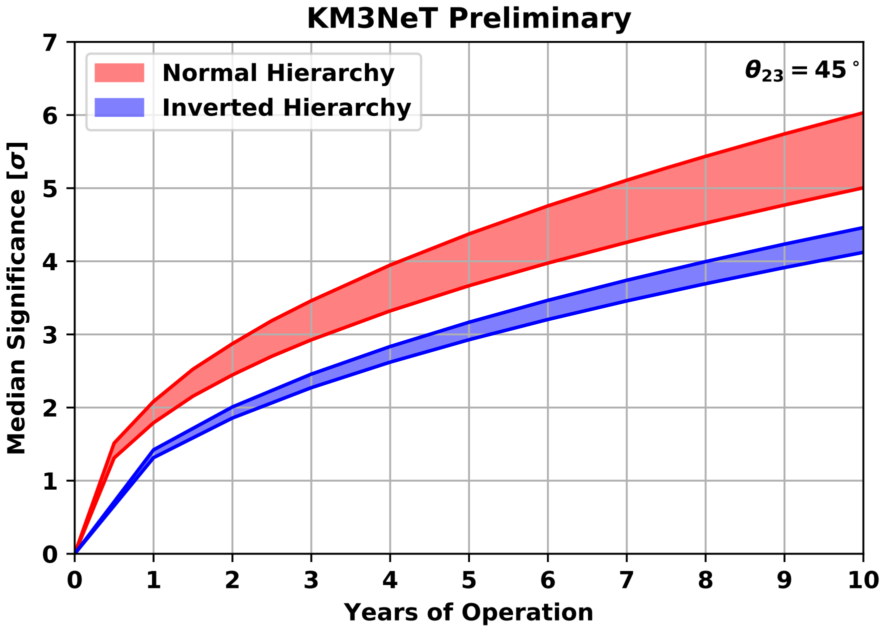

Figure 5.26: The median significance to reject the wrong NMH hypothesis as a function of time, for $\theta_{23} = 45°$. The coloured bands represent the range of sensitivities between $\delta^{CP} = 0°$ and $\delta^{CP} = 180°$.

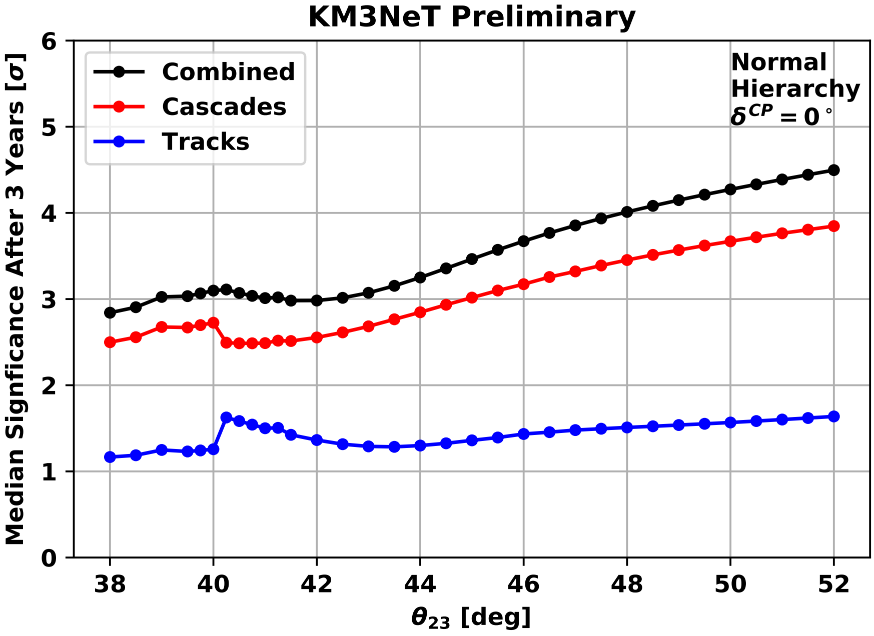

Figure 5.27: The median significance to reject the wrong NMH hypothesis after 3 years, broken down by channel, using $\delta^{CP} = 0°$ and the normal hierarchy. It can be seen that the cascade channel makes the greatest contribution to the overall sensitivity.

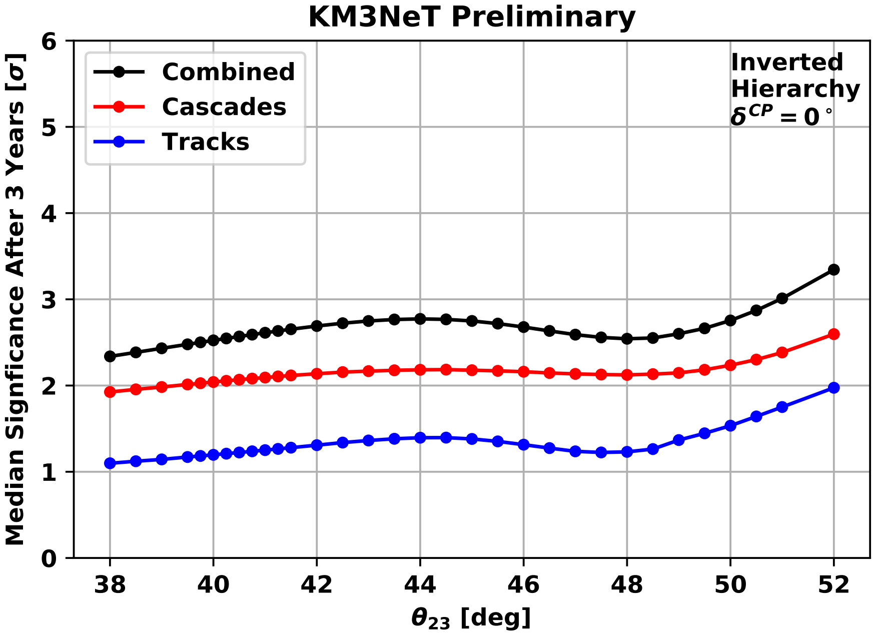

Figure 5.28: The median significance to reject the wrong NMH hypothesis after 3 years, broken down by channel, using $\delta^{CP} = 0°$ and the inverted hierarchy. It can be seen that the cascade channel makes the greatest contribution to the overall sensitivity.

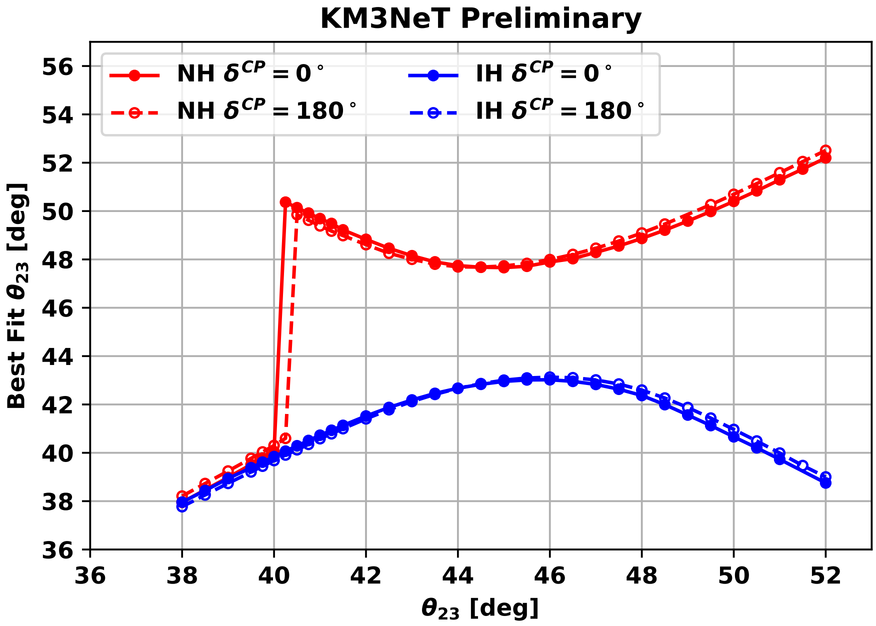

Figure 5.29: The fitted values of θ_{23} for each true value of θ_{23}. The best fit value is preferentially found in the first octant for the NH and the second octant for the IH.

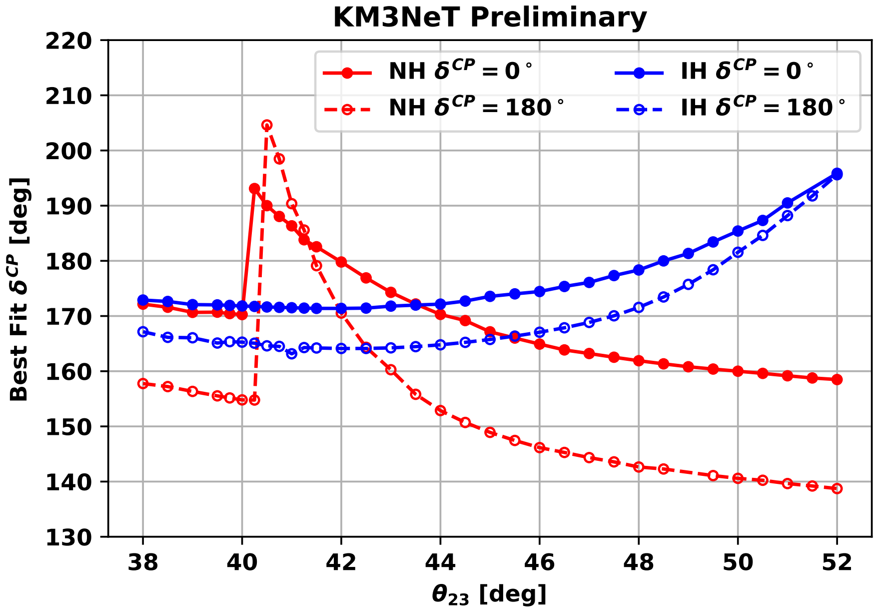

Figure 5.30: The best fit values of δ_{CP} for each true value of θ_{23}.

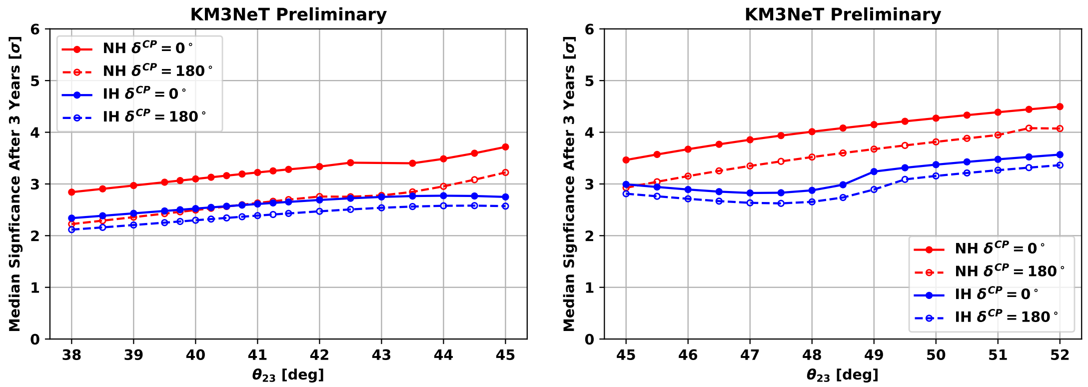

(a) First octant (b) Second octant

Figure 5.31: The median significance after 3 years, as a function of θ_{23}, in the special case where the octant of θ_{23} is known.

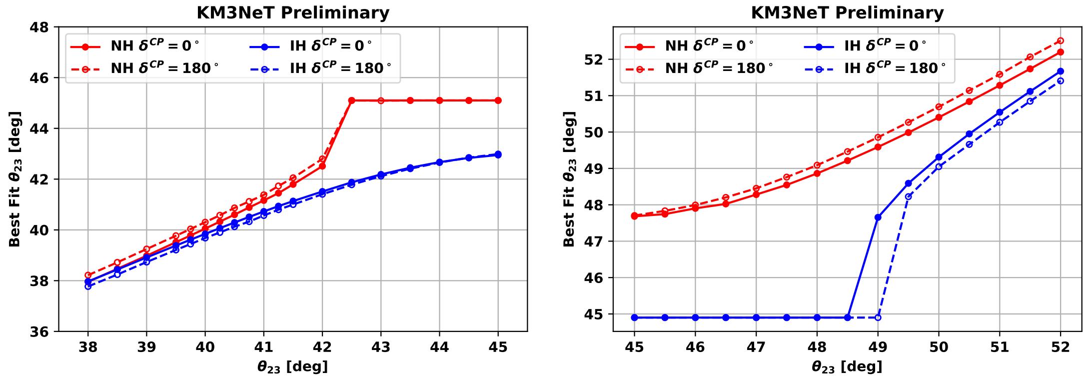

(a) First octant (b) Second octant

Figure 5.32: The fitted values of θ_{23} for each true value of θ_{23}, in the special case where the octant of θ_{23} is known.

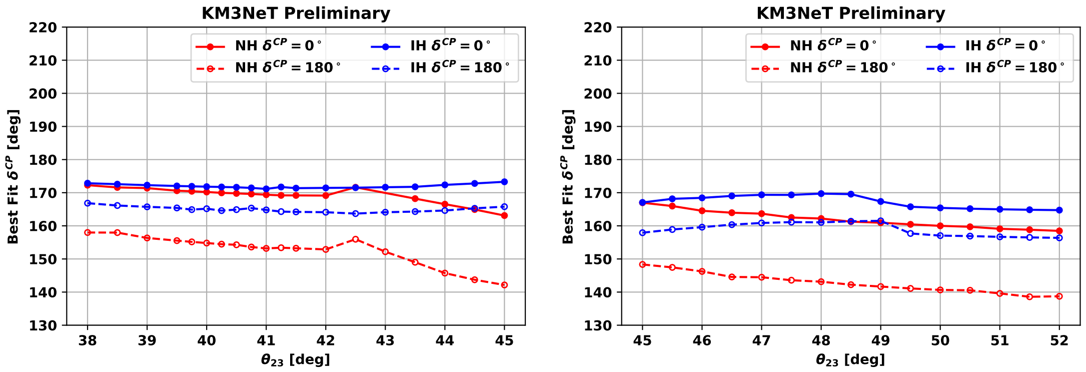

(a) First octant (b) Second octant

Figure 5.33: The fitted values of δ_{CP} for each true value of θ_{23}, in the special case where the octant of θ_{23} is known.

It is therefore interesting to examine the special case where the octant of θ_{23} is already known. If θ_{23} is constrained to its true octant (see Fig. 5.31), then the sensitivity curve takes on the form seen in Figs. 5.23 and 5.24 and improves by as much as 0.5σ in the regions where θ_{23} would otherwise be found in the wrong octant. For an idea of the $\Delta\chi^2$ landscape and the degeneracy in θ_{23}, see Figs. 5.32 and 5.33. For values of θ_{23} in the range $42 - 45°$ for a NH and $45 - 49.5°$ for a IH, there is no local minimum of θ_{23} in the correct octant. In Figs. 5.27 and 5.28, it can be seen that the cascade channel is the main contributor to the NMH sensitivity, however, as will be discussed in section 5.5.2, the track channel is important for constraining θ_{23}. This is hinted at in Fig. 5.27, where the sensitivity from tracks increases and the sensitivity from cascades decreases near to $\theta_{23} = 40°$, where its best fit value flips octant.

In this section, it has been shown that ORCA will be able to measure the NMH with an expected median significance of 3σ after a few years of data taking. It is also clear that better control over the octant of θ_{23}, would lead to a substantial improvement in the sensitivity. This could take the form of either external experimental constraints or a separately-optimised θ_{23} measurement within ORCA with which to constrain the NMH measurement.

5.5.2 θ_{23} and Δm^2_{32}

In this section, the same set of oscillation and nuisance parameters from Table 5.1 are used, with the same treatment, except for the following: the NMH is assumed to be normal unless stated otherwise, $\theta_{23} = 45°$ and $\delta^{CP} = 0°$ are assumed. The sensitivity to Δm^2_{32} and θ_{23} is represented by the contour of alternative values which could be rejected with C.L. 90%. Here, the same statistical test described in Section 5.3.2 is applied, where $\mathcal{H}_1$ and $\mathcal{H}_0$ are the assumed and alternative set of

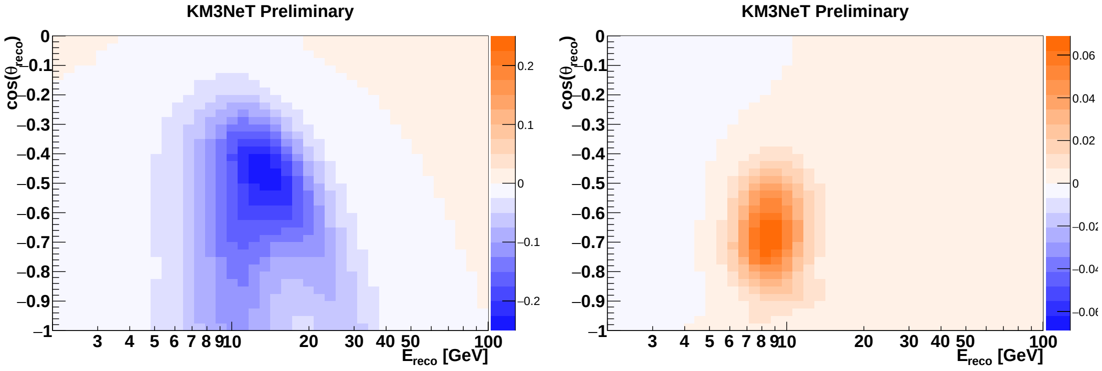

(a) Tracks (b) Cascades

Figure 5.34: The signed χ^2_A between θ_{23} values of 45° and 40°, assuming normal hierarchy and $\delta^{CP} = 0°$. A positive value on the Z axis means that more events are expected if $\theta_{23} = 45°$ than if $\theta_{23} = 40°$.

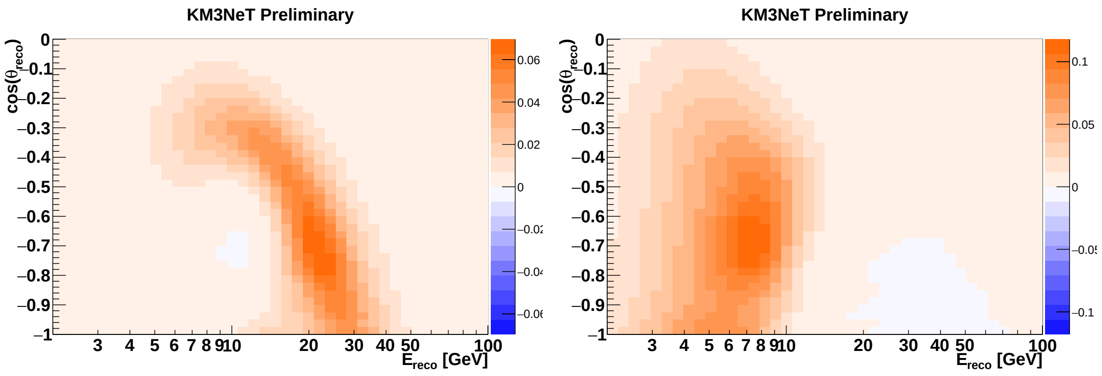

(a) Tracks

(b) Cascades

Figure 5.35: The signed χ^2_A between θ_{23} values of 45° and 50°, assuming normal hierarchy and $\delta^{CP} = 0°$. A positive value on the Z axis means that more events are expected if $\theta_{23} = 50°$ than if $\theta_{23} = 45°$.

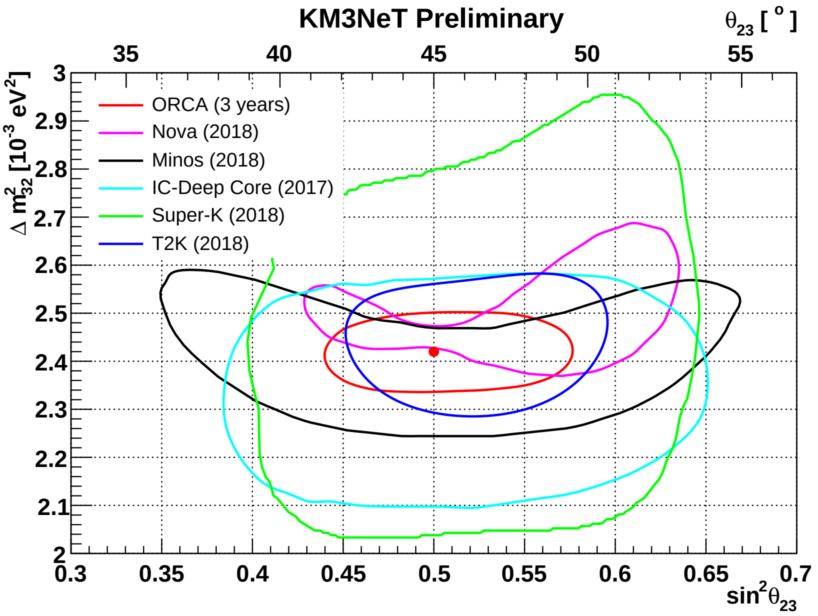

Figure 5.36: The 90% CL contour, shown alongside current results from NOvA [46], Minos [66], IceCube [6], Super-Kamiokande [115], and T2K [116].

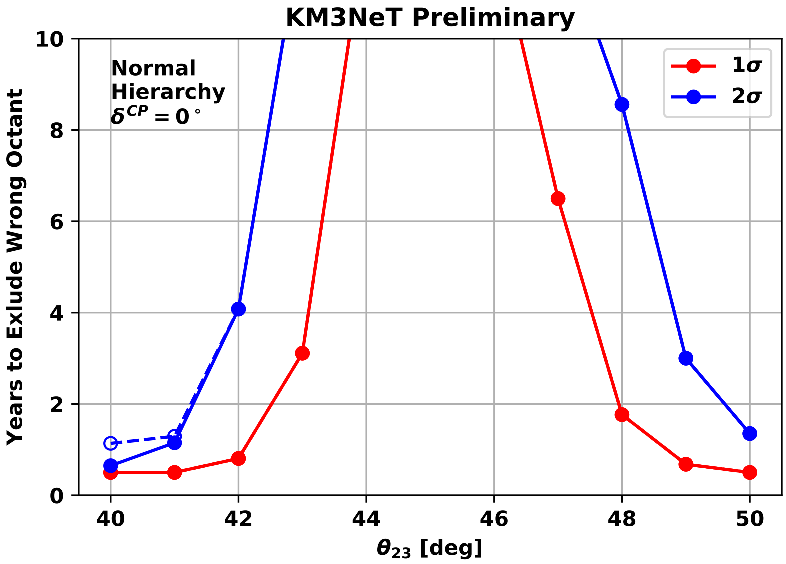

Figure 5.37: The amount of operation time necessary to exclude the wrong θ_{23} octant, assuming the NMH is normal. The solid line represents the case where the NMH is known to be normal. If it is allowed to vary, then the best value in the wrong octant also has the wrong NMH, which is represented with a dashed line.

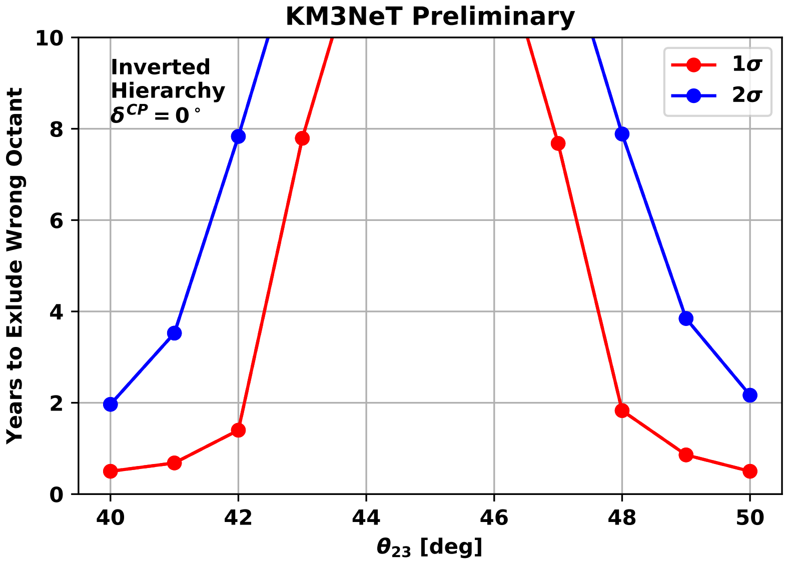

Figure 5.38: The amount of operation time necessary to exclude the wrong θ_{23} octant, assuming the NMH is inverted. In this case, the NMH is always also inverted for the best fit value in the wrong octant.

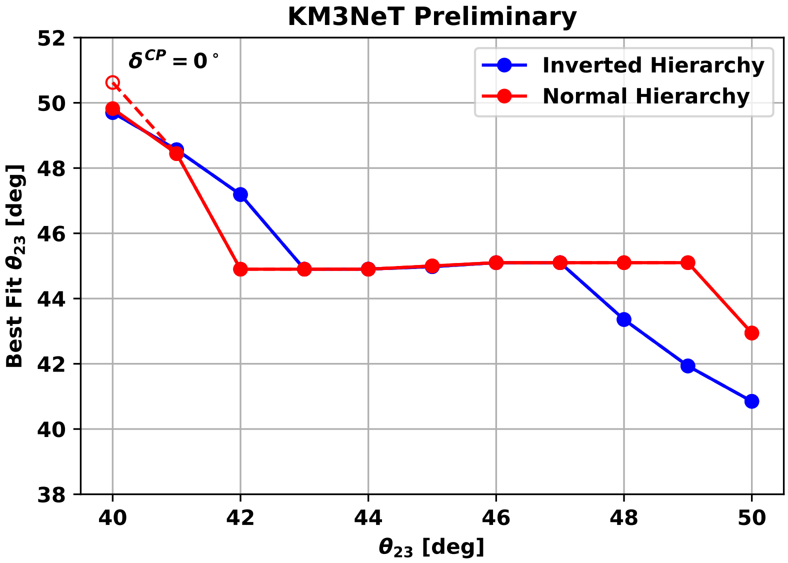

Figure 5.39: The best fit value of θ_{23} in the wrong octant after three years, as a function of the true value of θ_{23}. The dashed line represents the case where the NMH is allowed to vary in the fit, which gives the same result as keeping it fixed for all but one point.

oscillation parameters, with the NMH remaining fixed. As in Section 5.3.2, the signed variant of the Asimov chi square is shown in Figs. 5.34 and 5.35, in order to understand which channels, energies and zenith angles contribute most to the significance and whether ν appearance or disappearance is being measured. It is clear that the tracks make a more important contribution to measuring θ_{23} than they do to the NMH sensitivity, particularly in the first octant. Fig. 5.36 puts ORCA in to context, alongside current results from NOvA [46], Minos [66], IceCube [6], Super-Kamiokande [115], and T2K [116], with which it will be competitive after a few years of data taking.

Where other experiments have not found maximal mixing (i.e. $\theta_{23} = 45°$), a best fit value of θ_{23} can often be found in each octant; a particularly notable case of this was the 2017 NOvA measurement [117]. It is therefore of interest to explore this degeneracy further and determine the significance with which the wrong octant can be excluded. In Fig. 5.37 and 5.38, it is shown that ORCA will be able to exclude the wrong octant with a significance of 1σ within two years, if θ_{23} is outside the range $42 - 48°$. The best fit value of θ_{23} in the wrong octant, evaluated at the three years mark, can be found in Fig. 5.39. Here it can be seen that the octant degeneracy is stronger for the IH than the NH; a best fit value other than 45° indicates the presence of a local minimum in the wrong octant.

Chapter 6

Conclusion and Summary

Neutrino oscillations, and hence mass, are the first known indications of physics beyond the standard model. A wide variety of approaches are needed within the neutrino sector to measure the neutrino masses and mixing angles. ORCA, which sensitive to atmospheric neutrino oscillations, enhanced by matter effects in the $1 - 15$ GeV range, can determine the NMH with a median sensitivity of 3σ after a few years of data taking. This sensitivity can improve by $0.5 - 1.5\sigma$, if the octant of θ_{23} has already been correctly determined. Regardless, it will also be possible to measure θ_{23} and Δm^2_{32} with a precision competitive with the current best measurements. If mixing is far from maximal, i.e. $\theta_{23} \lesssim 42°$ or $\theta_{23} \gtrsim 48°$, then ORCA will also be able to exclude one θ_{23} octant within 3 years, although this scenario is currently disfavoured by global fits. These results were found by applying the Asimov approach, which was chosen for its speed compared to the more rigourous LLR method. However, the Asimov approach is also expected to be more conservative, so it is now necessary to evaluate the sensitivity with the LLR method, whose results should be more optimistic and more correct.

The successful deployment of the first ORCA DU has shown that the KM3NeT design and software works as expected. A handful of potential neutrino candidates have already been identified, but more data is needed before starting to quantify the statistical significance of this measurement. In any case, no oscillation study can take place until more lines have been deplyed, which will allow for the energy reconstruction and cascade reconstruction to be applied to real data. Now the focus needs to be on scaling up, deploying more lines, taking more data, and simulating the sea conditions and detector response in greater detail. Once sufficient DUs have been deployed (~ 5 DUs), ORCA will start to be able to distinguish neutrino flavours and measure oscillations, as its effective mass approaches and overtakes ANTARES.

6.1 Comparison with Other Experiments

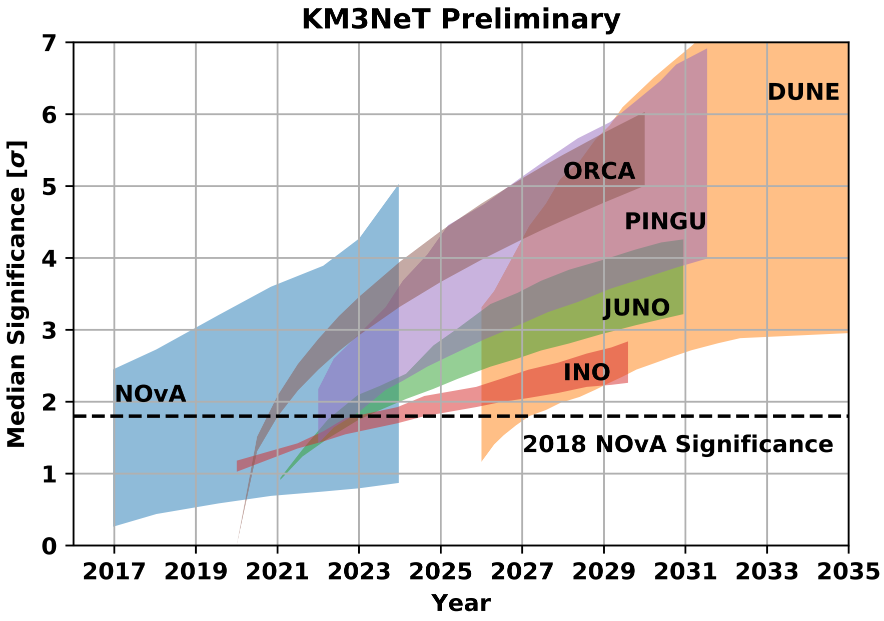

Figure 6.1: The projected sensitivity to the NMH over the next two decades, in the NH case. Curves were taken from Ref [118], with the exception of the ORCA and NOvA sensitivities, which come from this work and Ref. [4] respectively. Experiment start dates have been adjusted in line with the most recent annoucements: ORCA [1], INO [119], DUNE [120], and JUNO [54]. The PINGU Letter of Intent [50] does not contain a definitive start date, but does state that construction at the Antarctic site will take three seasons; an optimistic start year of 2022 has therefore been chosen. Experiment start dates are also subject to funding concerns and construction delays; they should be taken as estimates only. For PINGU and INO, the bands correspond to the θ_{23} range $40-50°$. For NOvA, the band also includes the full range of possible δ^{CP} values, and assumed planned beam intensitivity improvements [121] For DUNE, the band corresponds only to the δ^{CP} range $0-360°$ and a detector mass of 10 kton has been assumed. For JUNO, the band corresponds to energy resolutions of 3% and 3.5%.

In Fig. 6.1, the expected ORCA sensitivity in the NH case is shown compared to PINGU, INO, JUNO, NOvA, and DUNE. Sensitivities over time for upcoming experiments are based on the comparative study performed in Ref. [118]. In the case of NOvA, the NH is currently favoured over the IH with a significance of 1.8σ [4]. Whether ORCA or NOvA will be the first to reach 3σ is largely dependent on the true value of the CP phase; NOvA is very sensitive to the NMH if $\delta^{CP} \sim 270°$, as was presented in January of this year [46]. However, after the recent addition of antineutrino data, NOvA now favours a value closer to 0°, for which it is less sensitive to the NMH (see Section 1.7.5).

Regardless of which experiment reaches 3σ first, ORCA is well placed to offer a competitive measurement of the NMH using atmospheric neutrinos within a few years of data taking. By carrying out a variety of complementary, independent measurements, with different assumptions and systematic errors, the question of the NMH will be definitely resolved within the next decade.

6.2 Future Improvements

In this section, potential improvements to the analysis will be suggested, both in terms of its accuracy and in terms exploiting hitherto unused information which may improve the sensitivity further.

6.2.1 Systematic Errors

Flux Uncertainties

The atmospheric neutrino flux uncertainties are currently modelled as energy and angle independent skews applied to the ν_e/ν_μ and $\nu/\bar{\nu}$ ratios in the unoscillated flux, as well as a spectral tilt around $E_\nu = 6$ GeV. However, Ref. [114] presents a strong angular and energy dependence, with flux uncertainties typically smaller at low energies and closer to the horizon. A skew to the flux, currently implemented as

$$\Phi_\nu(E_\nu, \theta_\nu) \rightarrow (1 + \delta_\nu)\Phi_\nu(E_\nu, \theta_\nu), \tag{6.1}$$

could have the skew parameter δ_ν replaced by a function, reflecting the shape of the flux uncertainties, whose normalisation could still be constrained in the fit. Another option is to use the recently released MCEq package [122] for calculating atmospheric muon and neutrino fluxes, which also incorporates an error estimate.

Cross Section Uncertainties

At present, only the relative difference between the CC and NC cross sections and the absolute normalisation have been taken into account. However, the internal cross section parameterisation in GENIE allows for events to be reweighted according to the uncertainties in each constituent interaction model [123]. A study was carried out in the PINGU Letter of Intent, in which only a small impact on the NMH sensitivity was found [50]. Nevertheless, this is not a reason for complacency and an equivalent study should be carried out in ORCA.

One possibility for reducing the impact of cross section uncertainties is to measure both the downgoing (unoscillated) and upgoing (oscillated) neutrino flux, which is possible with a robust muon veto. A feasibility study [124] was carried out, in which the atmospheric muon contamination could be reduced to $\sim 1\%$ at the cost of a factor 2 reduction in effective mass. This has yet to be incorporated into neutrino oscillation analysis, however. Particular care would also need to be taken to account for any up/down asymmetry in the detector response.

Detector Response

The effect of detector ageing and environmental processes, such as sendimentation and biofouling, will require in situ measurements. Measurements were taken of light transmission in 17" glass spheres at the ANTARES site [125], in which light transmission deteriorated significantly on upward-facing parts of the sphere ($\theta < 20°$) - an area on which the KM3NeT DOM has no PMTs. Optical module efficiency measurements in ANTARES data also show a modest loss of 20%, after almost a decade of data taking [77]. Experience of ANTARES therefore indicates that some loss in efficiency is to be expected and the effect is likely to be more pronounced on upwards-facing PMTs, due to settling sendimentation.

In order to investigate these effects on the NMH and oscillation parameter measurements ahead of time, a Monte Carlo production should be prepared with reduced PMT efficiencies. An energy scale shift is expected, as was already included in this analysis, but more subtle shape effects may also be observed. This is of particular importance for the PID performance. The RDF's robustness against deviations from the training sample can be tested by first training it on an ideal detector and then applying it to the degraded one. However, once data acquisition is underway, PMT efficiencies can be continuously monitored, as was done for ANTARES and any degradation included in the simulations.

6.2.2 Detector Geometry

The results of an optimisation study into the vertical DOM spacing on the DU was presented in Ref. [1]. However, the horizontal DU separation has not yet been optimised. A denser detector geometry may improve the PID and reconstruction performances, giving a greater degree of granularity over length measurements of emerging muons, for example. A new Monte Carlo production is underway in which the average inter-DU distance has been reduced from 23 m to 20 m, which, although it will be completed too late for this thesis, will lead to further insight on this issue and potentially improved sensitivities.

6.2.3 Reconstruction and Particle Identification

At present, the only input from the hadronic cascade in the track reconstruction is in the energy correction. As a significant part of the light emission from a ν_μ-CC comes from the cascade and the PID algorithm currently can only identify emerging 5 GeV muons 50% of the time. It might therefore be useful to combine the track and cascade reconstructions, by starting with a cascade and then explicitly trying to find an emerging muon, for which a likelihood can be calculated. The light emission profiles of muon tracks, EM cascades, hadronic cascades are already well known, accepting the inevitable fluctuations in the latter case. The difficulty with a combined approach is that track reconstructions [103, 126] are designed to be reliant on minimising time residuals, whereas cascade reconstructions [86, 127] typically do not use time information to find the cascade energy or direction. The shape of the event is used instead for which the PMTs that were not hit provide crucial information. A combined algorithm would therefore have to use both.

In Section 3.7.2, it was shown that the PID performance is driven by the energy of the outgoing muon. Separation is close to perfect for $E_\mu > 8$ GeV, below which it starts to degrade. Preliminary studies are underway using Deep Learning, instead of an RDF, which show modest improvements [128].

6.2.4 Inelasticity

As alluded to in Section 1.2, the inelasticity distribution for detected neutrino and antineutrino events differs. This could allow for some statistical separation between neutrinos and antineutrinos. Recalling from Fig. 1.14, the matter enhancements to the oscillation probabilities are reversed for neutrinos and antineutrinos. It is only due to their different cross sections and abundances in the atmospheric neutrino flux that ORCA is still able to measure an overall asymmetry. Measuring an asymmetry between two 3D event distributions, in energy, zenith angle and inelasticity, may yield an improved sensitivity overall. See Ref. [129] for an in-depth discussion.

6.2.5 Sensitivity Calculation

This thesis has exclusively used the Asimov approach to calculate the median significance to reject the wrong NMH hypothesis, described in Section 5.3.2. In this section, it was also argued that the Asimov approach should be more conservative than the LLR method. In a preliminary version of the ORCA sensitivity study, presented at Neutrino 2018 [130], a more optimistic sensitivity was indeed found using the LLR method. It therefore stands to reason that the sensitivity will also improve once assessed with the LLR method again.

6.3 Conclusions and Outlook

Precise measurements of the neutrino mixing angles and masses require an ensemble of approaches, from solar neutrino measurements ($\theta_{12}, \Delta m^2_{12}$), reactor neutrino measurements (θ_{13}), and atmospheric and accelerator neutrino measurements ($\theta_{23}, \Delta m^2_{32}$). ORCA can contribute to our understanding of the neutrino sector by quickly resolving one of the remaining outstanding questions, the neutrino mass hierarchy, as well as providing competitive constraints on θ_{23} and Δm^2_{32}.

A more sophisticated treatment of flux and cross section uncertainties is foreseen in the near future. A better understanding of the detector response is expected as construction continues, but previous experience with ANTARES shows that only a small reduction in optical module efficiency is expected over a 10 year period. There also remains some potential to improve the ORCA performance by further optimising the horizontal DU spacing and by exploiting the inelasticity to achieve a statistical separation of neutrinos and antineutrinos. Modest improvements may also be achieved by improving the reconstruction and PID performance.

While there is always work left to do and improvements still to implement, the ORCA subgroup of the KM3NeT experiment is in a good position. The KM3NeT DU design has been successfully deployed and tested, and dedicated triggering and reconstruction algorithms tested on real data. It has been shown that the atmospheric muon background behaves as predicted, barring some fine tuning, and the first definitive neutrino measurement is expected later this year. Once the full 115 DU array has been deployed, ORCA is expected to be the first atmospheric neutrino experiment to measure the NMH with a significance of 3σ, complimenting long baseline measurements.

Preliminary studies are also underway to create an expanded particule physics experiment and astrophysics observatory on the Mediterranean seafloor. In order to start searching for CP violation, the option of sending a neutrino beam from Protvino, Russia to ORCA is being studied [113]. A low-intensity 90kW beam could confirm the atmospheric NMH measurement with a significance of 5σ within 5 years (or within a single year with a higher intensity 450kW beam) and start to probe for CP violation at the $> 2\sigma$ level within 15 years (3 years at 450kW). Denser ORCA configurations are also under consideration. A very preliminary, idealised study [131] has shown that a detector ten times denser than the standard ORCA geometry, a so-called Super ORCA, might measure the CP phase in atmospheric neutrinos at the 2σ level within 5 years. The prospect of combining a neutrino beam with a denser detector geometry is also being studied, using a similar, parameterised approach to the one used in this work (see Chapter 5) [132].

Neutrino physics is entering an exciting new era. Neutrino oscillations, and hence mass, still represent the first known departure from the standard model at time of writing. In order to construct a new theory of particle physics, it is necessary to gather information, to determine the relationship between neutrino flavour and mass and to establish whether or not the CP symmetry is violated in the lepton sector. It has been shown that ORCA will make a strong contribution to our understanding of neutrinos and that the answers to some of the unresolved questions in particle physics can be found at the bottom of the sea.

Bibliography

[1] S. Adrián-Martínez et al (The KM3NeT Collaboration). “Letter of Intent for KM3NeT 2.0”. In: *Journal of Physics G* 43.8 (June 2016). DOI: `10.1088/0954-3899/43/8/084001`.

[2] P. Amram et al (The ANTARES Collaboration). “The ANTARES Optical Module”. In: *Nuclear Instruments and Methods in Physics Research Section A: Accelerators, Spectrometers, Detectors and Associated Equipment* 484.1 (2002), pp. 369–383. DOI: `10.1016/S0168-9002(01)02026-5`.

[3] K. Hanson and O. Tarasova. “Design and production of the IceCube digital optical module”. In: *Nuclear Instruments and Methods in Physics Research Section A: Accelerators, Spectrometers, Detectors and Associated Equipment* 567.1 (2006). Proceedings of the 4th International Conference on New Developments in Photodetection, pp. 214–217.

[4] Mayly Sanchez, on behalf of the NOvA Collaboration. *NOvA Results and Prospects*. Talk at the XXVIII International Conference on Neutrino Physics and Astrophysics in Heidelberg, Germany. June 2018. DOI: `10.5281/zenodo.1286757`.

[5] Adam Aurisano, on behalf of the MINOS Collaboration. *Recent Results from MINOS and MINOS+*. Talk at the XXVIII International Conference on Neutrino Physics and Astrophysics in Heidelberg, Germany. June 2018. DOI: `10.5281/zenodo.1286759`.

[6] M. G. Aartsen et al (The IceCube Collaboration). “Measurement of Atmospheric Neutrino Oscillations at 6–56 GeV with IceCube DeepCore”. In: *Phys. Rev. Lett.* 120 (Feb. 2018), p. 071801. DOI: `10.1103/PhysRevLett.120.071801`.

[7] K. Abe et al (the Super Kamiokande Collaboration). “Atmospheric Neutrino Oscillation Analysis with External Constraints in Super-Kamiokande I-IV”. In: *Phys. Rev. D* 97 (Apr. 2018), p. 072001. DOI: `10.1103/PhysRevD.97.072001`.

[8] Morgan Wascko, on behalf of the T2K Collaboration. *T2K Status Results and Plans*. Talk at the XXVIII International Conference on Neutrino

Physics and Astrophysics in Heidelberg, Germany. June 2018. DOI: `10.5281/zenodo.1286751`.

[9] J. A. Formaggio and G. P. Zeller. "From eV to EeV: Neutrino cross sections across energy scales". In: *Rev. Mod. Phys.* 84 (3 Sept. 2012), pp. 1307–1341. DOI: `10.1103/RevModPhys.84.1307`.

[10] Kevin McFarland. *Neutrino Interactions.* Proceedings of the 61st Scottish Universities Summer School in Physics. arXiv:0804.3899. 2008.

[11] C. L. Cowan et al. "Detection of the Free Neutrino: a Confirmation". In: *Science* 124.3212 (1956), pp. 103–104. DOI: `10.1126/science.124.3212.103`.

[12] F. Reines et al. "Detection of the Free Antineutrino". In: *Phys. Rev.* 117 (Jan. 1960), pp. 159–173. DOI: `10.1103/PhysRev.117.159`.

[13] Raymond Davis. "A Review of the Homestake Solar Neutrino Experiment". In: *Progress in Particle and Nuclear Physics* 32 (1994), pp. 13–32. DOI: `10.1016/0146-6410(94)90004-3`.

[14] V. Gribov and B. Pontecorvo. "Neutrino Astronomy and Lepton Charge". In: *Physics Letters B* 28.7 (1969), pp. 493–496.

[15] Y. Fukuda et al (the Super-Kamiokande Collaboration). "Evidence for Oscillation of Atmospheric Neutrinos". In: *Phys. Rev. Lett.* 81 (Aug. 1998), pp. 1562–1567. DOI: `10.1103/PhysRevLett.81.1562`.

[16] K. Abe et al (the Super-Kamiokande Collaboration). "Evidence for the Appearance of Atmospheric Tau Neutrinos in Super-Kamiokande". In: *Phys. Rev. Lett.* 110 (May 2013), p. 181802. DOI: `10.1103/PhysRevLett.110.181802`.

[17] K. Abe et al (the Super-Kamiokande Collaboration). "Measurement of the tau neutrino cross section in atmospheric neutrino oscillations with Super-Kamiokande". In: *Phys. Rev. D* 98 (Sept. 2018), p. 052006. DOI: `10.1103/PhysRevD.98.052006`.

[18] J.Boger et al (the SNO Collaboration). "The Sudbury Neutrino Observatory". In: *Nuclear Instruments and Methods in Physics Research Section A: Accelerators, Spectrometers, Detectors and Associated Equipment* 449.1 (2000), pp. 172–207. DOI: `10.1016/S0168-9002(99)01469-2`.

[19] Q. R. Ahmad et al (the SNO Collaboration). "Direct Evidence for Neutrino Flavor Transformation from Neutral-Current Interactions in the Sudbury Neutrino Observatory". In: *Phys. Rev. Lett.* 89 (June 2002), p. 011301. DOI: `10.1103/PhysRevLett.89.011301`.

[20] K. Eguchi et al (the KamLAND Collaboration). "First Results from KamLAND: Evidence for Reactor Antineutrino Disappearance". In: *Phys. Rev. Lett.* 90 (Jan. 2003), p. 021802. DOI: `10.1103/PhysRevLett.90.021802`.

[21] K. A. Olive et al. “Review of Particle Physics”. In: *Chin. Phys.* C38 (2014), p. 090001. DOI: `10.1088/1674-1137/38/9/090001`.

[22] M. Honda et al. “Atmospheric neutrino flux calculation using the NRLMSISE-00 atmospheric model”. In: *Phys. Rev. D* 92 (2 July 2015), p. 023004. DOI: `10.1103/PhysRevD.92.023004`.

[23] K. A. Olive et al (Particle Data Group). “Review of Particle Physics”. In: *Chin. Phys.* C38 (2014), p. 090001. DOI: `10.1088/1674-1137/38/9/090001`.

[24] J. H. Christenson et al. “Evidence for the 2π Decay of the K_2^0 Meson”. In: *Phys. Rev. Lett.* 13 (July 1964), pp. 138–140. DOI: `10.1103/PhysRevLett.13.138`.

[25] A. Alavi-Harati et al (The KTeV Collaboration). “Observation of Direct CP Violation in $K_{S,L} \to \pi\pi$ Decays”. In: *Phys. Rev. Lett.* 83 (July 1999), pp. 22–27. DOI: `10.1103/PhysRevLett.83.22`.

[26] Martin Freund. “Analytic approximations for three neutrino oscillation parameters and probabilities in matter”. In: *Phys. Rev. D* 64 (July 2001), p. 053003. DOI: `10.1103/PhysRevD.64.053003`.

[27] Zhi-Zhong Xing and Shun Zhou. *Neutrinos in Particle Physics, Astronomy and Cosmology.* Springer and Zhejiang University Press, 2011.

[28] L. Wolfenstein. “Neutrino Oscillations in Matter”. In: *Phys. Rev. D* 17 (May 1978), pp. 2369–2374. DOI: `10.1103/PhysRevD.17.2369`.

[29] S. P. Mikheyev and A. Yu. Smirnov. “Resonant amplification of ν oscillations in matter and solar-neutrino spectroscopy”. In: *Il Nuovo Cimento C* 9.1 (Jan. 1986), pp. 17–26. DOI: `10.1007/BF02508049`.

[30] J. J. Sakurai. *Modern Quantum Mechanics.* Pearson, 1985.

[31] J.P. Yáñez and A. Kouchner. “Measurement of Atmospheric Neutrino Oscillations with Very Large Volume Neutrino Telescopes”. In: *Advances in High Energy Physics* 2015 (2015). DOI: `doi:10.1155/2015/271968`.

[32] Sandhya Choubey and Probir Roy. “Probing the deviation from maximal mixing of atmospheric neutrinos”. In: *Phys. Rev. D* 73 (1 Jan. 2006), p. 013006. DOI: `10.1103/PhysRevD.73.013006`.

[33] Adam M. Dziewonski and Don L. Anderson. “Preliminary reference Earth model”. In: *Physics of the Earth and Planetary Interiors* 25.4 (1981), pp. 297–356. DOI: `10.1016/0031-9201(81)90046-7`.

[34] João Coelho. *OscProb Neutrino Oscillation Calculator.* URL: `https://github.com/joaoabcoelho/OscProb`.

[35] Ivan Esteban et al. “Updated fit to three neutrino mixing: exploring the accelerator-reactor complementarity”. In: *Journal of High Energy Physics* 2017.1 (Jan. 2017), p. 87. DOI: `10.1007/JHEP01(2017)087`.

[36] V. N. Aseev et al. “Upper limit on the electron antineutrino mass from the Troitsk experiment”. In: *Phys. Rev. D* 84 (11 Dec. 2011), p. 112003. DOI: `10.1103/PhysRevD.84.112003`.

[37] Ch Kraus et al. “Final results from phase II of the Mainz neutrino mass searchin tritium β decay”. In: *The European Physical Journal C - Particles and Fields* 40.4 (Apr. 2005), pp. 447–468. DOI: `10.1140/epjc/s2005-02139-7`.

[38] G. Alimonti et al (The Borexino Collaboration). “The Borexino detector at the Laboratori Nazionali del Gran Sasso”. In: *Nuclear Instruments and Methods in Physics Research Section A: Accelerators, Spectrometers, Detectors and Associated Equipment* 600.3 (2009), pp. 568–593. DOI: `10.1016/j.nima.2008.11.076`.

[39] P. Anselmann et al (The GALLEX Collaboration). “Solar neutrinos observed by GALLEX at Gran Sasso”. In: *Physics Letters B* 285.4 (1992), pp. 376–389. DOI: `10.1016/0370-2693(92)91521-A`.

[40] M. Tanabashi et al (Particle Data Group). “Review of Particle Physics”. In: *Phys. Rev. D* 98 (Aug. 2018), p. 030001. DOI: `10.1103/PhysRevD.98.030001`.

[41] A. Yu. Smirnov. *The MSW Effect and Solar Neutrinos.* Invited talk given at the 11th workshop on Neutrino Telescopes. arXiv:hep-ph/0305106. 2003.

[42] Sacha E. Kopp. “Accelerator Neutrino Beams”. In: *Physics Reports* 439.3 (2007), pp. 101–159. DOI: `10.1016/j.physrep.2006.11.004`.

[43] Y. Abe et al (The Double Chooz Collaboration). “Measurement of θ_{13} in Double Chooz using neutron captures on hydrogen with novel background rejection techniques”. In: *Journal of High Energy Physics* 2016.1 (Jan. 2016), p. 163. DOI: `10.1007/JHEP01(2016)163`.

[44] F. P. An et al (The Daya Bay Collaboration). “Spectral Measurement of Electron Antineutrino Oscillation Amplitude and Frequency at Daya Bay”. In: *Phys. Rev. Lett.* 112 (Feb. 2014). DOI: `10.1103/PhysRevLett.112.061801`.

[45] J.K Ahn et al (The RENO Collaboration). “Observation of Reactor Electron Antineutrinos Disappearance in the RENO Experiment”. In: *Phys. Rev. Lett.* 108 (May 2012), p. 191802. DOI: `10.1103/PhysRevLett.108.191802`.

[46] M. A. Acero et al (The NOvA Collaboration). *New Constraints on Oscillation Parameters from ν_e Appearance and ν_μ Disappearance in the NOvA Experiment.* arXiv:1806.00096. 2018.

[47] P. Adamson et al (The MINOS Collaboration). “Electron Neutrino and Antineutrino Appearance in the Full MINOS Data Sample”. In: *Phys. Rev. Lett.* 110 (Apr. 2013), p. 171801. DOI: `10.1103/PhysRevLett.110.171801`.

[48] K. Abe et al (The T2K Collaboration). "Observation of Electron Neutrino Appearance in a Muon Neutrino Beam". In: *Phys. Rev. Lett.* 112 (Feb. 2014), p. 061802. DOI: `10.1103/PhysRevLett.112.061802`.

[49] P. Adamson et al (The NOvA Collaboration). "First Measurement of Electron Neutrino Appearance in NOvA". In: *Phys. Rev. Lett.* 116 (Apr. 2016), p. 151806. DOI: `10.1103/PhysRevLett.116.151806`.

[50] M.G. Aartsen et al (The IceCube PINGU Collaboration). *Letter of Intent: The Precision IceCube Next Generation Upgrade (PINGU).* arXiv:1401.2046v2. 2017.

[51] A. Kumar et al (the INO Collaboration). "Invited review: Physics potential of the ICAL detector at the India-based Neutrino Observatory (INO)". In: *Pramana* 88.5 (Apr. 2017), p. 79. DOI: `10.1007/s12043-017-1373-4`.

[52] Anushree Ghosh, Tarak Thakore, and Sandhya Choubey. "Determining the neutrino mass hierarchy with INO, T2K, NOvA and reactor experiments". In: *Journal of High Energy Physics* 2013.4 (Apr. 2013), p. 9. DOI: `10.1007/JHEP04(2013)009`.

[53] Fengpeng An et al (The JUNO Collaboration). "Neutrino physics with JUNO". In: *Journal of Physics G: Nuclear and Particle Physics* 43.3 (2016), p. 030401.

[54] Björn Wosnak, on behalf of the JUNO Collaboration. *Status and Prospects of the JUNO Experiment.* Talk at the XXVIII International Conference on Neutrino Physics and Astrophysics in Heidelberg, Germany. June 2018. DOI: `10.5281/zenodo.1286849`.

[55] R. Acciarri et al (The DUNE Collaboration). "Long-Baseline Neutrino Facility (LBNF) and Deep Underground Neutrino Experiment (DUNE) Conceptual Design Report Volume 2: The Physics Program for DUNE at LBNF". In: (2016). arXiv:1512.06148.

[56] Alexei Yu. Smirnov. Private Communication. 2018.

[57] M. C. Gonzalez-Garcia and Yosef Nir. *Neutrino masses and mixing: evidence and implications.* Mar. 2003. DOI: `10.1103/RevModPhys.75.345`.

[58] W. Buchmüller, R.D. Peccei, and T. Yanagida. "LEPTOGENESIS AS THE ORIGIN OF MATTER". In: *Annual Review of Nuclear and Particle Science* 55.1 (2005), pp. 311–355. DOI: `10.1146/annurev.nucl.55.090704.151558`.

[59] J.J. Gomez Cadenas et al. "The Search for Neutrinoless Double Beta Decay". In: *Riv. Nuovo Cim.* 35 (2012). DOI: `10.1393/ncr/i2012-10074-9`.

[60] Stefano Dell'Oro, Simone Marcocci, and Matteo Viel. "Neutrinoless Double Beta Decay: 2015 Review". In: *Advances in High Energy Physics* 2016 (2016). DOI: `10.1155/2016/2162659`.

[61] Stefano Dell'Oro, Simone Marcocci, and Francesco Vissani. "New Expectations and Uncertainties on Neutrinoless Double Beta Decay". In: *Phys. Rev. D* 90 (Aug. 2014), p. 033005. DOI: `10.1103/PhysRevD.90.033005`.

[62] Huaiyu Duan, George M. Fuller, and Yong-Zhong Qian. "Collective Neutrino Oscillations". In: *Annual Review of Nuclear and Particle Science* 60.1 (2010), pp. 569–594. DOI: `10.1146/annurev.nucl.012809.104524`.

[63] Basudeb Dasgupta et al. "Multiple Spectral Splits of Supernova Neutrinos". In: *Phys. Rev. Lett.* 103 (July 2009), p. 051105. DOI: `10.1103/PhysRevLett.103.051105`.

[64] Pasquale D. Serpico et al. "Probing the Neutrino Mass Hierarchy with the Rise Time of a Supernova Burst". In: *Phys. Rev. D* 85 (Apr. 2012), p. 085031. DOI: `10.1103/PhysRevD.85.085031`.

[65] Marta Colomer. Private Communication. 2018.

[66] P. Adamson et al (The MINOS Collaboration). "Combined Analysis of ν_μ Disappearance and $\nu_\mu \to \nu_e$ Appearance in MINOS Using Accelerator and Atmospheric Neutrinos". In: *Phys. Rev. Lett.* 112 (May 2014), p. 191801. DOI: `10.1103/PhysRevLett.112.191801`.

[67] G. Riccobene et al (The NEMO Collaboration). "Deep seawater inherent optical properties in the Southern Ionian Sea". In: *Astroparticle Physics* 27.1 (2007), pp. 1–9.

[68] P. A. Čerenkov. "Visible Radiation Produced by Electrons Moving in a Medium with Velocities Exceeding that of Light". In: *Phys. Rev.* 52 (4 Aug. 1937), pp. 378–379. DOI: `10.1103/PhysRev.52.378`.

[69] Raymond C. Smith and Karen S. Baker. "Optical properties of the clearest natural waters (200–800 nm)". In: *Appl. Opt.* 20.2 (Jan. 1981), pp. 177–184. DOI: `10.1364/AO.20.000177`.

[70] Maarten de Jong. *The Probability Density Function of the Arrival Time of Light*. KM3NeT Internal Note. 2012.

[71] S. Klimushin, E. Bugaev, and I. Sokalski. *Precise Parametrizations of Muon Energy Losses in Water*. Proceedings of ICRC 2001.

[72] Claudio Kopper. "Performance Studies for the KM3NeT Neutrino Telescope". PhD thesis. University of Erlangen Nürnberg, 2010.

[73] R. Mirani. "Parametrisation of EM-showers in the ANTARES Detector-Volume". PhD thesis. University of Amsterdam, 2002.

[74] Apostolos Tsirigotis. *Detector Simulations for KM3NeT*. KM3NeT Internal Note. 2014.

[75] Diego Real, David Calvo, and on behalf of the KM3NeT Collaboration. "Nanobeacon and Laser Beacon: KM3NeT Time Calibration Devices". In: *PoS* TIPP2014 (2015), p. 365.

[76] S. Adrián-Martínez et al (The KM3NeT Collaboration). “Deep Sea Tests of a Prototype of the KM3NeT Digital Optical Module”. In: *The European Physical Journal C* 74.9 (Sept. 2014), p. 3056. DOI: `10.1140/epjc/s10052-014-3056-3`.

[77] A. Albert et al (The ANTARES Collaboration). *Long-Term Monitoring of the ANTARES Optical Module Efficiencies Using* ^{40}K *Decays in Water.* arXiv:1805.08675c1. 2018.

[78] M. Ageron et al (The ANTARES Collaboration). “ANTARES: The first Undersea Neutrino Telescope”. In: *Nuclear Instruments and Methods in Physics Research Section A: Accelerators, Spectrometers, Detectors and Associated Equipment* 656.1 (2011), pp. 11–38. DOI: `10.1016/j.nima.2011.06.103`.

[79] C. Andreopoulos et al. “The GENIE Neutrino Monte Carlo Generator”. In: *Nuclear Instruments and Methods in Physics Research Section A: Accelerators, Spectrometers, Detectors and Associated Equipment* 614.1 (2010), pp. 87–104. DOI: `10.1016/j.nima.2009.12.009`.

[80] Carla Distefano. “gSeaGen: A GENIE-Based Code for Neutrino Telescopes”. In: *EPJ Web of Conferences* 116 (2016), p. 08001. DOI: `10.1051/epjconf/201611608001`.

[81] G. Carminati et al. “Atmospheric MUons from PArametric formulas: a fast GEnerator for neutrino telescopes (MUPAGE)”. In: *Computer Physics Communications* 179.12 (2008), pp. 915–923. DOI: `10.1016/j.cpc.2008.07.014`.

[82] G. Battistoni, C. Forti, and J. Ranft. “Study of the High Energy Cosmic Ray Cascades Using the Dual Parton Model”. In: *Astroparticle Physics* 3.2 (1995), pp. 157–184. DOI: `10.1016/0927-6505(94)00039-6`.

[83] J.A. Aguilar et al. (The ANTARES Collaboration). “Zenith Distribution and Flux of Atmospheric Muons Measured with the 5-Line ANTARES Detector”. In: *Astroparticle Physics* 34.3 (2010), pp. 179–184. DOI: `10.1016/j.astropartphys.2010.07.001`.

[84] A.G. Tsirigotis, A. Leisos, and S.E. Tzamarias. “HOU Reconstruction and Simulation (HOURS): A Complete Simulation and Reconstruction Package for Very Large Volume Underwater Neutrino Telescopes”. In: *Nuclear Instruments and Methods in Physics Research Section A: Accelerators, Spectrometers, Detectors and Associated Equipment* 626-627 (2011), S185–S187. DOI: `10.1016/j.nima.2010.06.258`.

[85] David Bailey. “Monte Carlo Tools and Analysis Methods for Understanding the ANTARES Experiment and Predicting its Sensitivity to Dark Matter”. PhD thesis. Oxford University, 2002.

[86] Jannik Hofestädt. “Measuring the Neutrino Mass Hierarchy with the Future KM3NeT/ORCA Detector”. PhD thesis. University of Erlangen Nürnberg, 2017.

[87] Martijn Jongen. “Neutrino Studies in the Mediterranean Sea”. PhD thesis. University of Amsterdam, 2018.

[88] Marco Taoso, Gianfranco Bertone, and Antonio Masiero. “Dark Matter Candidates: A Ten-Point Test”. In: *Journal of Cosmology and Astroparticle Physics* 2008.03 (2008), p. 022.

[89] S. Adrián-Martínez et al (the ANTARES Collaboration). “Limits on Dark Matter Annihilation in the Sun Using the ANTARES Neutrino Telescope”. In: *Physics Letters B* 759 (2016), pp. 69–74. DOI: `10.1016/j.physletb.2016.05.019`.

[90] M.G Aartsen et al (the IceCube Collaboration). “Search for Annihilating Dark Matter in the Sun with 3 Years of IceCube Data”. In: *The European Physical Journal C* 77.3 (Mar. 2017), p. 146. DOI: `10.1140/epjc/s10052-017-4689-9`.

[91] A. Albert et al (the ANTARES Collaboration). “Search for Dark Matter Annihilation in the Earth Using the ANTARES Neutrino Telescope”. In: *Physics of the Dark Universe* 16 (2017). DOI: `10.1016/j.dark.2017.04.005`.

[92] M. G. Aartsen et al (the IceCube Collaboration). “First Search For Dark Matter Annihilations in the Earth with the IceCube Detector”. In: *The European Physical Journal C* 77.2 (Feb. 2017), p. 82. DOI: `10.1140/epjc/s10052-016-4582-y`.

[93] M. G. Aartsen et al (the IceCube Collaboration). “Search For Neutrinos From Dark Matter Self-Annihilations in the Center of the Milky Way with 3 Years of IceCube/DeepCore”. In: *The European Physical Journal C* 77.9 (Sept. 2017), p. 627. DOI: `10.1140/epjc/s10052-017-5213-y`.

[94] S. Adrián-Martinez et al (the ANTARES collaboration). “Search of Dark Matter Annihilation in the Galactic Centre Using the ANTARES Neutrino Telescope”. In: *Journal of Cosmology and Astroparticle Physics* 2015.10 (2015), p. 068.

[95] M.G. Aartsen et al (the IceCube Collaboration). “Search for Dark Matter Annihilation in the Galactic Center with IceCube-79”. In: *The European Physical Journal C* 75.10 (Oct. 2015), p. 492. DOI: `10.1140/epjc/s10052-015-3713-1`.

[96] M.G. Aartsen et al (the IceCube Collaboration). “IceCube search for dark matter annihilation in nearby galaxies and galaxy clusters”. In: *Phys. Rev. D* 88 (Dec. 2013), p. 122001. DOI: `10.1103/PhysRevD.88.122001`.

[97] Damien Dornic et al, on behalf of the KM3NeT Collaboration). *Detailed KM3NeT Optical Module Simulation with Geant4 and Supernova Neutrino Detection Study.* Proceedings of ICRC 2017. 2017. DOI: `10.22323/1.301.0983`.

[98] J. Becker Tjus. *Neutrinos from Colliding Wind Binaries: Future Prospects for PINGU and ORCA.* Conference Proceedings in Wind Bubbles, Astrospheres and the Heliosphere: Environments and Cosmic Rays, Bochum, Germany. arXiv:1405.0471. 2014.

[99] Katsuaki Asano and Kohta Murase. “Gamma-Ray Bursts as Multienergy Neutrino Sources”. In: *Advances in Astronomy* 2015 (2015). DOI: `10.1155/2015/568516`.

[100] C. Rott, A. Taketa, and D. Bose. “Spectrometry of the Earth using Neutrino Oscillations”. In: *Scientific Reports* 5 (2015). DOI: `10.1038/srep15225`.

[101] Maarten de Jong. *Partial Linearisation of the Track Fit Problem.* KM3NeT Internal Note. 2007.

[102] J. A. Nelder and R. Mead. “A Simplex Method for Function Minimization”. In: *The Computer Journal* 7.4 (1965), pp. 308–313. DOI: `10.1093/comjnl/7.4.308`.

[103] Aart Heijboer. “Track Reconstruction and Point Searches with ANTARES”. PhD thesis. University of Amsterdam, 2004.

[104] Donald W. Marquardt. “An Algorithm for Least-Squares Estimation of Nonlinear Parameters”. In: *Journal of the Society for Industrial and Applied Mathematics* 11.2 (1963).

[105] S. Adrián-Martínez et al (KM3NeT Collaboration). “Intrinsic Limits on Resolutions in Muon and Electron-Neutrino Charged-Current Events in the KM3NeT/ORCA detector”. In: *Journal of High Energy Physics* 2017.5 (May 2017), p. 8. DOI: `10.1007/JHEP05(2017)008`.

[106] Leo Breiman. “Random Forests”. In: *Machine Learning* 45.1 (2001). DOI: `10.1023/A:1010933404324`.

[107] Simon Bourret. Private Communication. 2018.

[108] Francesco Capozzi, Eligio Lisi, and Antonio Marrone. “Probing the Neutrino Mass Ordering with KM3NeT-ORCA: Analysis and Perspectives”. In: *Journal of Physics G: Nuclear and Particle Physics* 45.2 (2018).

[109] Glen Cowan et al. “Asymptotic Formulae for Likelihood-Based Tests of New Physics”. In: *The European Physical Journal C* 71.2 (Feb. 2011), p. 1554. DOI: `10.1140/epjc/s10052-011-1554-0`.

[110] S.S. Wilks. “The Large-Sample Distribution of the Likelihood Ratio for Testing Composite Hypotheses”. In: *Ann. Math. Statist.* 9 (1938).

[111] A. Wald". "Tests of Satistical Hypotheses Concerning Several Parameters When the Number of Observations is Large". In: *Transactions of the American Mathematical Society* 54 (1943).

[112] F. James. "MINUIT Function Minimization and Error Analysis: Reference Manual Version 94.1". In: (1994).

[113] Dmitry Zaborov, on behalf of the KM3NeT Collaboration. *The KM3NeT Neutrino Telescope and the Potential of a Neutrino Beam from Russia to the Mediterranean Sea*. Proceedings of the 18th Lomonosov Conference on Elementary Particle Physics. arXiv:1803.08017. 2017.

[114] G. D. Barr et al. "Uncertainties in Atmospheric Neutrino Fluxes". In: *Phys. Rev. D* 74 (9 Nov. 2006), p. 094009. DOI: `10.1103/PhysRevD.74.094009`.

[115] T. Kajita, E. Kearns, and
M. Shiozawa (The Super Kamiokande Collaboration). "Establishing atmospheric neutrino oscillations with Super-Kamiokande". In: *Nuclear Physics B* 908 (2016). Neutrino Oscillations: Celebrating the Nobel Prize in Physics 2015, pp. 14–29. DOI: `10.1016/j.nuclphysb.2016.04.017`.

[116] K. Abe et al (The T2K Collaboration). "Measurements of neutrino oscillation in appearance and disappearance channels by the T2K experiment with 6.6×10^{20} protons on target". In: *Phys. Rev. D* 91 (Apr. 2015), p. 072010. DOI: `10.1103/PhysRevD.91.072010`.

[117] P. Adamson et al (The NOvA Collaboration). "Measurement of the Neutrino Mixing Angle θ_{23} in NOvA". In: *Phys. Rev. Lett.* 118 (Apr. 2017), p. 151802. DOI: `10.1103/PhysRevLett.118.151802`.

[118] Mattias Blennow et al. "Quantifying the Sensitivity of Oscillation Experiments to the Neutrino Mass Ordering". In: *Journal of High Energy Physics* 2014.3 (Mar. 2014), p. 28. DOI: `10.1007/JHEP03(2014)028`.

[119] Tarak Thakore. Private Communication. 2018.

[120] Elizabeth Worcestershire, on behalf of the DUNE Collaboration. *DUNE: Status and Science*. Talk at the XXVIII International Conference on Neutrino Physics and Astrophysics in Heidelberg, Germany. June 2018. DOI: `10.5281/zenodo.1286759`.

[121] Ashley Back and Liudmila Kolupaeva, on behalf of the NOvA Collaboration. *NOvA Joint $\nu_e + \nu_\mu$ Oscillation Results in Neutrino and Antineutrino Modes*. Poster at the XXVIII International Conference on Neutrino Physics and Astrophysics in Heidelberg, Germany. June 2018. DOI: `10.5281/zenodo.1300928`.

[122] Anatoli Fedynitch et al. *Calculation of Conventional and Prompt Lepton Fluxes at Very High Energy*. Proceedings of the International Symposium for Very-High Energy Cosmic-Ray Interactions. arXiv:1503.00544. 2015. URL: `https://github.com/afedynitch/MCEq`.

[123] Costas Andreopoulos et al. *The GENIE Neutrino Monte Carlo Generator: Physics and User Manual.* arXiv:1510.05494. 2015.

[124] Marco Volkert. *A Muon Veto for the Measurement of the Downgoing Neutrino Flux with KM3NeT/ORCA.* Masters Thesis. 2017.

[125] P. Amram et al (The ANTARES Collaboration). "Sedimentation and fouling of optical surfaces at the ANTARES site". In: *Astroparticle Physics* 19.2 (2003), pp. 253–267. DOI: `10.1016/S0927-6505(02)00202-5`.

[126] J.A. Aguilar et al (the ANTARES Collaboration). "A Fast Algorithm for Muon Track Reconstruction and its Application to the ANTARES Neutrino Telescope". In: *Astroparticle Physics* 34.9 (2011), pp. 652–662. DOI: `10.1016/j.astropartphys.2011.01.003`.

[127] A. Albert et al (the ANTARES Collaboration). "An Algorithm for the Reconstruction of Neutrino-induced Showers in the ANTARES Neutrino Telescope". In: *The Astronomical Journal* 154.6 (2017), p. 275.

[128] Thomas Eberl et al, on behalf of the KM3NeT Collaboration. *Tau Neutrino Appearance with KM3NeT / ORCA.* Poster at the XXVIII International Conference on Neutrino Physics and Astrophysics in Heidelberg, Germany. June 2018. DOI: `10.5281/zenodo.1292823`.

[129] Mathieu Ribordy and A. Yu. Smirnov. "Improving the Neutrino Mass Hierarchy Identification with Inelasticity Measurement in PINGU and ORCA". In: *Phys. Rev. D* 87 (June 2013), p. 113007. DOI: `10.1103/PhysRevD.87.113007`.

[130] Simon Bourret and Liam Quinn, on behalf of the KM3NeT Collaboration. *Sensitivity of ORCA to the Neutrino Mass Ordering and Oscillation Parameters.* Poster at the XXVIII International Conference on Neutrino Physics and Astrophysics in Heidelberg, Germany. June 2018. DOI: `10.5281/zenodo.1300771`.

[131] Jannik Hofestädt et al, on behalf of the KM3NeT Collaboration. *KM3NeT/Super-ORCA: Measuring the Leptonic CP Phase with Atmospheric Neutrinos: A Feasibility Study.* Poster at the XXVIII International Conference on Neutrino Physics and Astrophysics in Heidelberg, Germany. June 2018. DOI: `10.5281/zenodo.1292936`.

[132] Jürgen Brunner and Dmitry Zaborov. Private Communication. 2018.

Appendix A

A.1 Detector Resolution Parameterisations

$\bar{\nu}_e$-CC classified as cascades

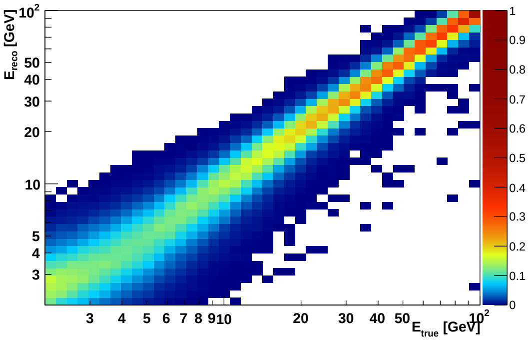

$\bar{\nu}_e$-CC, classified as cascades

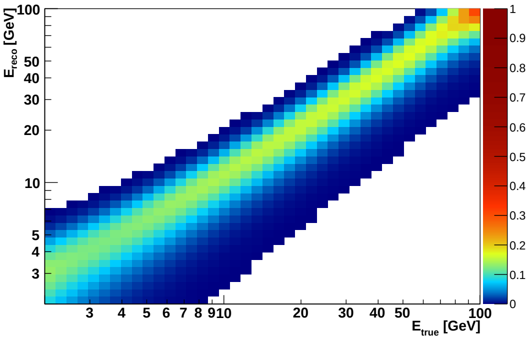

$\bar{\nu}_\mu$-CC classified as cascades

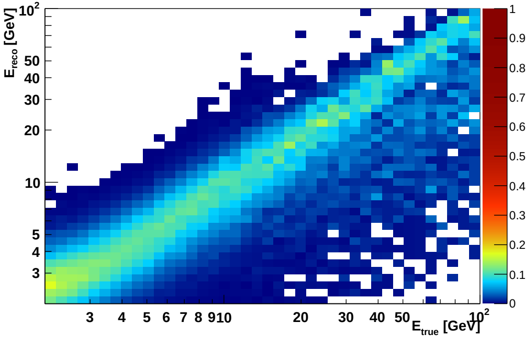

$\bar{\nu}_\mu$-CC, classified as cascades

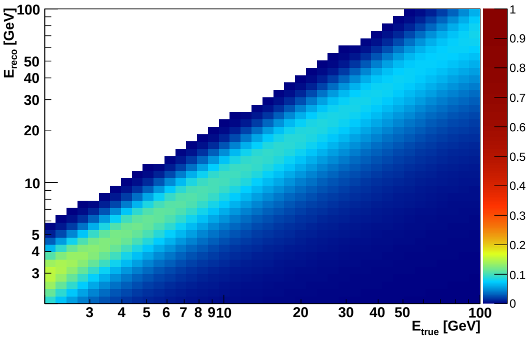

$\bar{\nu}_\tau$-CC classified as cascades

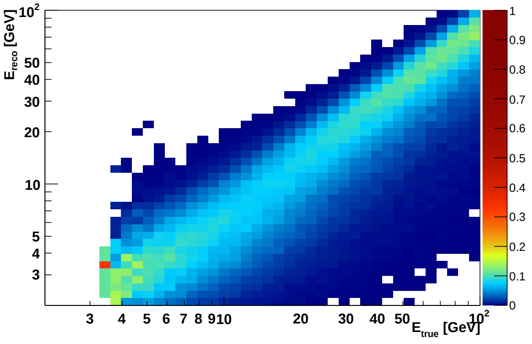

$\bar{\nu}_\tau$-CC, classified as cascades

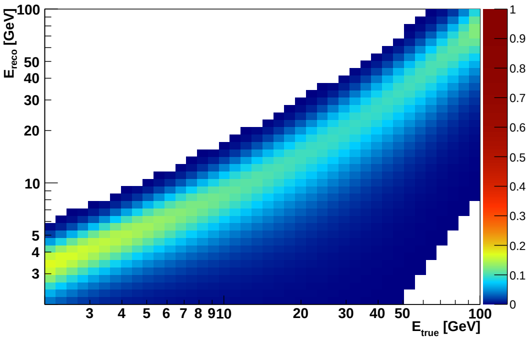

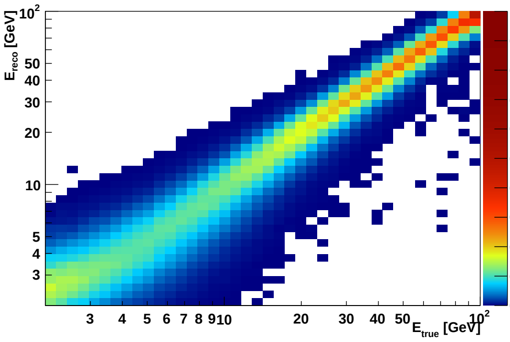

ν_e-CC classified as cascades

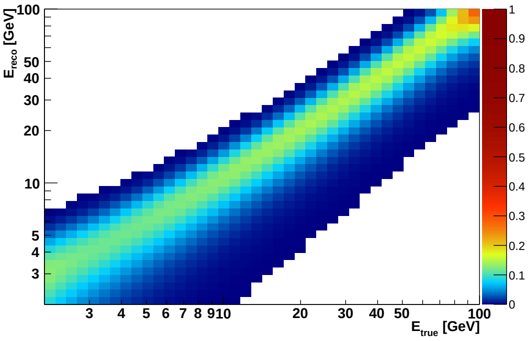

ν_e-CC, classified as cascades

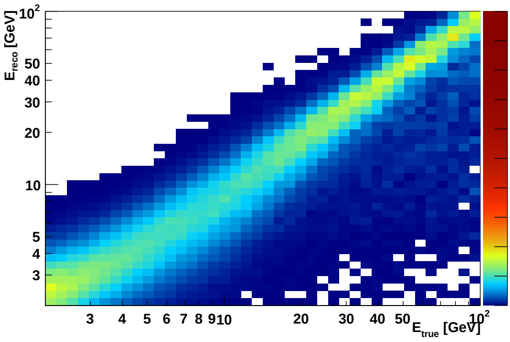

ν_μ-CC classified as cascades

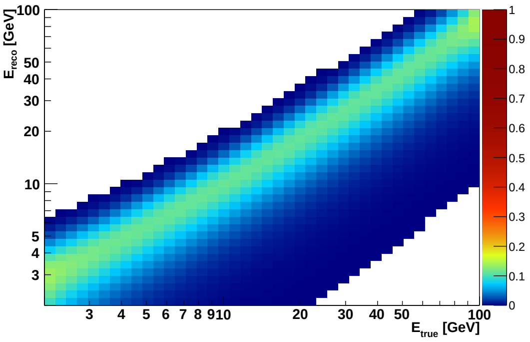

ν_μ-CC, classified as cascades

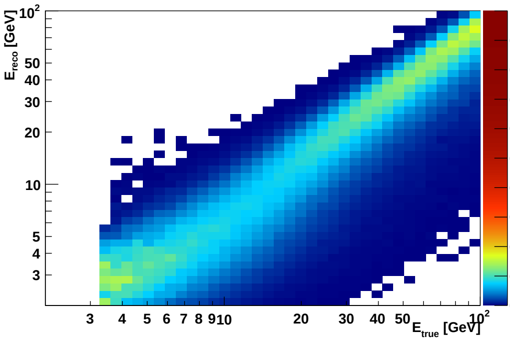

ν_τ-CC classified as cascades

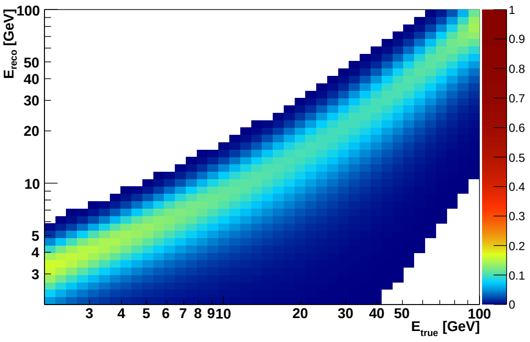

ν_τ-CC, classified as cascades

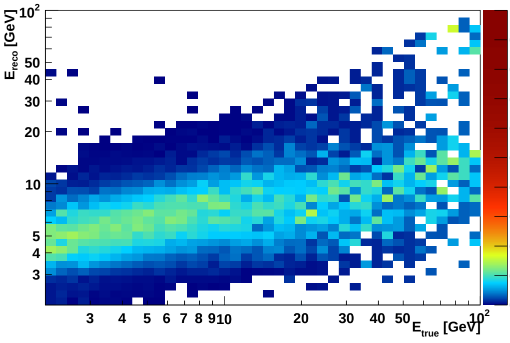

$\overline{\nu}_e$-CC classified as tracks

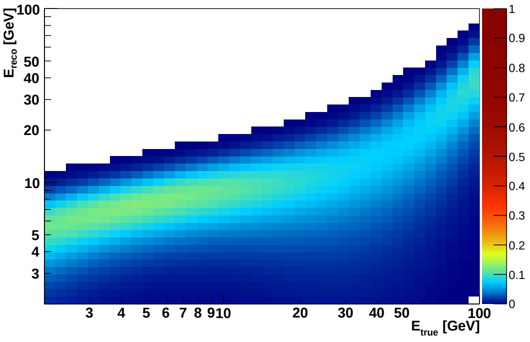

$\overline{\nu}_e$-CC, classified as tracks

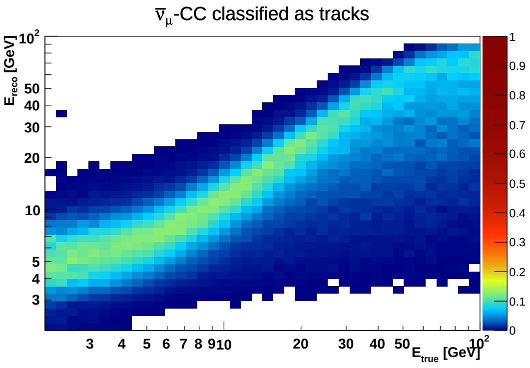

$\bar{\nu}_\mu$-CC classified as tracks

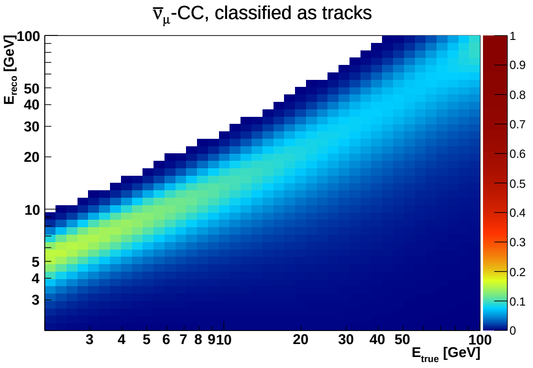

$\bar{\nu}_\mu$-CC, classified as tracks

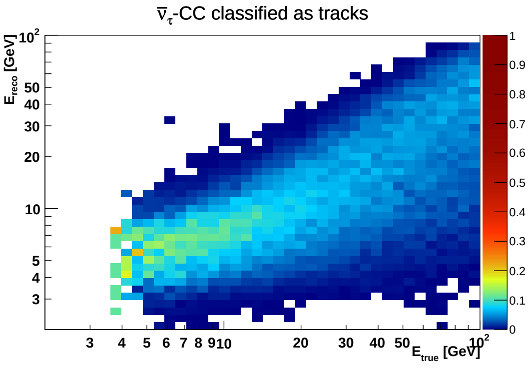

$\bar{\nu}_\tau$-CC classified as tracks

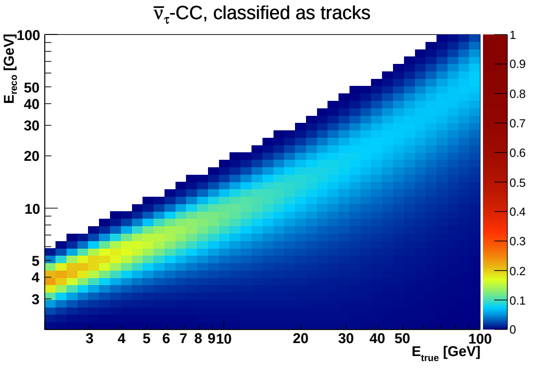

$\bar{\nu}_\tau$-CC, classified as tracks

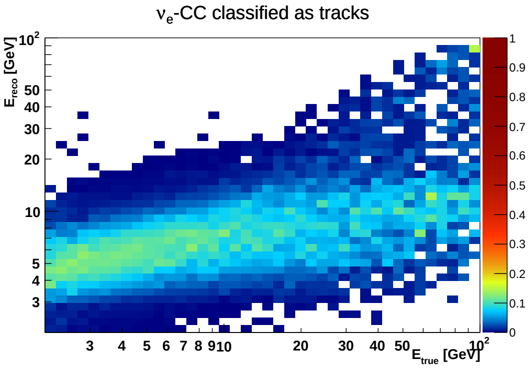

ν_e-CC classified as tracks

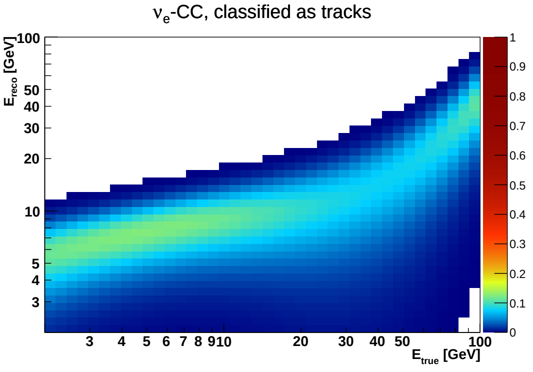

ν_e-CC, classified as tracks

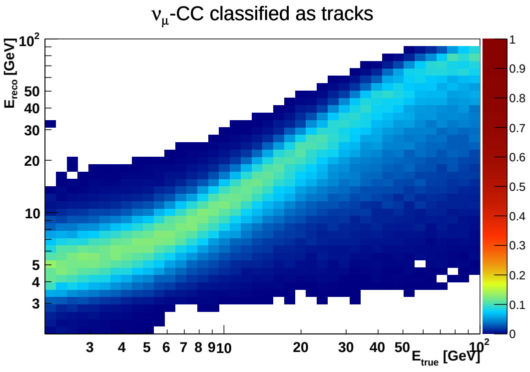

ν_μ-CC classified as tracks

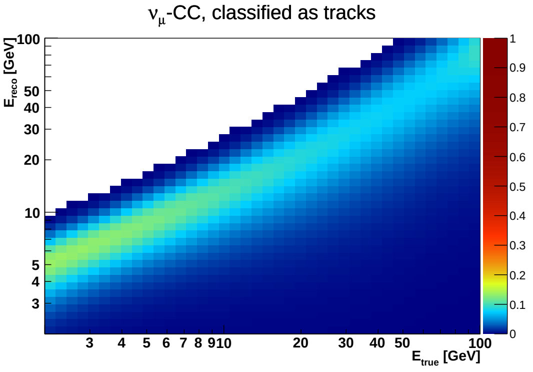

ν_μ-CC, classified as tracks

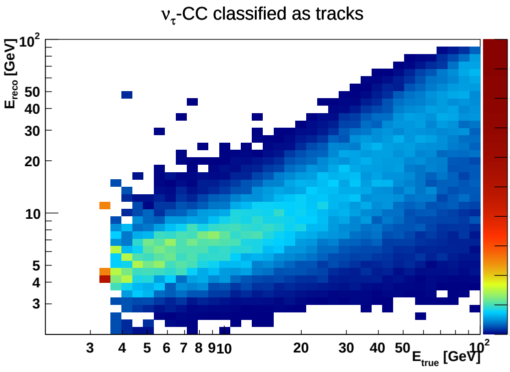
ν_τ-CC classified as tracks

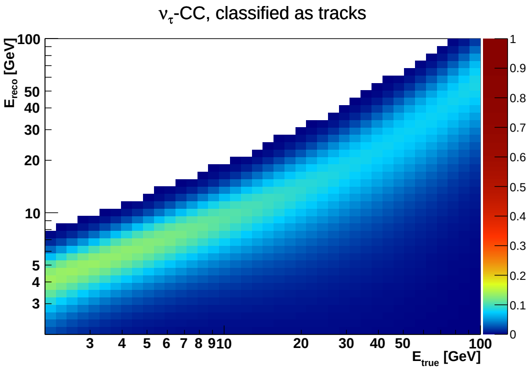
ν_τ-CC, classified as tracks

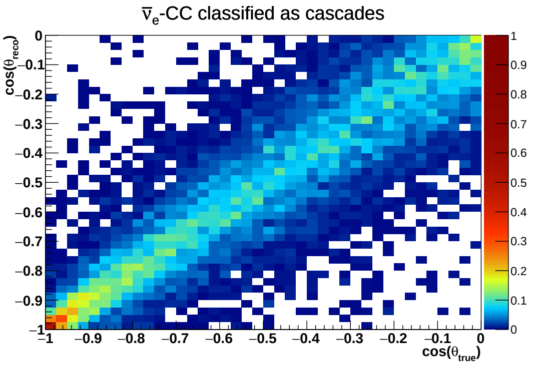
$\overline{\nu}_e$-CC classified as cascades

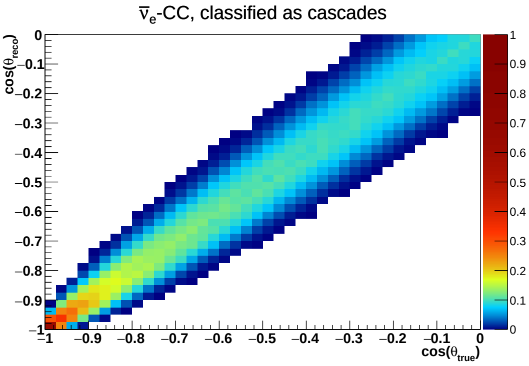
$\overline{\nu}_e$-CC, classified as cascades

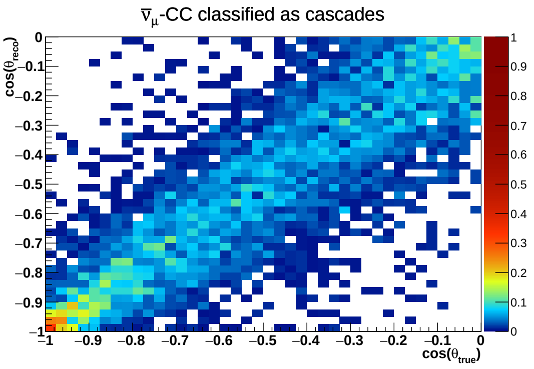
$\overline{\nu}_\mu$-CC classified as cascades

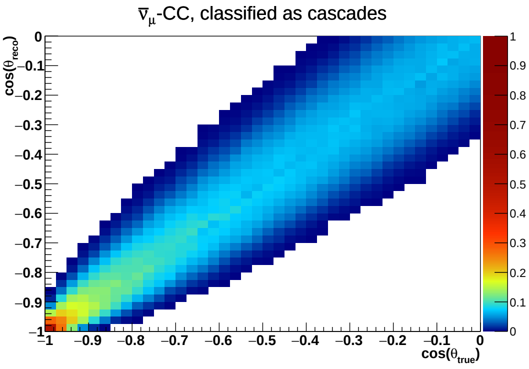
$\overline{\nu}_\mu$-CC, classified as cascades

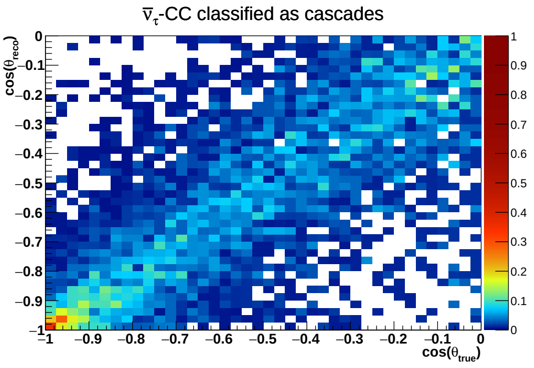
$\overline{\nu}_\tau$-CC classified as cascades

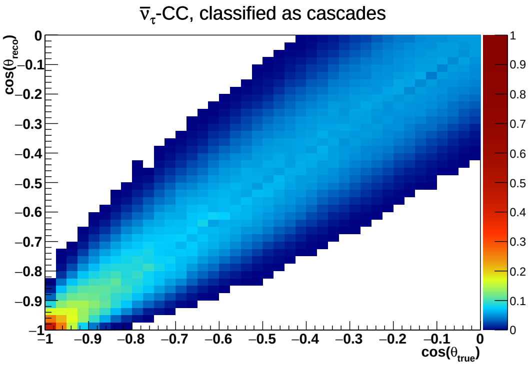
$\overline{\nu}_\tau$-CC, classified as cascades

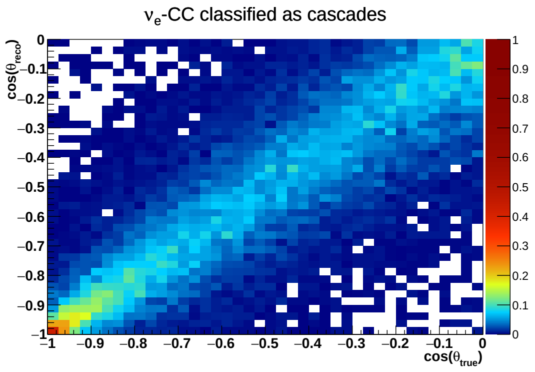
ν_e-CC classified as cascades

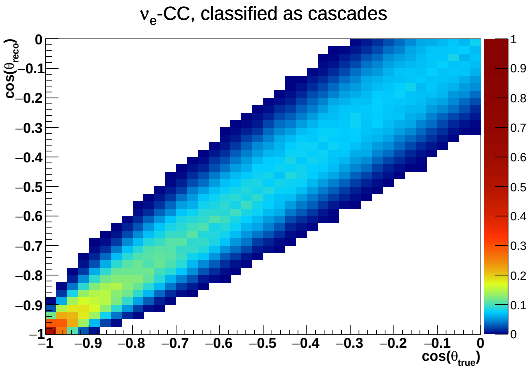
ν_e-CC, classified as cascades

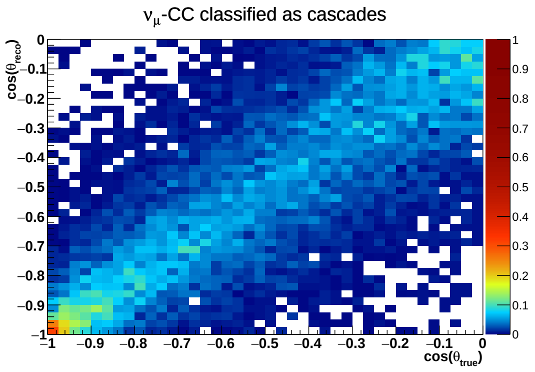
ν_μ-CC classified as cascades

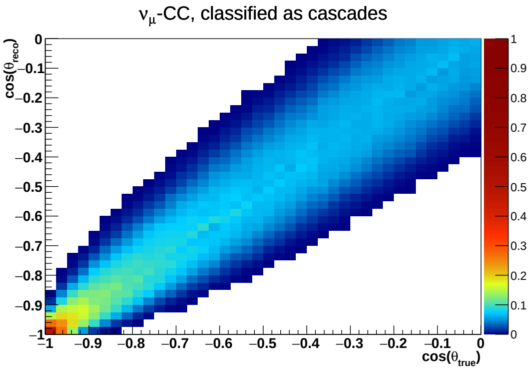
ν_μ-CC, classified as cascades

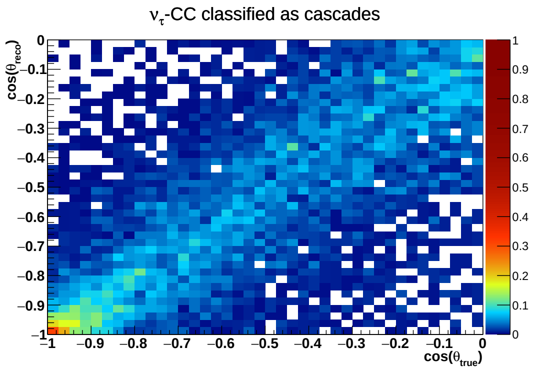
ν_τ-CC classified as cascades

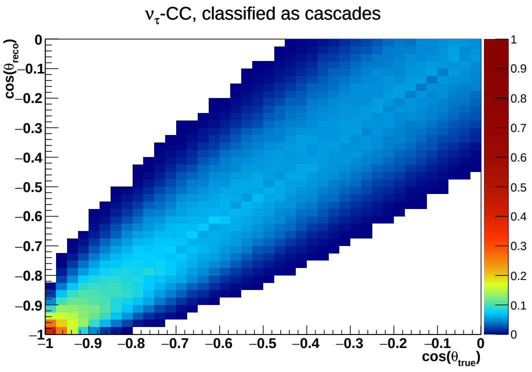
ν_τ-CC, classified as cascades

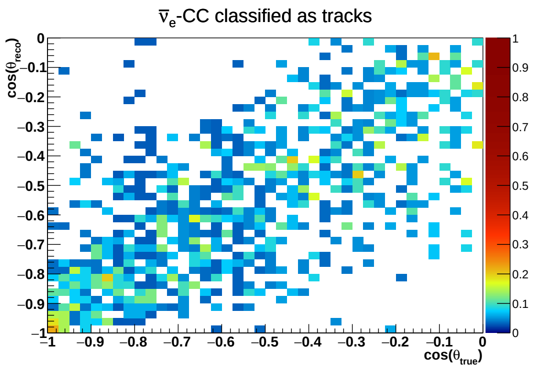
$\overline{\nu}_e$-CC classified as tracks

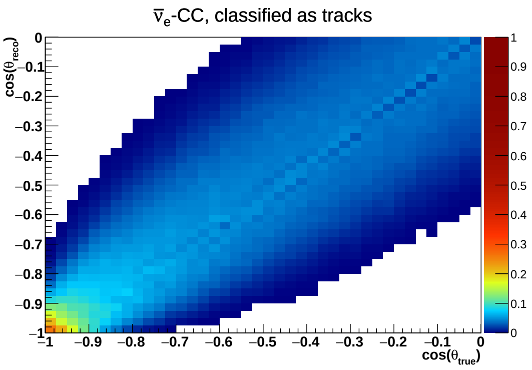
$\overline{\nu}_e$-CC, classified as tracks

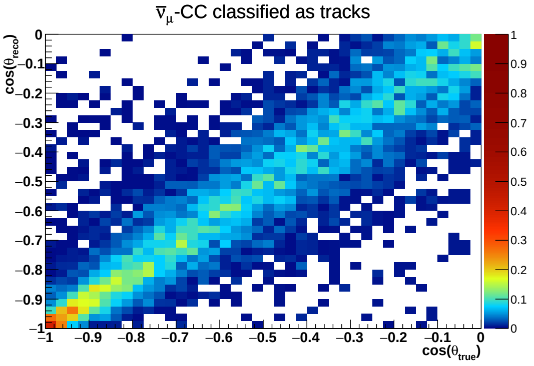
$\bar{\nu}_\mu$-CC classified as tracks

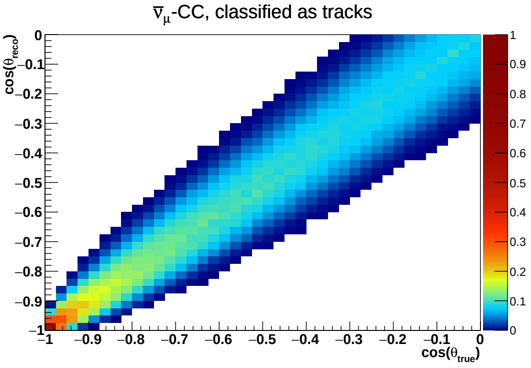
$\bar{\nu}_\mu$-CC, classified as tracks

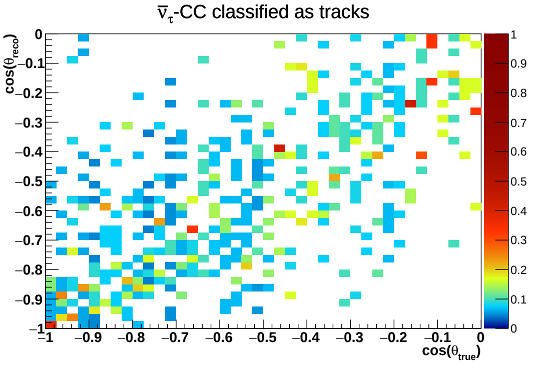
$\bar{\nu}_\tau$-CC classified as tracks

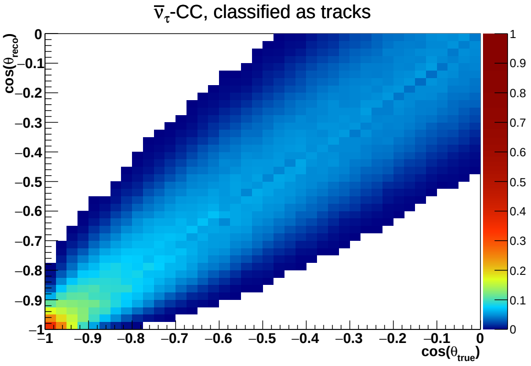
$\bar{\nu}_\tau$-CC, classified as tracks

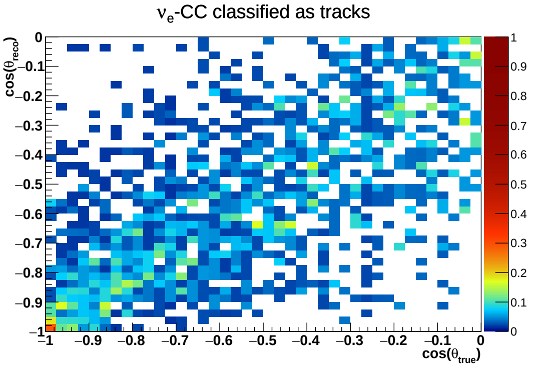
ν_e-CC classified as tracks

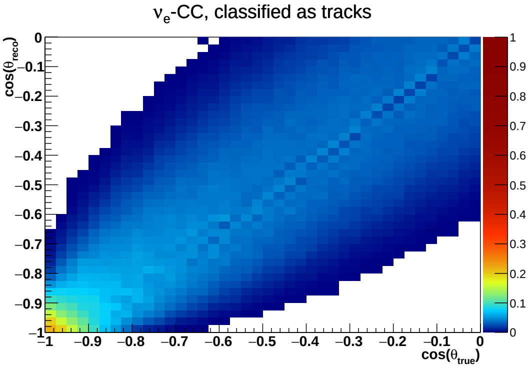
ν_e-CC, classified as tracks

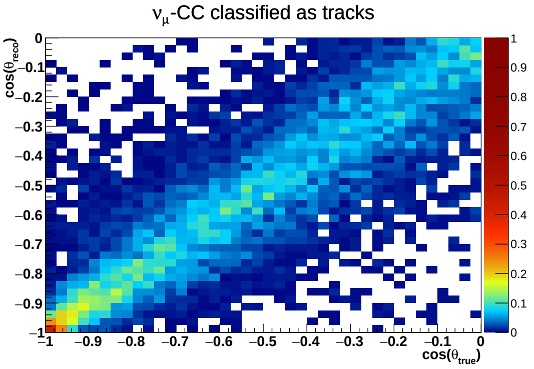
ν_μ-CC classified as tracks

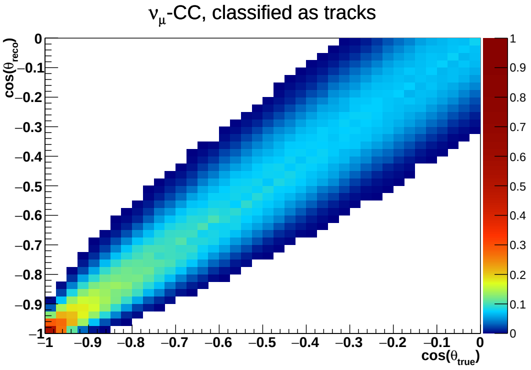
ν_μ-CC, classified as tracks

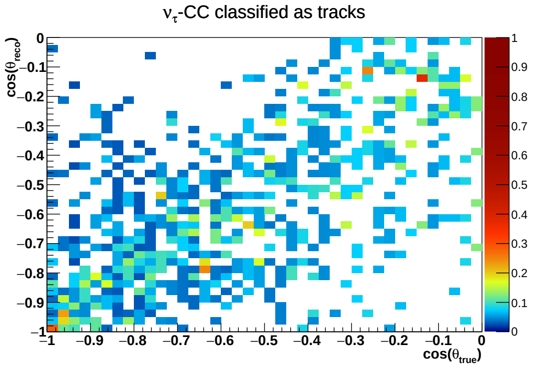
ν_τ-CC classified as tracks
cos(θ_{reco})
0
−0.1
−0.2
−0.3
−0.4
−0.5
−0.6
−0.7
−0.8
−0.9
−1
−0.9
−0.8
−0.7
−0.6
−0.5
−0.4
−0.3
−0.2
−0.1
0
cos(θ_{true})
1
0.9
0.8
0.7
0.6
0.5
0.4
0.3
0.2
0.1
0

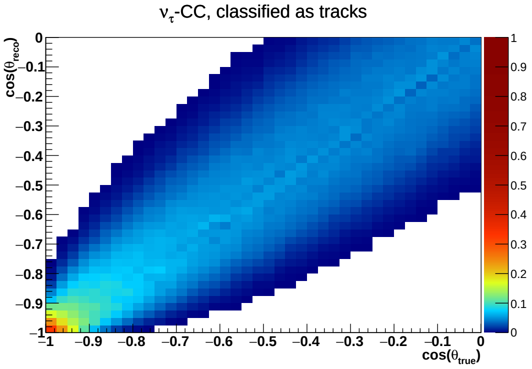
ν_τ-CC, classified as tracks
cos(θ_{reco})
0
−0.1
−0.2
−0.3
−0.4
−0.5
−0.6
−0.7
−0.8
−0.9
−1
−0.9
−0.8
−0.7
−0.6
−0.5
−0.4
−0.3
−0.2
−0.1
0
cos(θ_{true})
1
0.9
0.8
0.7
0.6
0.5
0.4
0.3
0.2
0.1
0

A.2 PREM Model

Radial Distance from Centre [km]	Density [g/km^3]	Z/A	Layer
200.0	13.088	0.4691	Inner Core
400.0	13.080	0.4691	
600.0	13.054	0.4691	
800.0	13.010	0.4691	
1000.0	12.949	0.4691	
1200.0	12.871	0.4691	
1221.5	12.775	0.4691	
1400.0	12.166	0.4691	Outer Core
1600.0	12.069	0.4691	
1800.0	11.947	0.4691	
2000.0	11.809	0.4691	
2200.0	11.655	0.4691	
2400.0	11.483	0.4691	
2600.0	11.293	0.4691	
2800.0	11.083	0.4691	
3000.0	10.853	0.4691	
3200.0	10.602	0.4691	
3400.0	10.327	0.4691	
3480.0	10.029	0.4691	
3600.0	5.566	0.4954	Mantle
3630.0	5.506	0.4954	
3800.0	5.491	0.4954	
4000.0	5.407	0.4954	
4200.0	5.307	0.4954	
4400.0	5.207	0.4954	
4600.0	5.106	0.4954	
4800.0	5.003	0.4954	
5000.0	4.898	0.4954	
5200.0	4.790	0.4954	
5400.0	4.678	0.4954	
5600.0	4.563	0.4954	
5701.0	4.443	0.4954	
5771.0	3.992	0.4954	Crust, Sea & Atmosphere
5871.0	3.976	0.4954	
5971.0	3.850	0.4954	
6061.0	3.543	0.4954	
6151.0	3.490	0.4954	
6221.0	3.360	0.4954	
6291.0	3.367	0.4954	
6346.6	3.375	0.4954	
6356.0	2.900	0.4956	
6368.0	2.600	0.4956	
6371.0	1.027	0.5525	
6386.0	0.001	0.4991	

Table A.1: The full PREM model parameterisation used throughout this work.